

---

Electronic Thesis and Dissertation Repository

---

10-22-2020 2:00 PM

## Lanthanide Nanoparticles as Contrast Agents for In Vivo Dual Energy Microcomputed Tomography of the Mouse Vasculature

Charmainne Cruje, *The University of Western Ontario*

Supervisor: Drangova, Maria, *The University of Western Ontario*

Joint Supervisor: Gillies, Elizabeth R., *The University of Western Ontario*

A thesis submitted in partial fulfillment of the requirements for the Doctor of Philosophy degree in Medical Biophysics

© Charmainne Cruje 2020

Follow this and additional works at: <https://ir.lib.uwo.ca/etd>

 Part of the [Biomedical Devices and Instrumentation Commons](#), and the [Nanoscience and Nanotechnology Commons](#)

---

### Recommended Citation

Cruje, Charmainne, "Lanthanide Nanoparticles as Contrast Agents for In Vivo Dual Energy Microcomputed Tomography of the Mouse Vasculature" (2020). *Electronic Thesis and Dissertation Repository*. 7395. <https://ir.lib.uwo.ca/etd/7395>

This Dissertation/Thesis is brought to you for free and open access by Scholarship@Western. It has been accepted for inclusion in Electronic Thesis and Dissertation Repository by an authorized administrator of Scholarship@Western. For more information, please contact [wlsadmin@uwo.ca](mailto:wlsadmin@uwo.ca).

## Abstract

Dual energy (DE) computed tomography (CT) has the capability to influence medicine and pre-clinical research by providing quantitative information that can detect nascent lesions, identify perfusion restoration or inhomogeneities within tissues, and recognize the presence of calcium deposits. A wide variety of instrumentation techniques and scan protocols have been developed for DE CT, with a common goal of acquiring a pair of images that reports the attenuation of a given volume to two different x-ray distributions. While DE image acquisition has benefitted from technical advancements in CT, the contrast agents that are used are still predominantly composed of iodinated small molecules, which first appeared in the 1970s. Recent work has demonstrated that lanthanide-based contrast agents have optimized properties for DE decomposition, specifically when using *in vivo* micro-CT scanners. By adopting nanoparticle design strategies that were developed for disease therapeutics and diagnosis, this thesis takes advantage of existing technical advancements in nanotechnology and polymer science to develop a long-circulating contrast agent that can be used for *in vivo* micro-CT and DE micro-CT imaging of the mouse vasculature. The contrast agents that were developed provided a high loading of 100 mg/mL of lanthanide for intravenous injections of mice, and introduced CT contrast enhancements of at least 245 HU. The contrast was maintained for at least 30 minutes, and for as long as one hour, which exceeds the *in vivo* micro-CT scan time requirements. Furthermore, although the synthesis techniques and *in vivo* scans were demonstrated using model lanthanides such as gadolinium and erbium, they can easily be substituted by any other lanthanide. By using a fast-filter switcher to obtain interleaved scans, the feasibility of an *in vivo* DE CT technique that produces decomposed quantitative images of soft tissue, bone and gadolinium-enhanced vessels was demonstrated, which can be used with any pre-clinical, gantry-based micro-CT scanner. When used in combination with the DE CT technique presented, the long-circulating lanthanide contrast agents that were developed in this thesis have the potential to become powerful tools for pre-clinical research on the microvasculature.

## Keywords

Contrast agent, micro-computed tomography, dual energy, nanoparticles, gadolinium, lanthanides, vasculature, long circulation

## Summary for Lay Audience

Cardiovascular disease is studied in mouse models so that treatment and prevention methods can be developed for humans. To study the heart and vessels, 3D images of the mouse body can be obtained using computed tomography (CT). CT uses x-rays, and results into greyscale 3D images that represent the density of the volume being captured. For instance, low density organs like the lungs may appear black or dark grey, and high-density tissue like bone appears white. Since vessels have comparable densities as other soft tissues, they result in similar greyscale values, unless a dye containing a high-density material is injected into the blood. However, dyed vessels appear like bone in CT images and become difficult to distinguish when they are inside or near bone. A technique called Dual Energy CT allows us to discriminate between soft tissue, bone, and dyed vessels. Two chapters of this thesis feature the development of a dye that can be used in living mice so that vessels can be mapped by Dual Energy CT without the need for surgery. The physical properties of the dyes that were developed were modeled after existing pharmaceutical drugs composed of nanoparticles within polymers. Nanoparticles are materials sized in the nanometer range, and polymers are large molecules with repeated subunits. The dye was composed of a type of metal called a lanthanide, which can successfully map mouse vessels post-mortem by Dual Energy CT. A chapter of this thesis demonstrates that the lanthanide dye – when used in combination with Dual Energy CT – gives researchers the ability to distinguish between soft tissue, bone, and dyed vessels in living mice. The presented Dual Energy CT technique and dye design can allow researchers to track anatomical changes in the same mice over time, which can provide new information and further understanding of vascular diseases.

## Co-Authorship Statement

The following thesis contains three manuscripts that are accepted, submitted, and in preparation for scientific journals. Chapter 2 is an original research article entitled “Polymer assembly encapsulation of lanthanide nanoparticles as contrast agents for *in vivo* micro-CT” and was published in *Biomacromolecules* in February 2018. This manuscript was co-authored by Charmainne Cruje, Joy Dunmore-Buyze, Jarret P. MacDonald, David W. Holdsworth, Maria Drangova, and Elizabeth R. Gillies. I was responsible for the experimental design, the synthesis and characterization of all contrast agents, micro-CT scanning and image reconstructions, statistical and data analysis, data interpretation, and finally manuscript preparation. Joy Dunmore-Buyze aided in animal handling and input during manuscript preparation. Jarret P. MacDonald aided in data analysis and manuscript preparation. David W. Holdsworth contributed to data analysis and editorial input. Maria Drangova and Elizabeth R. Gillies, as the principal investigators and supervisors, were responsible for the project’s conception, provided guidance on the experimental design, and contributed editorial input.

Chapter 3 is an original research article entitled “PEG-modified gadolinium nanoparticles as contrast agent for *in vivo* micro-CT” and will be submitted to *Scientific Reports*. This manuscript was co-authored by Charmainne Cruje, Joy Dunmore-Buyze, Eric Grolman, David W. Holdsworth, Elizabeth R. Gillies, and Maria Drangova. I was responsible for the experimental design, the synthesis and characterization of all contrast agents, micro-CT scanning and reconstruction, statistical and data analysis, data interpretation, and finally manuscript preparation. Joy Dunmore-Buyze aided in animal handling and manuscript preparation. Eric Grolman aided in the characterization of the contrast agents and manuscript preparation. David W. Holdsworth contributed to data analysis and editorial input. Elizabeth R. Gillies and Maria Drangova, as the principal investigators and supervisors, were responsible for the project’s conception, provided guidance on the experimental design, and contributed editorial input.

Chapter 4 is an original research article entitled “*In vivo* dual energy micro-computed tomography of the mouse vasculature using gadolinium nanoparticles as contrast agent” and is in preparation for submission to the *Journal of Medical Imaging* in 2020. This manuscript was co-authored by Charmainne Cruje, Danny Poinapen, Paul Picot, Joy Dunmore-Buyze, Eric

Grolman, David W. Holdsworth, Elizabeth R. Gillies, and Maria Drangova. I was responsible for the experimental design, the synthesis and characterization of the contrast agent, micro-CT scanning, statistical and data analysis, data interpretation, and finally manuscript preparation. Danny Poinapen was responsible for the micro-CT image reconstruction. Paul Picot was responsible for the liquid filter fabrication, fast filter switcher and scan protocol modifications. Joy Dunmore-Buyze aided in animal handling and manuscript preparation. Eric Grolman aided in the characterization of the contrast agents and manuscript preparation. David W. Holdsworth contributed to data analysis and editorial input. Elizabeth R. Gillies and Maria Drangova, as the principal investigators and supervisors, were responsible for the project's conception, provided guidance on the experimental design, and contributed editorial input.

## Acknowledgments

First and foremost, I would like to express my sincere gratitude to my supervisors, Dr. Maria Drangova and Dr. Elizabeth R. Gillies, for guiding me during my tenure as a student, as a scientist, and as a person. Dr. Drangova has challenged me every step of the way, even during times when I did not know that I was capable of considerable growth, and always encouraged me to trust in my abilities. Dr. Gillies taught me a very important lesson – that I can find time and resources for things I truly want to accomplish. I would also like to extend my gratitude to my advisor, Dr. David W. Holdsworth. His knowledge and experience in a vast number of fields taught me to approach problems from various angles and his expertise in CT imaging helped me plan experiments.

I would also like to thank the Heart and Stroke Foundation, the Ontario Graduate Scholarship, the Western Graduate Research Scholarship, the Nellie Farthing Fellowship in Medical Sciences, and the Norman E. Nixon Marie Rämö Nixon Award for the financial support.

The Drangova and Gillies lab members have been amazing companions through my journey. Special mentions go to Joy Dunmore-Buyze and Zahra Hosseini, for sharing enjoyable conversations with me and for always being there to support me not only during experiments, but also personally. I would also like to especially thank my mentor, Olivier Nguon, for his undying patience and encouragement through the past five years. I would like to thank Paul Picot for his assistance with the filter exchanger, Aneta Borecki for her help with chemical analyses, and Jennifer Hadway for always finding time in her busy schedule for my animal experiments. Special thanks also go to members of the Holdsworth group, especially Danny Poinapen for his help with image reconstructions, and Chris Norley, Hristo Nikolov, Steven Pollmann, and Jaques Milner for their assistance with the CT scanners and image processing. I would also like to thank Justin Tse for all of the helpful discussions and advice.

Most importantly, I would like to thank my family and friends for their constant love and support. I am forever grateful to my husband for always believing in my abilities, my brother and my sister for encouraging me to explore outside my comfort zone, my father for his relentless curiosity and passion for learning, and last but not least, my mother, whose bravery, strength and dedication inspire me.

# Table of Contents

Abstract.....	ii
Summary for Lay Audience.....	iv
Co-Authorship Statement.....	v
Acknowledgments.....	vii
Table of Contents.....	viii
Abbreviations.....	xii
Variables.....	xv
List of Tables.....	xvi
List of Figures.....	xvii
List of Appendices.....	xxii
Chapter 1.....	1
1 INTRODUCTION.....	1
1.1 X-ray Spectra in DE CT.....	2
1.1.1 Clinical X-ray Spectra.....	2
1.1.2 DE Micro-CT Spectra.....	3
1.2 Tissue and Contrast Material Attenuation.....	5
1.3 Technical Approaches to DE CT imaging.....	8
1.3.1 Acquisition of DE CT Images.....	8
1.3.2 Material Decomposition Algorithm.....	11
1.4 Contrast Agents.....	11
1.4.1 Iodine-based Contrast Agents.....	12
1.4.2 Size-Dependent Pharmacokinetics of Contrast Agents.....	13
1.4.3 Polyethylene Glycol in Intravenous Applications.....	15
1.5 The Development of Nanoparticle-Based Contrast Agents for Micro-CT.....	18

1.5.1	Commercially Available Pre-Clinical Agents .....	18
1.5.2	Metal-Based Contrast Agents .....	20
1.5.3	DE Micro-CT Using Metal-Based Agents.....	22
1.6	Thesis outline .....	25
1.7	References.....	28
Chapter 2.....		39
2	Polymer Assembly Encapsulation of Lanthanide Nanoparticles as Contrast Agents for <i>In Vivo</i> Micro-CT.....	39
2.1	Introduction.....	39
2.2	Experimental Section .....	42
2.2.1	Materials and General Methods .....	42
2.2.2	Nanoprecipitation for Self-Assembly of Polymeric Nanoparticles Containing Erbium Nanoparticles.....	42
2.2.3	Colloidal Stability of the Polymeric Nanoparticles .....	43
2.2.4	Varying the Polymer Content of the Nanoparticles .....	43
2.2.5	General Micro-CT Imaging and Analysis Methods.....	44
2.2.6	Micro-CT Imaging of Erbium-Containing Polymeric Nanoparticles.....	44
2.2.7	Toxicity of the Contrast Agent .....	44
2.2.8	Intravenous Administration of the Contrast Agent and Characterization of Distribution <i>In Vivo</i> .....	45
2.3	Results and Discussion .....	45
2.3.1	Synthesis and Characterization of Oleate-Coated ErNP.....	45
2.3.2	Synthesis and Characterization of Diblock Copolymers .....	46
2.3.3	Polymer Self-Assembly and ErNP Encapsulation.....	48
2.3.4	Redispersion and Characterization of the Lyophilized Polymer-Encapsulated ErNP .....	52
2.3.5	Characterization of the Assemblies Formed with PEG <sub>114</sub> -PLA <sub>53</sub> .....	53
2.3.6	Erbium Content in ErNP Determined <i>Via</i> Micro-CT .....	56

2.3.7	Toxicity of the Contrast Agent .....	56
2.3.8	Distribution of the Contrast Agent <i>In Vivo</i> .....	57
2.4	Conclusions.....	58
2.5	References.....	60
Chapter 3.....		64
3	PEG-Modified Gadolinium Nanoparticles as Contrast Agents for <i>In Vivo</i> Micro-CT	64
3.1	Introduction.....	64
3.2	Methods.....	67
3.2.1	Contrast Agent Preparation and Physical Characterization .....	67
3.2.2	<i>In Vivo</i> Characterization .....	69
3.3	Results.....	70
3.3.1	Physical Characterization.....	70
3.3.2	<i>In Vitro</i> and <i>In Vivo</i> Characterization .....	72
3.4	Discussion.....	77
3.5	Conclusions.....	80
3.6	References.....	81
Chapter 4.....		86
4	<i>In Vivo</i> Dual Energy Micro-Computed Tomography Imaging of the Mouse Vasculature Using Gadolinium Nanoparticles as Contrast Agent .....	86
4.1	Introduction.....	86
4.2	Materials and Methods.....	88
4.2.1	Spectral Modeling .....	88
4.2.2	X-ray Filter Fabrication and Automation .....	88
4.2.3	Image Co-Registration .....	89
4.2.4	Dual-Energy Micro-Computed Tomography .....	90
4.2.5	Image Decomposition and Evaluation of Results.....	91

4.3 Results.....	92
4.3.1 Spectral Modeling.....	92
4.3.2 Image Co-Registration.....	92
4.3.3 Material Decomposition.....	93
4.3.4 Quantification of Tissue Decomposition Results.....	96
4.4 Discussion.....	98
4.5 Conclusions.....	102
4.6 References.....	103
Chapter 5.....	106
5 Conclusion and Future Directions.....	106
5.1 Summary of Thesis Results.....	106
5.2 Future Directions.....	108
5.2.1 Non-rigid Nanoparticles as Contrast Agents.....	108
5.2.2 Imaging Abnormal Tissues <i>via</i> Vascular Permeability.....	109
5.2.3 Evaluating <i>In Vivo</i> Vessel Density.....	110
5.3 Summary.....	110
5.4 References.....	111
Appendix A: Supporting Information for Chapter 2.....	113
Appendix B: Supporting Information for Chapter 3.....	136
Appendix C: Supporting Information for Chapter 4.....	144
Appendix D: Copyright Permissions.....	147
Curriculum Vitae.....	160

## Abbreviations

$^1\text{H}$ NMR	proton nuclear magnetic resonance
ANOVA	analysis of variance
CAC	critical aggregation concentration
$\text{CDCl}_3$	deuterated chloroform
CT	computed tomography
$D$	molar mass dispersity
DE	dual energy
DIPEA	diisopropylethylamine
DLS	dynamic light scattering
DMF	dimethylformamide
DMSO	dimethyl sulfoxide
ECG	electrocardiogram
ErNP	erbium nanoparticles
FDA	Food and Drug Administration
GdNP	gadolinium nanoparticles
GFB	glomerular filtration barrier
HU	Hounsfield units
ICP-MS	inductively coupled plasma-mass spectrometry
kVp	peak kilovoltage

Ln	lanthanide
micro-CT	micro-computed tomography
$M_n$	average molecular weight
mPEG	methyl-terminated poly(ethylene glycol)
MPS	mononuclear phagocytic system
MRI	magnetic resonance imaging
MTT	3-(4,5- dimethylthiazol-2-yl)-2,5-diphenyltetrazolium bromide
NaErF <sub>4</sub>	sodium erbium tetrafluoride nanoparticles
NaGdF <sub>4</sub>	sodium gadolinium tetrafluoride nanoparticles
OA	oleate
PCL	poly(caprolactone)
PDI	polydispersity index of hydrodynamic diameters
PEG	poly(ethylene glycol)
PEtG	poly(ethyl glyoxylate)
PLA	poly(L-lactide)
PPG	poly(propylene glycol)
RES	reticuloendothelial system
ROI	region-of-interest
SIP	self-immolative polymer
TBD	1,5,7-triazabicyclo[4.4.0]dec-5-ene

TEM	transmission electron microscopy
THF	tetrahydrofuran
VMC	virtual monochromatic images
$\epsilon$ -CL	$\epsilon$ -caprolactone

## Variables

$a$	mass fraction of an element in compound
$C$	CT number
$h$	Planck's constant
$f$	volume fraction of a material in a voxel
$Z$	atomic number
$Z_{eff}$	effective atomic number
$\frac{\epsilon}{\rho}$	mass attenuation coefficient due to coherent scatter
$\mu$	linear attenuation coefficient
$\frac{\mu}{\rho}$	total mass attenuation coefficient
$\frac{\sigma}{\rho}$	mass attenuation coefficient due to the Compton effect
$\frac{\tau}{\rho}$	mass attenuation coefficient due to the photoelectric effect
$\nu$	photon frequency

## List of Tables

Table 2.1 SEC and <sup>1</sup> H NMR characterization results of diblock copolymers. <sup>a</sup> Determined by <sup>1</sup> H NMR spectroscopy; <sup>b</sup> Determined by SEC.....	47
Table 2.2 Z-average diameters and PDIs obtained using DLS for the self-assembly of block copolymers without ErNP. Each assembly was prepared and measured in triplicate and the error measurements correspond to the standard deviations on these batches. ....	49
Table 2.3 Characterization data for the polymer-encapsulated ErNP obtained from DLS and ICP-MS both as initially prepared and after lyophilization followed by resuspension in saline. The polymer:ErNP mass ratios were 4:1 unless otherwise indicated. Each assembly was prepared and measured in triplicate and the error measurements correspond to the standard deviations on these batches. <sup>a</sup> Determined by DLS; <sup>b</sup> Determined by ICP-MS where 780 µg/L would correspond to encapsulation of 100% of the Er added during self-assembly.....	50
Table 3.1 Gadolinium content of mouse blood and clearance organs determined by ICP-MS. <sup>a</sup> Reported w/w% were rounded up.....	76
Table 4.1 Quantitative assessment of in vitro DE decomposition. Percentages of correct material classifications are underlined.....	94

# List of Figures

Figure 1.1 Standard energy distributions of photons used by clinical DE CT protocols. a) Energy distributions of incident 80 and 140 kVp photons filtered inherently with 0.2 mm copper and 2.5 mm aluminum, and 140 kVp photons filtered inherently and an additional 0.4 mm of tin. b) Once attenuated by 30 cm of soft tissue, the energy distribution shifts to the right as the beam is hardened. Spectra were simulated using SPEKTR 3.0.<sup>14, 15</sup> ..... 3

Figure 1.2 Standard energy distributions of photons used by pre-clinical DE micro-CT protocols. a) Incident 40 and 80 kVp photons filtered inherently with 0.25 mm beryllium, and 140 kVp photons filtered with additional 0.4 mm of tin. b) Once attenuated by 3 cm of soft tissue, the energy distribution shifts to the right as the beam is hardened..... 4

Figure 1.3 Linear attenuation coefficients of a) soft tissue, cortical bone and iodine, and b) contrast elements as a function of energy. In clinical DE CT, attenuation stays the same for soft tissue and cortical bone, while iodine has lower attenuation with increased energy..... 7

Figure 1.4 Bone subtraction for improved conspicuity of hemorrhages. a) A slice from a conventional CT image from a 75-year-old patient after a fall. b) DE CT produces the bone-subtracted CT image, confirming a subdural hemorrhage (arrow). c) A conventional image and d) the bone-subtracted image from a 59-year-old patient with a headache after a fall indicating a subdural hemorrhage (arrow). The subdural hemorrhages appear subtle in the conventional images (a, c) but more conspicuous on the corresponding bone-subtracted images (b, d) due to the exclusion of surrounding bone. Reused from reference with permission from the Radiological Society of North America.<sup>26</sup> ..... 9

Figure 1.5 Properties of the four classes of iodinated contrast agents. Reused from reference with permission from Elsevier.<sup>48</sup> ..... 13

Figure 1.6 The physical properties of nanoparticles and their effect on tissue accumulation. a) Spherical nanoparticles that are larger than 150 nm accumulate readily in the lung microvessels, liver and spleen. The kidneys clear the smallest nanoparticles.<sup>51</sup> b) The shape of nanoparticles can affect their localization, due to morphology-related flow characteristics that substantially alter circulating lifetimes, cell membrane interactions and macrophage uptake.<sup>63</sup>

c) Surface electrostatic charge influences opsonization, circulation times, and interaction with resident macrophages of RES organs, where positively charged particles are more prone to clearance by macrophages in the lungs, liver and spleen. Neutral and slightly negatively charged nanoparticles have longer circulation lifetimes and lower RES clearance rates.<sup>64</sup> Reused from reference with permission from Springer Nature.<sup>62</sup> ..... 15

Figure 1.7 a) Schematic representation of amphiphilic lipids. I) Amphiphiles consist of hydrophilic and hydrophobic portions. Examples include II) micelle-forming lipids, III) bilayer-forming lipids, IV) PEG–lipids, and (V) cholesterol. b) Amphiphiles can be used to form assemblies such as I) micelles, II) conventional liposomes III) PEG- or cholesterol-stabilized liposomes, IV) microemulsions, V) micelles containing a hydrophobic core, and VI) bilayers on metal or metalloid nanoparticles. Reused from reference with permission from John Wiley and Sons.<sup>89</sup> ..... 17

Figure 1.8 Visual representations of commercially available pre-clinical agents. a) Fenestra LC from MediLumine is an oil-in-water lipid nanoemulsion composed of polyiodinated triglycerides, and its PEG-coated version is Fenestra VC.<sup>104</sup> b) The iodinated ExiTron U, P, and V from Miltenyi Biotec represent the molecular micro-CT agents that are available. The ExiTron nano 6000 and 12000 are alkali earth metal nanoparticle agents that are also supplied by Miltenyi Biotec. c) Nanoprobes specializes in gold nanoparticle agents and fabricate AuroVist 1.9 nm and 15 nm for micro-CT imaging. Schematics and cartoons of the ExiTron series was reused with permission from Miltenyi Biotec,<sup>105</sup> and the structure for Fenestra LC and VC, and AuroVist were based on descriptions or illustrations from MediLumine<sup>106</sup> or Nanoprobes,<sup>107</sup> respectively. .... 19

Figure 1.9 Nanoparticle design of long-circulating a) tantalum- and b) ytterbium-based contrast agents that provide high vascular contrast in micro-CT images of live mice. The ytterbium nanoparticles were encapsulated within DSPE-PEG and have been used to fabricate stealth liposomes,<sup>88</sup> and the PEG-coated tantalum-based nanoparticles were prepared using the sol-gel method. Reused from publications with permission from RSC Publishing and Wiley-VCH (Germany).<sup>112, 115</sup> ..... 21

Figure 1.10 DE CT results from a rat hindlimb perfused with an erbium-based *ex vivo* agent. b) low- and b) high-energy images are decomposed into quantitative c) bone- and d) vessel

volumes. This figure was taken from an article by Tse et al, <sup>114</sup> published under the Creative Commons (CC BY 4.0) - Gold Open Access. ....	24
Figure 2.1 Schematic representation of self-assembled erbium-based nanoparticles as a pre-clinical blood pool contrast agent. ....	42
Figure 2.2 a) Volume diameter distribution of ErNP in THF measured by DLS. b) A TEM image of the oleate-coated ErNP. ....	46
Figure 2.3 Chemical structures of the amphiphilic block copolymers that were used to form the polymeric assemblies. ....	47
Figure 2.4 DLS volume (%) diameter distributions and the corresponding TEM images of polymer-encapsulated ErNP using a) PEG <sub>76</sub> -PPG <sub>22</sub> -PEG <sub>76</sub> , b) PEG <sub>137</sub> -PPG <sub>34</sub> -PEG <sub>137</sub> , c) PEG <sub>45</sub> -PCL <sub>20</sub> , d) PEG <sub>45</sub> -PCL <sub>51</sub> , e) PEG <sub>114</sub> -PCL <sub>51</sub> , f) PEG <sub>114</sub> -PCL <sub>97</sub> , g) PEG <sub>45</sub> -PLA <sub>25</sub> , h) PEG <sub>45</sub> -PLA <sub>52</sub> , i) PEG <sub>114</sub> -PLA <sub>53</sub> , and j) PEG <sub>114</sub> -PLA <sub>122</sub> . ....	51
Figure 2.5 Time-course DLS results at 37 °C for PEG <sub>114</sub> -PLA <sub>53</sub> -encapsulated ErNP post-lyophilization after redispersion in a) saline and b) mouse serum mimic. ....	54
Figure 2.6 TEM images of the PEG <sub>114</sub> -PLA <sub>53</sub> -encapsulated ErNP using polymer:ErNP mass ratios of a) 4:1, b) 2:1, c) 1:1, d) 0.5:1. ....	55
Figure 2.7 Representative coronal micro-CT images showing the heart, liver, aorta, jugular veins and bladder of mice that received contrast agent formulated at a) 1:1 and b) 0.5:1 PEG <sub>114</sub> -PLA <sub>53</sub> :ErNP mass ratios. All times are reported from the completion of the contrast agent injection. In the 2 minute image in a), the external jugular veins (double arrowheads) and the axillary veins (arrows) are clearly visible. ....	57
Figure 3.1 The synthesis of a) PPEG <sub>2000</sub> -GdNP and b) PPEG <sub>5000</sub> -PPEG <sub>1000</sub> -GdNP. OA is displaced by PPEG through ligand exchange, and the solution is purified by dialysis and vacuum sterile filtration to eliminate OA and excess PPEG. ....	68
Figure 3.2 Size distributions and microscopy images of the synthesized GdNPs. a) DLS volume diameter distributions of OA-GdNP in cyclohexane, and PEG <sub>2000</sub> -GdNP and PEG <sub>5000</sub> -	

PEG<sub>1000</sub>-GdNP in water. Representative TEM images of b) OA-GdNP, c) PEG<sub>2000</sub>-GdNP and d) PEG<sub>5000</sub>-PEG<sub>1000</sub>-GdNP. The scale bar in b) applies to all TEM images. .... 71

Figure 3.3 Time-course diameters of resuspended PPEG<sub>2000</sub>-GdNP and PPEG<sub>5000</sub>-PPEG<sub>1000</sub>-GdNP at 37 °C. The contrast agents were redispersed in a) saline and b) a mouse serum mimic for characterization. .... 72

Figure 3.4 Representative coronal micro-CT images showing the heart, liver, jugular veins, and spleen of mice that received contrast agent formulated with a) PPEG<sub>2000</sub>-GdNP and b) PPEG<sub>5000</sub>-PPEG<sub>1000</sub>-GdNP. All times were reported from the completion of the contrast agent injection. In the 5-minute image in a), the blood in the chambers of the heart (circle), liver (arrow) and the external jugular veins (double arrowheads) are clearly visible. In the 2- and 5-day images, the blood pool in the heart is no longer visible, the liver remains visible, and the spleen (arrowheads) becomes visible. Adjacent anatomical slices were shown for the images acquired within 60 minutes, while slices located 1 cm posterior were shown in the 2- and 5-day images, to demonstrate the high contrast in the previously indistinguishable spleen. .... 73

Figure 3.5 Contrast enhancement in the organs of mice that were injected with a) PPEG<sub>2000</sub>-GdNP and b) PPEG<sub>5000</sub>-PPEG<sub>1000</sub>-GdNP displayed similar trends over time, where decreased attenuation in the vasculature was accompanied by increased attenuation in the liver after day 3 (Fig. 3.6). There were no significant differences between daily mass measurements ( $p = 0.30$ ). .... 74

Figure 3.6 Effect of the contrast-agent injection procedure on subject mass. .... 75

Figure 3.7 Representative histology images for control and injected mice taken from tissues after 5 days of injection. Liver tissues appear normal, while the spleen tissues of the injected mice indicate basophilic nuclear contents in the cytoplasm and lower nuclear densities than the control tissue. .... 76

Figure 4.1 DE micro-CT setup for a gantry-based micro-CT. a) Custom 3D-printed mouse bed designed with a bridge over the bed (arrow in a) enables the custom filters to slide reproducibly over the subject. b) The filter switching mechanism, with the filter in the high-energy state. 89

Figure 4.2 Modelled spectral distributions of the unfiltered 90 kVp spectra, and with the addition of the copper or liquid gadolinium filters to produce the low- and high-energy x-rays for DE micro-CT..... 92

Figure 4.3 Representative a) coronal, b) sagittal, and c) axial slices from the difference between non-registered (left) and co-registered (right) images. .... 93

Figure 4.4 Coronal slices of the acrylic phantom containing water, bone, and gadolinium calibrators. Material decomposition resulted in a) water, b) gadolinium, and c) bone volumes. d) Representative slice from the high-energy image. The top scale bar represents percentage compositions for decomposition images and bottom scale bar represents CT contrast in the high-energy image. .... 94

Figure 4.5 Maximum intensity projections through a) the bone and b) gadolinium-enhanced vessels volumes demonstrate the quality of the decomposition. For comparison, MIPs through the high c) and low d) energy volumes are also shown. The window and level were set to optimize visualization of the vessels..... 96

Figure 4.6 Tissue decomposition results averaged from all subjects. Misclassifications are nearly absent for bone in the soft tissue image, and for soft tissue and blood vessels in the bone image..... 97

Figure 4.7 Thick 1.5-cm oblique MIPs of the left pelvic and hindlimb region. The decomposed a) bone and b) gadolinium-enhanced vessels volumes show additional vessels (arrow) originating from the common iliac artery and vein (single arrowhead), apart from the femoral artery and vein (double arrowheads). Smaller vessels are otherwise difficult to identify in the c) low-energy or d) high-energy image. A tight window and level were used to display c) and d) to favor the visibility of blood vessels..... 98

## List of Appendices

Appendix A: Supporting Information for Chapter 2.....	113
Appendix B: Supporting Information for Chapter 3.....	136
Appendix C: Supporting Information for Chapter 4.....	144
Appendix D: Copyright Permissions .....	147

## Chapter 1

### 1 INTRODUCTION

Dual energy (DE) computed tomography (CT) is an imaging technique that can differentiate materials within a given volume using a pair of CT images that were obtained from distinct x-ray spectra.<sup>1,2</sup> DE imaging takes advantage of the change in a material's attenuation of x rays when the energy spectrum is modified.<sup>3</sup> The capability to distinguish between specific materials within imaging volumes is beneficial when differentiating structures that have similar CT attenuation values. For example, the composition of renal calculi can be identified through DE CT by using the inherent difference in x-ray attenuation of each calculus type when the energy spectrum is varied.<sup>4</sup> Another application of DE CT is the identification of calcified plaques within a vessel lumen that contains a vascular contrast agent. In addition to tissue separation, DE CT can also be used to quantify the concentration of the contrast element within a volume.<sup>1</sup> This would enable the detection of revascularization within injured tissues, or the identification of hypoperfusion in tissues. Regardless of the reason for DE CT, the material decomposition results can be used to understand pathologies in more detail than the information acquired from conventional single energy CT, so that further tissue characterization or appropriate disease treatment may proceed.

Recent developments in DE CT have made the acquisition of DE images feasible on clinical scanners and in pre-clinical research. Advancements in clinical DE CT imaging include the development of dual source-dual detector systems,<sup>5</sup> dual layer detectors,<sup>6</sup> and rapid kVp switching,<sup>7</sup> which enables acquisition of DE images in under a minute. In pre-clinical DE CT using micro-CT scanners, spectral tuning can be achieved using filters that can shift the average photon energy to acquire the desired spectra,<sup>8</sup> providing DE images in 10 minutes. Both clinical and pre-clinical cases require the use of a contrast agent, and these are predominantly based on iodine. Iodinated agents have been used in x-ray imaging since the 1970s, as they were initially developed for use in radiography.<sup>9,10</sup> While there are some benefits to using iodine, more effective DE decomposition can be achieved using higher Z elements.<sup>11</sup> Despite developments in the technical aspects of DE CT, there has

been a lag in the parallel development of novel contrast agents for DE CT. This thesis describes the development of a new lanthanide-based contrast agent for use in micro-CT studies of mouse models. Using one of the developed contrast agents, an *in vivo* DE CT technique that produces quantitative images of decomposed soft tissue, bone, and gadolinium volumes is demonstrated, which can be used with any pre-clinical, gantry-based micro-CT scanner. To introduce the topic, I will summarize the principles behind DE CT and the pharmacokinetics of contrast agents.

## 1.1 X-ray Spectra in DE CT

The separation between the low- and high-energy spectrum (*i.e.* spectral separation) is important when using widely available iodinated agents because it maximizes the difference between the low attenuation of the iodine-containing tissues in the high-energy image, and high attenuation in the low energy image due to the K-edge, which will be discussed in the next section. Ideally, DE CT would utilize photons of two energies - one just below and one just above the K-edge of the contrast agent being used.<sup>12</sup> However, available x-ray sources (x-ray tubes) generate polychromatic x-ray spectra composed of a continuous spectrum of bremsstrahlung radiation superimposed with characteristic lines of the tungsten material of the anode. Hence there are two x-ray spectra rather than two distinct photon energies. The maximum energy of the photons is defined by the peak voltage (kVp), while the mean energies are significantly lower.

### 1.1.1 Clinical X-ray Spectra

Typically, in clinical settings, filtered 80 and 140 kVp x-rays are used because they are readily available, and provide optimized spectral separation with standard x-ray tubes.<sup>13</sup> Example normalized spectra of 80 and 140 kVp photons from a standard tungsten tube (filtered by 0.2 mm of copper and 2.5 mm of aluminum) are shown in Figure 1.1A. There is a significant overlap between the energy distributions of the 80 and 140 kVp photons – reflected by their respective mean energies of 51 and 68 keV – necessitating additional filtration. A filter is applied to remove low energy photons from the high energy spectra (*i.e.* harden the beam), thereby decreasing the overlap between the pair of beams. For

example, filtering the 140 kVp photons with 0.4 mm of tin hardens the beam, resulting in a mean energy of 89 keV (Figure 1.1a).

The mean energy is further increased by the patient volume. For example, placing a cylinder of soft tissue with a diameter of 30 cm in the field of the x rays hardens the 80 kVp, 140 kVp and tin-filtered 140 kVp beams, such that the exiting x-rays have higher mean energies (60, 87, and 98 keV, respectively in Figure 1.1b). While there is spectral separation between 80 and 140 kVp beams post beam hardening, the overlap worsens with increasing patient size. Spectra at energies higher than 140 kVp are generally not available with today's tubes but could offer better spectral separation.<sup>13</sup>

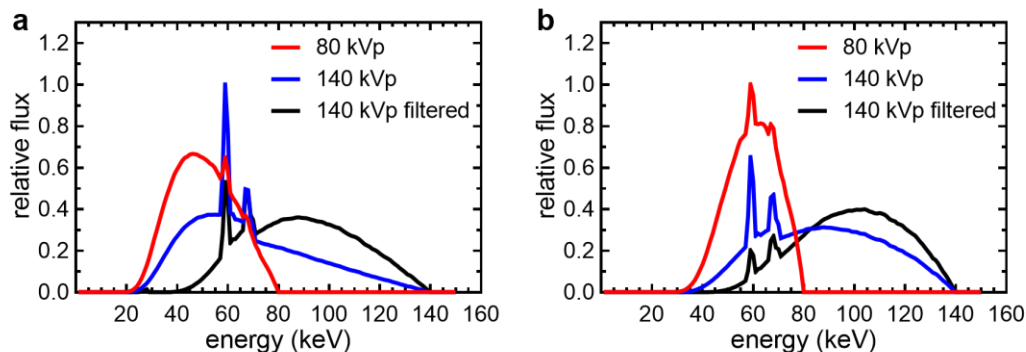


Figure 1.1 Standard energy distributions of photons used by clinical DE CT protocols. a) Energy distributions of incident 80 and 140 kVp photons filtered inherently with 0.2 mm copper and 2.5 mm aluminum, and 140 kVp photons filtered inherently and an additional 0.4 mm of tin. b) Once attenuated by 30 cm of soft tissue, the energy distribution shifts to the right as the beam is hardened. Spectra were simulated using SPEKTR 3.0.<sup>14, 15</sup>

### 1.1.2 DE Micro-CT Spectra

While DE imaging using clinical CT scanners and micro-CT scanners share common x-ray spectra principles, micro-CTs have some limitations. Micro-CT scanners operate in a more limited energy domain (*i.e.* 30-90 kVp being common, with some scanners using tubes capable of generating 120 kVp spectra) than clinical CTs (*i.e.* 30-140 kVp). This limitation makes the use of filters vital in obtaining ample spectral separation between the two spectra's mean energies.<sup>16</sup> DE micro-CT commonly uses 40 and 80 kVp photons,<sup>17</sup> with

SPEKTR 3.0-calculated mean energies of 15 and 28 keV, respectively.<sup>14, 15</sup> Normalized energy distributions of incident DE micro-CT photons are shown in Figure 1.2a for 40 and 80 kVp photons filtered with 0.25 mm of beryllium (inherent), and 80 kVp photons filtered with an additional 0.1 mm of copper. Filtering 80 kVp photons with 0.1 mm of copper reduces overlap between the energy distributions and shifts the mean energy from 28 to 44 keV in the high-energy spectrum. When a cylinder composed of 30 mm of soft tissue is placed in the field of the x-rays to mimic a commonly scanned mouse, higher mean energies of 28 and 42 keV are observed for the inherently-filtered 40 and 80 kVp photons, while the mean energy increases from 44 to only 48 keV for the copper-filtered 80 kVp photons (Figure 1.2b). While material decomposition is feasible with DE images acquired using 40 and 80 kVp photons, these require sequential scans where the low-energy images are acquired separately from high-energy energy scans. Most micro-CTs are not yet capable of simultaneous or near-simultaneous frame acquisitions. So far, the best means to obtaining frames almost simultaneously at each energy is by using an external fast-filter switcher, while the peak energy is kept constant throughout the micro-CT scan.

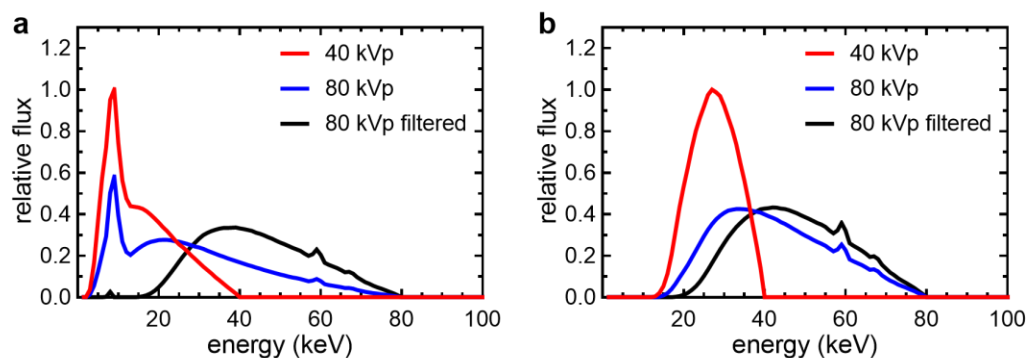


Figure 1.2 Standard energy distributions of photons used by pre-clinical DE micro-CT protocols. a) Incident 40 and 80 kVp photons filtered inherently with 0.25 mm beryllium, and 140 kVp photons filtered with additional 0.4 mm of tin. b) Once attenuated by 3 cm of soft tissue, the energy distribution shifts to the right as the beam is hardened.

## 1.2 Tissue and Contrast Material Attenuation

To allow tissue differentiation in CT, there must be a contrast between the linear attenuations of the tissue of interest and its surroundings. CT number ( $C$ ) is measured in Hounsfield units (HU), and is calculated using the linear attenuation coefficient ( $\mu$ ) of specific tissues to x-rays as follows:

$$C = \frac{\mu_{tissue} - \mu_{water}}{\mu_{water} - \mu_{air}} \times 1000 \quad (1)$$

Water and air are assigned  $C$  of 0 HU and -1000 HU, respectively, by convention. The linear attenuation coefficient is the fraction of photons that is attenuated by a given thickness of material. For the energy range used in CT imaging, this property is the sum of coefficients attributed to the Compton effect ( $\sigma$ ), coherent scatter ( $\varepsilon$ ), and the photoelectric effect ( $\tau$ ).<sup>18, 19</sup> By dividing the linear attenuation coefficient ( $\mu$ ) by the density of the attenuating material ( $\rho$ ), the total mass attenuation coefficient can be calculated (Figure 1.3), along with the contributions due to each event.

$$\frac{\mu}{\rho} = \frac{\sigma}{\rho} + \frac{\varepsilon}{\rho} + \frac{\tau}{\rho} \quad (2)$$

The mass attenuation due to the photoelectric effect, given by  $\frac{\tau}{\rho}$ , is strongly dependent on the atomic number ( $Z$ ) of the material as well as the energy of the incident photons given by  $h\nu$ ,<sup>20</sup> where  $h$  is Planck's constant and  $\nu$  is the photon's frequency (Equation 3).

$$\frac{\tau}{\rho} \propto \left(\frac{Z}{h\nu}\right)^3 \quad (3)$$

Since tissues are composed of compounds rather than single elements, an effective atomic number ( $Z_{eff}$ ) replaces  $Z$  in Equation 3, which is defined as follows (Equation 4).

$$Z_{eff} = \sqrt[7]{\sum_i (a_i Z_i)^2} \quad (4)$$

Since the photoelectric effect strongly increases with atomic number, most tissues in the body, composed mainly of hydrogen ( $Z = 1$ ), carbon ( $Z = 6$ ) and oxygen ( $Z = 8$ ), have a

weak photoelectric effect ( $Z_{eff} = 7.5$ ). Some atoms in the body, such as calcium ( $Z = 20$ ) in bone, have higher atomic numbers, so combined with other bone elements produce  $Z_{eff}$  values between 11.6 and 13.8 and have higher photoelectric effect, while soft tissues have lower  $Z_{eff}$  (7.5). Various soft tissues have only slightly different values from each other. Contrast agents are required to temporarily increase the  $Z_{eff}$  of the soft tissue it localizes in during micro-CT scanning – hence increasing contrast – and allows its differentiation from other soft tissues.

Currently available CT contrast agents are predominantly based on iodine, ( $Z = 53$ ),<sup>21</sup> which was adapted from traditional radiography where the energies are lower. In addition to its high  $Z$ , iodine has a special property known as the K-edge at 33.2 keV. The K-edge is the energy required to liberate an electron from the innermost shell (*i.e.* K-shell) of an atom (Figure 1.3). Since incoming photons have sufficient energies to liberate a K-shell electron, a sudden increase in attenuation occurs at the K-edge. The K-edge of iodine occurs near the low energy region of the CT spectra, which in addition to its higher  $Z$  than soft tissue alone, enhances contrast when the incident photons have energies just above 33.2 keV. Hence, by obtaining a pair of images at 80 and 140 kVp, the attenuation information in the presence of an iodinated contrast agent can be used to decompose a volume image into bone, soft tissue only, and iodine-containing soft tissue. This decomposition can be achieved because bone and soft tissue have similar attenuation properties at both energies, while iodine has higher attenuation in the low energy image than in the high energy image, which reflects the attenuation trends in Figure 1.3a.

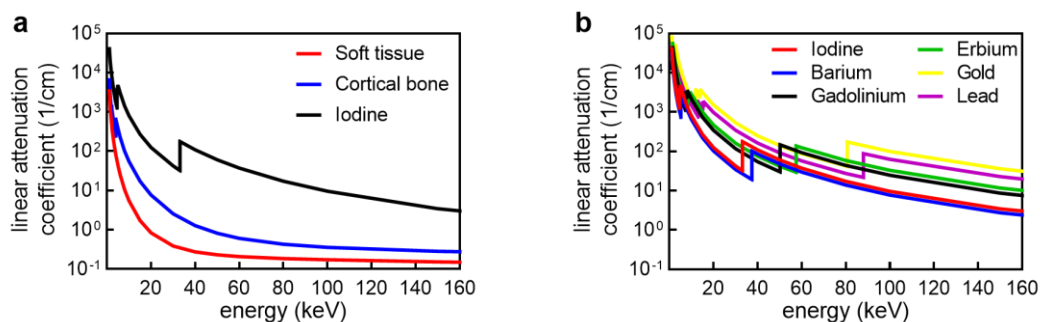


Figure 1.3 Linear attenuation coefficients of a) soft tissue, cortical bone and iodine, and b) contrast elements as a function of energy. In clinical DE CT, attenuation stays the same for soft tissue and cortical bone, while iodine has lower attenuation with increased energy.

Alternatively, a pair of images can be obtained by using photons with energies that are just below and just above the K-edge. When iodinated agents with a K-edge of 33.2 keV are used, the image volume can then be decomposed into tissue components by using *a priori* information that bone and soft tissue have decreasing attenuation properties, while iodine has higher attenuation in the high energy image than in the low energy image. This technique takes greater advantage of the K-edge property since the contrast element demonstrates an opposite attenuation trend as endogenous materials in the body. However, it is difficult to obtain photons below the K-edge of iodine in the clinical setting, as most photons with energies below 33.2 keV are absorbed by the patient volume, contributing only to radiation dose, and not image contrast. An alternative method to obtain mean energies below and above the K-edge is to use elements with higher K-edges than iodine. Figure 1.3b shows the linear attenuation coefficients of high-density elements that have higher  $Z$ , and thus have more optimized K-edge energies for DE CT compared to iodine. Reported work on the use of other elements as contrast materials in DE CT is discussed in the contrast media section of this review. The selection of contrast material should be considered upon evaluating the technical capabilities of existing dual energy scanners, and in particular their spectral separation methods.

## 1.3 Technical Approaches to DE CT imaging

### 1.3.1 Acquisition of DE CT Images

#### 1.3.1.1 Acquisition in Clinical CTs

The simplest method of acquiring DE CT images is through sequential imaging, where a separate rotation of the source and detector is required per energy. This method of acquiring DE images would be accessible to current installations of scanners, as the only requirement would be an image registration method between the pair of scans and the use of filters (*i.e.* metal foils mounted at the x-ray tube port). In clinical scanners, it also requires additional table movement per energy. Hence, sequential scans are more susceptible to subject movement in between energies. Although clinical scans can be acquired in under a minute, contrast agent localization can vary in between scans. For example, a blood pool contrast agents may preferentially localize in the vasculature during the first scan, while it may have increased concentration in the kidneys in the second scan.<sup>22, 23</sup>

Technical developments in CT have made simultaneous and near-simultaneous acquisition of DE images in clinical imaging feasible. Dual source-dual detector systems that are 90° apart within a single bore have been developed by Siemens with the SOMATOM Definition Drive, Flash and Force.<sup>5</sup> Rapid kVp switching can be achieved with the GE Gsi Xstream, where a cycle time as fast as 0.25 ms per kVp per angle is achievable.<sup>7</sup> Dual layer detectors are also available in Philips scanners with spectral detector computed tomography, where the first layer of detectors absorbs low energy photons and the second layer absorbs high energy photons.<sup>6</sup> As Petersilka and co-authors have reported, while there is an angular offset between both spiral paths for dual source systems,<sup>24</sup> the advantage in acquiring DE projections simultaneously lies in the fact that the volume is in the same state in low and high energy images. This approach minimizes image artifacts related to patient movement. Simultaneous image acquisition also ensures that the subject organs are in the same exact state in both the low-energy and high-energy image

### 1.3.1.2 Clinical Application of DE CT

The utility of DE CT in clinical applications and in pre-clinical research are well-described, and the accessibility of processed images to users with no additional time or special setup procedures has facilitated the translation of DE CT into clinical settings.<sup>25, 26</sup> For example, the Sodickson group in the Brigham and Women's Hospital uses the Dual-source dual-detector Somatom Definition Flash scanner to detect subtle subdural hematoma by observing the bone-removed images (Figure 1.4).<sup>27</sup>

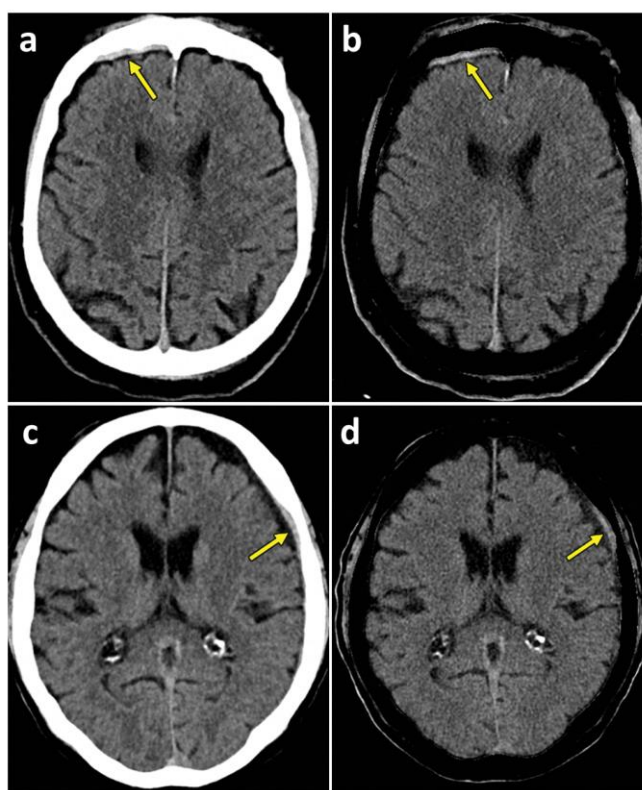


Figure 1.4 Bone subtraction for improved conspicuity of hemorrhages. a) A slice from a conventional CT image from a 75-year-old patient after a fall. b) DE CT produces the bone-subtracted CT image, confirming a subdural hemorrhage (arrow). c) A conventional image and d) the bone-subtracted image from a 59-year-old patient with a headache after a fall indicating a subdural hemorrhage (arrow). The subdural hemorrhages appear subtle in the conventional images (a, c) but more conspicuous on the corresponding bone-subtracted images (b, d) due to the exclusion of surrounding bone. Reused from reference with permission from the Radiological Society of North America.<sup>26</sup>

While it is challenging to find publications that disclose which DE CT protocols are used for patient diagnosis or disease management, further clinical applications of DE CT include assessing pulmonary thromboembolism,<sup>28</sup> bone marrow edema,<sup>29, 30</sup> gout,<sup>31, 32</sup> and vascular imaging.<sup>33-36</sup> Conceivably, the most widely attractive capability of DE CT is that it can overcome the partial volume effect, specifically using the iodine image, which can indicate contrast agent localization within soft tissue or bony structures. The partial volume effect is the averaging of attenuation coefficients in voxels composed of more than one material, which results in a discrete linear attenuation that actually corresponds to the average of the attenuation of subvoxel materials (*i.e.* structures with dimensions smaller than the imaging resolution), or to that of a border between materials with very different attenuation properties.<sup>37</sup> The presence of subvoxel lesions or vessels can be detected in the iodine image, which would otherwise not be visible in conventional single energy images. Specifically, the detection of subvoxel vessels can be useful to track perfusion within tissues, which can be used to identify regions that have abnormally low blood flow.<sup>38, 39</sup>

### 1.3.1.3 Spectral Separation in Micro-CT Scanners

Contrary to most clinical CT filtration techniques, where metal foils are mounted at the x-ray tube port, a cylindrical shell filter that surrounds the scan bed yet fits within the scanner bore – controlled by an external filter switcher – has been used to achieve spectral separation in pre-clinical DE CT. The addition of a mechanism to mount and switch the filters on the tube port may interfere with the gantry balance and the normal operation of the scanner. This approach to filtration avoids modifications to the scanner and is compatible with gantry-based scanners. The cylindrical shell filters the x-rays before and after the object is scanned, providing a total attenuation that is equivalent to a mounted filter with the same path length. This technique was demonstrated in an *ex vivo* study that successfully decompose soft tissue, bone, and contrast agent in the microvessels into quantitative images, and is described in Section 1.5.3.<sup>40</sup> This technique is also applied in Chapter 4 of this thesis.

### 1.3.2 Material Decomposition Algorithm

DE CT scanners have the capability to produce routine diagnostic images and material decomposition images.<sup>41, 42</sup> Routine diagnostic images are either created through a combination of the acquired pair of images to produce a blended image that simulates a standard 120 kVp acquisition, or virtual monochromatic (VMC) images that simulate a scan that was obtained at a single energy. VMC images can be simulated from 40-140 keV but commonly provide more reliable attenuation measurements compared to polychromatic CT. VMC images can be customized to a specific energy level for various clinical applications, but are commonly 45-55 keV for angiography, 60-75 keV for soft tissue assessment, or 95-140 keV for metal artifact reduction.<sup>41</sup>

Material decomposition images calculate the concentrations of each material that would be necessary to produce the measured attenuation within each image voxel. The effective linear attenuation coefficient ( $\mu$ ) measured in each voxel of a CT image, can be expressed as a linear combination of the attenuation coefficients of the tissues within the voxel, multiplied by their volume fraction ( $f$ ).<sup>43</sup> For example, in a voxel containing soft tissue, iodine, and fat, the linear attenuation of each material ( $\mu_{soft\ tissue}$ ,  $\mu_{iodine}$ , and  $\mu_{fat}$  respectively) contributes to the total linear attenuation coefficient of that voxel  $\mu_V$  as shown in Equation 5.

$$\mu_{soft\ tissue}f_{soft\ tissue} + \mu_{iodine}f_{iodine} + \mu_{fat}f_{fat} = \mu_V \quad (5)$$

Each voxel is assumed to contain a fraction of soft tissue ( $f_{soft\ tissue}$ ), fat ( $f_{fat}$ ) and iodine ( $f_{iodine}$ ).

## 1.4 Contrast Agents

Contrast agents are commonly administered intravenously for *in vivo* vascular imaging or for tissue-specific imaging *via* passive targeting. After intravenous injection, the contrast agent in clinical CT is typically present at peak concentrations within minutes, which is often too short for use with pre-clinical micro-CT scanners that can capture the smallest blood vessels (*i.e.* at least 10 minutes of scan time to resolve down to tens of microns). In addition, small animals, which are commonly used in pre-clinical research, have much

faster clearance rates than humans. Small-molecule agents clear from the blood pool to the kidneys within seconds of intravenous administration.<sup>44-46</sup> As the Pornrini group demonstrated, while small-molecule contrast agents can provide high kidney contrast, these are not ideal for imaging of other tissues or organs.<sup>46</sup> For instance, imaging the vasculature would require long-circulating contrast agents, while hepatic imaging would require contrast agent localization in the liver.<sup>47</sup> Nonetheless, both scenarios require the evasion of rapid agent clearance from the blood pool through the kidneys.

### 1.4.1 Iodine-based Contrast Agents

Clinical CT agents are predominantly based on iodine and were primarily developed for use in radiography. These contrast agents were adapted for use in CT imaging due to their wide availability and US Food and Drug Administration (FDA) approved status, while pre-clinical iodinated versions were developed, despite iodine not being an ideal element for achieving higher contrast in CT or micro-CT imaging.<sup>11</sup> Clinical iodinated agents are divided into four main classes depending on their ionization state (ionic or nonionic) and whether they are monomeric or dimeric (Figure 1.5).<sup>48</sup> Between the two types of ionization states, ionic agents such as Diatrizoate and Ioxaglate have been shown to be more toxic and could potentially contribute to contrast media-induced neuropathy once localized in the kidneys, which makes non-ionic contrast agents (*i.e.* neutral in charge such as Iohexol and Iodixanol) more attractive. A contrast agent's fate once injected into the bloodstream is determined by electrostatic charge and size.<sup>48, 49</sup>

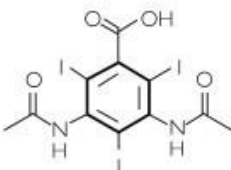
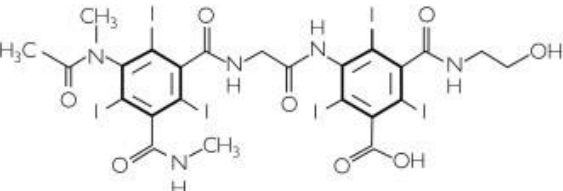
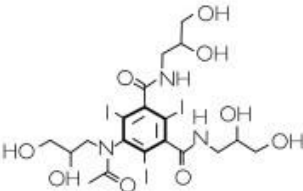
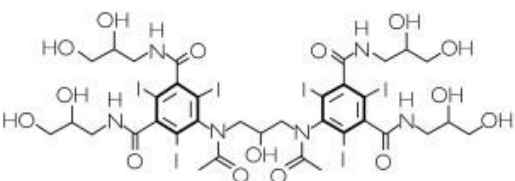
Ionization	Polymer	Structure	Example	Osmolarity
Ionic	Monomer		Diatrizoate (Hypaque)	1400-2400 mOsm/L
Ionic	Dimer		Ioxaglate (Hexabrix)	600 mOsm/L
Nonionic	Monomer		Isohexol (Omnipaque)	290-860 mOsm/L
Nonionic	Dimer		Iodixanol (Visipaque)	280 mOsm/L

Figure 1.5 Properties of the four classes of iodinated contrast agents. Reused from reference with permission from Elsevier.<sup>48</sup>

### 1.4.2 Size-Dependent Pharmacokinetics of Contrast Agents

The removal of intravenously injected materials from circulation (*i.e.* clearance) is determined by the molecule's size and surface charge.<sup>48</sup> The glomerular filtration barrier (GFB) in the kidneys controls the passage of molecules from the blood pool into the kidneys. The GFB endothelial cells are electrostatically negative in charge. Hence, it is believed that molecules with neutral and negatively charged surfaces have much lower chances of passing the barrier and have higher retention than molecules with positively charged surfaces. The size of the fenestrations also limits the size of the molecules that can pass.<sup>50</sup> Renal fenestrations can be 6-8 nm in diameter which allow passage of molecules that are smaller than 6–8 nm (Figure 1.6). Contrast agents that are large enough to evade renal clearance can potentially exhibit longer circulation times during micro-CT imaging.

Nanoparticles – materials with diameters in the nanometer range – can either be composed of polymers with pendent cargo along the chains, or can have a core-shell design, where the cargo is in the core and is encapsulated by a stabilizing molecule. The cargo is elements or molecules of interest, which can be contrast agents or drug molecules. As mentioned previously, for pre-clinical imaging, injected materials must evade renal clearance to have a chance to circulate in vessels. While renal fenestrations are 6-8 nm in diameter,<sup>51</sup> a conservative size cut off that is used to evade renal clearance is 10 nm.<sup>52-54</sup> Hence, to avoid side effects that may be associated with kidney accumulation or to accomplish extrarenal functions, such as blood pool imaging, tumor imaging or drug delivery, nanoparticles larger than 10 nm in size are typically studied. On the other hand, a variety of upper size limits have been declared for intravascular applications to avoid blood flow interruption in the smallest vessels,<sup>55</sup> with the least conservative being an upper size restriction of 1  $\mu\text{m}$ .<sup>56</sup> However, an upper size limit of 200 nm is commonly reported due to the success of smaller nanoparticles entering abnormal tissues with increased vascular permeability and altered interstitial environment.<sup>57-59</sup>

The reticuloendothelial system (RES) is responsible for removing nanoparticles that are larger than 10 nm. The reticuloendothelial system (RES) is composed of phagocytic and pinocytic cells that are found in the blood pool and within tissues, and is responsible for removing foreign material from vascular circulation.<sup>60, 61</sup> The RES includes phagocytic monocytes in the blood, and macrophages in connective tissue, lymphoid organs (*e.g.* spleen), bone marrow, bone, liver, and lung, and pinocytic liver sinusoidal endothelial cells. The RES sequesters removed materials into the liver, spleen and lungs, based on the nanoparticle's size, shape and surface charge (Figure 1.6).<sup>62</sup> For instance, nanospheres were found to evade clearance longer than nanocylinders and nanodiscs, with dominant clearance by the liver, as previously demonstrated in rigid metal core nanoparticles.<sup>63</sup> While biodistribution differences have been attributed to geometry-dependent flow characteristics,<sup>63</sup> it is undeniable that the surface area to volume ratio of these nanoparticles influence their exposure to clearance mechanisms, and the fact that nanospheres have lower ratios potentially decrease their chances of being detected. The electrostatic charge also affects clearance rates, where positively charged nanoparticles are easily detected by RES cells, which are inherently negatively charged.

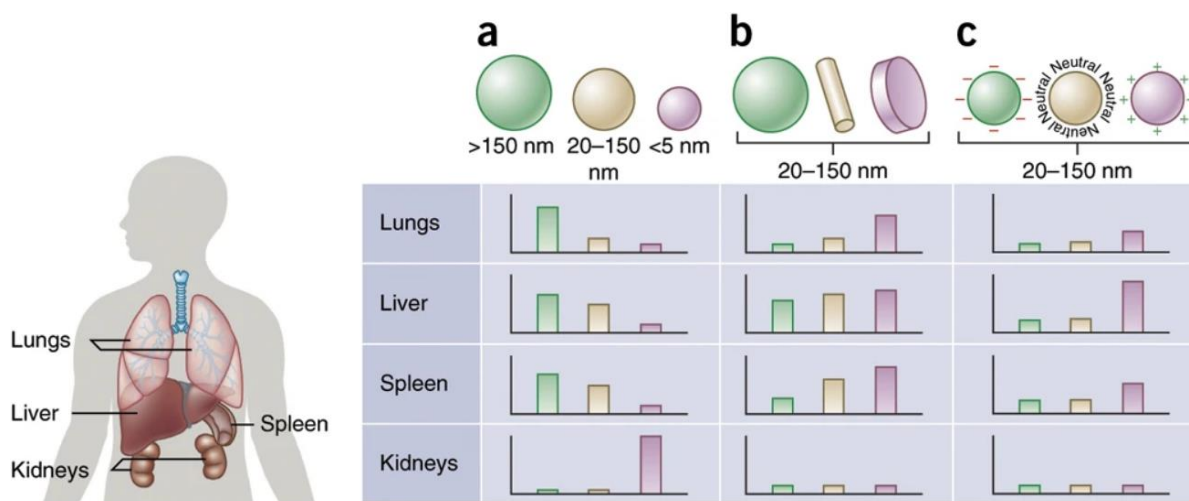


Figure 1.6 The physical properties of nanoparticles and their effect on tissue accumulation. a) Spherical nanoparticles that are larger than 150 nm accumulate readily in the lung microvessels, liver and spleen. The kidneys clear the smallest nanoparticles.<sup>51</sup> b) The shape of nanoparticles can affect their localization, due to morphology-related flow characteristics that substantially alter circulating lifetimes, cell membrane interactions and macrophage uptake.<sup>63</sup> c) Surface electrostatic charge influences opsonization, circulation times, and interaction with resident macrophages of RES organs, where positively charged particles are more prone to clearance by macrophages in the lungs, liver and spleen. Neutral and slightly negatively charged nanoparticles have longer circulation lifetimes and lower RES clearance rates.<sup>64</sup> Reused from reference with permission from Springer Nature.<sup>62</sup>

### 1.4.3 Polyethylene Glycol in Intravenous Applications

In the 1970s, appending a fragment of PEG to nonhuman bioactive proteins for therapy was found to substantially reduce the adverse immunological responses produced by these proteins.<sup>65, 66</sup> By coupling the proteins with a methyl-terminated PEG (mPEG), researchers also found that the circulation times of the short-lived human derived proteins were improved. Thus, modification of proteins with PEG – referred to as PEGylation – provided a pathway for the development of protein pharmaceuticals.<sup>67-73</sup> PEGylation was also extended to novel drug delivery carriers, such as nanoparticles and liposomes, to overcome their RES uptake, leakage of cargo, colloidal stability, and tissue toxicity. Specifically, by evading renal clearance and RES uptake, and demonstrating colloidal stability in the blood pool, PEGylated materials can have long residence times in the vasculature and have a

higher chance of arriving at their target destinations.<sup>74-79</sup> The most reliable strategy to prevent cellular recognition and protein adsorption is the immobilization of PEG at the particle surface. PEG is an ideal hydrophilic polymer with a flexible, unbranched structure, and terminal hydroxyl groups available for activation and linking to proteins and particles.

Hydrophobic particles are removed faster from circulation than hydrophilic particles, due to their colloidal instability in the blood pool and affinity to immune system markers that promote their removal from circulation.<sup>80-82</sup> Several therapeutic drugs (*e.g.* paclitaxel, doxorubicin) are hydrophobic, and contrast elements (*e.g.* iodine, gadolinium) are commonly incorporated into hydrophobic nanoparticles. The detection of nanoparticles by the immune system *via* protein markers (*e.g.* opsonin) occurs with greater affinity on hydrophobic surfaces than on hydrophilic surfaces, facilitating RES clearance.<sup>80</sup> Stealth shielding on the surface can reduce the recognition of these particles, increasing circulation time from a few seconds to hours.<sup>83</sup> Instead of the direct PEGylation of hydrophobic surfaces, stabilization can be achieved by adsorption or chemical binding of amphiphilic molecules.<sup>84-87</sup> An amphiphilic molecule comprises a hydrophobic part, such as a lipid that will interact with the hydrophobic cargo, and a hydrophilic part, such as PEG, that protrudes into the aqueous environment to protect the cargo from immune system detection. Various designs have been explored to achieve prolonged circulation times of nanoparticles using amphiphilic molecules (Figure 1.7). Stabilized liposomes, or PEG-coated liposomal nanoparticles (Figure 1.7B) have been demonstrated to achieve prolonged circulation times.<sup>88</sup> These nanoparticles been dubbed as stealth liposomes and can be fabricated using lipid conjugates of PEG, such as PEG-destearoyl-phosphatidylethanolamine (PEG-DSPE).<sup>88</sup>

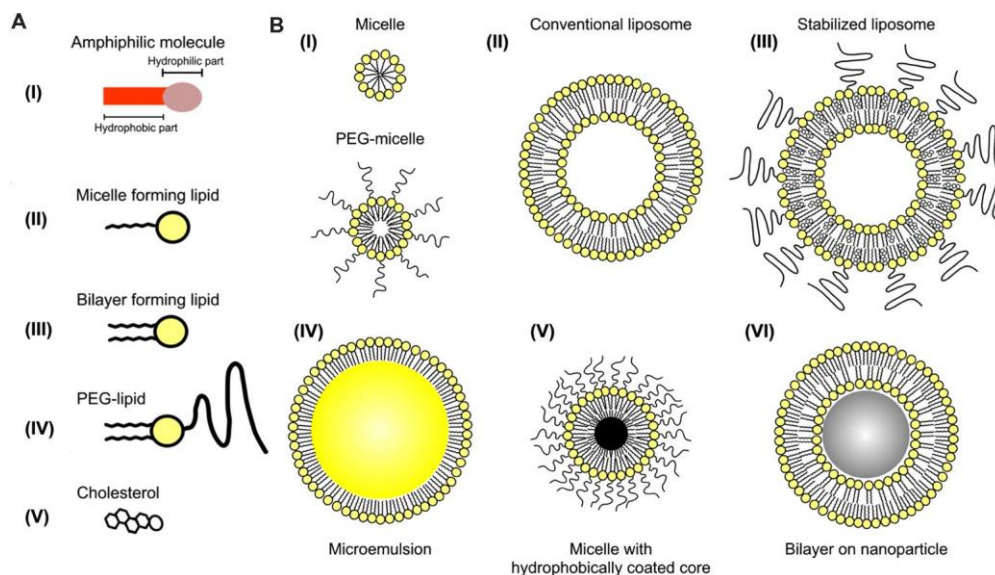


Figure 1.7 a) Schematic representation of amphiphilic lipids. I) Amphiphiles consist of hydrophilic and hydrophobic portions. Examples include II) micelle-forming lipids, III) bilayer-forming lipids, IV) PEG-lipids, and V) cholesterol. b) Amphiphiles can be used to form assemblies such as I) micelles, II) conventional liposomes III) PEG- or cholesterol-stabilized liposomes, IV) microemulsions, V) micelles containing a hydrophobic core, and VI) bilayers on metal or metalloid nanoparticles. Reused from reference with permission from John Wiley and Sons.<sup>89</sup>

A wide range of polymer synthesis techniques are now available and permit the fabrication of polymers with diverse properties,<sup>90</sup> including customized chain lengths,<sup>91</sup> the capacity to link functional groups or cargo for specific *in vivo* purposes,<sup>92</sup> amphiphilicity through polymer conjugation,<sup>93</sup> and even the ability to degrade upon exposure to specific stimuli.<sup>94</sup> While the initial development of *in vivo* agents was dominated by liposomal formulations or PEG-linked lipids, there has been a recent surge in nanoparticles encapsulated with amphiphilic diblock copolymers, containing hydrophobic cargos. Therapeutic drugs have been predominantly reported as cargo of such carriers, and some metal-core nanoparticles that have been synthesized with hydrophobic surfaces can also be encapsulated and have been shown to achieve prolonged circulation times in small animals. In these polymers, PEG is coupled with hydrophobic polymers such as polylactide, polycaprolactone, or poly(propylene glycol).<sup>95-97</sup>

## 1.5 The Development of Nanoparticle-Based Contrast Agents for Micro-CT

### 1.5.1 Commercially Available Pre-Clinical Agents

The prolonged circulation times of nanoparticle-based therapeutics, and their abilities to target the liver instead of the kidneys, have inspired the development of nanoparticle-based contrast agents. There are commercially available contrast agents that are used for pre-clinical imaging by micro-CT, and these are based on iodine, alkaline earth metals, and gold (Figure 1.8).

MediLumine's Fenestra LC and VC are composed of oil-in-water lipid nanoemulsions composed of the polyiodinated triglyceride 1,3-bis-[7-(3-amino-2,4,6-triiodophenyl)-heptanoyl]-2-oleoyl glycerol, which contains 50 mg/mL of iodine (Figure 1.8a), while Miltenyi Biotec currently has agents containing greater iodine concentrations of at least 120 mg/mL composed of iodinated small molecules or covalently bound iodine on a polymer backbone (Figure 1.8b). Alkaline earth metal nanoparticles – identified as barium in some publications<sup>98, 99</sup> – were developed by the same company and provide promising CT contrast and circulation times. Like their drug delivery vehicle analogues, non-PEGylated nanoparticles containing iodine evaded renal clearance and localized in the liver, making excellent liver contrast agents (i.e. Fenestra LC), while small molecule agents localize in kidneys for renal imaging (Figure 1.8). Once coated with PEG, long circulation times were observed in small animals. In particular, Fenestra VC, ExiTron nano 6000, ExiTron nano 12000, and AuroVist 15 nm (Figure 1.8c) demonstrate high contrast in the blood pool for hours, which well exceeds micro-CT imaging. AuroVist 15 nm and 1.9 nm can contain up to 200 mg/mL of gold nanoparticles in saline.

Unlike clinically available agents, the companies that manufacture these pre-clinical agents do not make the precise chemical formulations, let alone the nanoparticle type, available, which makes it difficult to predict their performance as micro-CT agents. For instance, the structures of Binitio Biomedical's eXIA NANO, eXIA 160/160XL, and eXUS, which are pre-clinical micro-CT agents based on barium, iodine, and an unknown element, respectively,<sup>100</sup> are not readily available to non-customers, although some of their structures

have been stated in previous publications.<sup>101, 102</sup> Comprehensive studies comparing the vascular contrast enhancement, circulation time, and biodistribution of these contrast agents have been reported,<sup>101, 103</sup> so scientists may purchase agents that cater to their research requirements.

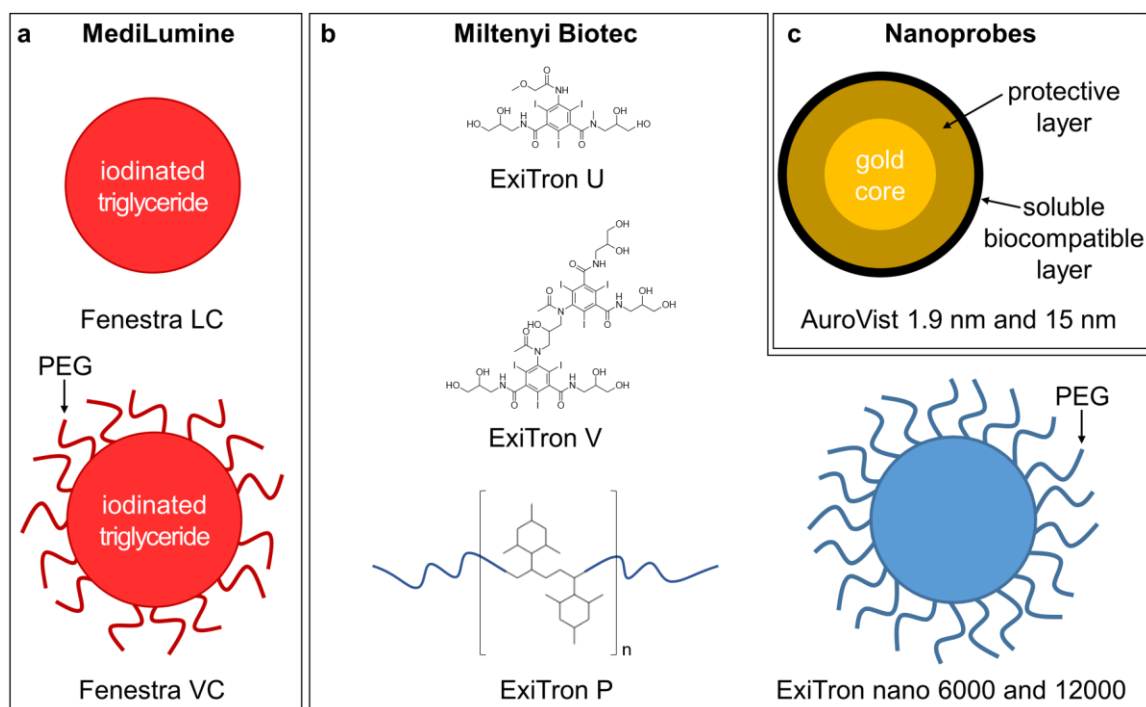


Figure 1.8 Visual representations of commercially available pre-clinical agents. a) Fenestra LC from MediLumine is an oil-in-water lipid nanoemulsion composed of polyiodinated triglycerides, and its PEG-coated version is Fenestra VC.<sup>104</sup> b) The iodinated ExiTTron U, P, and V from Miltenyi Biotec represent the molecular micro-CT agents that are available. The ExiTTron nano 6000 and 12000 are alkali earth metal nanoparticle agents that are also supplied by Miltenyi Biotec. c) Nanoprobes specializes in gold nanoparticle agents and fabricate AuroVist 1.9 nm and 15 nm for micro-CT imaging. Schematics and cartoons of the ExiTTron series were based on product descriptions from Miltenyi Biotec,<sup>105</sup> and the structure for Fenestra LC and VC, and AuroVist were based on descriptions or illustrations from MediLumine<sup>106</sup> or Nanoprobes,<sup>107</sup> respectively.

### 1.5.2 Metal-Based Contrast Agents

Over the past several years, metal nanoparticle agents have been developed that incorporate a wide variety of elements for CT imaging. The most commonly studied metal nanoparticles for micro-CT consist of gold. Gold nanoparticles produce greater CT enhancement than iodinated agents because of the high atomic number of gold.<sup>108, 109</sup> Gold nanoparticles are particularly promising for *in vivo* imaging applications – hence the availability for purchase – because gold is very inert and gold nanoparticles can be readily synthesized and modified with several types of surface-linked molecules to render them biocompatible.<sup>110, 111</sup> While it provides the highest contrast for all x-ray energies relevant due to its high density, its K-edge of 80.7 keV falls in the middle of the clinical CT spectra and closer to the upper limit of most *in vivo* micro-CT scanners, making it less ideal than other metals for DE micro-CT imaging.

Apart from gold, metal-based agents such as transition metals have been reported. A recent study by Chakravarty et al. presented the fabrication and characterization of PEG-coated tantalum oxide nanoparticles by a sol–gel method (Figure 1.9a).<sup>112</sup> One of the synthesized agents can provide vascular contrast in micro-CT images (> 50 HU) for at least 3 hours when using a peak voltage of 90 kVp. Although tantalum is high density and has a K-edge of 67 keV, its K-edge is still slightly higher than the average micro-CT energies (*i.e.* 50-60 keV).

Another class of metals that is ideally suited for micro-CT is the lanthanides (*e.g.* gadolinium, erbium).<sup>11</sup> They have k edges of 38-64 keV,<sup>113</sup> some of which coincide with the peaks of the x-ray energy distributions typically used in high-resolution *in vivo* micro-CT scanners. The ideal position of the K-edges offers potential to increase contrast attenuation for single-energy micro-CT scans<sup>11</sup> and, more importantly, offers the opportunity to match the available x-ray spectrum and contrast agent in dual-energy micro-CT.<sup>114</sup>

Lanthanide agents designed for *in vivo* vascular micro-CT are not commercially available, but studies are emerging demonstrating the utility of PEG-modified lanthanide nanoparticles in microimaging.<sup>115-118</sup> To prepare lanthanides that can be used in the *in vivo*

milieu in small animals, common methods include the use of clinically-available MRI agents to formulate nanoparticles that evade rapid renal clearance, or the synthesis of hydrophobic lanthanide nanoparticles encapsulated within a shell of phospholipid-polymer conjugate molecules (*i.e.* liposomes or lipid nanoparticles). For instance, Liu et al. demonstrated that DSPE-PEG can be used to encapsulate sodium ytterbium tetrafluoride nanoparticles at a concentration of 70 mg/mL. The resulting agent provides high vascular contrast for at least 20 minutes when imaging at a tube potential of 120 kVp (Figure 1.9b).<sup>108</sup> Although ytterbium has a K-edge of 61.3 keV, which is slightly higher than mean energies of the micro-CT spectrum, any synthesis method that is presented for lanthanides is transferrable to the rest of the elements within the series due to their very similar chemistry. However, like other lanthanide contrast agent publications that demonstrate the utility of polymer-encapsulated lanthanides in micro-CT,<sup>115, 116</sup> their lanthanide concentrations need improvement as the agents have typically only been formulated at less than 100 mg/mL of lanthanide (*i.e.* 1 g/kg body weight in small animals).

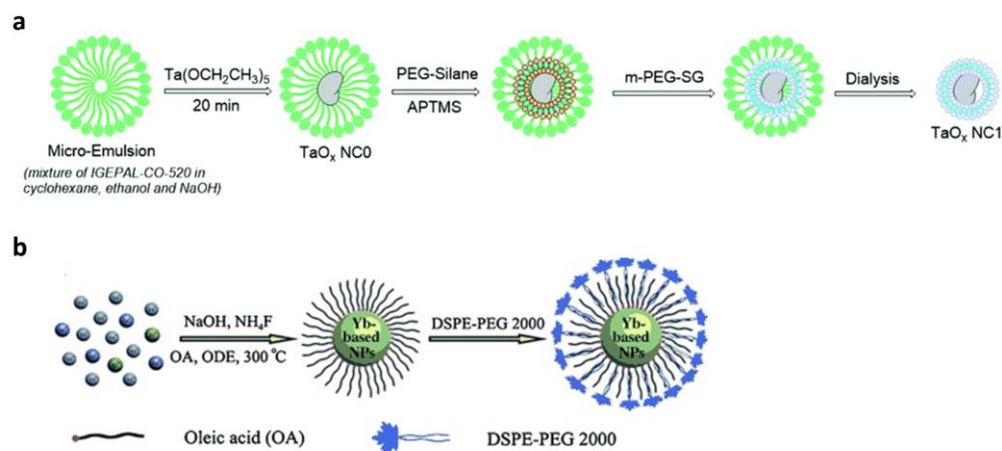


Figure 1.9 Nanoparticle design of long-circulating a) tantalum- and b) ytterbium-based contrast agents that provide high vascular contrast in micro-CT images of live mice. The ytterbium nanoparticles were encapsulated within DSPE-PEG and have been used to fabricate stealth liposomes,<sup>88</sup> and the PEG-coated tantalum-based nanoparticles were prepared using the sol-gel method. Reused from publications with permission from RSC Publishing and Wiley-VCH (Germany).<sup>112, 115</sup>

### 1.5.3 DE Micro-CT Using Metal-Based Agents

Of the metal nanoparticles that have been reported, gold and metals from the lanthanide series have been used in DE micro-CT. Despite the K-edge of gold being too high (81 keV) for ample spectral separation in a large installed base of micro-CT scanners, it can separate low and high energy photons sufficiently in clinical scanners that use 80 and 140 kVp. It has also been demonstrated to perform well when using 40 and 80 kVp photons, which most micro-CTs are capable of producing.<sup>119</sup> In this latter case, it functioned similarly to iodine, where a decrease in attenuation was observed with higher energy photons. Rather than using the K-edge property of the contrast element, the high density of gold was taken advantage of to decompose tissue volumes.

In pre-clinical research using small animals, K-edge DE decomposition has been demonstrated successfully by *ex vivo* agents using lead- and lanthanide-based contrast agents. The lead-based Microfil MV 122 (Flowtech Inc, USA), which is a commercially available *ex vivo* contrast agent, is widely used in pre-clinical research. By using the K-edge of lead at 88 keV, material-specific decomposition that utilized x-ray spectra below and above the K-edge (*i.e.* using 96 and 140 kVp photons) was demonstrated.<sup>120</sup> Microfil is used in pre-clinical studies that image the vasculature with single-energy micro-CT,<sup>121-123</sup> but as for DE imaging, its K-edge may be more ideal for clinical scanners. In addition, the toxicity of lead does not make it a feasible *in vivo* contrast element, nor does it make it ideal for *ex vivo* purposes due to handling hazards for the researchers.

Recently, an *ex vivo* agent that is analogous to Microfil was developed, except it contains erbium, which is a lanthanide, instead of lead.<sup>124</sup> Lanthanides have K-edges between 38 and 64 keV that fall in the middle of the energy range most high-resolution *in vivo* micro-CT scanners produce.<sup>113</sup> When using lanthanides in DE imaging, K-edge decomposition can be performed. These K-edge energies also coincide with mean energies most single energy CT or micro-CT imaging protocols use. The erbium-based *ex vivo* agent was composed of nanoparticles with diameters in the nanometer range (*i.e.* nominal diameter in the tens of nm), and hence did not extravasate from the vessels when perfused intravenously post-mortem. Moreover, the use of a curing agent permitted the agent to remain in the lumen, such that CT contrast values of at least 4000 HU were measured in

the inferior vena cava of mice. The K-edge of erbium at 57.5 keV permitted K-edge decomposition when used in DE micro-CT scans of rat hindlimbs (Figure 1.9).<sup>114</sup> The DE images were acquired with erbium-filtered 70 kVp and copper-filtered 90 kVp, with the goal of using the filters to optimize spectral separation by minimizing the overlap between the photon distributions. While the DE study obtained the scans sequentially, the filters are controlled by an automatic filter switcher that is capable of fast filter switching for interleaved scans *in vivo*. Contrary to most clinical CT filtration techniques, where metal foils are mounted at the x-ray tube port, a cylindrical shell filter that surrounds the scan bed yet fits within the scanner bore was controlled by an external filter switcher. The addition of a mechanism to mount and switch the filters on the tube port may interfere with the gantry balance and the normal operation of the scanner. This approach to filtration avoids modifications to the scanner and is compatible with gantry-based scanners. The cylindrical shell filters the x-rays before and after the object being scanned, providing a total attenuation that is equivalent to a mounted filter of with the same path length.

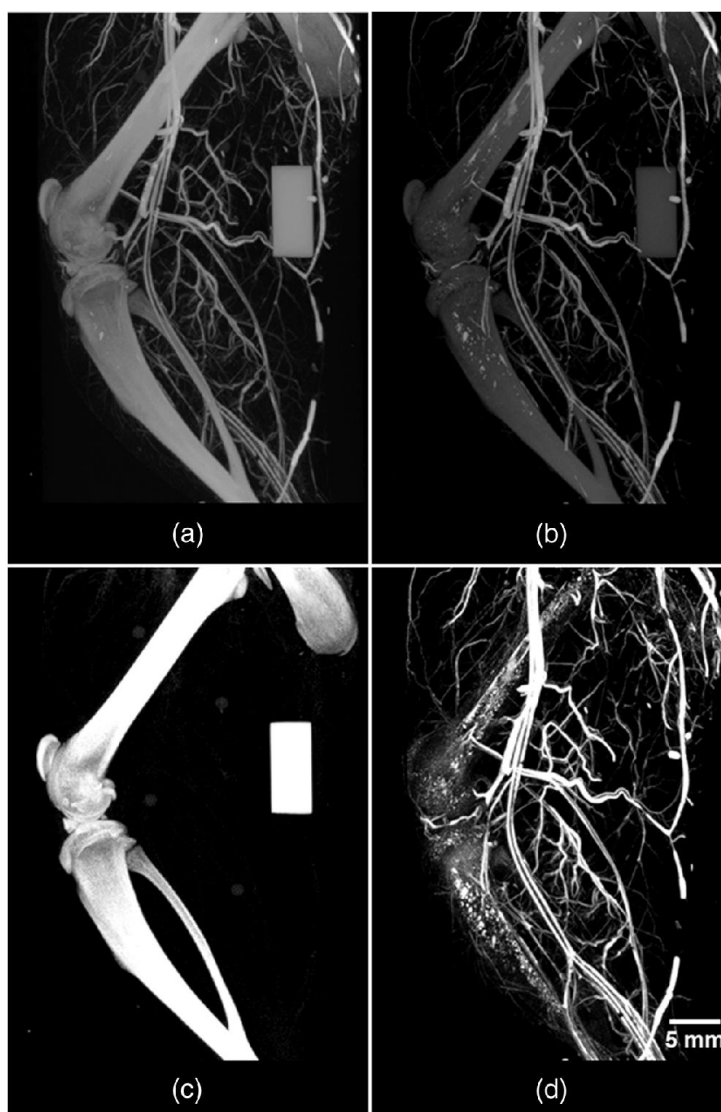


Figure 1.10 DE CT results from a rat hindlimb perfused with an erbium-based *ex vivo* agent. b) low- and b) high-energy images are decomposed into quantitative c) bone- and d) vessel volumes. This figure was taken from an article by Tse et al,<sup>114</sup> published under the Creative Commons (CC BY 4.0) - Gold Open Access.

Gadolinium is another lanthanide and is used as a contrast agent in MRI. Gadovist, which is a clinical MRI contrast agent containing 157 mg/mL of gadolinium, was used in a recent study that used DE micro-CT to develop a quantitative measure of contrast agent accumulation in soaked tissues.<sup>125</sup> By using unfiltered 70.1 kVp and calcium-filtered 140 kVp, regions in the esophagus and airways where gadolinium had accumulated were identified. While Gadovist can be used in micro-CT scans of the kidneys *in vivo* due to its

rapid renal clearance rates, the agent cannot be used to visualize the vasculature and tissues despite its high gadolinium loading and will likely accumulate at toxic doses in kidneys. Additionally, in *ex vivo* and *in situ* imaging, although small molecule agents permit the observation of parenchymal tissue as demonstrated by the Gadovist soaking study, only a negative opacification of the vessels in micro-CT images will be observed. This is due to their small size, enabling the extravasation from the vasculature.

While *ex vivo* studies in tissue specimens and small animals post-mortem can be beneficial to pre-clinical research, being able to study subjects *in vivo* can provide physiological information and longitudinal evidence that are essential to studying disease and drug development. The objective of my thesis work was to develop a lanthanide-based contrast agent that can be used for DE micro-CT of small animals *in vivo*. Advancements in nanotechnology and polymer sciences were taken advantage of to develop a long-circulating, nanoparticle-based contrast agent that contains at least 100 mg/mL of lanthanides that provides vessel opacification in micro-CT images, and permits K-edge decomposition of DE images in live mice.

## 1.6 Thesis outline

In this thesis, (1) I developed a novel lanthanide nanoparticle agent composed of high-erbium content nanoparticles, and an optimized amphiphilic polymer that contains PEG, (2) explored an alternative design composed of individually-coated gadolinium nanoparticles to improve subject viability, and (3) demonstrated the utility of the novel contrast agent in DE imaging of live mice by using a cylindrical shell controlled by a fast filter switcher, to obtain interleaved scans. The ultimate results of each chapter are summarized as follows.

Chapter 2 describes the synthesis of assemblies of erbium nanoparticles encapsulated in micelles composed of PEG-containing amphiphilic block copolymers. A library of amphiphilic block copolymers was investigated and included copolymers which were either purchased or synthesized in customized lengths. The colloidal stability was observed *in vitro* by dynamic light scattering measurements of the diameter in water, saline and a mouse serum mimic, and erbium concentrations were measured by inductively-coupled

plasma mass spectrometry. PEG-poly(lactic acid) as the coating polymer provided the most promising *in vitro* characteristics and was used to concentrate 100 mg/mL of erbium for intravenous injections of mice. The injected subjects were imaged by micro-CT and CT contrast enhancements of over 250 HU was observed in the vasculature for at least an hour, which well exceeds *in vivo* micro-CT scan time requirements. This work, entitled “Polymer assembly encapsulation of lanthanide nanoparticles as contrast agents for *in vivo* micro-CT,” was published in *Biomacromolecules* in February 2018. To our knowledge, this is the first demonstration of the successful synthesis of an *in vivo* micro-CT blood pool agent that can be dispersed into colloidally stable assemblies containing 100 mg/mL of erbium.

For Chapter 3, in lieu of using an amphiphilic polymer to encapsulate multiple nanoparticles within micelles cores, I altered the contrast agent design so that PEG was grafted onto the nanoparticle surface directly and smaller particles were synthesized. These modifications were done to improve the viability of the mice that were injected with the contrast agent, to permit longitudinal studies of the same subjects. While our formulation in chapter 2 permitted survival for up to 2 days, the new formulation permitted survival for at least 5 days and caused toxicity only to the spleen. CT contrast enhancements of at least 245 HU was observed in the blood pool, which slowly started decreasing at least 10 minutes after injections. This study, entitled “PEG-modified gadolinium nanoparticles as contrast agent for *in vivo* micro-CT,” will be submitted this fall. To our knowledge, like Chapter 2, this is the first demonstration of the successful synthesis of an *in vivo* micro-CT blood pool agent that can be dispersed into colloidally stable assemblies containing 100 mg/mL of gadolinium, and also reports the effects of high intravenous doses of gadolinium (*i.e.* 20 mg per subject) on mouse tissues 5 days after a single injection.

Chapter 4 describes the feasibility of *in vivo* DE micro-CT using the contrast agent that was formulated in Chapter 2. I optimized the pair of spectra that were used to obtain the DE images using SPEKTR 3.0. DE decomposition of the acquired images into quantitative soft tissue, bone and gadolinium-containing vessel volumes are demonstrated. This work is entitled “*In vivo* dual energy micro-computed tomography imaging of the mouse vasculature using gadolinium nanoparticles as contrast agent” will be submitted in the fall,

and is the first demonstration of an *in vivo* DE CT technique using a lanthanide-based contrast agent, which can be used with any pre-clinical, gantry-based micro-CT scanner.

Chapter 5, is a summary of the main objectives and results of Chapters 2 through 4. Additionally, I present future research opportunities that may benefit from the work that is presented within this thesis.

## 1.7 References

- (1) Johnson, T. R.; Krauss, B.; Sedlmair, M.; Grasruck, M.; Bruder, H.; Morhard, D.; Fink, C.; Weckbach, S.; Lenhard, M.; Schmidt, B.; Flohr, T.; Reiser, M. F.; Becker, C. R. Material differentiation by dual energy CT: initial experience. *Eur Radiol* **2007**, *17*, 1510-1517.
- (2) Graser, A.; Johnson, T. R.; Chandarana, H.; Macari, M. Dual energy CT: preliminary observations and potential clinical applications in the abdomen. *Eur Radiol* **2009**, *19*, 13-23.
- (3) Avrin, D. E.; Macovski, A.; Zatz, L. E. Clinical application of Compton and photoelectric reconstruction in computed tomography: preliminary results. *Invest Radiol* **1978**, *13*, 217-222.
- (4) Primak, A.; Vrtiska, T. J.; McCollough, C., Dual energy: characterization of kidney stone composition. In *Dual source CT imaging*, Seidensticker, P. R.; Hofmann, L. K., Eds. Springer Berlin Heidelberg: Berlin, Heidelberg, 2008; pp 252-261.
- (5) McCollough, C. H.; Primak, A. N.; Saba, O.; Bruder, H.; Stierstorfer, K.; Raupach, R.; Suess, C.; Schmidt, B.; Ohnesorge, B. M.; Flohr, T. G. Dose performance of a 64-channel dual-source CT scanner. *Radiology* **2007**, *243*, 775-784.
- (6) Ananthakrishnan, L.; Duan, X.; Xi, Y.; Lewis, M. A.; Pearle, M. S.; Antonelli, J. A.; Goerne, H.; Kolitz, E. M.; Abbara, S.; Lenkinski, R. E.; Fielding, J. R.; Leyendecker, J. R. Dual-layer spectral detector CT: non-inferiority assessment compared to dual-source dual-energy CT in discriminating uric acid from non-uric acid renal stones ex vivo. *Abdom Radiol (NY)* **2018**, *43*, 3075-3081.
- (7) Zarzour, J. G.; Milner, D.; Valentin, R.; Jackson, B. E.; Gordetsky, J.; West, J.; Rais-Bahrami, S.; Morgan, D. E. Quantitative iodine content threshold for discrimination of renal cell carcinomas using rapid kV-switching dual-energy CT. *Abdom Radiol (NY)* **2017**, *42*, 727-734.
- (8) Tse, J. J.; Dunmore-Buyze, J.; Drangova, M.; Holdsworth, D. W. Dual-energy computed tomography using a gantry-based preclinical cone-beam microcomputed tomography scanner. *J Med Imaging* **2018**, *5*.
- (9) Amundsen, P.; Skalpe, I. O.; Presthus, J.; Torbergsen, T.; Kaada, B. Metrizamide, the new water-soluble non-ionic contrast medium for myelography. Clinical experience. *Acta Radiol Suppl* **1976**, *347*, 453-458.
- (10) Hindmarsh, T. Myelography with the non-ionic water-soluble contrast medium metrizamide. *Acta Radiol Diagn (Stockh)* **1975**, *16*, 417-435.
- (11) Cardinal, H. N.; Holdsworth, D. W.; Drangova, M.; Hobbs, B. B.; Fenster, A. Experimental and theoretical x-ray imaging performance comparison of iodine and lanthanide contrast agents. *Med Phys* **1993**, *20*, 15-31.

- (12) Johnson, T. R. Dual-energy CT: general principles. *AJR Am J Roentgenol* **2012**, *199*, S3-8.
- (13) Primak, A. N.; Ramirez Giraldo, J. C.; Liu, X.; Yu, L.; McCollough, C. H. Improved dual-energy material discrimination for dual-source CT by means of additional spectral filtration. *Med Phys* **2009**, *36*, 1359-1369.
- (14) Siewerdsen, J. H.; Waese, A. M.; Moseley, D. J.; Richard, S.; Jaffray, D. A. Spektr: a computational tool for x-ray spectral analysis and imaging system optimization. *Med Phys* **2004**, *31*, 3057-3067.
- (15) Punnoose, J.; Xu, J.; Sisniega, A.; Zbijewski, W.; Siewerdsen, J. H. Technical Note: spektr 3.0-A computational tool for x-ray spectrum modeling and analysis. *Med Phys* **2016**, *43*, 4711.
- (16) Badea, C. T.; Drangova, M.; Holdsworth, D. W.; Johnson, G. A. In vivo small-animal imaging using micro-CT and digital subtraction angiography. *Phys Med Biol* **2008**, *53*, R319-350.
- (17) Ashton, J. R.; Clark, D. P.; Moding, E. J.; Ghaghada, K.; Kirsch, D. G.; West, J. L.; Badea, C. T. Dual-energy micro-CT functional imaging of primary lung cancer in mice using gold and iodine nanoparticle contrast agents: a validation study. *PLoS One* **2014**, *9*, e88129.
- (18) Boone, J. M.; Chavez, A. E. Comparison of x-ray cross sections for diagnostic and therapeutic medical physics. *Med Phys* **1996**, *23*, 1997-2005.
- (19) Morin, L. R.; Berroir, A. Calculation of x-ray single scattering in diagnostic radiology. *Phys Med Biol* **1983**, *28*, 789-797.
- (20) Podgoršak, E. B.; Agency, I. A. E., *Radiation oncology physics : a handbook for teachers and students*. International Atomic Energy Agency: Vienna, 2005; p 657 p.
- (21) Yeh, B. M.; FitzGerald, P. F.; Edic, P. M.; Lambert, J. W.; Colborn, R. E.; Marino, M. E.; Evans, P. M.; Roberts, J. C.; Wang, Z. J.; Wong, M. J.; Bonitatibus, P. J., Jr. Opportunities for new CT contrast agents to maximize the diagnostic potential of emerging spectral CT technologies. *Adv Drug Deliv Rev* **2017**, *113*, 201-222.
- (22) Canty, J. M., Jr.; Judd, R. M.; Brody, A. S.; Klocke, F. J. First-pass entry of nonionic contrast agent into the myocardial extravascular space. Effects on radiographic estimates of transit time and blood volume. *Circulation* **1991**, *84*, 2071-2078.
- (23) Silvennoinen, H. M.; Hamberg, L. M.; Valanne, L.; Hunter, G. J. Increasing contrast agent concentration improves enhancement in first-pass CT perfusion. *AJNR Am J Neuroradiol* **2007**, *28*, 1299-1303.
- (24) Petersilka, M.; Bruder, H.; Krauss, B.; Stierstorfer, K.; Flohr, T. G. Technical principles of dual source CT. *Eur J Radiol* **2008**, *68*, 362-368.

- (25) Forghani, R.; De Man, B.; Gupta, R. Dual-Energy Computed Tomography: Physical Principles, Approaches to Scanning, Usage, and Implementation: Part 2. *Neuroimaging Clin N Am* **2017**, *27*, 385-400.
- (26) Sodickson, A. D.; Keraliya, A.; Czakowski, B.; Primak, A.; Wortman, J.; Uyeda, J. W. Dual energy CT in clinical routine: how it works and how it adds value. *Emerg Radiol* **2020**.
- (27) Potter, C. A.; Sodickson, A. D. Dual-energy CT in emergency neuroimaging: added value and novel applications. *Radiographics* **2016**, *36*, 2186-2198.
- (28) Fink, C.; Johnson, T. R.; Michaely, H. J.; Morhard, D.; Becker, C.; Reiser, M.; Nikolaou, K. Dual-energy CT angiography of the lung in patients with suspected pulmonary embolism: initial results. *Rofo* **2008**, *180*, 879-883.
- (29) Ai, S.; Qu, M.; Glazebrook, K. N.; Liu, Y.; Rhee, P. C.; Leng, S.; McCollough, C. H. Use of dual-energy CT and virtual non-calcium techniques to evaluate post-traumatic bone bruises in knees in the subacute setting. *Skeletal radiology* **2014**, *43*, 1289-1295.
- (30) Guggenberger, R.; Gnannt, R.; Hodler, J.; Krauss, B.; Wanner, G. A.; Csuka, E.; Payne, B.; Frauenfelder, T.; Andreisek, G.; Alkadhi, H. Diagnostic performance of dual-energy CT for the detection of traumatic bone marrow lesions in the ankle: comparison with MR imaging. *Radiology* **2012**, *264*, 164-173.
- (31) Breuer, G. S.; Bogot, N.; Neshet, G. Dual-energy computed tomography as a diagnostic tool for gout during intercritical periods. *Int J Rheum Dis* **2016**, *19*, 1337-1341.
- (32) Chou, H.; Chin, T. Y.; Peh, W. C. Dual-energy CT in gout - A review of current concepts and applications. *J Med Radiat Sci* **2017**, *64*, 41-51.
- (33) De Santis, D.; Eid, M.; De Cecco, C. N.; Jacobs, B. E.; Albrecht, M. H.; Varga-Szemes, A.; Tesche, C.; Caruso, D.; Laghi, A.; Schoepf, U. J. Dual-Energy Computed Tomography in Cardiothoracic Vascular Imaging. *Radiol Clin North Am* **2018**, *56*, 521-534.
- (34) Hagspiel, K. D. Increasing Role of Dual-Energy CT in Noninvasive Vascular Imaging. *J Vasc Interv Radiol* **2017**, *28*, 1267-1268.
- (35) Sugawara, H.; Suzuki, S.; Katada, Y.; Ishikawa, T.; Fukui, R.; Yamamoto, Y.; Abe, O. Measurement of Vascular Diameter in Computed Tomography Angiography With Reduced Iodine Load: Comparison of Virtual Monochromatic Imaging in Dual-Energy Computed Tomography and Conventional Polychromatic Scan In Vitro. *J Comput Assist Tomogr* **2018**, *42*, 919-924.
- (36) Wan, Y.; Li, Z.; Ji, N.; Gao, J. Comparison of gastric vascular anatomy by monochromatic and polychromatic dual-energy spectral computed tomography imaging. *J Int Med Res* **2014**, *42*, 26-34.

- (37) Langheinrich, A. C.; Kampschulte, M.; Crossmann, C.; Moritz, R.; Rau, W. S.; Bohle, R. M.; Ritman, E. L. Role of computed tomography voxel size in detection and discrimination of calcium and iron deposits in atherosclerotic human coronary artery specimens. *J Comput Assist Tomogr* **2009**, *33*, 517-522.
- (38) Kay, F. U.; Beraldo, M. A.; Nakamura, M. A. M.; De Santis Santiago, R.; Torsani, V.; Gomes, S.; Roldan, R.; Tucci, M. R.; Abbara, S.; Amato, M. B. P.; Amaro, E., Jr. Quantitative Dual-Energy Computed Tomography Predicts Regional Perfusion Heterogeneity in a Model of Acute Lung Injury. *J Comput Assist Tomogr* **2018**, *42*, 866-872.
- (39) Mulé, S.; Pigneur, F.; Quelever, R.; Tenenhaus, A.; Baranes, L.; Richard, P.; Tacher, V.; Herin, E.; Pasquier, H.; Ronot, M.; Rahmouni, A.; Vilgrain, V.; Luciani, A. Can dual-energy CT replace perfusion CT for the functional evaluation of advanced hepatocellular carcinoma? *Eur Radiol* **2018**, *28*, 1977-1985.
- (40) Tse, J. J.; Dunmore-Buyze, J.; Drangova, M.; Holdsworth, D. W. Dual-energy computed tomography using a gantry-based preclinical cone-beam microcomputed tomography scanner. *J. Med. Imaging* **2018**, *5*.
- (41) Patino, M.; Prochowski, A.; Agrawal, M. D.; Simeone, F. J.; Gupta, R.; Hahn, P. F.; Sahani, D. V. Material separation using dual-energy CT: current and emerging applications. *Radiographics* **2016**, *36*, 1087-1105.
- (42) Pedersen, C. K.; Mackey, J. E.; Teytelboym, O. M. Protocol Optimization and Implementation of Dual-Energy and Dual-Source Computed Tomography in Clinical Practice: Field of View, Speed, or Material Separation? *J Comput Assist Tomogr* **2020**.
- (43) Vinegar, H. J.; Wellington, S. L. Tomographic imaging of three-phase flow experiments. *Review of Scientific Instruments* **1987**, *58*, 96-107.
- (44) Hogstrom, B.; Hietala, S. O.; Rooth, P. In vivo fluorescence microscopy of microcirculation in the renal cortex of mice. Part V. Effects of mannitol and iohexol infusions in normal, obese/hyperglycemic and diabetic mice. *Acta Radiol* **1994**, *35*, 176-181.
- (45) Hogstrom, B.; Hietala, S. O.; Rooth, P. Effects of mannitol and iohexol infusions on the renal cortical blood flow in dehydrated mice. *Acta Radiol* **1996**, *37*, 591-595.
- (46) Luis-Lima, S.; Rodriguez-Rodriguez, A. E.; Martin-Higueras, C.; Sierra-Ramos, C.; Carrara, F.; Arnau, M. R.; Alvarez de la Rosa, D.; Salido, E.; Gaspari, F.; Porrini, E. Iohexol plasma clearance, a simple and reliable method to measure renal function in conscious mice. *Pflugers Arch* **2016**, *468*, 1587-1594.
- (47) Leander, P.; Golman, K.; Strande, P.; Klaveness, J.; Besjakov, J.; Falt, K. A comparison between IEEC, a new biodegradable particulate contrast medium, and iohexol in a tumor model of computed tomography imaging of the liver. *Invest Radiol* **1993**, *28*, 513-519.

- (48) Pasternak, J. J.; Williamson, E. E. Clinical pharmacology, uses, and adverse reactions of iodinated contrast agents: a primer for the non-radiologist. *Mayo Clin Proc* **2012**, *87*, 390-402.
- (49) Lee, H. C.; Chang, J. G.; Yen, H. W.; Liu, I. H.; Lai, W. T.; Sheu, S. H. Ionic contrast media induced more apoptosis in diabetic kidney than nonionic contrast media. *J Nephrol* **2011**, *24*, 376-380.
- (50) Satchell, S. C.; Braet, F. Glomerular endothelial cell fenestrations: an integral component of the glomerular filtration barrier. *Am J Physiol Renal Physiol* **2009**, *296*, F947-956.
- (51) Longmire, M.; Choyke, P. L.; Kobayashi, H. Clearance properties of nano-sized particles and molecules as imaging agents: considerations and caveats. *Nanomedicine (Lond)* **2008**, *3*, 703-717.
- (52) Choi, C. H.; Zuckerman, J. E.; Webster, P.; Davis, M. E. Targeting kidney mesangium by nanoparticles of defined size. *Proc Natl Acad Sci U S A* **2011**, *108*, 6656-6661.
- (53) Tang, S.; Chen, M.; Zheng, N. Sub-10-nm Pd nanosheets with renal clearance for efficient near-infrared photothermal cancer therapy. *Small* **2014**, *10*, 3139-3144.
- (54) Tang, S.; Peng, C.; Xu, J.; Du, B.; Wang, Q.; Vinluan, R. D., 3rd; Yu, M.; Kim, M. J.; Zheng, J. Tailoring Renal Clearance and Tumor Targeting of Ultrasmall Metal Nanoparticles with Particle Density. *Angew Chem Int Ed Engl* **2016**, *55*, 16039-16043.
- (55) Swami, A.; Shi, J.; Gadde, S.; Votruba, A.; Kolishetti, N.; Farokhzad, O., Nanoparticles for targeted and temporally controlled drug delivery. In *Multifunctional nanoparticles for drug delivery applications: imaging, targeting, and delivery*, 1st ed. 2012. ed.; Svenson, S.; Prud'homme, R. K., Eds. Springer New York: New York, NY, 2012; pp 9-29.
- (56) Douziech-Eyrolles, L.; Marchais, H.; Herve, K.; Munnier, E.; Souce, M.; Linassier, C.; Dubois, P.; Chourpa, I. Nanovectors for anticancer agents based on superparamagnetic iron oxide nanoparticles. *Int J Nanomedicine* **2007**, *2*, 541-550.
- (57) Lundy, D. J.; Chen, K. H.; Toh, E. K.; Hsieh, P. C. Distribution of Systemically Administered Nanoparticles Reveals a Size-Dependent Effect Immediately following Cardiac Ischaemia-Reperfusion Injury. *Sci Rep* **2016**, *6*, 25613.
- (58) Liu, R.; Hu, C.; Yang, Y.; Zhang, J.; Gao, H. Theranostic nanoparticles with tumor-specific enzyme-triggered size reduction and drug release to perform photothermal therapy for breast cancer treatment. *Acta Pharm Sin B* **2019**, *9*, 410-420.
- (59) Tang, L.; Gabrielson, N. P.; Uckun, F. M.; Fan, T. M.; Cheng, J. Size-dependent tumor penetration and in vivo efficacy of monodisperse drug-silica nanoconjugates. *Mol Pharm* **2013**, *10*, 883-892.

- (60) Reticuloendothelial system. In *Rheumatology and immunology therapy*, Abbott, J. D.; Ball, G.; Boumpas, D.; Bridges, S. L.; Chatham, W.; Curtis, J.; Daniel, C.; Hughes, L. B.; Kao, A. H.; Langford, C.; Lovell, D.; Manzi, S.; Müller-Ladner, U.; Patel, H. C.; Roubey, R. A. S.; Saag, K.; Sabatine, J. M.; Shanahan, J.; Simms, R.; Smith, E.; Sundry, J.; Szalai, A. J.; Wimmer, T.; Moreland, L. W., Eds. Springer Berlin Heidelberg: Berlin, Heidelberg, 2004; pp 759-759.
- (61) Anderson, C. L. The liver sinusoidal endothelium reappears after being eclipsed by the Kupffer cell: a 20th century biological delusion corrected. *J Leukoc Biol* **2015**, *98*, 875-876.
- (62) Blanco, E.; Shen, H.; Ferrari, M. Principles of nanoparticle design for overcoming biological barriers to drug delivery. *Nat Biotechnol* **2015**, *33*, 941-951.
- (63) Black, K. C.; Wang, Y.; Luehmann, H. P.; Cai, X.; Xing, W.; Pang, B.; Zhao, Y.; Cutler, C. S.; Wang, L. V.; Liu, Y.; Xia, Y. Radioactive <sup>198</sup>Au-doped nanostructures with different shapes for *in vivo* analyses of their biodistribution, tumor uptake, and intratumoral distribution. *ACS Nano* **2014**, *8*, 4385-4394.
- (64) Xiao, K.; Li, Y.; Luo, J.; Lee, J. S.; Xiao, W.; Gonik, A. M.; Agarwal, R. G.; Lam, K. S. The effect of surface charge on *in vivo* biodistribution of PEG-oligocholic acid based micellar nanoparticles. *Biomaterials* **2011**, *32*, 3435-3446.
- (65) Davis, F. F.; Van Es, T.; Palczuk, N. C. Non-immunogenic polypeptides. 1977.
- (66) Davis, S.; Abuchowski, A.; Park, Y. K.; Davis, F. F. Alteration of the circulating life and antigenic properties of bovine adenosine deaminase in mice by attachment of polyethylene glycol. *Clin Exp Immunol* **1981**, *46*, 649-652.
- (67) Hershfield, M. S.; Buckley, R. H.; Greenberg, M. L.; Melton, A. L.; Schiff, R.; Hatem, C.; Kurtzberg, J.; Markert, M. L.; Kobayashi, R. H.; Kobayashi, A. L.; et al. Treatment of adenosine deaminase deficiency with polyethylene glycol-modified adenosine deaminase. *N Engl J Med* **1987**, *316*, 589-596.
- (68) Kelly, S. J.; Delnomdedieu, M.; Oliverio, M. I.; Williams, L. D.; Saifer, M. G.; Sherman, M. R.; Coffman, T. M.; Johnson, G. A.; Hershfield, M. S. Diabetes insipidus in uricase-deficient mice: a model for evaluating therapy with poly(ethylene glycol)-modified uricase. *J Am Soc Nephrol* **2001**, *12*, 1001-1009.
- (69) Saifer, M. G.; Somack, R.; Williams, L. D. Conjugates of superoxide dismutase coupled to high molecular weight polyalkylene glycols. 1992.
- (70) Saifer, M. G.; Somack, R.; Williams, L. D. Conjugates of superoxide dismutase coupled to high molecular weight polyalkylene glycols. 1992.
- (71) Saifer, M. G.; Somack, R.; Williams, L. D. Plasma clearance and immunologic properties of long-acting superoxide dismutase prepared using 35,000 to 120,000 dalton poly-ethylene glycol. *Adv Exp Med Biol* **1994**, *366*, 377-387.

- (72) Sherman, M. R.; Saifer, M. G.; Williams, L. D.; Hershfield, M. S.; Kelly, S. J. Aggregate-free urate oxidase for preparation of non-immunogenic polymer conjugates. 2011.
- (73) Williams, L. D.; Hershfield, M. S.; Kelly, S. J.; Saifer, M. G.; Sherman, M. R. PEG-urate oxidase conjugates and use thereof. 2003.
- (74) Gabizon, A.; Catane, R.; Uziely, B.; Kaufman, B.; Safra, T.; Cohen, R.; Martin, F.; Huang, A.; Barenholz, Y. Prolonged circulation time and enhanced accumulation in malignant exudates of doxorubicin encapsulated in polyethylene-glycol coated liposomes. *Cancer Res* **1994**, *54*, 987-992.
- (75) Gabizon, A.; Martin, F. Polyethylene glycol-coated (pegylated) liposomal doxorubicin. Rationale for use in solid tumours. *Drugs* **1997**, *54 Suppl 4*, 15-21.
- (76) Li, C.; Wallace, S.; Yu, D. F.; Yang, D. J. Water soluble paclitaxel prodrugs. 1999.
- (77) Zhang, Z.; Feng, S. S. The drug encapsulation efficiency, *in vitro* drug release, cellular uptake and cytotoxicity of paclitaxel-loaded poly(lactide)-tocopheryl polyethylene glycol succinate nanoparticles. *Biomaterials* **2006**, *27*, 4025-4033.
- (78) Lv, S.; Li, M.; Tang, Z.; Song, W.; Sun, H.; Liu, H.; Chen, X. Doxorubicin-loaded amphiphilic polypeptide-based nanoparticles as an efficient drug delivery system for cancer therapy. *Acta Biomater* **2013**, *9*, 9330-9342.
- (79) Radosz, M.; Xu, P.; Shen, Y. Nanoparticles for cytoplasmic drug delivery to cancer cells. 2015.
- (80) Frank, M. M.; Fries, L. F. The role of complement in inflammation and phagocytosis. *Immunol Today* **1991**, *12*, 322-326.
- (81) Carrstensen, H.; Muller, R. H.; Muller, B. W. Particle size, surface hydrophobicity and interaction with serum of parenteral fat emulsions and model drug carriers as parameters related to RES uptake. *Clin Nutr* **1992**, *11*, 289-297.
- (82) Norman, M. E.; Williams, P.; Illum, L. Human serum albumin as a probe for surface conditioning (opsonization) of block copolymer-coated microspheres. *Biomaterials* **1992**, *13*, 841-849.
- (83) Suk, J. S.; Xu, Q.; Kim, N.; Hanes, J.; Ensign, L. M. PEGylation as a strategy for improving nanoparticle-based drug and gene delivery. *Adv Drug Deliv Rev* **2016**, *99*, 28-51.
- (84) Endres, T.; Zheng, M.; Kilic, A.; Turowska, A.; Beck-Broichsitter, M.; Renz, H.; Merkel, O. M.; Kissel, T. Amphiphilic biodegradable PEG-PCL-PEI triblock copolymers for FRET-capable *in vitro* and *in vivo* delivery of siRNA and quantum dots. *Mol Pharm* **2014**, *11*, 1273-1281.

- (85) Endres, T. K.; Beck-Broichsitter, M.; Samsonova, O.; Renette, T.; Kissel, T. H. Self-assembled biodegradable amphiphilic PEG-PCL-IPEI triblock copolymers at the borderline between micelles and nanoparticles designed for drug and gene delivery. *Biomaterials* **2011**, *32*, 7721-7731.
- (86) Li, L. L.; Zhang, R.; Yin, L.; Zheng, K.; Qin, W.; Selvin, P. R.; Lu, Y. Biomimetic surface engineering of lanthanide-doped upconversion nanoparticles as versatile bioprobes. *Angew Chem Int Ed Engl* **2012**, *51*, 6121-6125.
- (87) Wang, H.; Zhao, Y.; Wu, Y.; Hu, Y. L.; Nan, K.; Nie, G.; Chen, H. Enhanced anti-tumor efficacy by co-delivery of doxorubicin and paclitaxel with amphiphilic methoxy PEG-PLGA copolymer nanoparticles. *Biomaterials* **2011**, *32*, 8281-8290.
- (88) Immordino, M. L.; Dosio, F.; Cattel, L. Stealth liposomes: review of the basic science, rationale, and clinical applications, existing and potential. *Int J Nanomedicine* **2006**, *1*, 297-315.
- (89) Mulder, W. J.; Strijkers, G. J.; van Tilborg, G. A.; Griffioen, A. W.; Nicolay, K. Lipid-based nanoparticles for contrast-enhanced MRI and molecular imaging. *NMR Biomed* **2006**, *19*, 142-164.
- (90) Advincula, R. C. Review of Conjugated Polymer Synthesis: Methods and Reactions. *Journal of the American Chemical Society* **2011**, *133*, 5622-5622.
- (91) Schubert, S.; Delaney, J. J.; Schubert, U. Nanoprecipitation and nanoformulation of polymers: from history to powerful possibilities beyond poly(lactic acid). *Soft Matter* **2011**, *7*, 1581-1588.
- (92) Redhead, H. M.; Davis, S. S.; Illum, L. Drug delivery in poly(lactide-co-glycolide) nanoparticles surface modified with poloxamer 407 and poloxamine 908: *in vitro* characterisation and *in vivo* evaluation. *J. Control. Release* **2001**, *70*, 353-363.
- (93) Perinelli, D. R.; Cespi, M.; Bonacucina, G.; Palmieri, G. F. PEGylated polylactide (PLA) and poly (lactic-co-glycolic acid) (PLGA) copolymers for the design of drug delivery systems. *Journal of Pharmaceutical Investigation* **2019**, *49*, 443-458.
- (94) Fan, B.; Gillies, E. R., Self-immolative polymers. In *Encyclopedia of polymer science and technology*, Wiley-VCH Verlag: 2015; pp 1-35.
- (95) Cho, H.; Gao, J.; Kwon, G. S. PEG-b-PLA micelles and PLGA-b-PEG-b-PLGA sol-gels for drug delivery. *J Control Release* **2016**, *240*, 191-201.
- (96) Peracchia, M. T.; Gref, R.; Minamitake, Y.; Domb, A.; Lotan, N.; Langer, R. In *PEG-coated nanospheres from amphiphilic diblock and multiblock copolymers: Investigation of their drug encapsulation and release characteristics*, 1997; 1997.

- (97) Zhang, K.; Tang, X.; Zhang, J.; Lu, W.; Lin, X.; Zhang, Y.; Tian, B.; Yang, H.; He, H. PEG-PLGA copolymers: their structure and structure-influenced drug delivery applications. *J Control Release* **2014**, *183*, 77-86.
- (98) Cassol, F.; Portal, L.; Richelme, S.; Dupont, M.; Boursier, Y.; Arechederra, M.; Auphan-Anezin, N.; Chasson, L.; Laprie, C.; Fernandez, S.; Balasse, L.; Lamballe, F.; Dono, R.; Guillet, B.; Lawrence, T.; Morel, C.; Maina, F. Tracking Dynamics of Spontaneous Tumors in Mice Using Photon-Counting Computed Tomography. *iScience* **2019**, *21*, 68-83.
- (99) Clark, D. P.; Holbrook, M.; Badea, C. T. In *Multi-energy CT decomposition using convolutional neural networks*, Proc.SPIE, 2018; 2018.
- (100) Binitio Biomedical Inc. Products. <https://www.binitio.com/index.php?Page=Products>
- (101) Attia, M. F.; Anton, N.; Akasov, R.; Chipper, M.; Markvicheva, E.; Vandamme, T. F. Biodistribution and Toxicity of X-Ray Iodinated Contrast Agent in Nano-emulsions in Function of Their Size. *Pharm Res* **2016**, *33*, 603-614.
- (102) Xing, R.; De Wilde, D.; McCann, G.; Ridwan, Y.; Schrauwen, J. T.; van der Steen, A. F.; Gijssen, F. J.; Van der Heiden, K. Contrast-enhanced micro-CT imaging in murine carotid arteries: a new protocol for computing wall shear stress. *Biomed Eng Online* **2016**, *15*, 156.
- (103) Mannheim, J. G.; Schlichthaerle, T.; Kuebler, L.; Quintanilla-Martinez, L.; Kohlhofer, U.; Kneilling, M.; Pichler, B. J. Comparison of small animal CT contrast agents. *Contrast Media Mol Imaging* **2016**, *11*, 272-284.
- (104) Bakan, D. A.; Weichert, J. P.; Longino, M. A.; Counsell, R. E. Polyiodinated triglyceride lipid emulsions for use as hepatoselective contrast agents in CT: effects of physicochemical properties on biodistribution and imaging profiles. *Invest Radiol* **2000**, *35*, 158-169.
- (105) Miltenyi Biotec. Viscover™ Imaging - *in vivo* contrast agents for pre-clinical imaging. <https://www.miltenyibiotec.com/CA-en/>
- (106) MediLumine. Micro-CT contrast agents. <https://www.medilumine.com/product-category/reagents/micro-ct-contrast-agents/>
- (107) Nanoprobes. Seeing gold means seeing more: gold nanoparticles as x-ray contrast agents. [https://www.nanoprobes.com/newsletters/Vol11\\_Iss03\\_gold-nanoparticles-as-xray-contrast-agents.html](https://www.nanoprobes.com/newsletters/Vol11_Iss03_gold-nanoparticles-as-xray-contrast-agents.html)
- (108) Guo, R.; Wang, H.; Peng, C.; Shen, M.; Pan, M.; Cao, X.; Zhang, G.; Shi, X. X-ray Attenuation Property of Dendrimer-Entrapped Gold Nanoparticles. *The Journal of Physical Chemistry C* **2010**, *114*, 50-56.

- (109) Shi, F.; Yang, Y.; Chen, J.; Sha, Y.; Shu, Y.; Wu, H. Dendrimer-Entrapped Gold Nanoparticles as Potential CT Contrast Agents for Localizing Sentinel Lymph Node via Indirect CT Lymphography on Rabbit Model. *Biomed Res Int* **2018**, *2018*, 1230151.
- (110) Nicol, J. R.; Dixon, D.; Coulter, J. A. Gold nanoparticle surface functionalization: a necessary requirement in the development of novel nanotherapeutics. *Nanomedicine (Lond)* **2015**, *10*, 1315-1326.
- (111) Rana, S.; Bajaj, A.; Mout, R.; Rotello, V. M. Monolayer coated gold nanoparticles for delivery applications. *Adv Drug Deliv Rev* **2012**, *64*, 200-216.
- (112) Chakravarty, S.; Hix, J. M. L.; Wiewiora, K. A.; Volk, M. C.; Kenyon, E.; Shuboni-Mulligan, D. D.; Blanco-Fernandez, B.; Kiupel, M.; Thomas, J.; Sempere, L. F.; Shapiro, E. M. Tantalum oxide nanoparticles as versatile contrast agents for X-ray computed tomography. *Nanoscale* **2020**, *12*, 7720-7734.
- (113) Niranjana, K. M.; Badiger, N. M. K shell parameters of some lanthanide elements using bremsstrahlung. *Radiat. Phys. Chem.* **2015**, *107*, 59-64.
- (114) Tse, J. J.; Dunmore-Buyze, J.; Drangova, M.; Holdsworth, D. W. Dual-energy computed tomography using a gantry-based preclinical cone-beam microcomputed tomography scanner. *J Med Imaging (Bellingham)* **2018**, *5*, 033503.
- (115) Liu, Y.; Ai, K.; Liu, J.; Yuan, Q.; He, Y.; Lu, L. A high-performance ytterbium-based nanoparticulate contrast agent for in vivo X-ray computed tomography imaging. *Angew Chem Int Ed Engl* **2012**, *51*, 1437-1442.
- (116) Zhou, J.; Zhu, X.; Chen, M.; Sun, Y.; Li, F. Water-stable NaLuF<sub>4</sub>-based upconversion nanophosphors with long-term validity for multimodal lymphatic imaging. *Biomaterials* **2012**, *33*, 6201-6210.
- (117) Badea, C. T.; Clark, D. P.; Holbrook, M.; Srivastava, M.; Mowery, Y.; Ghaghada, K. B. Functional imaging of tumor vasculature using iodine and gadolinium-based nanoparticle contrast agents: a comparison of spectral micro-CT using energy integrating and photon counting detectors. *Phys. Med. Biol.* **2019**, *64*, 065007.
- (118) Bridot, J. L.; Faure, A. C.; Laurent, S.; Riviere, C.; Billotey, C.; Hiba, B.; Janier, M.; Jossierand, V.; Coll, J. L.; Elst, L. V.; Muller, R.; Roux, S.; Perriat, P.; Tillement, O. Hybrid gadolinium oxide nanoparticles: multimodal contrast agents for *in vivo* imaging. *J. Am. Chem. Soc.* **2007**, *129*, 5076-5084.
- (119) Ashton, J. R.; Castle, K. D.; Qi, Y.; Kirsch, D. G.; West, J. L.; Badea, C. T. Dual-energy CT imaging of tumor liposome delivery after gold nanoparticle-augmented radiation therapy. *Theranostics* **2018**, *8*, 1782-1797.
- (120) Granton, P. V.; Pollmann, S. I.; Ford, N. L.; Drangova, M.; Holdsworth, D. W. Implementation of dual- and triple-energy cone-beam micro-CT for postreconstruction material decomposition. *Med Phys* **2008**, *35*, 5030-5042.

- (121) Holdsworth, D. W.; Thornton, M. M. Micro-CT in small animal and specimen imaging. *Trends in Biotechnology* **2002**, *20*, S34-S39.
- (122) Langheinrich, A. C.; Vorman, S.; Seidenstucker, J.; Kampschulte, M.; Bohle, R. M.; Wienhard, J.; Zygmunt, M. Quantitative 3D micro-CT imaging of the human fetoplacental vasculature in intrauterine growth restriction. *Placenta* **2008**, *29*, 937-941.
- (123) Wang, H. K.; Wang, Y. X.; Xue, C. B.; Li, Z. M.; Huang, J.; Zhao, Y. H.; Yang, Y. M.; Gu, X. S. Angiogenesis in tissue-engineered nerves evaluated objectively using MICROFIL perfusion and micro-CT scanning. *Neural Regen Res* **2016**, *11*, 168-173.
- (124) Tse, J. J.; Dunmore-Buyze, P. J.; Drangova, M.; Holdsworth, D. W. Erbium-Based Perfusion Contrast Agent for Small-Animal Microvessel Imaging. *Contrast Media Mol Imaging* **2017**, *2017*, 7368384.
- (125) Martins de Souza E Silva, J.; Utsch, J.; Kimm, M. A.; Allner, S.; Epple, M. F.; Achterhold, K.; Pfeiffer, F. Dual-energy micro-CT for quantifying the time-course and staining characteristics of ex-vivo animal organs treated with iodine- and gadolinium-based contrast agents. *Scientific reports* **2017**, *7*, 17387-17387.

## Chapter 2

### 2 Polymer Assembly Encapsulation of Lanthanide Nanoparticles as Contrast Agents for *In Vivo* Micro-CT

Despite recent technological advancements in microcomputed tomography (micro-CT) and contrast agent development, pre-clinical contrast agents are still predominantly iodine based. Higher contrast can be achieved when using elements with higher atomic numbers, such as lanthanides; lanthanides also have x-ray attenuation properties that are ideal for spectral CT. However, the formulation of lanthanide-based contrast agents at the high concentrations required for vascular imaging presents a significant challenge. In this work, we developed an erbium-based contrast agent that meets micro-CT imaging requirements, which include colloidal stability upon redispersion at high concentrations, evasion of rapid renal clearance, and circulation times of tens of minutes in small animals. Through systematic studies with poly(ethylene glycol) (PEG)-poly(propylene glycol), PEG-polycaprolactone, and PEG-poly(L-lactide) (PLA) block copolymers, the amphiphilic block copolymer PEG<sub>114</sub>-PLA<sub>53</sub> was identified to be ideal for encapsulating oleate-coated lanthanide-based nanoparticles for *in vivo* intravenous administration. We were able to synthesize a contrast agent containing 100 mg/mL of erbium that could be redispersed into colloiddally stable nanoparticles in saline after lyophilization. Contrast enhancement of over 250 HU was achieved in the blood pool for up to an hour, thereby meeting the requirements of live animal micro-CT.

#### 2.1 Introduction

With the ultimate goal of developing methods to treat human disease, small animal models are used extensively in cardiovascular, orthopedic, and cancer research.<sup>1-3</sup> The advantages of using small animals include short gestation times, low maintenance costs and ease of genetic manipulation.<sup>4</sup> In order to study disease at scales suitable for small animals, high-resolution imaging techniques (i.e., micro-imaging) have been developed; these include micro magnetic resonance imaging,<sup>5, 6</sup> micro positron emission tomography,<sup>7</sup> micro-ultrasound,<sup>8,9</sup> and micro computed tomography (micro-CT).<sup>10</sup> Among these, micro-CT has been the most utilized, based on scientific publications in the last five years.

Micro-CT's ubiquity is attributable to the fact that the modality is quantitative, three-dimensional, non-destructive, fast and cost-effective. Contrast in micro-CT is derived from the differential attenuation of x-rays by various tissues. Unfortunately, soft tissues, which have similar densities, have little differential CT contrast and exogenous agents are required to provide contrast. For example, to image the vasculature, x-ray attenuating contrast agents are injected intravenously to "opacify" the vessels during the acquisition of the micro-CT scan. With these contrast agents, vascular imaging by micro-CT can be potentially utilized to reliably track the development of blood vessels during the process of angiogenesis and in studying the effect of novel therapies for re-vascularization.<sup>11</sup> For human imaging, CT contrast agents are typically small iodinated molecules, which are cleared within a few minutes through the renal system. However, micro-CT scan times can be as long as tens of minutes and successful imaging of the vasculature requires the use of contrast agents that clear from the blood over extended time periods. These agents are referred to as "blood pool" contrast agents.

Several CT blood pool contrast agents are available commercially for *in vivo* small animal research.<sup>12, 13</sup> These have been made possible by advances in nanotechnology and consist of particles large enough to evade immediate renal clearance (i.e. > 10 nm).<sup>14</sup> Initially, commercially available nanoparticle-based blood pool contrast agents were iodine-based to take advantage of the strong attenuation of iodine at low energies (K-edge = 33.2 keV) and included Fenestra VC (containing 50 mg/mL of iodine) and eXia 160 XL (containing 160 mg/mL of iodine).<sup>13, 15</sup> More recently gold-based agents have been developed (e.g. AuroVist 15 nm, containing 200 mg/mL of gold), which take advantage of the high density of gold.<sup>16</sup> These agents have been developed with the intent to deliver a high loading of metal (x-ray attenuator) in a small volume of contrast agent and thereby to provide higher contrast between the vessels and surrounding tissue.

Another class of metals appropriate for CT contrast agents is the lanthanides. These elements are of particular interest because they have K-edges near the average energies used in micro-CT (between 80 kVp and 120 kVp). This property makes the lanthanides ideally suited to use with specialized micro-CT techniques that take advantage of the spectral properties of materials, such as dual-energy imaging and spectral CT. Of the

lanthanides, gadolinium has been used most extensively as a contrast agent for magnetic resonance imaging (MRI). Polymeric nanoparticles decorated with gadolinium, such as the chelated derivative of diethylenetriaminepentaacetic acid and Gd(III) on a cross linked polymer nanogel, have been synthesized and used for vessel imaging of mice, but have gadolinium loading that is too low for CT imaging (typically  $< 0.5$  mg/mL).<sup>17-19</sup>

Lanthanide-based nanoparticles have also been explored for imaging, largely due to their abilities to alter proton relaxation times in MRI in the case of gadolinium<sup>20, 21</sup> or their photon upconversion capabilities in the case of NaLnF<sub>4</sub> (where Ln is a lanthanide and the system is co-doped).<sup>22-24</sup> However, such particles are usually synthesized with hydrophobic ligands,<sup>25</sup> making it challenging to disperse them with high stability in blood. Chatterjee et al. achieved this by coating lanthanide-based nanoparticles with polyethyleneimine, reaching concentrations of 4.4 mg/mL (used subcutaneously for upconversion luminescence imaging).<sup>22</sup> Budijono et al. explored the encapsulation of lanthanide-based nanoparticles in block copolymer assemblies, and demonstrated the stability of these assemblies in serum media at low concentrations ( $< 1$  mg/mL).<sup>24</sup> Similarly, Zhu et al. used pH-responsive block copolymers to encapsulate gadolinium-based nanoparticles, and demonstrated that it can stabilize the nanoparticles in aqueous solution at low concentrations ( $< 0.1$  mg/mL).<sup>21</sup> However, to date only Liu et al., have synthesized a lanthanide contrast agent with a concentration high enough for micro-CT imaging.<sup>26</sup> They encapsulated 70 mg/mL of ytterbium in 1,2-distearoyl-sn-glycero-3-phosphoethanolamine-terminated poly(ethylene glycol) (PEG) and demonstrated circulation in the blood pool for approximately 20 minutes. However, even higher lanthanide concentrations and blood circulation times are required for high resolution imaging of the vasculature.

In this study, we present a simple and systematic method to prepare a lanthanide-based contrast agent for micro-CT applications, which require high contrast-element loading ( $> 100$  mg/mL preferred) and long circulation times (ideally  $> 30$  minutes). The high lanthanide concentration poses a significant challenge, particularly when paired with the need to add polymers, which are required to achieve long circulation times. Erbium, which we have demonstrated to be an excellent contrast agent for *ex vivo* imaging, was selected

as the lanthanide.<sup>27</sup> Oleate-coated NaErF<sub>4</sub> nanoparticles (ErNP) were synthesized and encapsulated into core-shell nanoassemblies via nanoprecipitation using a series of amphiphilic block copolymers (Figure 2.1). A sequence of optimization steps was then performed to identify an ideal polymer, which encapsulates a high lanthanide content while remaining colloidally stable after redispersion in saline and a mouse-blood mimic. Once the ideal polymer was identified, the lanthanide-based contrast agent was evaluated *in vivo* over a period of one hour. To our knowledge, this is the first demonstration of the successful synthesis of an *in vivo* lanthanide-based blood pool agent that can be dispersed into colloidally stable assemblies containing 100 mg/mL of erbium.

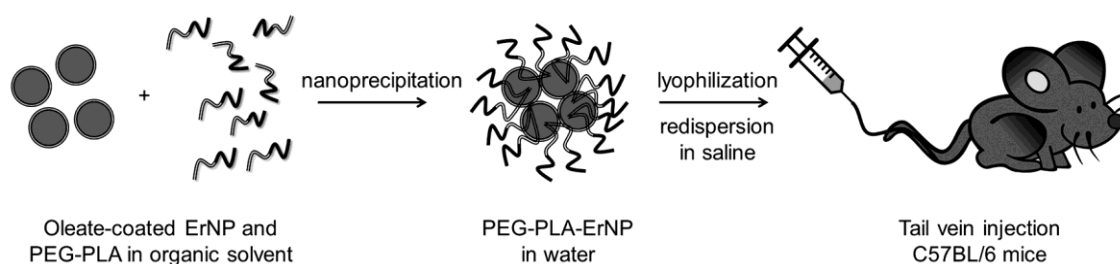


Figure 2.1 Schematic representation of self-assembled erbium-based nanoparticles as a pre-clinical blood pool contrast agent.

## 2.2 Experimental Section

### 2.2.1 Materials and General Methods

Reagents were purchased from commercial suppliers as described in Appendix A and were used without further purification unless otherwise noted. Methods used in the synthesis and characterization of the materials are also presented in Appendix A.

### 2.2.2 Nanoprecipitation for Self-Assembly of Polymeric Nanoparticles Containing Erbium Nanoparticles

Erbium nanoparticles (ErNP) were synthesized by a previously reported method.<sup>28, 29</sup> The ErNP were self-assembled with purchased poly(ethylene glycol) (PEG)-poly(propylene glycol) (PPG) triblock copolymers (PEG<sub>76</sub>-PPG<sub>22</sub>-PEG<sub>76</sub> and PEG<sub>137</sub>-PPG<sub>34</sub>-PEG<sub>137</sub> where the subscripts indicate the degree of polymerization of the blocks), or synthesized diblock

copolymers of PEG-poly( $\epsilon$ -caprolactone)(PCL) (PEG<sub>45</sub>-PCL<sub>20</sub>, PEG<sub>45</sub>-PCL<sub>51</sub>, PEG<sub>114</sub>-PCL<sub>51</sub>, PEG<sub>114</sub>-PCL<sub>97</sub>) or PEG-poly(L-lactide) (PEG<sub>45</sub>-PLA<sub>25</sub>, PEG<sub>45</sub>-PLA<sub>52</sub>, PEG<sub>114</sub>-PLA<sub>53</sub>, PEG<sub>114</sub>-PLA<sub>122</sub>).<sup>30, 31</sup> ErNP (2 mg) were dissolved in 0.1 mL of tetrahydrofuran (THF). Separately, 8 mg of copolymer was dissolved in 0.1 mL of THF. These solutions were then combined and added dropwise to 1.8 mL of deionized water under magnetic stirring. After 1 hour, stirring was stopped and the solution was left uncapped for 12 hours to allow for organic solvent evaporation. The solutions were then dialyzed against 100 mL of deionized water for 2 days with 5 solvent changes. A 450 nm syringe filter was used to remove large aggregates and the samples were characterized by dynamic light scattering (DLS), transmission electron microscopy (TEM) and inductively coupled plasma mass spectrometry (ICP-MS).

### 2.2.3 Colloidal Stability of the Polymeric Nanoparticles

The sterile polymeric nanoparticles containing ErNP were lyophilized prior to redispersion in saline. Saline is used as the solvent of the NPs prior to intravenous injection *in vivo* because it is isotonic with blood; therefore the particles must remain colloidally stable in that environment. DLS size measurements were performed on the redispersed ErNP and the average sizes of the samples were observed for up to one hour.

### 2.2.4 Varying the Polymer Content of the Nanoparticles

The polymeric nanoparticles containing ErNP that remained colloidally stable after freeze-drying and redispersion in saline, and that encapsulated relatively higher erbium amounts were selected (PEG<sub>114</sub>-PLA<sub>53</sub>). Solutions with varying mass ratios were prepared. Synthesized ErNP (80 mg dissolved in 4 mL of THF) were added to 320, 160, 80 or 40 mg of PEG<sub>114</sub>-PLA<sub>53</sub> in 4 mL of THF. These solutions were combined and added dropwise to 100 mL of deionized water under magnetic stirring. After 1 hour, stirring was stopped and the suspension was left uncapped for 12 hours to allow for organic solvent evaporation. The suspensions were then dialyzed against 500 mL of deionized water for 2 days with 5 solvent changes. A 450 nm syringe filter was used to remove large aggregates and the samples were characterized by DLS, TEM and ICP-MS. The samples were lyophilized, sterilized and re-dispersed in 400  $\mu$ L of saline. 10  $\mu$ L of the samples were added to 990  $\mu$ L

of saline or mouse serum mimic for an hour-long time-course DLS study. The mouse serum mimic was pH 7.4 phosphate buffered saline containing 0.5  $\mu\text{g/mL}$  mouse immunoglobulins, 1 wt% bovine serum albumin and 0.1 wt% sodium azide. Colloidal stability in a mouse serum mimic *in vitro* will serve as an indicator of its stability *in vivo*; an increase in the average size signifies aggregation, which would lead to immune system detection followed by clearance from the blood pool *in vivo*.

### 2.2.5 General Micro-CT Imaging and Analysis Methods

Micro-CT images were acquired using the GE Locus Ultra (London, ON) with a protocol previously used to evaluate contrast agent distribution *in vivo*.<sup>15, 32</sup> Briefly, 1000 views (16 ms per view) were acquired at 80 kVp, 55 mA over 360° and reconstructed using a cone-beam reconstruction algorithm. The resulting images have a voxel size of 150 x 150 x 150  $\mu\text{m}$ . Images were analyzed using MicroView (Parallax Innovations, London, ON) and CT contrast was reported in Hounsfield Units (HU – a standard linear scale of x-ray attenuation coefficient, where air = -1000 HU and water = 0 HU). All HU values were measured over a volume of 450  $\times$  450  $\times$  150  $\mu\text{m}$ .

### 2.2.6 Micro-CT Imaging of Erbium-Containing Polymeric Nanoparticles

The relationship between CT contrast and erbium concentration was first determined by micro-CT. Erbium chloride was diluted in saline at erbium concentrations of 5, 10, 20 and 100 mg/mL, which acted as calibration standards. The linear regression between CT contrast (in HU) and erbium concentration was then used to measure the erbium concentrations resulting when 40 mg of each of the lyophilized 1:1 and 0.5:1 PEG<sub>114</sub>-PLA<sub>53</sub>:ErNP formulations were separately dispersed in 0.2 mL of saline.

### 2.2.7 Toxicity of the Contrast Agent

The 1:1 and 0.5:1 PEG<sub>114</sub>-PLA<sub>53</sub>:ErNP mass ratio formulations were tested. Details of these experiments are described in Appendix A. Briefly, an *in vitro* cell viability assay was done using C2C12 mouse myoblast cells from Millipore Sigma (Oakville, ON). The cells

were incubated with the contrast agent for 24 hours, after which cell viability was measured using a 3-(4,5-dimethylthiazol-2-yl)-2,5-diphenyltetrazolium bromide (MTT) assay.

Following *in vitro* tests, the *in vivo* toxicity of the contrast agent was evaluated using the dorsal interscapular subcutaneous tissue of C57BL/6 male mice (25-32 g). All animal studies were carried out in accordance with the regulations set out by the University of Western Ontario's Council on Animal Care, in agreement with the ARRIVE guidelines, and were carried out in accordance with the U.K. Animals Act, 1986 and associated guidelines.

### 2.2.8 Intravenous Administration of the Contrast Agent and Characterization of Distribution *In Vivo*

Five C57BL/6 male mice (25-32 g) were anesthetized initially with 4% isoflurane, and then 1.5% for maintenance, in O<sub>2</sub> via a nose cone placed on the snouts of the animals. The tail veins were catheterized using PE-20 polyethylene tubing. For each mouse, images were first acquired prior to contrast administration. The contrast agent (0.2 mL at 1 g/kg body weight) was injected over a period of 3 minutes and three scans were acquired, starting 2 minutes following the end of injection and ending 60 minutes post injection. The 1:1 PEG<sub>114</sub>-PLA<sub>53</sub>:ErNP (mass ratio) was tested in 3 mice and the 0.5:1 mass ratio formulation was evaluated in 2 mice.

## 2.3 Results and Discussion

### 2.3.1 Synthesis and Characterization of Oleate-Coated ErNP

NaErF<sub>4</sub> nanoparticles were synthesized based on a previously reported method.<sup>28, 29</sup> DLS measurements of ErNP in THF reported a Z-average diameter of  $50 \pm 1$  nm and a polydispersity index (PDI) of  $0.18 \pm 0.02$  (Figure 2.2a and Figure A.2, Appendix A). These results were supported by TEM imaging, which confirmed the synthesis of spherical nanoparticles (Figure 2.2b).

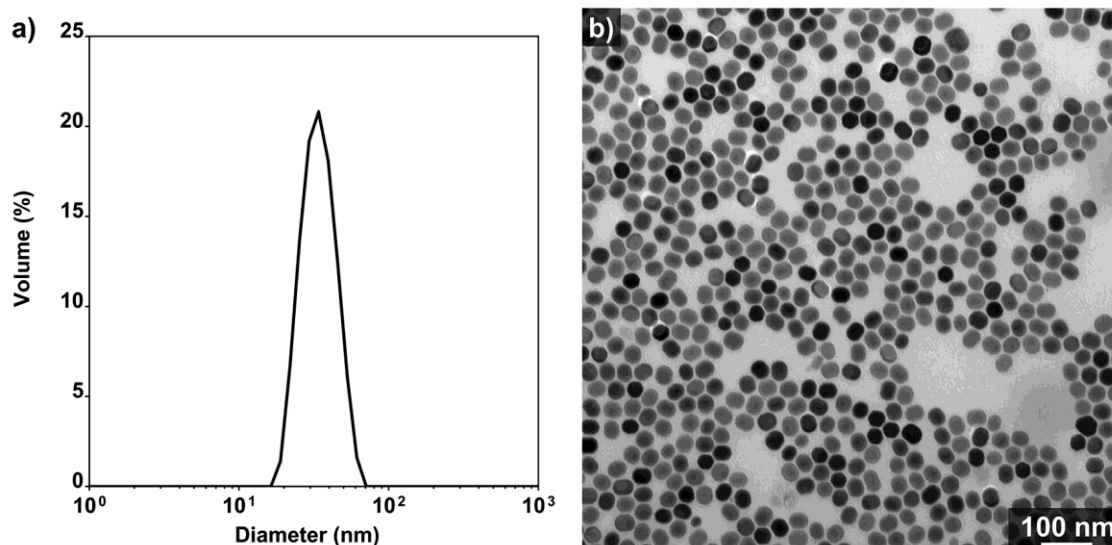


Figure 2.2 a) Volume diameter distribution of ErNP in THF measured by DLS. b) A TEM image of the oleate-coated ErNP.

### 2.3.2 Synthesis and Characterization of Diblock Copolymers

The ErNP are oleate-coated, which makes them incompatible with the aqueous blood pool.<sup>33</sup> It was envisioned that by nanoprecipitation of the ErNP with amphiphilic block copolymers, assemblies containing hydrophobic ErNP in the hydrophobic polymer cores and hydrophilic stabilizing polymer coronas would be formed (Figure 2.1). Polymers are relatively easy to prepare, are colloidally stable even at low concentration, and can be synthesized at different lengths using various monomers, making them tunable and versatile materials.<sup>34</sup> We used PEG as the hydrophilic block for its well-known stealth properties against the immune system.<sup>35, 36</sup> In lieu of displacing the oleate on the ErNP surface with polymers,<sup>29, 37</sup> we chose to synthesize polymeric micelles by nanoprecipitation, which is a fast, reproducible, and cost-effective means of suspending hydrophobic cargo in polar solvents.<sup>38</sup> Displacing the oleate on the ErNP surface would favor the suspension of individual nanoparticles in solution, which is not a requirement in micro-CT.

To identify a carrier that would encapsulate high erbium content while surviving lyophilization and redispersion in saline, a series of amphiphilic block copolymers was studied (Figure 2.3, Table 2.1). Two PEG-PPG-PEG triblock copolymers (commonly

referred to as poloxamers), which are commercially available, cost-effective and are FDA-approved for intravenous administration in humans, were used to form the polymeric assemblies.<sup>39</sup> In addition, several block lengths of PEG-PCL and PEG-PLA were synthesized and studied. These diblock copolymers were selected because they are used clinically as therapeutic drug carriers and are also currently in further clinical trials.<sup>40</sup> The characteristics of the polymeric micelles may change upon varying the copolymer's properties (i.e. hydrophobicity of the non-polar block, total block length, and PEG ratio).<sup>41</sup>

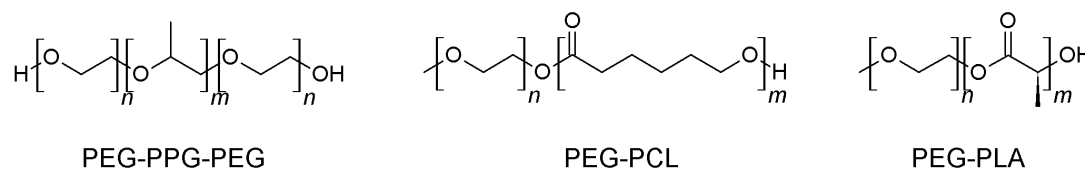


Figure 2.3 Chemical structures of the amphiphilic block copolymers that were used to form the polymeric assemblies.

Table 2.1 SEC and <sup>1</sup>H NMR characterization results of diblock copolymers. <sup>a</sup>Determined by <sup>1</sup>H NMR spectroscopy; <sup>b</sup>Determined by SEC.

Copolymer	PEG molar mass (g/mol)	Monomer feed (equiv.)	PCL or PLA molar mass <sup>a</sup>	M <sub>n</sub> <sup>a</sup>	M <sub>n</sub> <sup>b</sup>	D <sup>b</sup>	f value <sup>a</sup>
PEG <sub>76</sub> -PPG <sub>22</sub> -PEG <sub>76</sub>	6700	-	-	8400	-	-	0.80
PEG <sub>137</sub> -PPG <sub>34</sub> -PEG <sub>137</sub>	12000	-	-	14600	-	-	0.82
PEG <sub>45</sub> -PCL <sub>20</sub>	2000	18	2300	4300	5600	1.1	0.47
PEG <sub>45</sub> -PCL <sub>51</sub>	2000	35	5800	7800	6300	1.4	0.26
PEG <sub>114</sub> -PCL <sub>51</sub>	5000	44	5900	10900	9500	1.1	0.46
PEG <sub>114</sub> -PCL <sub>97</sub>	5000	88	11100	16100	10300	1.3	0.31
PEG <sub>45</sub> -PLA <sub>25</sub>	2000	22	2300	4300	5200	1.2	0.47
PEG <sub>45</sub> -PLA <sub>52</sub>	2000	44	4700	6700	9600	1.1	0.30
PEG <sub>114</sub> -PLA <sub>53</sub>	5000	56	4800	9800	10500	1.3	0.51
PEG <sub>114</sub> -PLA <sub>122</sub>	5000	111	11000	16000	13500	1.4	0.31

PEG-PCL and PEG-PLA were synthesized using PEG monomethyl ether (2000 or 5000 g/mol) as the initiator and the block ratios were tuned by varying the equivalents of ε-caprolactone or L-lactide to achieve PEG mass fractions (f) of approximately 0.5 and 0.3.

Methanesulfonic acid was used as the polymerization catalyst for the synthesis of PEG-PCL, while 1,5,7-triazabicyclo[4.4.0]dec-5-ene was used as the catalyst for PEG-PLA synthesis.<sup>30, 31</sup> A 1:1 ratio of catalyst:initiator was used in each case. Characterization of the diblock copolymers was performed using <sup>1</sup>H nuclear magnetic resonance (NMR) spectroscopy (Figures A.3-A.10) and size exclusion chromatography (SEC) relative to polystyrene standards (Figures A.11-A.14) and the results are summarized in Table 2.1. Typical signals of PEG, PCL and PLA components were utilized to calculate the molar ratios of polymerized monomers to PEG and thus the number average molecular weight ( $M_n$ ). The  $M_n$  and molar mass dispersities ( $D$ ) were also measured by SEC. The  $f$  values were calculated from the NMR data, as this should provide the most accurate assessment of the block ratios. The values indicated for the poloxamers were taken from their respective specification sheets. Overall, the measured  $M_n$  values, particularly from NMR spectroscopy, and  $f$  values were in good agreement with the target structures.

### 2.3.3 Polymer Self-Assembly and ErNP Encapsulation

First, the self-assembly of the block copolymers without ErNPs was investigated. The copolymers were dissolved in THF then this solution was added to water with stirring. After removal of THF by dialysis, the resulting nanoassemblies were characterized by DLS and TEM. The Z-average diameters measured by DLS ranged from 11 to 55 nm (Table 2.2, Figure A.15), consistent with self-assembly into micelles and TEM images confirmed that solid spherical particles were formed (Figure A.16). The PDIs ranged from 0.1 to 0.6, suggesting that some copolymers assembled into nanoparticles with a narrow size distribution ( $PDI < 0.3$ ), whereas others exhibited a large distribution of sizes ( $PDI > 0.3$ ). In general, the TEM results were in good agreement with the volume distributions obtained from DLS, except for both poloxamers (PEG<sub>76</sub>-PPG<sub>22</sub>-PEG<sub>76</sub> and PEG<sub>137</sub>-PPG<sub>34</sub>-PEG<sub>137</sub>). For these poloxamers, the volume distribution in DLS suggested the presence of small scatterers that could be unassembled copolymers in solution, whereas the corresponding TEM images showed larger nanoparticles that could result from aggregation during the drying process.

Table 2.2 Z-average diameters and PDIs obtained using DLS for the self-assembly of block copolymers without ErNP. Each assembly was prepared and measured in triplicate and the error measurements correspond to the standard deviations on these batches.

Polymer	Z-average diameter (nm)	PDI
PEG <sub>76</sub> -PPG <sub>22</sub> -PEG <sub>76</sub>	11 ± 2	0.6 ± 0.3
PEG <sub>137</sub> -PPG <sub>34</sub> -PEG <sub>137</sub>	17 ± 3	1.0 ± 0.4
PEG <sub>45</sub> -PCL <sub>20</sub>	20 ± 1	0.2 ± 0.1
PEG <sub>45</sub> -PCL <sub>51</sub>	17 ± 2	0.1 ± 0.1
PEG <sub>114</sub> -PCL <sub>51</sub>	18 ± 4	0.1 ± 0.1
PEG <sub>114</sub> -PCL <sub>97</sub>	31 ± 4	0.2 ± 0.1
PEG <sub>45</sub> -PLA <sub>25</sub>	26 ± 11	0.5 ± 0.2
PEG <sub>45</sub> -PLA <sub>52</sub>	29 ± 8	0.4 ± 0.1
PEG <sub>114</sub> -PLA <sub>122</sub>	31 ± 10	0.4 ± 0.2
PEG <sub>114</sub> -PLA <sub>53</sub>	55 ± 8	0.2 ± 0.1

Having confirmed the self-assembly behavior of the amphiphilic block copolymers alone, ErNPs were then added. Both the copolymer and ErNP were dissolved in THF and then nanoprecipitated into water to form suspensions of erbium-containing assemblies. The mass ratio of polymer:ErNP was 4:1. THF was removed by dialysis, then the suspensions were passed through a 0.45 μm filter. This filtration served to remove any ErNP that had not been encapsulated and consequently aggregated, as well as polymer-ErNP assemblies that were too large and would be preferentially cleared from the blood by the mononuclear phagocytic system (MPS).<sup>42, 43</sup> The resulting assemblies were characterized by DLS and TEM (Figure 2.4, Table 2.3). The TEM images showed individual ErNP or groups of ErNP across the grid, unlike the oleate-coated ones in Figure 2.2b, which displayed no specific organization or aggregation. This suggests the encapsulation of the ErNP within the amphiphilic block copolymers. It should be noted that the polymers were indiscernible in the TEM images because of the high contrast from the ErNP. The Z-average diameters that were measured by DLS ranged from 53 to 183 nm. This also supported the encapsulation of ErNP within the amphiphilic block copolymers, as these diameters were larger than those of the polymer-only micelles.

When PEG<sub>114</sub>-PLA<sub>122</sub> or any of the PEG-PCL diblock copolymers were used to form the assemblies, moderate PDIs (between 0.2 and 0.3) were observed. On the other hand, when using either poloxamers or the other PEG-PLA diblock copolymers good PDIs (< 0.2) were obtained. Because the contrast agent was simply required to remain in circulation (i.e. no tissue-targeting was required), obtaining low PDIs was not of utmost importance; meeting the size requirements that would allow evasion of immediate renal clearance and preferential uptake by the MPS was sufficient.

Table 2.3 Characterization data for the polymer-encapsulated ErNP obtained from DLS and ICP-MS both as initially prepared and after lyophilization followed by resuspension in saline. The polymer:ErNP mass ratios were 4:1 unless otherwise indicated. Each assembly was prepared and measured in triplicate and the error measurements correspond to the standard deviations on these batches. <sup>a</sup>Determined by DLS; <sup>b</sup>Determined by ICP-MS where 780 µg/L would correspond to encapsulation of 100% of the Er added during self-assembly.

Polymer	In water following initial preparation <sup>a</sup>		Post-lyophilization and resuspension in saline <sup>a</sup>		Erbium content (µg/L) <sup>b</sup>
	Z-average (nm)	PDI	Z-average (nm)	PDI	
PEG <sub>76</sub> -PPG <sub>22</sub> -PEG <sub>76</sub>	174 ± 4	0.1 ± 0.1	294 ± 34	0.2 ± 0.1	62 ± 6
PEG <sub>137</sub> -PPG <sub>34</sub> -PEG <sub>137</sub>	176 ± 6	0.1 ± 0.1	212 ± 2	0.2 ± 0.1	232 ± 1
PEG <sub>45</sub> -PCL <sub>20</sub>	98 ± 10	0.3 ± 0.1	2145 ± 179	0.2 ± 0.1	377 ± 25
PEG <sub>45</sub> -PCL <sub>51</sub>	82 ± 2	0.3 ± 0.1	3204 ± 416	0.2 ± 0.1	506 ± 3
PEG <sub>114</sub> -PCL <sub>51</sub>	53 ± 5	0.3 ± 0.1	1057 ± 32	0.6 ± 0.1	596 ± 21
PEG <sub>114</sub> -PCL <sub>97</sub>	84 ± 1	0.2 ± 0.1	2861 ± 9	0.4 ± 0.5	732 ± 22
PEG <sub>45</sub> -PLA <sub>25</sub>	165 ± 2	0.1 ± 0.1	192 ± 4	0.5 ± 0.1	407 ± 2
PEG <sub>45</sub> -PLA <sub>52</sub>	151 ± 2	0.2 ± 0.1	1597 ± 83	0.4 ± 0.1	149 ± 1
PEG <sub>114</sub> -PLA <sub>122</sub>	130 ± 2	0.2 ± 0.1	301 ± 13	0.4 ± 0.1	339 ± 4
PEG <sub>114</sub> -PLA <sub>53</sub>	154 ± 2	0.1 ± 0.1	134 ± 1	0.2 ± 0.1	599 ± 3
PEG <sub>114</sub> -PLA <sub>53</sub> (2:1)	180 ± 3	0.2 ± 0.1	180 ± 6	0.1 ± 0.1	583 ± 28
PEG <sub>114</sub> -PLA <sub>53</sub> (1:1)	179 ± 4	0.2 ± 0.1	171 ± 3	0.2 ± 0.1	607 ± 16
PEG <sub>114</sub> -PLA <sub>53</sub> (0.5:1)	183 ± 3	0.1 ± 0.1	185 ± 5	0.2 ± 0.1	533 ± 32

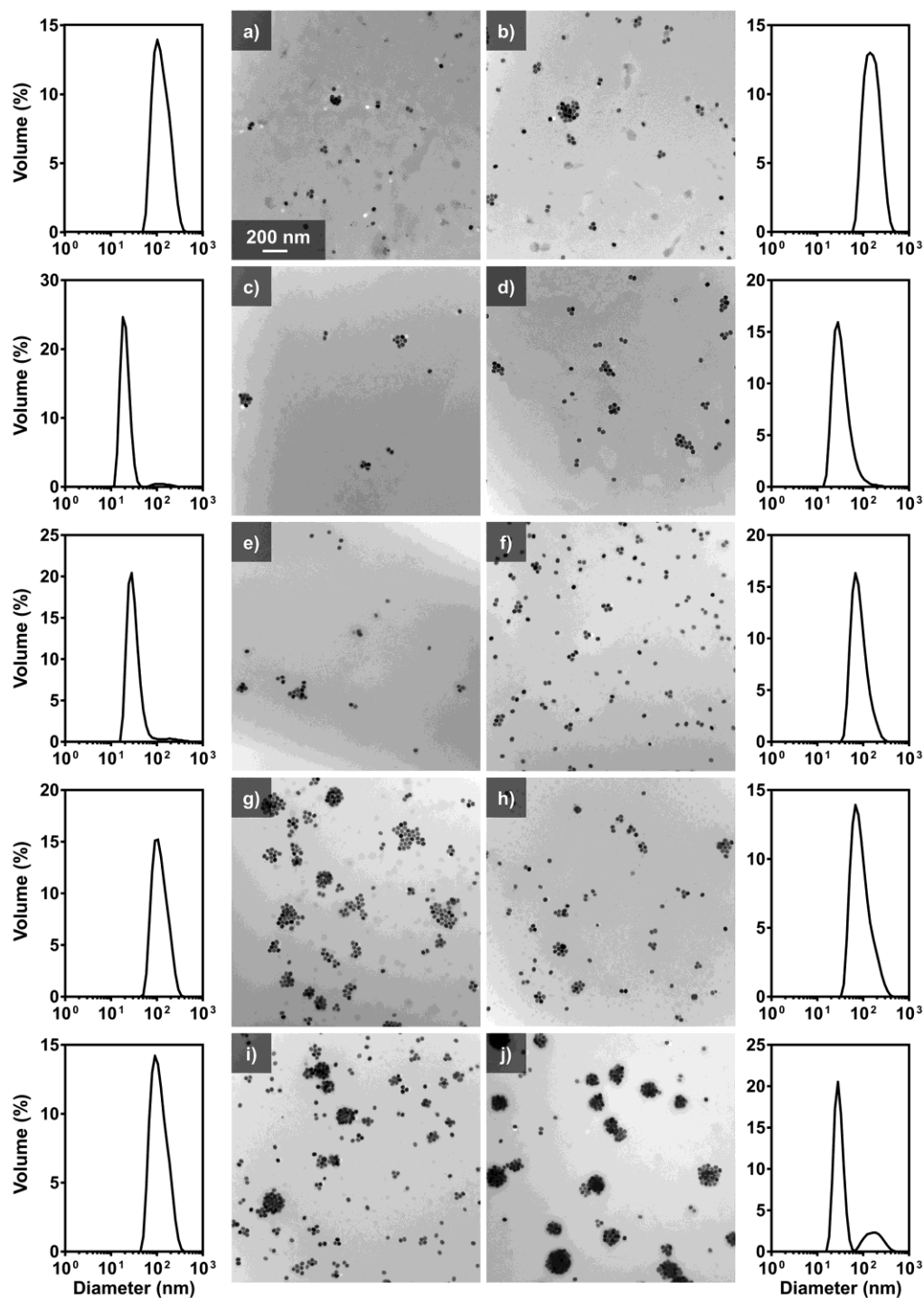


Figure 2.4 DLS volume (%) diameter distributions and the corresponding TEM images of polymer-encapsulated ErNP using a) PEG<sub>76</sub>-PPG<sub>22</sub>-PEG<sub>76</sub>, b) PEG<sub>137</sub>-PPG<sub>34</sub>-PEG<sub>137</sub>, c) PEG<sub>45</sub>-PCL<sub>20</sub>, d) PEG<sub>45</sub>-PCL<sub>51</sub>, e) PEG<sub>114</sub>-PCL<sub>51</sub>, f) PEG<sub>114</sub>-PCL<sub>97</sub>, g) PEG<sub>45</sub>-PLA<sub>25</sub>, h) PEG<sub>45</sub>-PLA<sub>52</sub>, i) PEG<sub>114</sub>-PLA<sub>53</sub>, and j) PEG<sub>114</sub>-PLA<sub>122</sub>.

### 2.3.4 Redispersion and Characterization of the Lyophilized Polymer-Encapsulated ErNP

Because the polymer-encapsulated ErNP were prepared by nanoprecipitation at low concentrations in water, the sample had to be lyophilized then redispersed at higher concentrations. The ability to lyophilize and resuspend the assemblies is also advantageous for their long-term storage. Dried samples were redispersed in 0.9% saline, which is isotonic with blood, and the Z-average diameters of the assemblies were measured by DLS (Table 2.3). No filtration was performed after redispersion. In addition, because colloidal stability of the contrast agent in its administration medium is required, the Z-average diameters of the redispersed ErNP-loaded assemblies were also observed by DLS over 60 minutes.

Relative to the pre-lyophilized diameters, minimal changes occurred for the PEG<sub>137</sub>-PPG<sub>34</sub>-PEG<sub>137</sub>, PEG<sub>45</sub>-PLA<sub>25</sub>, and PEG<sub>114</sub>-PLA<sub>53</sub> assemblies, while the remainder redispersed in saline at much larger hydrodynamic diameters, suggesting that they were aggregated. For example, the PEG<sub>76</sub>-PPG<sub>22</sub>-PEG<sub>76</sub> assemblies, which initially had a Z-average hydrodynamic diameter of  $174 \pm 4$  nm had a diameter of  $294 \pm 34$  nm after redispersion in saline, while the PEG<sub>137</sub>-PPG<sub>34</sub>-PEG<sub>137</sub> assemblies, which were initially  $176 \pm 6$  nm, were redispersed in saline at  $212 \pm 2$  nm (Figure A.17). Given the very similar *f* values for these polymers, the larger PEG block is likely capable or better stabilizing the particles. All PEG-PCL assemblies redispersed in saline as micrometer-sized particles, which was undesirable, as these particles would be rapidly cleared by the MPS (Figure A.18). The colloidal instabilities of PEG-PCL assemblies have been reported before, which makes them undesirable for use under normal physiological conditions. The PEG<sub>45</sub>-PLA<sub>52</sub> assemblies also redispersed as microparticles and PEG<sub>114</sub>-PLA<sub>122</sub> assemblies redispersed at an increased Z-average diameter of  $301 \pm 13$  nm compared to an initial diameter of  $130 \pm 2$  nm (Figure A.19). Both of these copolymers had low *f* values of  $\sim 0.3$ , which may contribute to their poor stability to redispersion. However, PEG<sub>45</sub>-PLA<sub>25</sub> and PEG<sub>114</sub>-PLA<sub>53</sub> assemblies retained Z-average diameters of  $192 \pm 4$  and  $134 \pm 1$  nm after redispersion in saline, similar to their initial diameters of  $165 \pm 2$  and  $154 \pm 2$  nm. Both

remained colloidally stable for up to 60 minutes. This stability may result from their increased  $f$  values of  $\sim 0.5$ .

ICP-MS was used to quantify the concentration of aqua regia-digested erbium that was encapsulated by each system (Table 2.3). These measurements were performed on the initially prepared samples after their filtration. If all of the added erbium had remained dispersed in assemblies less than  $0.45 \mu\text{m}$  in diameter, the expected erbium concentration of the suspensions would have been  $780 \mu\text{g/L}$ . The highest erbium content was observed for PEG<sub>114</sub>-PCL<sub>97</sub> at  $732 \pm 22 \mu\text{g/L}$ . The second highest concentration was obtained with PEG<sub>114</sub>-PLA<sub>53</sub> at  $599 \pm 3 \mu\text{g/L}$ , then PEG<sub>114</sub>-PCL<sub>51</sub> at  $596 \pm 21 \mu\text{g/L}$ . However, out of the assemblies formed by these block copolymers, only PEG<sub>114</sub>-PLA<sub>53</sub> assemblies could be redispersed without a substantial increase in Z-average diameter in saline. The other block copolymers that allowed size consistency had lower erbium content, with PEG<sub>137</sub>-PPG<sub>34</sub>-PEG<sub>137</sub> at  $232 \pm 1 \mu\text{g/L}$  and PEG<sub>45</sub>-PLA<sub>25</sub> at  $407 \pm 2 \mu\text{g/L}$ . Decreased erbium content resulted from the filtration of unencapsulated hydrophobic ErNP that aggregated in water or ErNP in assemblies larger than  $0.45 \mu\text{m}$  in diameter. Based on this analysis, further studies were performed with PEG<sub>114</sub>-PLA<sub>53</sub> as it was able to form stable assemblies with high erbium content.

### 2.3.5 Characterization of the Assemblies Formed with PEG<sub>114</sub>-PLA<sub>53</sub>

The polymer content of the contrast agent does not contribute to the attenuation of x-rays and hence will not contribute to higher contrast. It does however contribute to the total mass of the material in solution, and increases viscosity, thereby making administration of the suspension difficult. Thus, it would be desirable to decrease the polymer:ErNP ratio in the assemblies. However, decreasing the polymer content of the assemblies has one drawback, which is the potential decrease of their stealthiness and immune system evasion.<sup>36</sup> To investigate the possibility of lowering the polymer content of the contrast agent while retaining stability, assemblies were formed with lower PEG<sub>114</sub>-PLA<sub>53</sub>:ErNP mass ratios (from 4:1 to 2:1, 1:1 and 0.5:1). Their colloidal stabilities at  $37^\circ\text{C}$  in saline and in a mouse serum mimic were studied by DLS (Figure 2.5). The serum mimic contained bovine serum albumin and ions at concentrations that are similar to mouse blood.

The proteins can potentially contribute to polymer shedding, and thereby to nanoparticle aggregation *in vitro*. In the blood pool of the animal *in vivo*, polymer shedding leads to the detection by the immune system and clearance of the nanoparticles from the blood via the liver.<sup>35, 36</sup> In the DLS analysis, the proteins generated insignificant scattering that did not interfere with the analysis of the assemblies (Figure A.20-A.21). The Z-average diameters for the initially prepared assemblies ranged from 121-185 nm and did not vary significantly over a period of 60 minutes in saline or in the mouse blood mimic, indicating that each formulation was sufficiently stable.

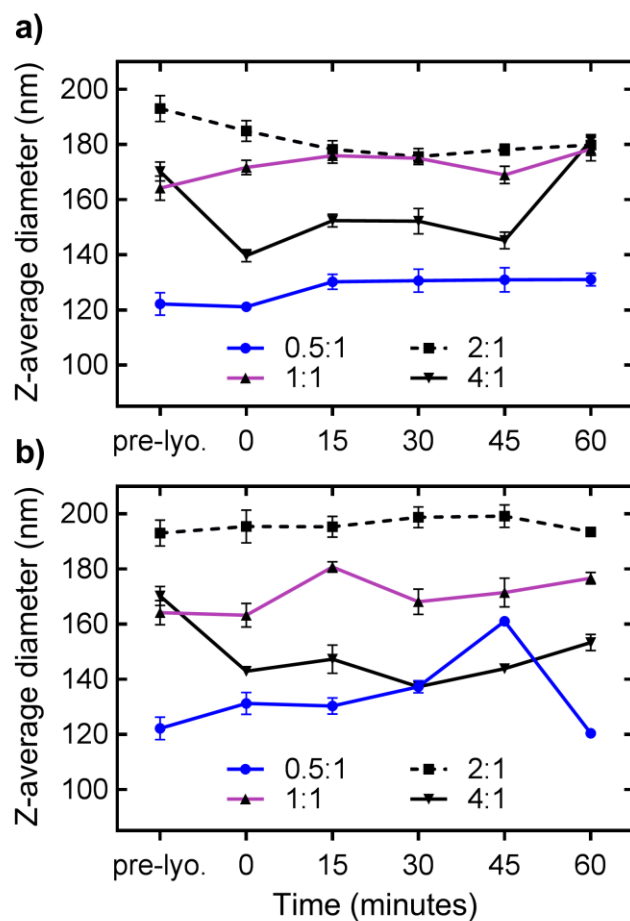


Figure 2.5 Time-course DLS results at 37 °C for PEG<sub>114</sub>-PLA<sub>53</sub>-encapsulated ErNP post-lyophilization after redispersion in a) saline and b) mouse serum mimic.

TEM imaging of the assemblies and analyses of their erbium content were also performed. Denser ErNP cores were observed when the polymer:ErNP ratio was reduced (Figure 2.6). Thus, decreasing the availability of polymers favored higher ErNP loading per assembly. ICP-MS results revealed similar erbium content in the suspensions for all of the mass ratios. Given this, and their colloidal stability *in vitro*, all the formulations should demonstrate similar contrast enhancement values over time once concentrated and administered to the blood pool. However, the concentrated solutions formed with polymer:ErNP mass ratios of 4:1 and 2:1 had high viscosities that made the solutions too challenging to administer *in vivo* through the 30 G needles. Hence, for subsequent studies, the assemblies containing PEG<sub>114</sub>-PLA<sub>53</sub>:ErNP mass ratios of 1:1 and 0.5:1 were used. Using pyrene as a fluorescent probe,<sup>44</sup> the critical aggregation concentrations (CACs) for these 1:1 and 0.5:1 formulations were measured and compared to that of PEG<sub>114</sub>-PLA<sub>53</sub> assemblies without ErNP. We found that the CAC of the block copolymer alone was 26 mg/L, whereas those of the 1:1 and 0.5:1 PEG<sub>114</sub>-PLA<sub>53</sub>:ErNP formulations were 96 mg/L and 117 mg/L respectively (Figures A.22-A.24). Thus, it is evident that the loading of ErNP destabilizes the assemblies to some extent. Nevertheless, these CAC values are much lower than the concentrations at which they would be administered, even after dilution into the blood pool.

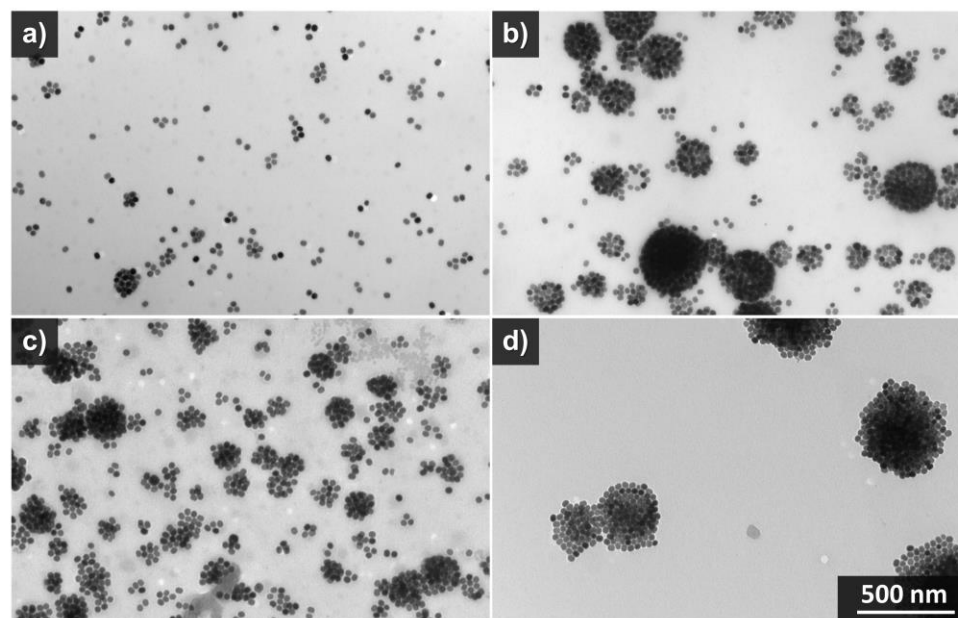


Figure 2.6 TEM images of the PEG<sub>114</sub>-PLA<sub>53</sub>-encapsulated ErNP using polymer:ErNP mass ratios of a) 4:1, b) 2:1, c) 1:1, d) 0.5:1.

### 2.3.6 Erbium Content in ErNP Determined *Via* Micro-CT

While ICP-MS was used to detect erbium content before lyophilization, micro-CT was used to confirm the erbium content of the redispersed and high concentration versions of the contrast agents. A linear relationship between an element's concentration and its attenuation of x-rays exists and does not depend on the specific chemical form of the element. This quantitative property of micro-CT contrast is one of its advantages as an imaging modality. Calibration standards containing erbium chloride dissolved in saline at concentrations of 0, 5, 10, 20 and 100 mg/mL of erbium were scanned. Using linear regression of the measured CT numbers of the standards (Figure A.25), it was determined that 40 mg of the lyophilized 1:1 and 0.5:1 PEG<sub>114</sub>-PLA<sub>53</sub>:ErNP formulations dispersed in 0.2 mL of saline resulted in contrast element concentrations of 48 and 74 mg/mL of erbium respectively. Therefore, 100 mg/mL is achieved when 42 mg of the 1:1 formulation and 27 mg of the 0.5:1 formulation is suspended in 0.1 mL of saline. Micro-CT scans of the high concentration suspensions verified that 100 mg/mL of erbium was achieved when the calculated amount of the agent was used (Figure A.26). While higher erbium loading can be achieved with more concentrated solutions, we restricted the experiments to 100 mg/mL in order to maintain low viscosities for intravenous injection in mice.

### 2.3.7 Toxicity of the Contrast Agent

The *in vitro* and *in vivo* toxicity of the contrast agent was evaluated prior to its intravenous administration. Based on MTT assays, greater than 80% viability relative to controls was observed for the 1:1 polymer to erbium mass ratio formulation up to concentrations of 0.5 mg/mL (Figure A.27). The 0.5:1 polymer to erbium formulation was even less toxic, with greater than 80% viability up to 1 mg/mL, the highest concentration tested. We also performed subcutaneous injections to study the materials *in vivo*. Subcutaneous tissue has slow absorption and clearance rates of exogenous materials, which provides an opportunity to study the reaction of tissues to the contrast agent over prolonged periods. Three-dimensional micro-CT images were obtained in mice before the subcutaneous injection of the 1:1 and 0.5:1 PEG<sub>114</sub>-PLA<sub>53</sub>:ErNP formulations and two weeks after the administration of the agent. Each scan took 16 seconds to acquire. Representative micro-CT images for each of the contrast agent formulation injections are shown in Figure A.28. The images

show that the contrast agent localized near the injection site for up to two weeks. Gross examination of the subcutaneous tissue confirmed the presence of some contrast agent near the injection site. No abnormalities were observed in either the subcutaneous tissue or the dermis (Figure A.29).

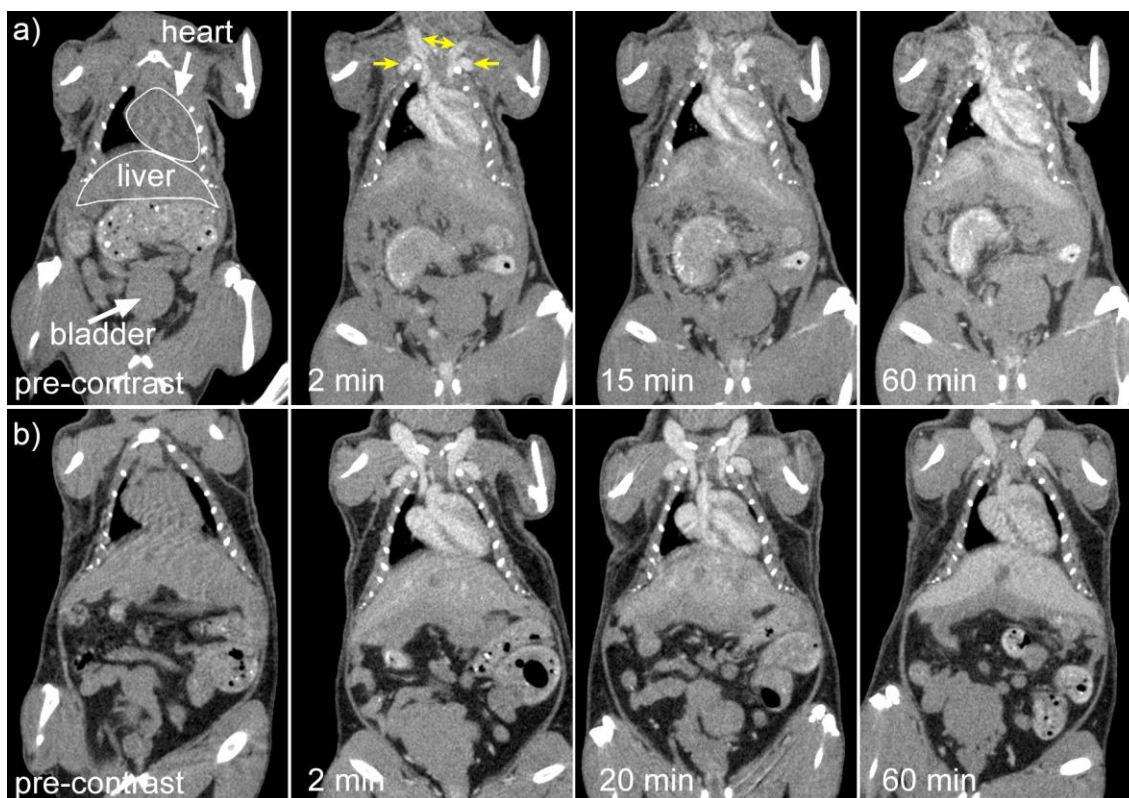


Figure 2.7 Representative coronal micro-CT images showing the heart, liver, aorta, jugular veins and bladder of mice that received contrast agent formulated at a) 1:1 and b) 0.5:1 PEG114-PLA53:ErNP mass ratios. All times are reported from the completion of the contrast agent injection. In the 2 minute image in a), the external jugular veins (double arrowheads) and the axillary veins (arrows) are clearly visible.

### 2.3.8 Distribution of the Contrast Agent *In Vivo*

Three-dimensional micro-CT images were obtained in mice before the intravenous administration of both contrast agent formulations and at three time points following the administration of the agent. Each scan took 16 seconds to acquire. Representative micro-CT images for each of the contrast agents are shown in Figure 2.7. After contrast agent

administration, all the major vessels – particularly the external jugular and axillary veins in Figure 2.7 – became clearly visible. For both formulations, there appeared to be no change in contrast in the chambers of the heart for up to 60 minutes. The contrast in the liver was seen as early as the 2-minute time point – demonstrated by the ability to distinguish liver from surrounding soft tissue.

Quantitative analysis indicated an increase in blood pool CT number of over 250 HU compared to pre-contrast values. The bladder was indistinguishable from pre-contrast values, indicating that the agent was not cleared through the renal system, as expected of materials that exceed the size of renal fenestrations.<sup>14</sup> By the one-hour mark, the liver and the spleen had increased up to  $180 \pm 15$  HU and  $278 \pm 18$  HU, respectively, for the 1:1 formulation, confirming the hypothesis that large nanoparticles are cleared through the MPS.<sup>35, 36</sup> In the myocardium, the CT number was just under 100 HU at all time points, which was expected of soft tissue in the absence of contrast material. As expected, the 0.5:1 polymer:ErNP assemblies demonstrated lower stealth activity, due to the lower amount of polymer used in the synthesis of the assembly, and were cleared from the blood more rapidly as indicated by the decreased intensity of the blood pool in the micro-CT images. Overall, this initial imaging study demonstrates that these new contrast agents can be dispersed and injected into mice at a concentration sufficient to achieve vascular contrast by micro-CT *in vivo*. Furthermore, the particles exhibited sufficient stealth properties to circulate in the vasculature for at least 1 hour. This suggests the promise of these new lanthanide-based agents for applications such as dual-energy imaging and spectral CT.

## 2.4 Conclusions

In this study, by systematically comparing a series of amphiphilic block copolymers composed of different hydrophobic blocks and different PEG mass fractions, we identified PEG<sub>114</sub>-PLA<sub>53</sub> as an amphiphilic copolymer that can encapsulate oleate-coated NaErF<sub>4</sub> nanoparticles. The PEG<sub>114</sub>-PLA<sub>53</sub>:ErNP assemblies redispersed into colloiddally stable particles in saline after lyophilization and remained in the blood pool *in vivo* for at least an hour – a time period that well exceeds live animal micro-CT requirements. Importantly, we were able to formulate the assemblies at a high concentration of 100 mg/mL of erbium using PEG<sub>114</sub>-PLA<sub>53</sub>. At a delivered dose of 0.2 mL per mouse, this new contrast agent

formulation resulted in the enhancement of blood pool in micro-CT images (at 80 kVp) by approximately 250 HU (above a soft tissue baseline of 100 HU) for at least an hour following contrast agent administration. This system should be readily adaptable for a variety of lanthanides, as the metal can be easily substituted in the oleate-coated NaErF<sub>4</sub> while retaining very similar properties, suggesting its promise as a new class of contrast agents for micro-CT as well as other imaging modalities such as MRI and optical imaging, in which lanthanides are utilized. Future studies will explore further the biodistribution and toxicity profiles of these agents.

## 2.5 References

- (1) Abarbanell, A. M.; Herrmann, J. L.; Weil, B. R.; Wang, Y.; Tan, J.; Moberly, S. P.; Fiege, J. W.; Meldrum, D. R. Animal models of myocardial and vascular injury. *J. Surg. Res.* **2010**, *162*, 239-249.
- (2) Camacho, P.; Fan, H.; Liu, Z.; He, J. Q. Small mammalian animal models of heart disease. *Am. J. Cardiovasc. Dis.* **2016**, *6*, 70-80.
- (3) Day, C. P.; Merlino, G.; Van Dyke, T. Preclinical mouse cancer models: a maze of opportunities and challenges. *Cell* **2015**, *163*, 39-53.
- (4) Xu, H.; Baldini, A. Genetic pathways to mammalian heart development: Recent progress from manipulation of the mouse genome. *Semin. Cell Dev. Biol.* **2007**, *18*, 77-83.
- (5) Lancelot, E.; Amirbekian, V.; Brigger, I.; Raynaud, J. S.; Ballet, S.; David, C.; Rousseaux, O.; Le Greneur, S.; Port, M.; Lijnen, H. R.; Bruneval, P.; Michel, J. B.; Ouimet, T.; Roques, B.; Amirbekian, S.; Hyafil, F.; Vucic, E.; Aguinaldo, J. G.; Corot, C.; Fayad, Z. A. Evaluation of matrix metalloproteinases in atherosclerosis using a novel noninvasive imaging approach. *Arterioscler. Thromb. Vasc. Biol.* **2008**, *28*, 425-432.
- (6) Mateo, J.; Benito, M.; Espana, S.; Sanz, J.; Jimenez-Borreguero, J.; Fuster, V.; Ruiz-Cabello, J. Magnetic resonance imaging of the atherosclerotic mouse aorta. *Methods Mol. Biol.* **2015**, *1339*, 387-394.
- (7) Ahmadi, A.; Thorn, S. L.; Alarcon, E. I.; Kordos, M.; Padavan, D. T.; Hadizad, T.; Cron, G. O.; Beanlands, R. S.; DaSilva, J. N.; Ruel, M.; deKemp, R. A.; Suuronen, E. J. PET imaging of a collagen matrix reveals its effective injection and targeted retention in a mouse model of myocardial infarction. *Biomaterials* **2015**, *49*, 18-26.
- (8) Bondoc, A. B.; Detombe, S.; Dunmore-Buyze, J.; Gutpell, K. M.; Liu, L.; Kaszuba, A.; Han, S.; McGirr, R.; Hadway, J.; Drangova, M.; Hoffman, L. M. Application of 3-d echocardiography and gated micro-computed tomography to assess cardiomyopathy in a mouse model of duchenne muscular dystrophy. *Ultrasound Med. Biol.* **2014**, *40*, 2857-2867.
- (9) Cherin, E.; Williams, R.; Needles, A.; Liu, G.; White, C.; Brown, A. S.; Zhou, Y. Q.; Foster, F. S. Ultrahigh frame rate retrospective ultrasound microimaging and blood flow visualization in mice *in vivo*. *Ultrasound Med. Biol.* **2006**, *32*, 683-691.
- (10) Badea, C. T.; Drangova, M.; Holdsworth, D. W.; Johnson, G. A. *In vivo* small-animal imaging using micro-CT and digital subtraction angiography. *Phys. Med. Biol.* **2008**, *53*, R319-350.
- (11) Poole, K. M.; Tucker-Schwartz, J. M.; Sit, W. W.; Walsh, A. J.; Duvall, C. L.; Skala, M. C. Quantitative optical imaging of vascular response *in vivo* in a model of peripheral arterial disease. *Am. J. Physiol. Heart Circ. Physiol.* **2013**, *305*, H1168-1180.

- (12) Detombe, S. A.; Ford, N. L.; Xiang, F.; Lu, X.; Feng, Q.; Drangova, M. Longitudinal follow-up of cardiac structure and functional changes in an infarct mouse model using retrospectively gated micro-computed tomography. *Invest. Radiol.* **2008**, *43*, 520-529.
- (13) Willekens, I.; Lahoutte, T.; Buls, N.; Vanhove, C.; Deklerck, R.; Bossuyt, A.; de Mey, J. Time-course of contrast enhancement in spleen and liver with Exia 160, Fenestra LC, and VC. *Mol. Imaging Biol.* **2009**, *11*, 128-135.
- (14) Choi, C. H.; Zuckerman, J. E.; Webster, P.; Davis, M. E. Targeting kidney mesangium by nanoparticles of defined size. *Proc. Natl. Acad. Sci. U.S.A.* **2011**, *108*, 6656-6661.
- (15) Detombe, S. A.; Dunmore-Buyze, J.; Drangova, M. Evaluation of eXIA 160 cardiac-related enhancement in C57BL/6 and BALB/c mice using micro-CT. *Contrast Media Mol. Imaging* **2012**, *7*, 240-246.
- (16) Ashton, J. R.; Clark, D. P.; Moding, E. J.; Ghaghada, K.; Kirsch, D. G.; West, J. L.; Badea, C. T. Dual-energy micro-CT functional imaging of primary lung cancer in mice using gold and iodine nanoparticle contrast agents: a validation study. *PLoS One* **2014**, *9*, e88129.
- (17) Jackson, A. W.; Chandrasekharan, P.; Shi, J.; Rannard, S. P.; Liu, Q.; Yang, C. T.; He, T. Synthesis and *in vivo* magnetic resonance imaging evaluation of biocompatible branched copolymer nanocontrast agents. *Int. J. Nanomed.* **2015**, *10*, 5895-5907.
- (18) Nazemi, A.; Martínez, F.; Scholl, T.; Gillies, E. Biodegradable dendritic polymersomes as modular, high-relaxivity MRI contrast agents. *RSC Adv.* **2012**, *2*, 7971-7973.
- (19) Soleimani, A.; Martínez, F.; Economopoulos, V.; Foster, P.; Scholl, T.; Gillies, E. Polymer cross-linking: a nanogel approach to enhancing the relaxivity of MRI contrast agents. *J. Mater. Chem. B* **2013**, *1*, 1027-1034.
- (20) Faucher, L.; Tremblay, M.; Lagueux, J.; Gossuin, Y.; Fortin, M. A. Rapid synthesis of PEGylated ultrasmall gadolinium oxide nanoparticles for cell labeling and tracking with MRI. *ACS Appl. Mater. Interfaces* **2012**, *4*, 4506-4515.
- (21) Zhu, L.; Yang, Y.; Farquhar, K.; Wang, J.; Tian, C.; Ranville, J.; Boyes, S. G. Surface modification of Gd nanoparticles with pH-responsive block copolymers for use as smart MRI contrast agents. *ACS Appl. Mater. Inter.* **2016**, *8*, 5040-5050.
- (22) Chatterjee, D. K.; Rufaihah, A. J.; Zhang, Y. Upconversion fluorescence imaging of cells and small animals using lanthanide doped nanocrystals. *Biomaterials* **2008**, *29*, 937-943.
- (23) Zhou, J.; Sun, Y.; Du, X.; Xiong, L.; Hu, H.; Li, F. Dual-modality *in vivo* imaging using rare-earth nanocrystals with near-infrared to near-infrared (NIR-to-NIR)

upconversion luminescence and magnetic resonance properties. *Biomaterials* **2010**, *31*, 3287-3295.

(24) Budijono, S. J.; Shan, J.; Yao, N.; Miura, Y.; Hoye, T.; Austin, R. H.; Ju, Y.; Prud'homme, R. K. Synthesis of stable block-copolymer-protected NaYF<sub>4</sub>:Yb<sup>3+</sup>, Er<sup>3+</sup> up-converting phosphor nanoparticles. *Chem. Mater.* **2010**, *22*, 311-318.

(25) Wang, M.; Abbineni, G.; Clevenger, A.; Mao, C.; Xu, S. Upconversion nanoparticles: synthesis, surface modification and biological applications. *Nanomedicine* **2011**, *7*, 710-729.

(26) Liu, Y.; Ai, K.; Liu, J.; Yuan, Q.; He, Y.; Lu, L. A high-performance ytterbium-based nanoparticulate contrast agent for in vivo X-ray computed tomography imaging. *Angew. Chem. Int. Ed.* **2012**, *51*, 1437-1442.

(27) Tse, J. J.; Dunmore-Buyze, P. J.; Drangova, M.; Holdsworth, D. W. Erbium-Based Perfusion Contrast Agent for Small-Animal Microvessel Imaging. *Contrast Media Mol. Imaging* **2017**, *2017*, 10.

(28) Li, Z.; Zhang, Y. An efficient and user-friendly method for the synthesis of hexagonal-phase NaYF<sub>4</sub>:Yb, Er/Tm nanocrystals with controllable shape and upconversion fluorescence. *Nanotechnology* **2008**, *19*, 345606-345610.

(29) Zhao, G.; Tong, L.; Cao, P.; Nitz, M.; Winnik, M. A. Functional PEG-PAMAM-tetraphosphonate capped NaLnF<sub>4</sub> nanoparticles and their colloidal stability in phosphate buffer. *Langmuir* **2014**, *30*, 6980-6989.

(30) Couffin, A.; Delcroix, D.; Martín-Vaca, B.; Bourissou, D.; Navarro, C. Mild and efficient preparation of block and gradient copolymers by methanesulfonic acid catalyzed ring-opening polymerization of caprolactone and trimethylene carbonate. *Macromolecules* **2013**, *46*, 4354-4360.

(31) Lohmeijer, B.; Pratt, R.; Leibfarth, F.; Logan, J.; Long, D.; Dove, A.; Nederberg, F.; Choi, J.; Wade, C.; Waymouth, R.; Hedrick, J. Guanidine and amidine organocatalysts for ring-opening polymerization of cyclic esters. *Macromolecules* **2006**, *39*, 8574-8583.

(32) Ford, N. L.; McCaig, L.; Jeklin, A.; Lewis, J. F.; Veldhuizen, R. A.; Holdsworth, D. W.; Drangova, M. A respiratory-gated micro-CT comparison of respiratory patterns in free-breathing and mechanically ventilated rats. *Physiol. Rep.* **2017**, *5*, e13074.

(33) Aggarwal, P.; Hall, J. B.; McLeland, C. B.; Dobrovolskaia, M. A.; McNeil, S. E. Nanoparticle interaction with plasma proteins as it relates to particle biodistribution, biocompatibility and therapeutic efficacy. *Adv. Drug Deliv. Rev.* **2009**, *61*, 428-437.

(34) Kim, S.; Shi, Y.; Kim, J. Y.; Park, K.; Cheng, J. X. Overcoming the barriers in micellar drug delivery: loading efficiency, *in vivo* stability, and micelle-cell interaction. *Expert Opin. Drug. Deliv.* **2010**, *7*, 49-62.

- (35) Butcher, N. J.; Mortimer, G. M.; Minchin, R. F. Drug delivery: unravelling the stealth effect. *Nat. Nanotechnol.* **2016**, *11*, 310-311.
- (36) Yang, Q.; Jones, S. W.; Parker, C. L.; Zamboni, W. C.; Bear, J. E.; Lai, S. K. Evading immune cell uptake and clearance requires PEG grafting at densities substantially exceeding the minimum for brush conformation. *Mol. Pharmacol.* **2014**, *11*, 1250-1258.
- (37) Naccache, R.; Vetrone, F.; Mahalingam, V.; Cuccia, L.; Capobianco, J. Controlled synthesis and water dispersibility of hexagonal phase NaGdF<sub>4</sub>:Ho<sup>3+</sup>/Yb<sup>3+</sup> nanoparticles. *Chem. Mater.* **2009**, *21*, 717-723.
- (38) Schubert, S.; Delaney, J. J.; Schubert, U. Nanoprecipitation and nanoformulation of polymers: from history to powerful possibilities beyond poly(lactic acid). *Soft Matter* **2011**, *7*, 1581-1588.
- (39) Redhead, H. M.; Davis, S. S.; Illum, L. Drug delivery in poly(lactide-co-glycolide) nanoparticles surface modified with poloxamer 407 and poloxamine 908: *in vitro* characterisation and *in vivo* evaluation. *J. Control. Release* **2001**, *70*, 353-363.
- (40) Kamaly, N.; Yameen, B.; Wu, J.; Farokhzad, O. C. Degradable controlled-release polymers and polymeric nanoparticles: mechanisms of controlling drug release. *Chem. Rev.* **2016**, *116*, 2602-2663.
- (41) Curia, S.; Howdle, S. Towards sustainable polymeric nano-carriers and surfactants: facile low temperature enzymatic synthesis of bio-based amphiphilic copolymers in scCO<sub>2</sub>. *Polym. Chem.* **2016**, *7*, 2130-2142.
- (42) Pombo Garcia, K.; Zarschler, K.; Barbaro, L.; Barreto, J. A.; O'Malley, W.; Spiccia, L.; Stephan, H.; Graham, B. Zwitterionic-coated "stealth" nanoparticles for biomedical applications: recent advances in countering biomolecular corona formation and uptake by the mononuclear phagocyte system. *Small* **2014**, *10*, 2516-2529.
- (43) Manolova, V.; Flace, A.; Bauer, M.; Schwarz, K.; Saudan, P.; Bachmann, M. F. Nanoparticles target distinct dendritic cell populations according to their size. *Eur. J. Immunol.* **2008**, *38*, 1404-1413.
- (44) Basu Ray, G.; Chakraborty, I.; Moulik, S. P. Pyrene absorption can be a convenient method for probing critical micellar concentration (cmc) and indexing micellar polarity. *J. Colloid. Interface. Sci.* **2006**, *294*, 248-254.

## Chapter 3

### 3 PEG-Modified Gadolinium Nanoparticles as Contrast Agents for *In Vivo* Micro-CT

Vascular research is largely performed in rodents with the goal of developing treatments for human disease. Micro-computed tomography (micro-CT) provides non-destructive three-dimensional imaging that can be used to study the vasculature of rodents. However, to distinguish vasculature from other soft tissues, long-circulating contrast agents are required. In this study, we demonstrated that poly(ethylene glycol) (PEG)-coated gadolinium nanoparticles can be used as a vascular contrast agent in micro-CT. The coated particles could be lyophilized and then redispersed in an aqueous solution to achieve 100 mg/mL of gadolinium. After an intravenous injection of the contrast agent into mice, micro-CT scans showed blood pool contrast enhancements of at least 200 HU for 30 minutes. Imaging and quantitative analysis of gadolinium in tissues showed the presence of contrast agent in clearance organs including the liver and spleen and very low amounts in other organs. *In vitro* cell culture experiments, subcutaneous injections, and analysis of mouse body weight suggested that the agents exhibited low toxicity. Histological analysis of tissues 5 days after injection of the contrast agent showed cytotoxicity in the spleen, but no abnormalities were observed in the liver, lungs, kidneys, and bladder.

#### 3.1 Introduction

Micro-computed tomography (micro-CT) provides a quantitative, non-destructive, fast and cost-effective means of studying vascular disease in mouse models.<sup>1-9</sup> In live mice, micro-CT can provide imaging resolution down to tens of micrometers within tens of minutes. Because CT contrast is derived from the density-dependent attenuation of x rays, soft tissues, which have similar densities, provide little differential contrast. Hence, x-ray attenuating contrast agents are injected intravenously to distinguish the vasculature from surrounding soft tissues during a micro-CT scan, enabling visualization and quantitative tracking of blood vessels, including during studies of novel therapies for re-vascularization.<sup>10-12</sup> For optimal utility in *in vivo* imaging, contrast agents must have a high initial loading of a highly attenuating contrast element, circulate in the blood pool during

the course of the micro-CT scan, and be cleared from the body after imaging to enable longitudinal studies with repeated injections. Clinically used contrast agents comprise small molecules that are cleared renally within seconds of intravenous administration; while these contrast agents meet the requirements of human imaging where scan times are short, *in vivo* micro-CT protocols require circulation times in the order of tens of minutes.<sup>13-17</sup>

Advances in nanotechnology and polymer science have enabled the development of commercially available agents that can evade immediate blood pool clearance and circulate for prolonged periods in mice.<sup>16, 18</sup> These agents are composed of nanoparticles with diameters greater than 10 nm, thus avoiding clearance *via* the kidneys.<sup>5, 19-22</sup> To further evade clearance by the reticuloendothelial system (RES), carrier polymers that act as shields from the *in vivo* milieu are used to coat the nanoparticles. This “core-shell” design can also be used to deliver a high loading of contrast material in the core, making the design important for micro-CT contrast agents, where contrast-agent concentrations of at least 100 mg/mL are typically required. Poly(ethylene glycol) (PEG) has been widely utilized to coat nanoparticles to achieve long circulation times<sup>23, 24</sup> because of its stealthy properties with respect to the RES, high water solubility, low cytotoxicity, availability in different lengths, and a terminal group that can be modified into functional groups to coat nanoparticles.<sup>25, 26</sup> For example, phospholipid-terminated PEG is used in Fenestra VC, which encapsulates 50 mg/mL of iodine within lipid emulsions,<sup>8, 20, 27, 28</sup> while 15 nm gold nanoparticles are coated with thiol-terminated PEG in AuroVist, enabling contrast loading of 200 mg/mL.<sup>29-31</sup>

As iodine is the most commonly utilized clinical contrast agent, many of the micro-CT vascular agents rely on iodine’s attenuating properties. Apart from gold, which has higher attenuation than iodine across the entire energy spectrum, metal-based agents such as alkaline earth metals<sup>21</sup> and transition metals,<sup>32</sup> have been reported or commercialized. Another class of metals that is ideally suited for micro-CT are the lanthanides (*e.g.* gadolinium, erbium),<sup>33</sup> which have k edges (38-64 keV)<sup>34</sup> that coincide with the peaks of the x-ray energy distributions typically used in high-resolution *in vivo* micro-CT scanners (typically operating at below 100 kVp). The ideal position of the K-edges offers potential

to increase contrast attenuation for single-energy micro-CT scans<sup>33</sup> and, more importantly, offers the opportunity to match the available x-ray spectrum and contrast agent in dual-energy micro-CT, which is used to distinguish contrast-enhanced vessels from inherently high-attenuating tissues (*e.g.* bone, calcifications).<sup>35</sup>

Lanthanide agents designed for *in vivo* vascular micro-CT are not commercially available, but studies are emerging demonstrating the utility of PEG-modified lanthanide nanoparticles in microimaging.<sup>36-39</sup> To prepare lanthanides that can be used in the *in vivo* milieu in small animals, common methods include the use of clinically-available MRI agents to formulate nanoparticles that evade rapid renal clearance, or the synthesis of hydrophobic lanthanide nanoparticles encapsulated within a shell of phospholipid-polymer conjugate molecules (*i.e.* liposomes or lipid nanoparticles). While suspending high concentrations of lanthanides (*i.e.* at least 100 mg/mL) in an aqueous environments is challenging, we have recently reported the successful synthesis of block copolymer assembly encapsulations of erbium nanoparticles containing 100 mg/mL of erbium, and demonstrated its utility as a vascular contrast agent when operating at 90 kVp.<sup>40</sup> However, accumulation of the agent within the RES organs resulted in limited animal viability two days following *in vivo* contrast agents injection.

The purpose of this work was to synthesize a blood pool contrast agent with at least 100 mg/mL of lanthanide to be cleared by the RES. Instead of encapsulating multiple nanoparticles in block copolymer assemblies that were greater than 100 nm in diameter,<sup>40</sup> we hypothesized that an alternative approach of directly modifying the surface of gadolinium nanoparticles (GdNP) with PEG, would result in smaller polymer-coated nanoparticles, thereby assisting GdNP clearance from RES organs. We demonstrate that such agents can be synthesized, lyophilized and then redispersed to achieve 100 mg/mL of lanthanide in an injectable formulation. Our *in vivo* results show that the agents provide contrast enhancement values of at least 200 HU in the blood pool for 30 minutes before being processed in the liver and spleen. The agents were well tolerated with some gadolinium retention in clearance organs observed 5 days after a high dose injection. To our knowledge, this is the first report on the successful synthesis of colloiddally stable aqueous suspensions of gadolinium-based nanoparticles at 100 mg/mL that exhibit

sufficient circulation times rendering them a suitable contrast agent for vascular imaging by micro-CT.

## 3.2 Methods

The reagents and their commercial suppliers are available in Appendix B. Further details on synthesis and characterization methods are also presented in Appendix B.

### 3.2.1 Contrast Agent Preparation and Physical Characterization

#### 3.2.1.1 Synthesis of GdNP

Oleate (OA)-coated NaGdF<sub>4</sub> (OA-GdNP) were synthesized by a previously reported method.<sup>40</sup> Phosphate-terminated PEG<sub>1000</sub> (PPEG<sub>1000</sub>), PEG<sub>2000</sub> (PPEG<sub>2000</sub>), and PEG<sub>5000</sub> (PPEG<sub>5000</sub>), where the subscripts indicate PEG molar mass in g/mol, were also synthesized as previously reported.<sup>41</sup> Two versions of PPEG-coated GdNP were synthesized – one with PPEG<sub>2000</sub> only (PPEG<sub>2000</sub>-GdNP), and a formulation using both of PPEG<sub>5000</sub> and PPEG<sub>1000</sub> (PPEG<sub>5000</sub>-PPEG<sub>1000</sub>-GdNP). An overview of the PPEG-coating process is presented in Figure 3.1. Specifically, GdNP (1.0 g) and PPEG<sub>2000</sub> (1.0 g), each dissolved in 12.5 mL of tetrahydrofuran (THF), were combined. Under magnetic stirring, 225 mL of deionized water was added. After stirring for one hour, THF was evaporated and the nanoparticles were purified by dialysis and sterile vacuum filtration (see Appendix B for details). The purified GdNPs were lyophilized and stored at room temperature until they were redispersed immediately prior to use. The same procedure was followed for PPEG<sub>5000</sub>-PPEG<sub>1000</sub>-GdNP, except PPEG<sub>1000</sub> (1.0 g) dissolved in THF (12.5 mL) was added and the suspension was stirred for one hour before organic solvent evaporation.<sup>42</sup>

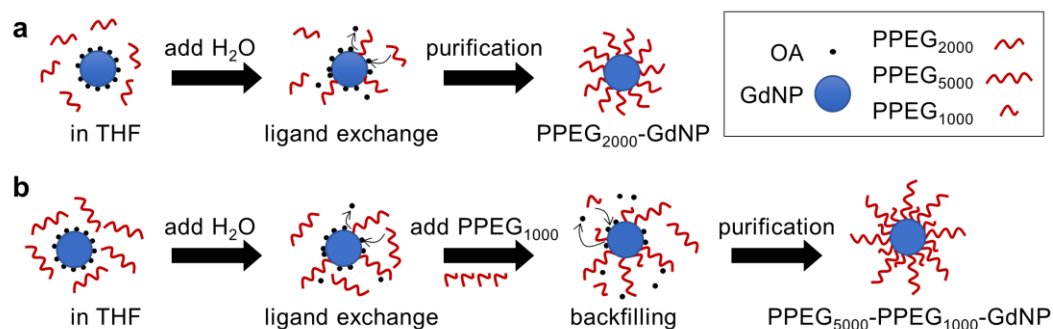


Figure 3.1 The synthesis of a) PEG<sub>2000</sub>-GdNP and b) PEG<sub>5000</sub>-PEG<sub>1000</sub>-GdNP. OA is displaced by PPEG through ligand exchange, and the solution is purified by dialysis and vacuum sterile filtration to eliminate OA and excess PPEG.

### 3.2.1.2 Physical Characterization

The hydrodynamic diameters of the GdNPs were measured by dynamic light scattering (DLS) and were visualized by transmission electron microscopy (TEM). The gadolinium concentration in the contrast agent was measured by inductively coupled plasma-mass spectrometry (ICP-MS) and the results were used to determine the mass of dried contrast agent required to achieve gadolinium concentrations of 100 mg/mL. Micro-CT imaging, where image intensity varies linearly with concentration, was also used to verify the contrast agent concentration (details in Appendix B).

### 3.2.1.3 Colloidal Stability

Saline, which is isotonic with blood, was selected as the solvent for the PPEG-GdNPs. The mouse serum mimic was composed of pH 7.4 phosphate buffered saline, 0.5 µg/mL mouse immunoglobulins, 10 mg/mL bovine serum albumin and 1 mg/mL sodium azide. Colloidal stability in a mouse serum mimic *in vitro* served as an indicator of stability in the blood *in vivo*. DLS size measurements were performed on the PPEG-GdNP redispersed at 4 mg/mL and the average sizes were observed for up to one hour.

### 3.2.1.4 Micro-CT scanning and image analysis

Scans were performed using a GE Locus Ultra micro-CT scanner (GE Healthcare, London ON). Whole-body mouse images were acquired over 1000 views (360°, 16 ms per view) at 80 kVp, 55 mA and reconstructed with an isotropic voxel spacing of 150 µm. Images

were analyzed using MicroView (Parallax Innovations, London, ON) and CT attenuation was reported in Hounsfield Units (HU). All HU values were measured over a volume of  $450\ (\mu\text{m})^3$ . The averaged CT attenuation in the bladder (pre-injection) was subtracted from measured tissue attenuations, to report tissue contrast enhancement throughout this paper.

### 3.2.1.5 Contrast Agent Effect on Cell Viability

An *in vitro* cell viability assay was performed using C2C12 mouse myoblast cells, which were incubated for 24 hours with contrast agent at concentrations from 0.063 to 1.0 mg/ml. Following incubation cell viability was measured using a 3-(4,5-dimethylthiazol-2-yl)-2,5-diphenyltetrazolium bromide (MTT) assay. Additional details are provided in Appendix B.

## 3.2.2 *In Vivo* Characterization

### 3.2.2.1 Animal Care and Handling

All animal studies were carried out in accordance with the regulations set out by the University of Western Ontario's Council on Animal Care (2018-001). The protocols that were used are in agreement with the ARRIVE guidelines and were carried out in accordance with the U.K. Animals Act, 1986 and associated guidelines. C57BL/6 male mice (25-32 g) were anesthetized prior to contrast-agent injection and during micro-CT scans with 3.5% isoflurane in O<sub>2</sub> *via* a nose cone, reduced to 1.5% for maintenance.

### 3.2.2.2 Subcutaneous Tissue Reaction Test

The *in vivo* toxicity of the contrast agent was evaluated by injecting PPEG<sub>2000</sub>-GdNP and PPEG<sub>5000</sub>-PPEG<sub>1000</sub>-GdNP (0.2 mL at 1 g/kg body weight,  $n=2$  each formulation) subcutaneously into the dorsal interscapular tissue. The animals were scanned immediately after and two weeks post-injection. The animals were euthanized and dissected for gross tissue observations. Additional details are provided in Appendix B.

### 3.2.2.3 Time-course contrast enhancement and biodistribution

The tail veins of seven mice were catheterized using PE-20 polyethylene tubing. PPEG<sub>2000</sub>-GdNP was injected over a period of 3 minutes (0.2 mL at 1 g/kg body weight,  $n=4$ ) while PPEG<sub>5000</sub>-PPEG<sub>1000</sub>-GdNP (0.2 mL at 1 g/kg body weight,  $n=3$ ) was injected over a period

of 5 minutes. Micro-CT scans of the animals were obtained at 5, 10, 15, 30, and 60 minutes post-injection, as well as 2 and 5 days after. The animals were weighed daily during the experiments, until the subjects were euthanized on day 5. Major organs were processed for gadolinium content measurements by ICP-MS and standard histological analyses.<sup>43</sup>

#### 3.2.2.4 Statistical analysis

All values are reported as means  $\pm$  standard deviations. A two-way repeated-measures analysis of variance (ANOVA) was performed in Prism 8 (GraphPad Software Inc., San Diego, CA, USA) for each formulation to evaluate differences between the contrast enhancement in the vasculature, variations between ICP-MS-measured gadolinium content of excised tissues on day 5, and to measure the effect of intravenous injections to mouse weight. Results were considered statistically significant at  $p < 0.05$ .

### 3.3 Results

#### 3.3.1 Physical Characterization

OA-GdNP and PPEG<sub>2000</sub>-GdNP had monomodal size distributions, with Z-average diameters of  $37 \pm 1$  nm and  $50 \pm 1$  nm, respectively, both with polydispersity indices (PDI) of  $0.20 \pm 0.01$  (Fig. 3.2a). PPEG<sub>5000</sub>-PPEG<sub>1000</sub>-GdNP had a bimodal size distribution, with a Z-average diameter of  $118 \pm 4$  nm and a PDI of  $0.30 \pm 0.01$ . The particle sizes measured by DLS were in good agreement with particle sizes observed in the TEM images (Fig. 3.2b, c, d). After lyophilization and redispersion, PPEG<sub>5000</sub>-PPEG<sub>1000</sub>-GdNP had diameters of  $202 \pm 8$  nm in saline and  $226 \pm 10$  nm in a mouse serum mimic (Fig. 3.3). Colloidal stability was retained for at least 2 hours with no substantial changes in Z-average diameters. Larger diameters were observed upon redispersion for PPEG<sub>2000</sub>-GdNP (from  $50 \pm 1$  nm to  $354 \pm 99$  nm in saline and  $201 \pm 27$  nm in a mouse serum mimic) and the diameters increased over time in saline and the mouse serum mimic.

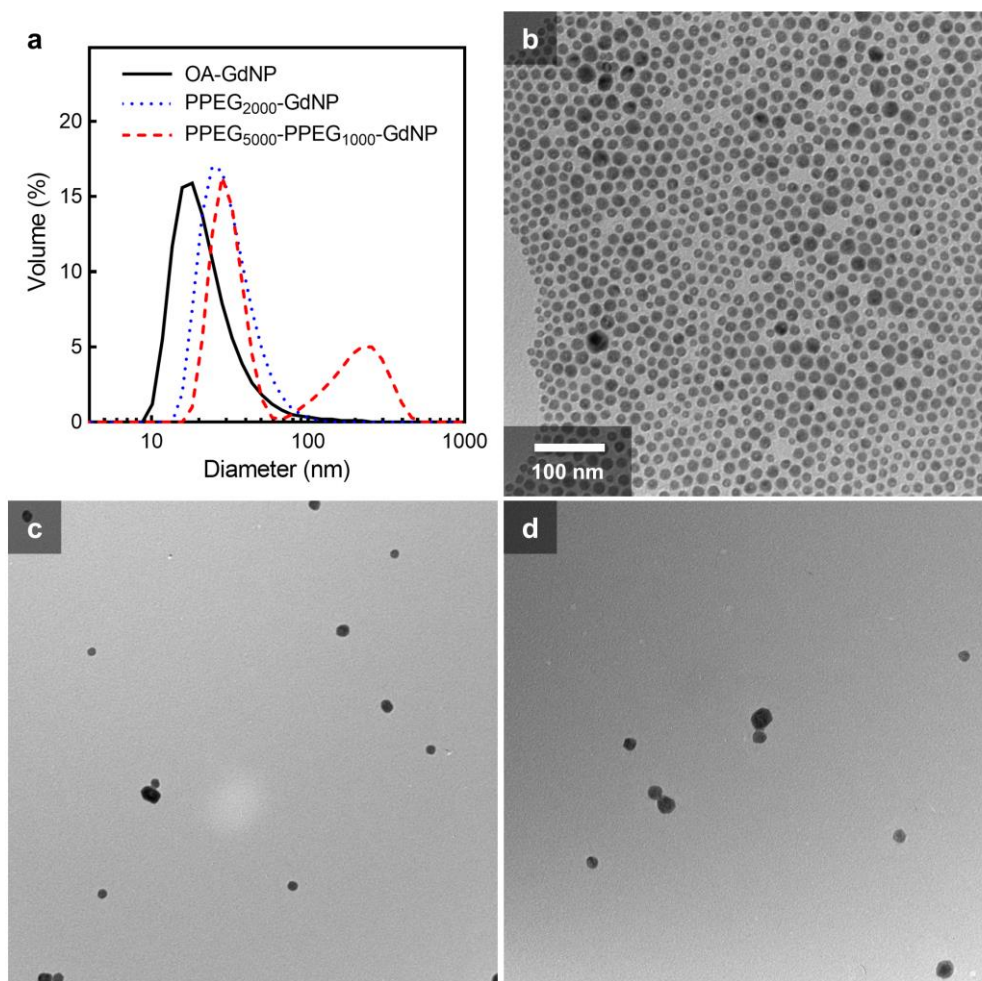


Figure 3.2 Size distributions and microscopy images of the synthesized GdNPs. a) DLS volume diameter distributions of OA-GdNP in cyclohexane, and PEG<sub>2000</sub>-GdNP and PEG<sub>5000</sub>-PEG<sub>1000</sub>-GdNP in water. Representative TEM images of b) OA-GdNP, c) PEG<sub>2000</sub>-GdNP and d) PEG<sub>5000</sub>-PEG<sub>1000</sub>-GdNP. The scale bar in b) applies to all TEM images.

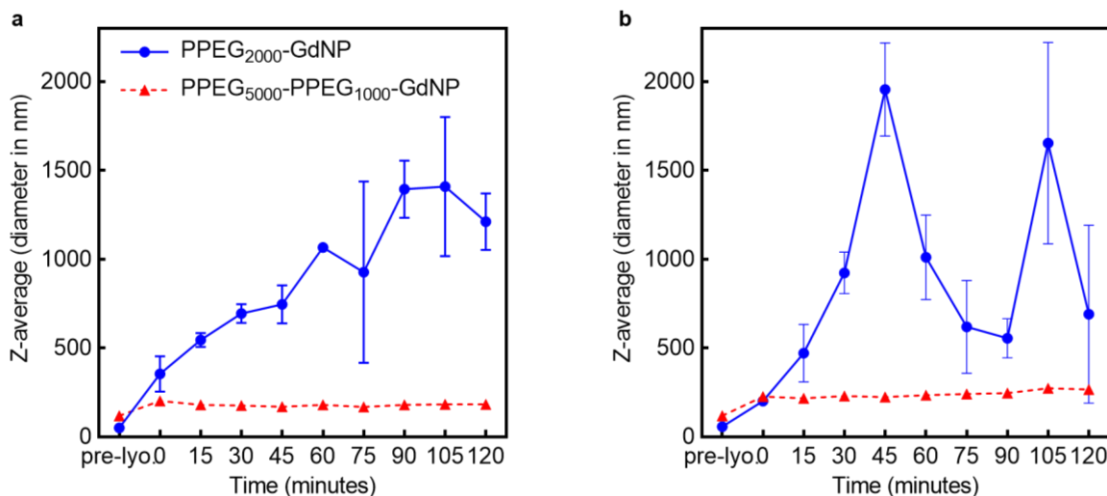


Figure 3.3 Time-course diameters of resuspended PEG<sub>2000</sub>-GdNP and PEG<sub>5000</sub>-PEG<sub>1000</sub>-GdNP at 37 °C. The contrast agents were redispersed in a) saline and b) a mouse serum mimic for characterization.

ICP-MS analysis of the contrast agents indicated a gadolinium content of  $30 \pm 5\%$  and  $22 \pm 3\%$  (*w/w*) for PEG<sub>2000</sub>-GdNP and PEG<sub>5000</sub>-PEG<sub>1000</sub>-GdNP, respectively. Hence, to achieve a gadolinium loading of 100 mg/mL in the contrast agent formulation,  $66 \pm 10$  mg of dried PEG<sub>2000</sub>-GdNP or  $90 \pm 14$  mg of PEG<sub>5000</sub>-PEG<sub>1000</sub>-GdNP need to be diluted in 200  $\mu$ L saline. The relation between CT contrast (HU) and gadolinium concentration in mg/mL ([Gd]) was calculated to be  $HU = 31[Gd] - 3$  (Figure B.1, Appendix B). Hence, a contrast value of 3100 HU is anticipated with 100 mg/mL of gadolinium. The CT contrast values obtained from PEG<sub>2000</sub>-GdNP and PEG<sub>5000</sub>-PEG<sub>1000</sub>-GdNP were  $3244 \pm 57$  HU and  $3195 \pm 62$  HU, respectively, corresponding to  $105 \pm 2$  mg/mL and  $103 \pm 2$  mg/mL of gadolinium respectively.

### 3.3.2 *In Vitro* and *In Vivo* Characterization

In cell culture experiments with PEG<sub>2000</sub>-GdNP and PEG<sub>5000</sub>-PEG<sub>1000</sub>-GdNP, greater than 75% viability of C2C12 mouse myoblast cells was found for all gadolinium concentrations evaluated, up to 1.0 mg/mL (Figure B.2, Appendix B); the GdNP are not considered toxic according to the American Society for Testing and Materials.<sup>44</sup> In addition, micro-CT images of the dorsal interscapular region following subcutaneous

injection (Figure B.3, Appendix B) showed contrast enhancement near the injection site was nearly gone after two weeks. Full body gross examinations showed normal tissues.

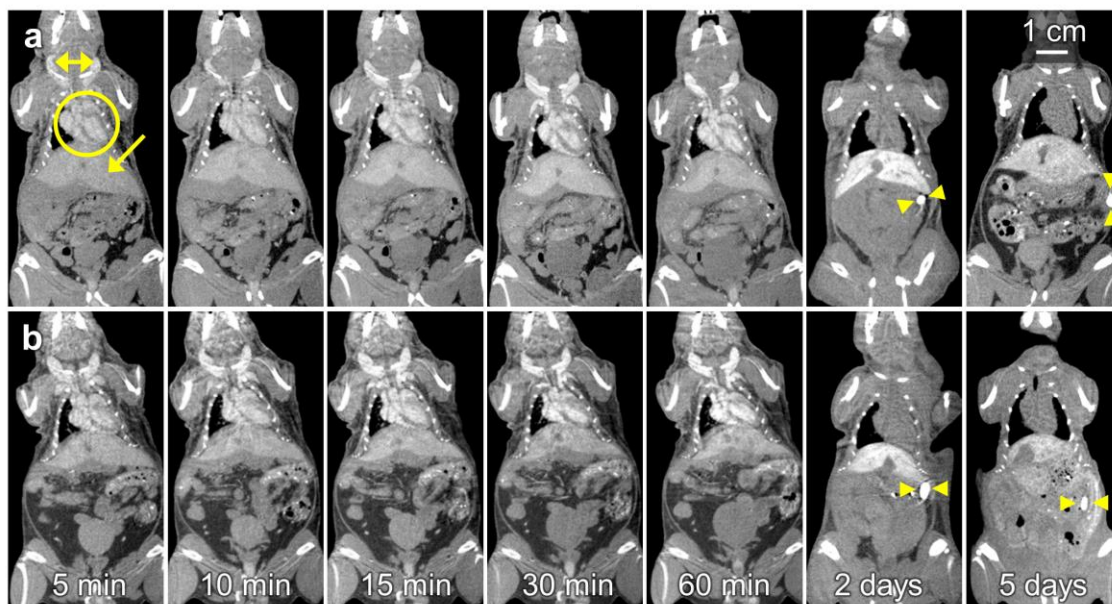


Figure 3.4 Representative coronal micro-CT images showing the heart, liver, jugular veins, and spleen of mice that received contrast agent formulated with a) PPEG<sub>2000</sub>-GdNP and b) PPEG<sub>5000</sub>-PPEG<sub>1000</sub>-GdNP. All times were reported from the completion of the contrast agent injection. In the 5-minute image in a), the blood in the chambers of the heart (circle), liver (arrow) and the external jugular veins (double arrowheads) are clearly visible. In the 2- and 5-day images, the blood pool in the heart is no longer visible, the liver remains visible, and the spleen (arrowheads) becomes visible. Adjacent anatomical slices were shown for the images acquired within 60 minutes, while slices located 1 cm posterior were shown in the 2- and 5-day images, to demonstrate the high contrast in the previously indistinguishable spleen.

Representative time-course micro-CT images of mice injected with the GdNPs are shown in Fig. 3.4. As expected, qualitative evaluation of the post-contrast images shows opacification of the blood pool (vessels, chambers of the heart), which remained high over the 60 minutes studied. Increased contrast was observed in the liver as early as 5 minutes, as demonstrated by the ability to distinguish the liver from surrounding soft tissues; contrast enhancement increased by the 2 day time point. Liver contrast decreased 5 days after agent injection, accompanied by increased contrast in the spleen. The renal cortex was

not distinguishable from surrounding tissues, confirming the evasion of renal clearance and clearance *via* the RES. Quantitative evaluation of the contrast enhancement in the vasculature and the RES organs is shown in Fig. 3.5. For PPEG<sub>2000</sub>-GdNP, an average attenuation of  $245 \pm 32$  HU was observed 5 minutes post-injection in the abdominal aorta, while an attenuation of  $278 \pm 33$  HU was observed for PPEG<sub>5000</sub>-PPEG<sub>1000</sub>-GdNP. Values of 200 HU were observed in the blood pool for at least 30 minutes for both formulations. No significant difference between the measured contrast enhancement of the vasculature for up to 60 minutes, and no effect on attenuation due to PEG chain length were observed (2-way ANOVA,  $p = 0.15$  and  $0.077$ , respectively).

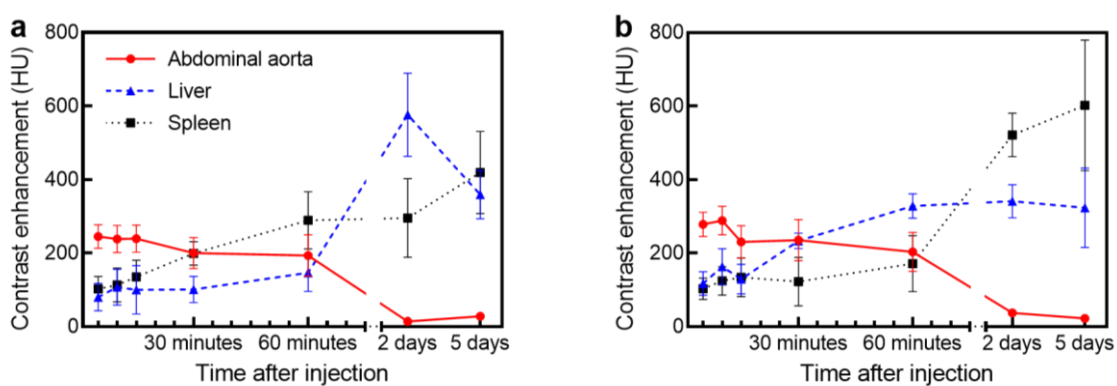


Figure 3.5 Contrast enhancement in the organs of mice that were injected with a) PPEG<sub>2000</sub>-GdNP and b) PPEG<sub>5000</sub>-PPEG<sub>1000</sub>-GdNP displayed similar trends over time, where decreased attenuation in the vasculature was accompanied by increased attenuation in the liver after day 3 (Fig. 3.6). There were no significant differences between daily mass measurements ( $p = 0.30$ ).

The mice were lethargic one day after injection; normal behavior resumed on the second day. The average mass of the injected animals decreased one day after agent injection for both formulations and stopped decreasing

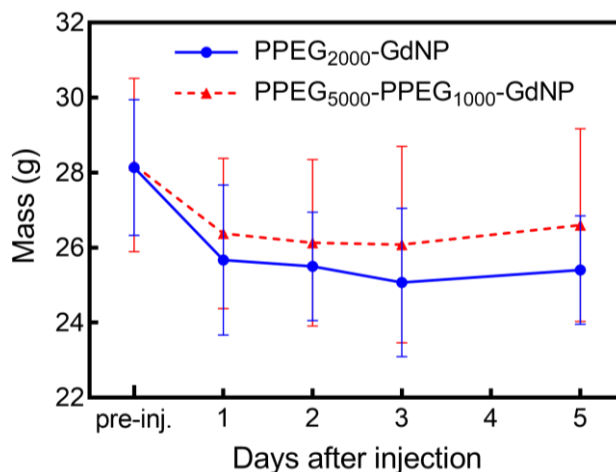


Figure 3.6 Effect of the contrast-agent injection procedure on subject mass.

Based on post-mortem ICP-MS analyses of the tissues, low gadolinium concentrations were found in the blood, while high gadolinium concentrations were observed in the liver and spleen, as expected (Table 3.1). The livers and spleens excised from PPEG<sub>5000</sub>-PPEG<sub>1000</sub>-GdNP-injected mice were visibly larger than the organs of mice that were injected with PPEG<sub>2000</sub>-GdNP. While contrast values do not depend on the size or mass of the organ, the total gadolinium contents of the organs were greater for PPEG<sub>5000</sub>-PPEG<sub>1000</sub>-GdNP than PPEG<sub>2000</sub>-GdNP due to organ mass differences ( $96 \pm 22 \mu\text{g}$  vs.  $58 \pm 14 \mu\text{g}$  for the liver, and  $68 \pm 19 \mu\text{g}$  vs.  $46 \pm 11 \mu\text{g}$  for the spleen, respectively). In the heart, kidneys and the bladder, gadolinium levels were below detection limits, but trace gadolinium was measured in the lungs of mice injected with PPEG<sub>5000</sub>-PPEG<sub>1000</sub>-GdNP.

The calibration between CT contrast and gadolinium concentration (Figure B.1, Appendix B) confirmed the agreement between HU values (Figure 3.5) and the ICP-MS results. The HU values in the liver were calculated to be  $298 \pm 66$  HU and  $345 \pm 108$  HU for PPEG<sub>2000</sub>-GdNP and PPEG<sub>5000</sub>-PPEG<sub>1000</sub>-GdNP, respectively, and were  $387 \pm 83$  HU and  $669 \pm 78$  HU in the spleen. The trace amounts of gadolinium found in the lungs by ICP-MS were far lower than the noise and too low to be detected in the CT images. Significant differences in the gadolinium content values between formulations were observed for the liver ( $p = 0.0006$ ) and the spleen ( $p < 0.0001$ ). Of the injected gadolinium, a total of  $5.6 \pm 1.0 \%$  and  $12.4 \pm 2.1 \%$  remained in the evaluated organs for PPEG<sub>2000</sub>-GdNP and PPEG<sub>5000</sub>-PPEG<sub>1000</sub>-GdNP, respectively.

Table 3.1 Gadolinium content of mouse blood and clearance organs determined by ICP-MS. <sup>a</sup>Reported w/w% were rounded up.

Tissue	PPEG <sub>2000</sub> -GdNP		PPEG <sub>5000</sub> -PPEG <sub>1000</sub> -GdNP	
	ppm	w/w % of injected gadolinium	ppm	w/w % of injected gadolinium
Blood <sup>a</sup>	1 ± 31	0.1 ± 0.2	5 ± 88	0.1 ± 0.8
Lungs	0	0	52 ± 92	0.1 ± 0.1
Brain	0	0	0	0
Liver	9322 ± 2060	2.7 ± 0.6	10780 ± 3350	5.2 ± 1.6
Spleen	12101 ± 2570	2.8 ± 0.6	20833 ± 2420	7.0 ± 0.8

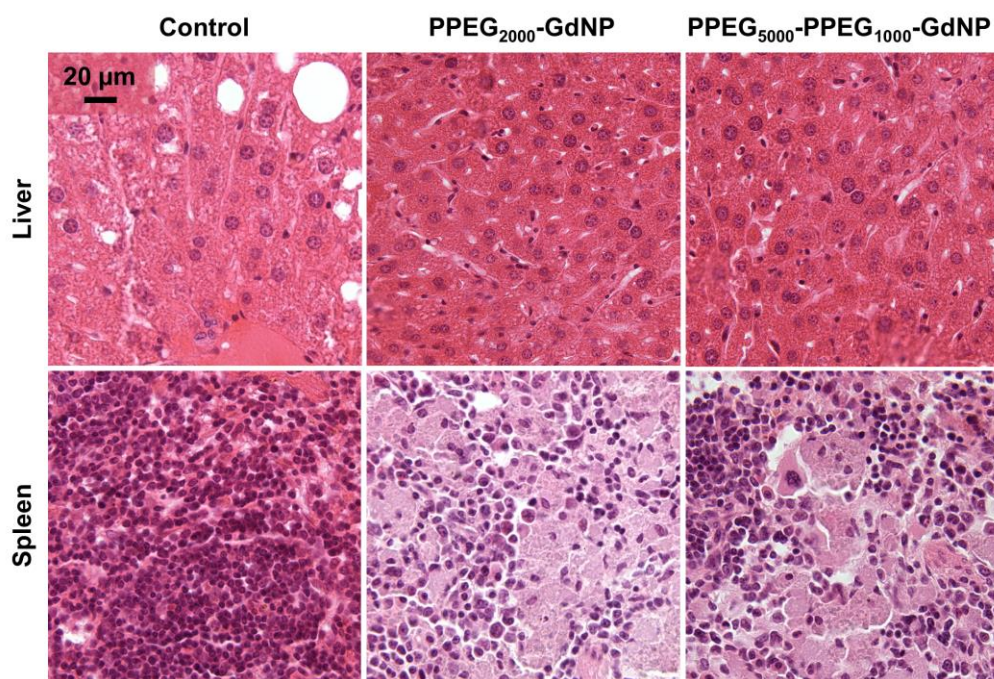


Figure 3.7 Representative histology images for control and injected mice taken from tissues after 5 days of injection. Liver tissues appear normal, while the spleen tissues of the injected mice indicate basophilic nuclear contents in the cytoplasm and lower nuclear densities than the control tissue.

Histological analysis revealed no differences between control and injected mouse liver (Fig. 3.7), lungs, heart, kidneys and bladder (Figure B.4, Appendix B). In spleen tissues, sections from the injected mice demonstrate the presence of basophilic nuclear contents in the cytoplasm and a lower density of nuclei than observed in the control spleen section.

### 3.4 Discussion

We successfully prepared a long-circulating Gd-nanoparticle-based vascular micro-CT contrast agent. The nanoparticles can be freeze-dried and redispersed into a contrast agent suspension that is colloidally stable and contains 100 mg/mL of gadolinium, which is difficult to achieve in an aqueous solution. Whole-body CT images demonstrate sufficient vascular enhancement ( $> 200$  HU) over the time period required for scanning, and along with histology and post mortem ICP-MS, confirm RES clearance of both agents. We report the condition of the RES organs days after a high-dose intravenous injection of lanthanide nanoparticles, which has rarely been reported previously. Our results are consistent with a comprehensive study that demonstrated the performance and *in vivo* fate of alkaline-earth metal and iodinated nanoparticles when used as vascular contrast agents for micro-CT.<sup>45</sup> Our agent provides comparable vascular contrast and similar clearance pathways as alkaline-earth metal nanoparticles, including their localization in RES organs post-circulation.

We selected PPEG<sub>2000</sub> and PPEG<sub>5000</sub> for this study since these are two of the most commonly used PEG chain lengths in long circulating nanoparticles.<sup>46,47</sup> While the original goal was to compare the performance of PPEG<sub>2000</sub>-GdNP and PPEG<sub>5000</sub>-GdNP, our preliminary studies showed that PPEG<sub>5000</sub>-GdNP could not be redispersed adequately in aqueous solution. It was suspected that exchange of PPEG<sub>5000</sub> chains onto the GdNP was more difficult than for PPEG<sub>2000</sub>, thus leaving some of the GdNP surface exposed. In attempts to improve the coverage of the GdNP surface, excess PPEG<sub>5000</sub> of up to five times the mass of the GdNP was used when preparing PPEG<sub>5000</sub>-GdNP. However, the nanoparticles could still not be entirely redispersed in water. Backfilling with a shorter PEG chain length was adopted, which previous studies have demonstrated to reduce interactions between nanoparticles and plasma proteins.<sup>42</sup> To backfill, PPEG<sub>1000</sub> was selected as this PEG length that was not expected to interfere with the performance of PPEG<sub>5000</sub> in repelling plasma proteins. The lyophilized PPEG<sub>5000</sub>-PPEG<sub>1000</sub>-GdNP redispersed without difficulty in saline and the mouse serum mimic to form particles with average diameters that were no more than twice the pre-lyophilization diameters. PPEG<sub>2000</sub>-GdNP redispersed at about 7-fold higher diameter than pre-lyophilization.

The PPEG<sub>5000</sub>-PPEG<sub>1000</sub>-GdNP formulation was observed (qualitatively) to have a higher viscosity than PPEG<sub>2000</sub>-GdNP at concentrations of 100 mg/mL of gadolinium. This resulted in longer injection times for PPEG<sub>5000</sub>-PPEG<sub>1000</sub>-GdNP, requiring 5-minute injections versus the 3-minute injections when using PPEG<sub>2000</sub>-GdNP. We attribute the higher viscosity of PPEG<sub>5000</sub>-PPEG<sub>1000</sub>-GdNP to the higher mass of polymer-coated particles used to achieve 100 mg/mL of gadolinium in this contrast agent, since the viscosity of a suspension containing solid spherical particles increases when a larger volume of the solution is occupied by the particles/polymer.<sup>48</sup> The longer PPEG<sub>5000</sub> chains on the particle surface may also contribute to higher viscosity compared to PPEG<sub>2000</sub>. Nonetheless, similar contrast enhancement of the vasculature (above 200 HU) was achieved for 30 minutes after injection for both formulations, with no significant change in time-course attenuation for up to 60 minutes. The similarity in *in vivo* performance of the reported formulations was unexpected because PPEG<sub>2000</sub>-GdNP showed poorer colloidal stability than PPEG<sub>5000</sub>-PPEG<sub>1000</sub>-GdNP in saline and in the mouse serum mimic. The indistinguishable performance of the two formulations *in vivo* demonstrates that *in vitro* tests cannot fully predict the *in vivo* behavior of nanoparticles in the vasculature. The nanoparticles reported in this paper exhibited the same circulation times and blood pool contrast enhancements as our previous formulation comprising NaErF<sub>4</sub> nanoparticles encapsulated in assemblies formed from PEG-poly(lactic acid) block copolymers,<sup>40</sup> which also had PEG surfaces. This current study and our previous paper are further testaments to the capabilities of PEG in temporarily promoting stealth properties against the RES and in providing its cargo with long circulation times in the vasculature, even at the high doses required for micro-CT.

No CT scans were performed after the first 60 minutes on day one or the day after injections to avoid complicating mouse health due to anesthesia.<sup>49</sup> The injected mice were clearly lethargic after being under anesthesia for 60 minutes, and this effect was still observed after one day. Two days following initial injection, the mice were placed under anesthesia for 5 minutes, only to permit micro-CT imaging; the mice were more active before and after imaging, and only needed a few minutes to recover from anesthesia. The daily mass measurements display a similar trend that coincides with mouse activity, food and water intake. While a limitation of this study is that no sham study was performed to differentiate

between the effect of the agent and the anesthesia, isoflurane was found to increase mouse latency in previous studies, and coincided with decreased animal weight for up to 2 days.<sup>50</sup>

Our results – micro-CT time course and post-mortem ICP-MS of relevant organs – clearly demonstrate that the agent’s clearance pathway is through the RES. This clearance mechanism was expected due to its physical properties and is similar to the clearance of other agents incorporating metal nanoparticles.<sup>32,36</sup> Some gadolinium was detected by ICP-MS in trace amounts in the blood, and in the lungs of PPEG<sub>5000</sub>-PPEG<sub>1000</sub>-GdNP-injected mice; the trace values found in the lungs can be attributed to reversible transient aggregation in capillary beds and has been previously observed for other intravenously injected nanoparticles.<sup>51, 52</sup> Because of concerns with free gadolinium being observed in humans post small-molecule contrast injection,<sup>53, 54</sup> we evaluated the gadolinium concentration in the brain and confirmed that our GdNP did not cross the blood brain barrier.

The ICP-MS results reported significantly higher gadolinium accumulation in the liver and in the spleen from PPEG<sub>5000</sub>-PPEG<sub>1000</sub>-GdNP than PPEG<sub>2000</sub>-GdNP. This could be attributed to a difference in morphology and grafting density of the PEG molecules in each version of the contrast agent, hence affecting its biodistribution.<sup>55, 56</sup> Considering greater RES organ accumulation, higher viscosity, and heavier excised livers and spleens from PPEG<sub>5000</sub>-PPEG<sub>1000</sub>-GdNP injections than from PPEG<sub>2000</sub>-GdNP, and no significant difference in time-course contrast enhancements of the vasculature, an advantage can be gained from using PPEG<sub>2000</sub>-GdNP instead of PPEG<sub>5000</sub>-PPEG<sub>1000</sub>-GdNP for *in vivo* micro-CT. This result was unexpected, because the nearly constant size of PPEG<sub>5000</sub>-PPEG<sub>1000</sub>-GdNP from the *in vitro* colloidal studies predicted that it would outperform PPEG<sub>2000</sub>-GdNP which was expected to aggregate *in vivo* as was observed *in vitro*. We suspect that the aggregation of PPEG<sub>2000</sub>-GdNP may be transient and reversible allowing mobility and reduced accumulation in RES organs in the dynamic environment *in vivo*.

Optical histology results showed that all tissues examined, except for the spleen, were normal. Since eosin stains the acidophilic cytosol and extracellular matrix, and hematoxylin stains the basophilic nucleus, the spleen sections indicate the presence of

nuclear content in the cytosol and extracellular matrix, and lower nuclear density, suggesting the need for further investigations. In this study, mice were euthanized after the 5-day time point because after that time point it is difficult to gauge if well-being is a result of the contrast agent or other factors. The contrast agent formulation that we report in this paper presents an improvement from our previously reported nanoparticle assembly formulation, where most mice died after 2 days.

Our surface-modified GdNP can be used to visualize the vasculature of live mice using micro-CT for up to 60 minutes. The contrast agent that we synthesized is an improvement from our previous formulation, since the injected mice survived for up to 5 days. Hence, the agent can potentially be injected up to two times to visualize and quantitatively track blood vessel development by micro-CT within 5 days. While further studies are required to enable the contrast agent's utility in long-term studies, our results show that switching from diblock polymer coated nanoparticle assemblies to grafting PEG directly on the surface – preferably with PEG<sub>2000</sub> – facilitated the exit of nanoparticles from the liver.

### 3.5 Conclusions

We synthesized long-circulating contrast agents composed of PEG-modified GdNP that can be suspended at 100 mg/mL of gadolinium and can be used to visualize the vasculature of live mice using micro-CT for up to 60 minutes. The alternative approach of modifying the surface of the nanoparticles with PEG in lieu of polymer-coated nanoparticle assemblies presents a step in the right direction towards making micro-CT contrast agents available for longitudinal vascular research.

### 3.6 References

- (1) Dobnikar, L.; Taylor, A. L.; Chappell, J.; Oldach, P.; Harman, J. L.; Oerton, E.; Dzierzak, E.; Bennett, M. R.; Spivakov, M.; Jorgensen, H. F. Disease-relevant transcriptional signatures identified in individual smooth muscle cells from healthy mouse vessels. *Nat. Commun.* **2018**, *9*, 4567.
- (2) Gordon-Keylock, S.; Sobiesiak, M.; Rybtsov, S.; Moore, K.; Medvinsky, A. Mouse extraembryonic arterial vessels harbor precursors capable of maturing into definitive HSCs. *Blood* **2013**, *122*, 2338-2345.
- (3) Trogan, E.; Fayad, Z. A.; Itskovich, V. V.; Aguinaldo, J. G.; Mani, V.; Fallon, J. T.; Chereshev, I.; Fisher, E. A. Serial studies of mouse atherosclerosis by *in vivo* magnetic resonance imaging detect lesion regression after correction of dyslipidemia. *Arterioscler. Thromb. Vasc. Biol.* **2004**, *24*, 1714-1719.
- (4) Vafaie, F.; Yin, H.; O'Neil, C.; Nong, Z.; Watson, A.; Arpino, J. M.; Chu, M. W.; Holdsworth, D. W.; Gros, R.; Pickering, J. G. Collagenase-resistant collagen promotes mouse aging and vascular cell senescence. *Aging Cell* **2014**, *13*, 121-130.
- (5) Ashton, J. R.; Befera, N.; Clark, D.; Qi, Y.; Mao, L.; Rockman, H. A.; Johnson, G. A.; Badea, C. T. Anatomical and functional imaging of myocardial infarction in mice using micro-CT and eXIA 160 contrast agent. *Contrast Media Mol. Imaging* **2014**, *9*, 161-168.
- (6) Foster, W. K.; Ford, N. L. Investigating the effect of longitudinal micro-CT imaging on tumour growth in mice. *Phys. Med. Biol.* **2011**, *56*, 315-326.
- (7) Ghanavati, S.; Yu, L. X.; Lerch, J. P.; Sled, J. G. A perfusion procedure for imaging of the mouse cerebral vasculature by x-ray micro-CT. *J. Neurosci. Methods* **2014**, *221*, 70-77.
- (8) Schambach, S. J.; Bag, S.; Groden, C.; Schilling, L.; Brockmann, M. A. Vascular imaging in small rodents using micro-CT. *Methods* **2010**, *50*, 26-35.
- (9) Wong, M. D.; Dorr, A. E.; Walls, J. R.; Lerch, J. P.; Henkelman, R. M. A novel 3D mouse embryo atlas based on micro-CT. *Development* **2012**, *139*, 3248-3256.
- (10) Ehling, J.; Lammers, T.; Kiessling, F. Non-invasive imaging for studying anti-angiogenic therapy effects. *Thromb. Haemost.* **2013**, *109*, 375-390.
- (11) Munce, N. R.; Strauss, B. H.; Qi, X.; Weisbrod, M. J.; Anderson, K. J.; Leung, G.; Sparkes, J. D.; Lockwood, J.; Jaffe, R.; Butany, J.; Teitelbaum, A. A.; Qiang, B.; Dick, A. J.; Wright, G. A. Intravascular and extravascular microvessel formation in chronic total occlusions a micro-CT imaging study. *JACC Cardiovasc. Imaging* **2010**, *3*, 797-805.
- (12) Udagawa, A.; Sato, S.; Hasuike, A.; Kishida, M.; Arai, Y.; Ito, K. Micro-CT observation of angiogenesis in bone regeneration. *Clin. Oral Implants Res.* **2013**, *24*, 787-792.

- (13) Brede, C.; Labhasetwar, V. Applications of nanoparticles in the detection and treatment of kidney diseases. *Adv. Chronic Kidney Dis.* **2013**, *20*, 454-465.
- (14) Choi, C. H.; Zuckerman, J. E.; Webster, P.; Davis, M. E. Targeting kidney mesangium by nanoparticles of defined size. *Proc Natl Acad Sci U S A* **2011**, *108*, 6656-6661.
- (15) Gomez-Vallejo, V.; Puigivila, M.; Plaza-Garcia, S.; Szczupak, B.; Pinol, R.; Murillo, J. L.; Sorribas, V.; Lou, G.; Veintemillas, S.; Ramos-Cabrer, P.; Llop, J.; Millan, A. PEG-copolymer-coated iron oxide nanoparticles that avoid the reticuloendothelial system and act as kidney MRI contrast agents. *Nanoscale* **2018**, *10*, 14153-14164.
- (16) Petros, R. A.; DeSimone, J. M. Strategies in the design of nanoparticles for therapeutic applications. *Nat. Rev. Drug Discov.* **2010**, *9*, 615-627.
- (17) Watermann, A.; Brieger, J. Mesoporous silica nanoparticles as drug delivery vehicles in cancer. *Nanomaterials* **2017**, *7*.
- (18) Blanco, E.; Shen, H.; Ferrari, M. Principles of nanoparticle design for overcoming biological barriers to drug delivery. *Nat Biotechnol* **2015**, *33*, 941-951.
- (19) Detombe, S. A.; Ford, N. L.; Xiang, F.; Lu, X.; Feng, Q.; Drangova, M. Longitudinal follow-up of cardiac structure and functional changes in an infarct mouse model using retrospectively gated micro-computed tomography. *Invest. Radiol.* **2008**, *43*, 520-529.
- (20) Willekens, I.; Lahoutte, T.; Buls, N.; Vanhove, C.; Deklerck, R.; Bossuyt, A.; de Mey, J. Time-course of contrast enhancement in spleen and liver with Exia 160, Fenestra LC, and VC. *Mol. Imaging Biol.* **2009**, *11*, 128-135.
- (21) Boll, H.; Figueiredo, G.; Fiebig, T.; Nittka, S.; Doyon, F.; Kerl, H. U.; Nolte, I.; Forster, A.; Kramer, M.; Brockmann, M. A. Comparison of Fenestra LC, ExiTron nano 6000, and ExiTron nano 12000 for micro-CT imaging of liver and spleen in mice. *Acad. Radiol.* **2013**, *20*, 1137-1143.
- (22) Rothe, J. H.; Rudolph, I.; Rohwer, N.; Kupitz, D.; Gregor-Mamoudou, B.; Derlin, T.; Furth, C.; Amthauer, H.; Brenner, W.; Buchert, R.; Cramer, T.; Apostolova, I. Time course of contrast enhancement by micro-CT with dedicated contrast agents in normal mice and mice with hepatocellular carcinoma: comparison of one iodinated and two nanoparticle-based agents. *Acad. Radiol.* **2015**, *22*, 169-178.
- (23) Butcher, N. J.; Mortimer, G. M.; Minchin, R. F. Drug delivery: unravelling the stealth effect. *Nat. Nanotechnol.* **2016**, *11*, 310-311.
- (24) Yang, Q.; Jones, S. W.; Parker, C. L.; Zamboni, W. C.; Bear, J. E.; Lai, S. K. Evading immune cell uptake and clearance requires PEG grafting at densities substantially exceeding the minimum for brush conformation. *Mol. Pharmacol.* **2014**, *11*, 1250-1258.

- (25) Xiao, R. Z.; Zeng, Z. W.; Zhou, G. L.; Wang, J. J.; Li, F. Z.; Wang, A. M. Recent advances in PEG-PLA block copolymer nanoparticles. *Int. J. Nanomedicine* **2010**, *5*, 1057-1065.
- (26) Zhao, Q.; Wang, C.; Liu, Y.; Wang, J.; Gao, Y.; Zhang, X.; Jiang, T.; Wang, S. PEGylated mesoporous silica as a redox-responsive drug delivery system for loading thiol-containing drugs. *Int. J. Pharm.* **2014**, *477*, 613-622.
- (27) Detombe, S. A.; Dunmore-Buyze, J.; Drangova, M. Evaluation of eXIA 160 cardiac-related enhancement in C57BL/6 and BALB/c mice using micro-CT. *Contrast Media Mol. Imaging* **2012**, *7*, 240-246.
- (28) Vandeghinste, B.; Trachet, B.; Renard, M.; Casteleyn, C.; Staelens, S.; Loeys, B.; Segers, P.; Vandenberghe, S. Replacing vascular corrosion casting by *in vivo* micro-CT imaging for building 3D cardiovascular models in mice. *Mol. Imaging Biol.* **2011**, *13*, 78-86.
- (29) Clark, D. P.; Ghaghada, K.; Moding, E. J.; Kirsch, D. G.; Badea, C. T. In vivo characterization of tumor vasculature using iodine and gold nanoparticles and dual energy micro-CT. *Phys Med Biol* **2013**, *58*, 1683-1704.
- (30) Domey, J.; Teichgraber, U.; Hilger, I. Gold nanoparticles allow detection of early-stage edema in mice via computed tomography imaging. *Int. J. Nanomedicine* **2015**, *10*, 3803-3814.
- (31) Hainfeld, J. F.; O'Connor, M. J.; Dilmanian, F. A.; Slatkin, D. N.; Adams, D. J.; Smilowitz, H. M. Micro-CT enables microlocalisation and quantification of Her2-targeted gold nanoparticles within tumour regions. *Br. J. Radiol.* **2011**, *84*, 526-533.
- (32) Chakravarty, S.; Hix, J. M. L.; Wiewiora, K. A.; Volk, M. C.; Kenyon, E.; Shuboni-Mulligan, D. D.; Blanco-Fernandez, B.; Kiupel, M.; Thomas, J.; Sempere, L. F.; Shapiro, E. M. Tantalum oxide nanoparticles as versatile contrast agents for X-ray computed tomography. *Nanoscale* **2020**, *12*, 7720-7734.
- (33) Cardinal, H. N.; Holdsworth, D. W.; Drangova, M.; Hobbs, B. B.; Fenster, A. Experimental and theoretical x-ray imaging performance comparison of iodine and lanthanide contrast agents. *Med Phys* **1993**, *20*, 15-31.
- (34) Niranjana, K. M.; Badiger, N. M. K shell parameters of some lanthanide elements using bremsstrahlung. *Radiat. Phys. Chem.* **2015**, *107*, 59-64.
- (35) Tse, J. J.; Dunmore-Buyze, J.; Drangova, M.; Holdsworth, D. W. Dual-energy computed tomography using a gantry-based preclinical cone-beam microcomputed tomography scanner. *J Med Imaging (Bellingham)* **2018**, *5*, 033503.
- (36) Liu, Y.; Ai, K.; Liu, J.; Yuan, Q.; He, Y.; Lu, L. A high-performance ytterbium-based nanoparticulate contrast agent for *in vivo* X-ray computed tomography imaging. *Angew Chem Int Ed Engl* **2012**, *51*, 1437-1442.

- (37) Zhou, J.; Zhu, X.; Chen, M.; Sun, Y.; Li, F. Water-stable NaLuF<sub>4</sub>-based upconversion nanophosphors with long-term validity for multimodal lymphatic imaging. *Biomaterials* **2012**, *33*, 6201-6210.
- (38) Badea, C. T.; Clark, D. P.; Holbrook, M.; Srivastava, M.; Mowery, Y.; Ghaghada, K. B. Functional imaging of tumor vasculature using iodine and gadolinium-based nanoparticle contrast agents: a comparison of spectral micro-CT using energy integrating and photon counting detectors. *Phys. Med. Biol.* **2019**, *64*, 065007.
- (39) Bridot, J. L.; Faure, A. C.; Laurent, S.; Riviere, C.; Billotey, C.; Hiba, B.; Janier, M.; Jossierand, V.; Coll, J. L.; Elst, L. V.; Muller, R.; Roux, S.; Perriat, P.; Tillement, O. Hybrid gadolinium oxide nanoparticles: multimodal contrast agents for *in vivo* imaging. *J. Am. Chem. Soc.* **2007**, *129*, 5076-5084.
- (40) Cruje, C.; Dunmore-Buyze, J.; MacDonald, J. P.; Holdsworth, D. W.; Drangova, M.; Gillies, E. R. Polymer assembly encapsulation of lanthanide nanoparticles as contrast agents for *in vivo* micro-CT. *Biomacromolecules* **2018**.
- (41) Sedlmeier, A.; Gorris, H. H. Surface modification and characterization of photon-upconverting nanoparticles for bioanalytical applications. *Chem. Soc. Rev.* **2015**, *44*, 1526-1560.
- (42) Dai, Q.; Walkey, C.; Chan, W. C. Polyethylene glycol backfilling mitigates the negative impact of the protein corona on nanoparticle cell targeting. *Angew. Chem. Int. Ed. Engl.* **2014**, *53*, 5093-5096.
- (43) *Theory and practice of histological techniques / [edited by] John D. Bancroft, Marilyn Gamble.* 6th ed. ed.; Churchill Livingstone Elsevier: Edinburgh, 2008.
- (44) Lewinski, N.; Colvin, V.; Drezek, R. Cytotoxicity of nanoparticles. *Small* **2008**, *4*, 26-49.
- (45) Mannheim, J. G.; Schlichthaerle, T.; Kuebler, L.; Quintanilla-Martinez, L.; Kohlhofer, U.; Kneilling, M.; Pichler, B. J. Comparison of small animal CT contrast agents. *Contrast Media Mol Imaging* **2016**, *11*, 272-284.
- (46) Gill, K. K.; Kaddoumi, A.; Nazzal, S. PEG-lipid micelles as drug carriers: physiochemical attributes, formulation principles and biological implication. *J. Drug Target.* **2015**, *23*, 222-231.
- (47) Jokerst, J. V.; Lobovkina, T.; Zare, R. N.; Gambhir, S. S. Nanoparticle PEGylation for imaging and therapy. *Nanomedicine (Lond.)* **2011**, *6*, 715-728.
- (48) Xu, F.; Kurskaya, E.; Matseevich, T.; Popova, M.; Askadskii, A.; Jiang, S. In *The calculation scheme for prediction of viscosity for polymeric nano-suspensions*, AIP Conference Proceedings, 2017/05/08, 2017; American Institute of Physics: 2017; p 020005.

- (49) Hankenson, F. C.; Braden-Weiss, G. C.; Blendy, J. A. Behavioral and activity assessment of laboratory mice (*Mus musculus*) after tail biopsy under isoflurane anesthesia. *J. Am. Assoc. Lab Anim. Sci.* **2011**, *50*, 686-694.
- (50) Hohlbaum, K.; Bert, B.; Dietze, S.; Palme, R.; Fink, H.; Thone-Reineke, C. Severity classification of repeated isoflurane anesthesia in C57BL/6JRj mice-Assessing the degree of distress. *PLoS One* **2017**, *12*, e0179588.
- (51) Kutscher, H. L.; Chao, P.; Deshmukh, M.; Singh, Y.; Hu, P.; Joseph, L. B.; Reimer, D. C.; Stein, S.; Laskin, D. L.; Sinko, P. J. Threshold size for optimal passive pulmonary targeting and retention of rigid microparticles in rats. *J Control Release* **2010**, *143*, 31-37.
- (52) Lee, S. Y.; Jung, E.; Park, J. H.; Park, J. W.; Shim, C. K.; Kim, D. D.; Yoon, I. S.; Cho, H. J. Transient aggregation of chitosan-modified poly(d,l-lactic-co-glycolic) acid nanoparticles in the blood stream and improved lung targeting efficiency. *J Colloid Interface Sci* **2016**, *480*, 102-108.
- (53) McDonald, R. J.; McDonald, J. S.; Kallmes, D. F.; Jentoft, M. E.; Murray, D. L.; Thielen, K. R.; Williamson, E. E.; Eckel, L. J. Intracranial gadolinium deposition after contrast-enhanced MR imaging. *Radiology* **2015**, *275*, 772-782.
- (54) Gulani, V.; Calamante, F.; Shellock, F. G.; Kanal, E.; Reeder, S. B.; International Society for Magnetic Resonance in, M. Gadolinium deposition in the brain: summary of evidence and recommendations. *Lancet Neurol* **2017**, *16*, 564-570.
- (55) Hoshyar, N.; Gray, S.; Han, H.; Bao, G. The effect of nanoparticle size on *in vivo* pharmacokinetics and cellular interaction. *Nanomedicine (Lond.)* **2016**, *11*, 673-692.
- (56) Lipka, J.; Semmler-Behnke, M.; Sperling, R. A.; Wenk, A.; Takenaka, S.; Schleh, C.; Kissel, T.; Parak, W. J.; Kreyling, W. G. Biodistribution of PEG-modified gold nanoparticles following intratracheal instillation and intravenous injection. *Biomaterials* **2010**, *31*, 6574-6581.

## Chapter 4

### 4 *In Vivo* Dual Energy Micro-Computed Tomography Imaging of the Mouse Vasculature Using Gadolinium Nanoparticles as Contrast Agent

#### 4.1 Introduction

Micro-computed tomography (micro-CT) is widely used to study the vasculature in mouse models of human disease.<sup>1-9</sup> Micro-CT can provide quantitative, non-invasive, three-dimensional and high-resolution images (*i.e.* tens of micrometers) of live mice within tens of minutes. Since contrast in micro-CT depends on the inherent density of tissues, contrast agents containing high-density elements are required to distinguish the vasculature from surrounding soft tissues. However, discriminating the contrast-enhanced vasculature from high-density tissues in the body, such as bone, can be challenging, especially for vessels that are inside or near bone. To identify contrast-enhanced vessels from bone, dual energy (DE) micro-CT can be performed.

DE micro-CT can differentiate materials within a given volume, using a pair of images acquired using different x-ray spectra.<sup>10-13</sup> The benefit of DE imaging is that it takes advantage of the sharp increase in attenuation of x-rays just above the K-edge of the contrast agent.<sup>14</sup> The K-edge is a unique signature that each element has, which corresponds to the energy required to liberate an inner shell electron. By selecting a pair of x-ray spectra that tunes in to the K-edge of the selected contrast element, the tissue containing the agent can be distinguished from the rest of the image. For instance, DE CT in humans relies on spectral separation for optimal use of iodine agents, where the low energy spectra (80 kVp) tunes in for high iodine attenuation due to the K-edge at 33.2 keV, and lower iodine attenuation when imaging with the high-energy spectra (140 kVp).<sup>15</sup> A large installed base of *in vivo* scanners operates between 30-90 kVp, which restricts spectral separation capabilities, as a limited energy spectrum is available. Spectral shaping, using added filtration, can be used to obtain high photon flux just below and just above the K-edge. This is difficult to achieve when the contrast material has a K-edge around 30 keV, due to the limited photon flux generated at the energies. Therefore, a contrast element

with a K-edge in the middle of the micro-CT x-ray spectrum (*i.e.* 50-60 kVp) would provide enhanced opportunity to perform DE decomposition.<sup>13</sup>

Like in human imaging, commercially available pre-clinical contrast agents are predominantly based on iodine, the K-edge of which is too low, making the generation of a sufficient number of photons difficult below the K-edge. While there are commercially available lead-based *ex vivo* agents, and more recently developed gold-based formulations for *in vivo* imaging of small animals,<sup>10, 16</sup> obtaining a sufficient photon flux above the K-edge of lead (88 keV) and gold (80.7 keV) requires high x-ray tube potential. With respect to x-ray attenuation properties, the ideal class of metals for DE micro CT are the lanthanides, which have K-edges between 38-64 keV – a range that coincides with the average energy of x-rays that most micro-CT scanners produce.<sup>17</sup> The use of lanthanide-based contrast agents for DE micro-CT has been recently demonstrated *ex vivo* by Tse *et al*<sup>18</sup> who used a vascular perfusion contrast agent comprised of homogeneously incorporated erbium nanoparticles (K-edge of 57.5 keV)<sup>13</sup> in combination with spectral shaping. This study demonstrated the successful implementation of optimized DE CT that can be used with any pre-clinical cone-beam micro-CT scanner, resulting in highly accurate decompositions of perfused rat hindlimbs into quantitative soft tissue, bone, and perfused vasculature volumes.

We have developed an *in vivo* analogue of a nanoparticle-based long-circulating contrast agent that can load 100 mg/mL of lanthanides. Our repeatable technique results in a contrast agent that remains in the vasculature for at least an hour, composed of NaErF<sub>4</sub> nanoparticles encapsulated in assemblies formed from PEG-poly(lactic acid) (PEG-PLA) block copolymers.<sup>19</sup> Hence, the purpose of this work was to demonstrate the feasibility of an *in vivo* DE CT technique that can decompose the mouse volume into soft tissue, bone and lanthanide-contrast-containing vessels. This study uses gadolinium as a model lanthanide (K-edge of 50.2 keV) and used the method from our previously published paper (Chapter 2) to synthesize the *in vivo* contrast agent.<sup>19</sup> To our knowledge, this is the first demonstration of an *in vivo* DE CT technique using a lanthanide-based contrast agent, which can be used with any pre-clinical, gantry-based micro-CT scanner.

## 4.2 Materials and Methods

### 4.2.1 Spectral Modeling

X-ray spectra were modelled using the SPEKTR 3.0,<sup>20</sup> computational tool for x-ray spectral simulation within MATLAB (R2018b, MathWorks Inc, Natick, MA). CT scanner-specific parameters were modelled to simulate the GE speCZT micro-CT (GE HealthCare, London, ON), including a target angle of 15°, source-to-isocenter distance of 22.59 cm, additional anode inherent filtration equivalent to 1.0 mm Al (Dunlee, DU 404), and 2 cm Lexan.

The maximum tube potential of 90 kVp was selected, and x-ray filters composed of copper and gadolinium were used to produce the low- and high-energy x rays. SPEKTR 3.0 was used to determine the thickness of each filter that would result in mean energies below and above the K-edge, while generating virtually similar photon flux.

### 4.2.2 X-ray Filter Fabrication and Automation

X-ray filters in the form of cylindrical shells that surround the scan bed and fit within the scanner bore were created (Figure 4.1).<sup>13</sup> The filter acts through a combination of pre- and post-object filtration, equivalent to a total attenuation of a pre-object filter of double the shell's thickness.

Two filters were fabricated – a copper filter for the high-energy spectrum and a gadolinium filter for the low-energy spectrum. The copper filter is comprised of three 80  $\mu\text{m}$  copper sheets wrapped around an acrylic shell, providing a total path length of 480  $\mu\text{m}$ . Since gadolinium foil is not available, a novel approach to filter design was utilized. Specifically, a cylindrical shell containing a 2.2 mm hollow cavity was printed via the fused deposition of polyamide. The cavity was filled with a 4% w/v gadolinium in distilled water (*i.e.* 95 mg of gadolinium trichloride hexahydrate per mL of water), equivalent to a total pathlength of 0.18 mm of gadolinium. The liquid filter is attached to an acrylic shell around which the copper filter is wrapped. The dimensions of the acrylic support tube were dictated by scanner dimensions and scan field of view; in this case the filters were 5 cm in height and 8 cm inner diameter. The filters are controlled by an exchange mechanism that

automatically switches the x-ray filters within the scanner bore in between frames, emulating the acquisition of interleaved low- and high-energy scans. This mechanism is a modification of the that described by Tse *et al.*<sup>18</sup> where the motor and motor driver were replaced to enable rapid filter switching that can be performed at every projection angle. A custom 3D printed mouse bed - featuring a bridge over the bed - was designed to facilitate reproducible filter switching over the subject (Figure 4.1).

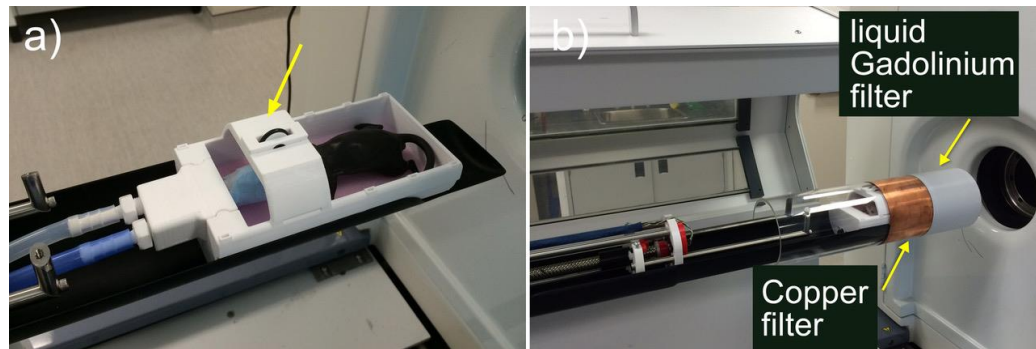


Figure 4.1 DE micro-CT setup for a gantry-based micro-CT. a) Custom 3D-printed mouse bed designed with a bridge over the bed (arrow in a) enables the custom filters to slide reproducibly over the subject. b) The filter switching mechanism, with the filter in the high-energy state.

### 4.2.3 Image Co-Registration

While the low and high-energy images were acquired in an interleaved fashion (see below), the potential for misalignment of the final volumes was mitigated by introducing fiducial markers beads around the edges of the custom-built bed. The method described by Tse *et al.*<sup>18</sup> was used. Briefly, polytetrafluoroethylene spheres (1.6 mm, Teflon™) were embedded in a distributed pattern throughout 2-mm thick polystyrene foam sheets lining the custom 3D-printed bed; Teflon™ was selected to facilitate marker segmentation. The centroids of a minimum of eight beads were used to register the high- and low-energy images with sub-voxel accuracy via rigid transformation. The original and registered low energy images were subtracted from their respective high-energy image to verify the success of the co-registration technique.

#### 4.2.4 Dual-Energy Micro-Computed Tomography

The DE acquisition and decomposition was first evaluated using a cylindrical acrylic phantom (4 cm outside diameter) containing a bone-mimicking calibrator (SB3, Gamex RMI, Middleton, USA), water, and 100 mg/mL of gadolinium in distilled water, prepared by diluting 168 mg of gadolinium chloride per mL of water. The Animal Care Committee of Western University Council for Animal Care approved all procedures. Male C57BL/6 mice (n=8, 25-30 g) were anesthetized initially using 3.5% of isoflurane in O<sub>2</sub>, followed by maintenance at 1.5%. Polymer encapsulations of gadolinium nanoparticles optimized for *in vivo* micro-CT imaging – specifically composed of sodium gadolinium tetrafluoride nanoparticles within assemblies of poly(ethylene glycol)-poly(L-lactide) – were prepared in powdered form as described in Chapter 2.<sup>19</sup> The nanoparticles were added to 0.2 mL of saline immediately before micro-CT scans at a concentration of 100 mg/mL of gadolinium, then intravenously administered *via* tail vein catheterization.

DE images were obtained with the GE speCZT micro-CT scanner. The x-ray technique was a two-phase electrocardiogram (ECG) gated scan acquired at 90 kVp, 32 mA, 4x4 binning (resulting in 100  $\mu$ m isotropic voxel spacing), 220 projections over 192°, 4 frames averaged per projection, and 16 ms per frame. To start the scan, the filter controller positions the copper filter in the field of view and produces an ECG pulse that instructs the scanner to acquire the first phase frames (*i.e.* high-energy images). The scanner sends a signal to the filter controller after high-energy image acquisition, followed by the filter controller placing the liquid gadolinium filter in the field of view. The controller produces another ECG pulse that instructs the scanner to acquire the second phase frames (*i.e.* low-energy images). The scanner sends a signal to the filter controller after low-energy image acquisition, and the cycle is repeated for 220 projections. The entire DE scan was acquired over 15 minutes.

The acquired frames were iteratively reconstructed using unregularized conjugate gradient least-squares optimization in the RTK 1.3.0 toolkit.<sup>21</sup> An in-house conjugate gradient least-squares programming utility was used with optimized reconstruction parameters to maintain adequate image quality (*i.e.* noise reduction and spatial resolution) in the 3D reconstructions from a reduced number of views (220). Following reconstruction, the

images were rescaled into Hounsfield units (HU) using vials of water and air within the field of view.

#### 4.2.5 Image Decomposition and Evaluation of Results

The decomposition of DE CT images was performed by matrix factorization, as previously reported by Granton *et al.*<sup>11</sup> and is described in detail in Appendix C. Briefly, the algorithm uses six CT numbers, represented by the mean CT number of soft-tissue, bone, and contrast-enhanced blood vessels in the low- and high-energy images. MicroView 2.6.0 (Parallax Innovations Inc., London, ON) was used to measure the mean CT number from  $(300\ \mu\text{m})^3$  regions-of-interest (ROI) in the bladder (soft tissue), femoral cortical bone, and abdominal aorta (gadolinium-enhanced vessel). The generated decomposed volumes represent quantitative maps of each individual material, with voxel values (0-10,000 arbitrary units) representing the volume fraction (0-100% respectively) or the percent contribution of the decomposed material within each individual voxel, assuming the sum of all three volume fractions equals 100%.

Quantitative evaluation on the accuracy of DE micro-CT decomposition was performed on the phantom and each mouse by quantifying the number and distribution of misclassified voxels within each decomposed volume. To quantify misclassified voxels, ROIs ( $300\ \mu\text{m} \times 300\ \mu\text{m} \times 300\ \mu\text{m}$ ) in the bladder, femoral cortical bone, and abdominal aorta were generated in each of the decomposed volumes, ensuring that the ROI coordinates were identical between volumes. Mean bone, soft tissue, and contrasted vessel values were recorded for each mouse. An accurate decomposition would have been 10,000 arbitrary units or 100% for bladder in the soft tissue image, for femoral cortical bone in the bone image, and for the abdominal aorta in the gadolinium-enhanced vessels image. The same quantitative analysis was performed in the phantom image, except in volumes within water, and in the bone and gadolinium calibrators. Statistical analysis was performed using Prism 8 (GraphPad Software, San Diego, USA).

## 4.3 Results

### 4.3.1 Spectral Modeling

The SPEKTR 3.0 simulated unfiltered 90 kVp spectrum and filtered low- and high-energy spectra are shown in Figure 4.2. The unfiltered 90 kVp spectrum yields an average energy of 43 keV; the copper and gadolinium filters shift the mean energy to 59 and 49 keV, respectively. The flux ratio of the high- and low-energy x-rays was 1.02 when 3 cm of cylindrical soft tissue is placed within the imaging field of view (0.91 without soft tissue).

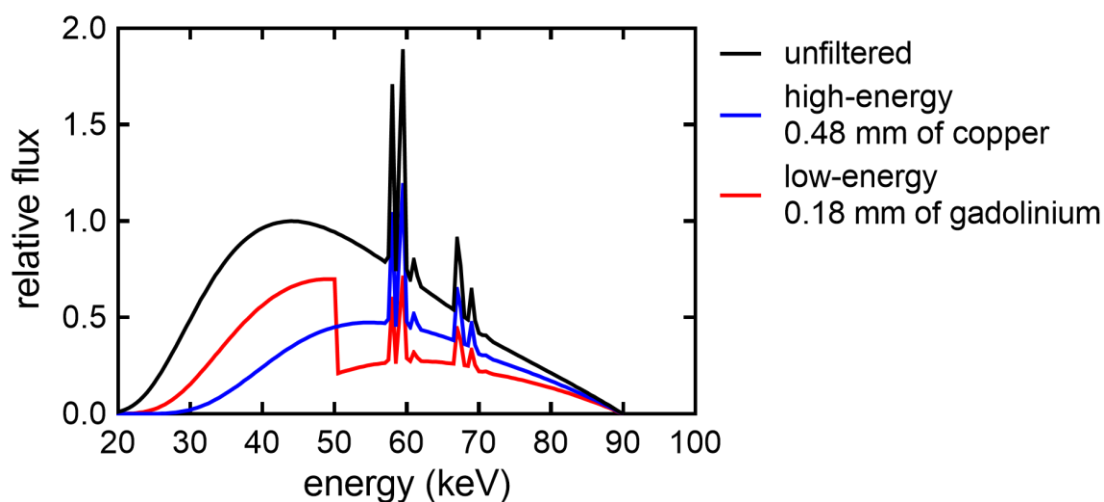


Figure 4.2 Modelled spectral distributions of the unfiltered 90 kVp spectra, and with the addition of the copper or liquid gadolinium filters to produce the low- and high-energy x-rays for DE micro-CT.

### 4.3.2 Image Co-Registration

To verify the effectiveness of the image registration technique, the difference between high-energy and low-energy images were examined. Representative slices from non-registered and co-registered difference images are shown in Figure 4.3. In the absence of image registration, the difference between the low - and high-energy image reveal obvious tissue borders, predominantly surrounding the bone and the mouse body, which are eliminated by co-registration. In the co-registered images, negative contrast is seen in bone, which can be attributed to spectral differences.

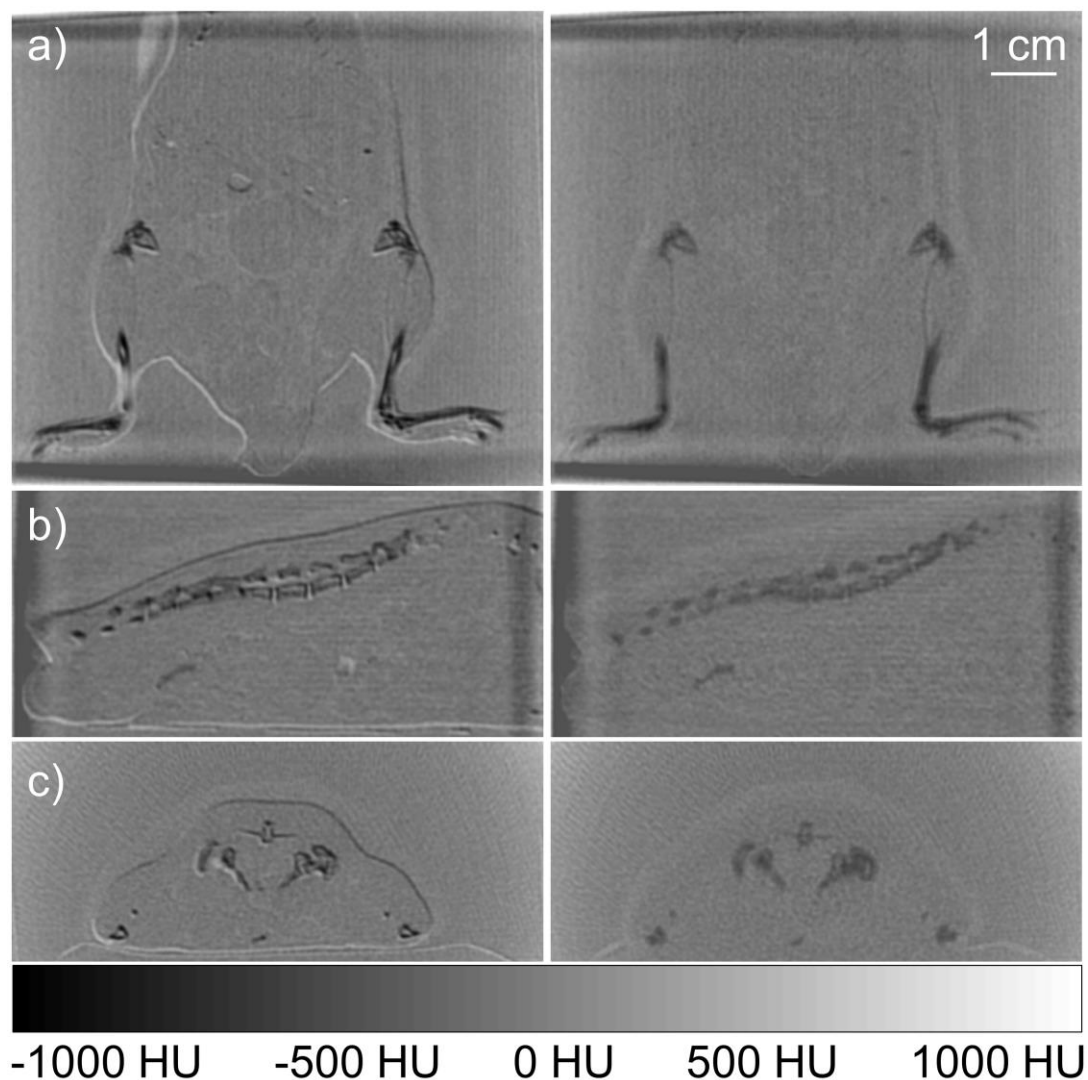


Figure 4.3 Representative a) coronal, b) sagittal, and c) axial slices from the difference between non-registered (left) and co-registered (right) images.

### 4.3.3 Material Decomposition

#### 4.3.3.1 *In vitro* Decomposition

Coronal slices from the material decomposition of an acrylic phantom containing water, a bone calibrator and a gadolinium calibrator, as well as a representative high-energy image are shown in Figure 4.4. The DE CT decomposition yielded accuracies of  $99.43 \pm 0.46 \%$ ,  $97.47 \pm 0.48 \%$ , and  $94.32 \pm 1.56 \%$  in the water, bone, and gadolinium volumes,

respectively (Table 4.1), averaged from three  $(300 \mu\text{m})^3$  ROIs within the same volume. All material misclassifications are below 6%.

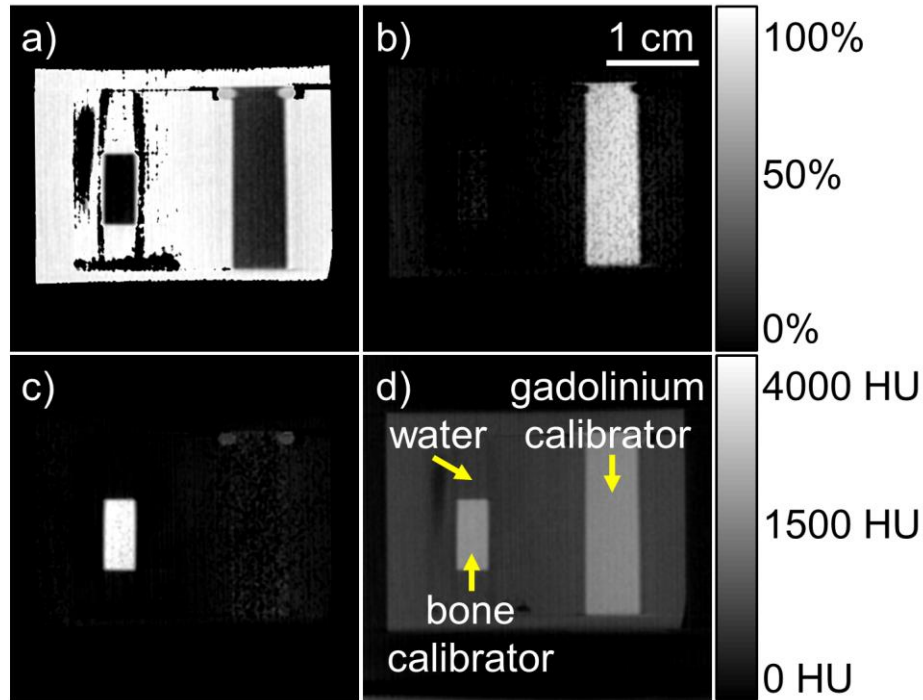


Figure 4.4 Coronal slices of the acrylic phantom containing water, bone, and gadolinium calibrators. Material decomposition resulted in a) water, b) gadolinium, and c) bone volumes. d) Representative slice from the high-energy image. The top scale bar represents percentage compositions for decomposition images and bottom scale bar represents CT contrast in the high-energy image.

Table 4.1 Quantitative assessment of in vitro DE decomposition. Percentages of correct material classifications are underlined.

Percentage of Material Classified	Decomposition Image		
	Water	Bone	Gadolinium
Water	<u><math>99.43 \pm 0.46</math></u>	$0.04 \pm 0.05$	$0.05 \pm 0.03$
Bone	$0.24 \pm 0.08$	<u><math>97.47 \pm 0.48</math></u>	$2.38 \pm 1.15$
Gadolinium	$4.94 \pm 0.05$	$2.73 \pm 0.54$	<u><math>94.32 \pm 1.56</math></u>

#### 4.3.3.2 *In vivo* Decomposition

Dual energy micro-CT images were acquired in each of the eight mice, with an average duration between contrast agent injection and start of scan of  $51 \pm 20$  minutes. Mouse-specific CT numbers were collected from ROIs of the bladder, femoral cortical bone, and the contrast-enhanced abdominal aorta, and are summarized in Table C.1. (Appendix C). When implemented with the matrix factorization decomposition technique, quantitative three-dimensional volumes of soft tissue, bone and gadolinium-enhanced vessels were generated for all mice. Representative bone and gadolinium-enhanced vessels volume images are shown in Figure 4.6 a and b, respectively. To further demonstrate the need for co-registration, volume decomposition was demonstrated in a representative mouse, which exhibited substantial misclassification of bone and soft tissue as gadolinium-enhanced vessels near tissue borders (Figure C.1, Appendix C).

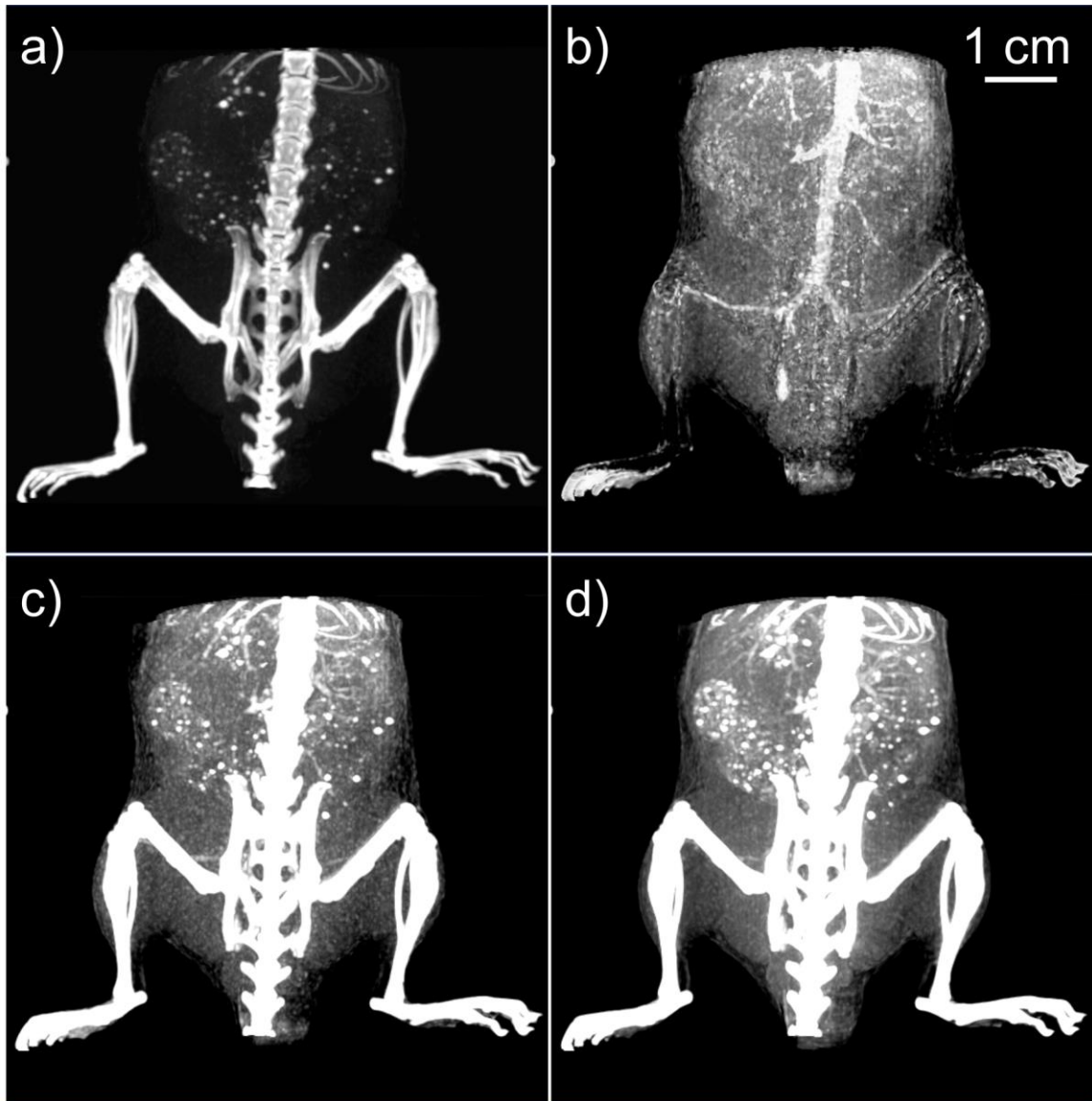


Figure 4.5 Maximum intensity projections through a) the bone and b) gadolinium-enhanced vessels volumes demonstrate the quality of the decomposition. For comparison, MIPs through the high c) and low d) energy volumes are also shown. The window and level were set to optimize visualization of the vessels.

#### 4.3.4 Quantification of Tissue Decomposition Results

The DE CT decomposition generated correct voxel classifications of  $93.00 \pm 8.53 \%$ ,  $95.60 \pm 3.52 \%$ , and  $83.39 \pm 12.47 \%$  for tissue, bone, and vessel volumes, respectively, as quantified from eight mice. The corresponding graph of the percentage of correctly

classified and misclassified voxels within each decomposed volume is illustrated in Figure 4.7.

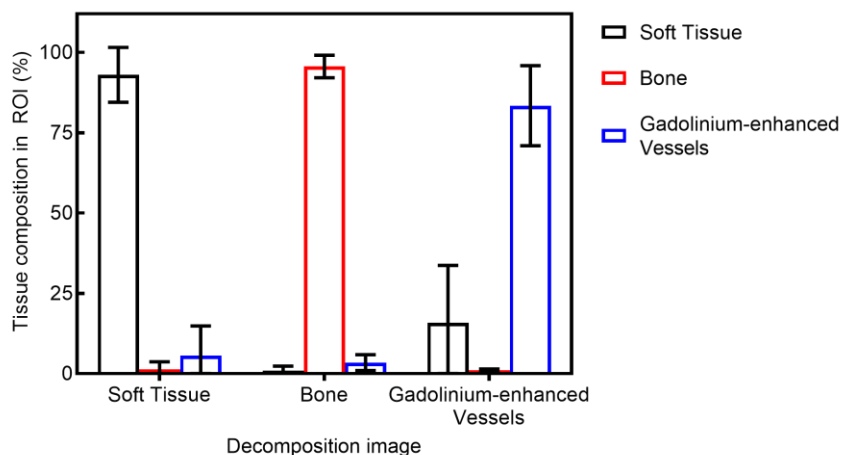


Figure 4.6 Tissue decomposition results averaged from all subjects. Misclassifications are nearly absent for bone in the soft tissue image, and for soft tissue and blood vessels in the bone image.

Examination of an oblique view of the left pelvic and hindlimb region of one of the mice demonstrated the improved visualization of the branching vessels from the common iliac artery and vein are identified in the gadolinium-enhanced vessels image (Figure 4.8); these branches are measured to be at least 0.25 mm in diameter and are difficult to distinguish from bone in the low-energy or high-energy images.

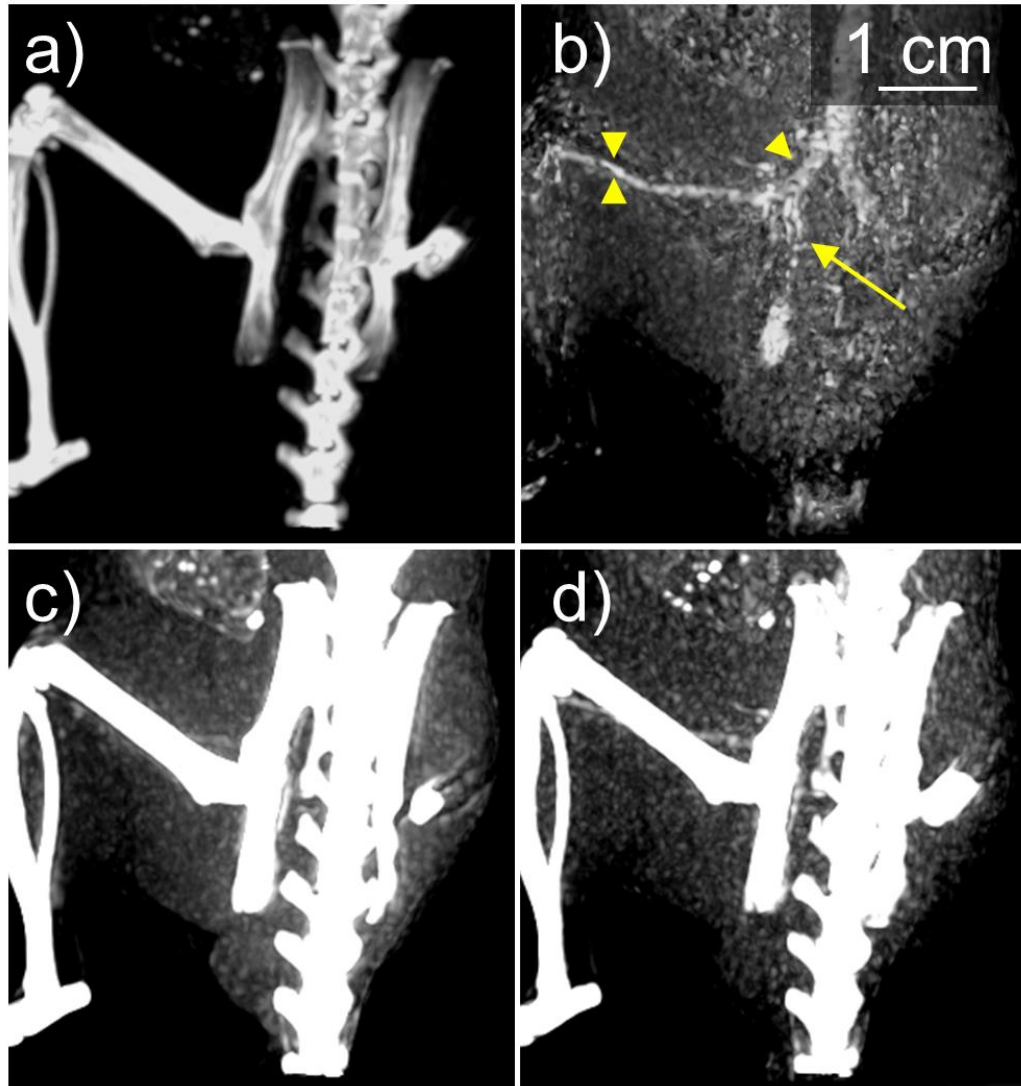


Figure 4.7 Thick 1.5-cm oblique MIPs of the left pelvic and hindlimb region. The decomposed a) bone and b) gadolinium-enhanced vessels volumes show additional vessels (arrow) originating from the common iliac artery and vein (single arrowhead), apart from the femoral artery and vein (double arrowheads). Smaller vessels are otherwise difficult to identify in the c) low-energy or d) high-energy image. A tight window and level were used to display c) and d) to favor the visibility of blood vessels.

#### 4.4 Discussion

In this study, we have implemented an *in vivo* DE CT technique using an optimized vascular contrast agent composed of polymer-encapsulated gadolinium nanoparticles, and supplementary apparatus composed of custom x-ray filtration, a liquid filter, an automated

filter-exchange mechanism, and fiducial marker-based image co-registration to successfully decompose images acquired from a pre-clinical gantry-based cone-beam micro-CT scanner. To date, this is the first demonstration of DE micro-CT of the vasculature of live mice using long-circulating gadolinium nanoparticles as contrast agent.

A constant tube potential of 90 kVp was selected, supplemented by custom filtration for spectral separation, to permit the acquisition of interleaved scans, with the original intent of avoiding the need for image co-registration. The tube potential was set to 90 kVp because it is typically the maximum tube potential of a large number of high-resolution *in vivo* micro-CT scanners most commonly utilized kVp to optimize image contrast and, signal-to-noise-ratio, and x-ray tube cooling. The mean energy of the unfiltered spectrum 43 keV is close to the K-edge of gadolinium (50.2 keV), which was anticipated to require the least filtration for optimal dual energy acquisition. Selecting a lower tube potential would have resulted in a lower mean energy, necessitating greater filtration to obtain the high-energy spectrum. Copper was selected to filter the high-energy spectrum because of its low cost, accessibility at varying thicknesses, and its current use in CT and micro-CT.<sup>11, 13, 22, 23</sup> While additional filtration can enhance spectral separation, the resulting diminished photon flux will result in images with poor signal-to-noise ratio, again compromising decomposition accuracy. To generate the low-energy spectrum, a gadolinium-based liquid filter was used, by filling a cylindrical polyamide shell with gadolinium chloride diluted in water, as it inherently attenuates photons above its K-edge. Implementing the use of a liquid filter allows the user to customize the choice of filtration material and control over the pathlength of the filter simply by changing the concentration of the gadolinium solution utilized.

As previously mentioned, the initial goal was to acquire interleaved scans to eliminate the need for image co-registration. However, the scanning table in the GE speCZT was not as rigid as anticipated, demonstrated by the displacement observed between low-energy and high-energy images, which is attributed to filter-position-specific sag introduced when the copper filter was positioned over the mouse. The misregistration between the low- and high-energy images is apparent in the difference images. Importantly, the fact that image registration was successful suggests that the table sag introduced by the filter was

reproducible between projection angles. While placing metal foils at the x-ray tube port, prior to the sample, would remove the need for the external filter assembly, the addition of a filter switching mechanism on the tube port may interfere with the gantry balance and the normal operation of the scanner. Therefore, a cylindrical shell filter that surrounds the scan bed yet fits within the scanner bore with an external filter switcher controller was used. This approach to filtration avoids modifications to the scanner and is compatible with gantry-based scanners. The cylindrical shell filters the x-rays before and after the object being scanned, providing a total attenuation that is equivalent to a mounted filter of with the same path length. Sub-voxel image co-registration of the volumes was enabled by embedded Teflon™ marker beads. While this co-registration was successful in removing filter-switcher-induced sag, were used as fiducial markers and were easily segmented. Operator intervention was only required to select seed points for an automated centroid calculation and co-registration.

Generally, CT numbers measured from “pure” calibrators or global values averaged from all scanned subjects are used in DE CT decomposition algorithms. However, this study used an *in vivo* vascular agent that introduces contrast to the blood pool that decreases over time. While DE CT images were acquired and processed seamlessly and uniformly, the main limitation in this study was the variability of the time required to set up the mouse bed and cylindrical filter over the subject (varying from 20 to 90 minutes), due to contrast agent injection occurring outside of the scanner. This is followed by filter positioning within the field of view, which required a quick scan for position verification, often leading to further delays due to repositioning. Hence, in this study, CT numbers specific to each mouse subject were collected and used in the matrix factorization algorithm for DE CT decomposition. More importantly, the delay between contrast agent injection and DE CT scan acquisition resulted in lower enhancement in the vasculature compared to the expected peak enhancement of approximately 250 HU.<sup>19</sup>

The quantitative assessment of DE CT decompositions resulted in at least 90 % accuracy, with the exception of  $15.87 \pm 17.81$  % soft tissue detection in the gadolinium-enhanced vessels image. A substantial percentage of misclassified voxels were coincident with scanned mouse subjects that had lower enhancement in the abdominal aorta. Since mouse-

specific CT numbers were used in volume decomposition, misclassifications were not anticipated. However, the difference between CT numbers that were used for detecting gadolinium-enhanced vessels approached that of soft tissue for mice that had low vascular contrast, resulting in an overlap between possible CT numbers for soft tissue and gadolinium-enhanced vessels (hence, the misclassifications).

Decomposing bone from major arteries and veins was successfully demonstrated in the pelvic region, where in the gadolinium-enhanced vessels image, the root or termination of connecting vessels at least 0.25 mm in diameter were detected. Smaller vessels were difficult to distinguish with the images composed of  $(100\ \mu\text{m})^3$  voxels in this study, due to low vascular contrast and partial volume effects. While previous work has suggested that DE CT may be partially resistant to partial volume effects,<sup>24, 25</sup> as DE CT may still allow for the detection and quantification of small vessels over varying spatial resolutions, higher gadolinium concentrations are required than presented in this work. This is possible in *ex vivo* perfusions where higher contrast agent concentrations can be achieved in the lumen or through the technique presented in this study, except with higher vascular contrast through reduced set up time and increased gadolinium loading in the contrast agent.

Our *in vivo* DE CT technique can be used to distinguish major vessels of live mice from surrounding bone using a pre-clinical, gantry-based micro-CT scanner. The technique presented allowed for the automatic decomposition of gadolinium agent-injected mice into quantitative images of soft-tissue, bone, and gadolinium-enhanced vessels. This decomposition was achieved by the interleaved acquisition of DE CT images, through custom x-ray filtration and an automated filter exchange mechanism. Fiducial marker beads enabled the co-registration of DE images, for volume decomposition by the matrix factorization algorithm. In regions near bone, vessels at least 0.25 mm in diameter can be identified and separated from the rest of the mouse volume. While further studies are required to optimize subject setup and to investigate the ability of this technique to overcome partial volume effects, our results demonstrate the feasibility of *in vivo* DE CT of the mouse vasculature.

## 4.5 Conclusions

We present an *in vivo* DE CT technique that can produce quantitative images of decomposed soft tissue, bone, and vessel volumes that can identify major vessels from surrounding bone, and can be used with any pre-clinical, gantry-based micro-CT scanner. Our promising results show that vessels at least 0.25 mm in diameter can be distinguished from bone, which can be improved by reducing set up time and increased *in vivo* vascular contrast agent concentration. The presented technique can be used as a quantitative tool to assess vessel densities in vascular research.

## 4.6 References

- (1) Dobnikar, L.; Taylor, A. L.; Chappell, J.; Oldach, P.; Harman, J. L.; Oerton, E.; Dzierzak, E.; Bennett, M. R.; Spivakov, M.; Jorgensen, H. F. Disease-relevant transcriptional signatures identified in individual smooth muscle cells from healthy mouse vessels. *Nat. Commun.* **2018**, *9*, 4567.
- (2) Gordon-Keylock, S.; Sobiesiak, M.; Rybtsov, S.; Moore, K.; Medvinsky, A. Mouse extraembryonic arterial vessels harbor precursors capable of maturing into definitive HSCs. *Blood* **2013**, *122*, 2338-2345.
- (3) Trogan, E.; Fayad, Z. A.; Itskovich, V. V.; Aguinaldo, J. G.; Mani, V.; Fallon, J. T.; Chereshev, I.; Fisher, E. A. Serial studies of mouse atherosclerosis by *in vivo* magnetic resonance imaging detect lesion regression after correction of dyslipidemia. *Arterioscler. Thromb. Vasc. Biol.* **2004**, *24*, 1714-1719.
- (4) Vafaie, F.; Yin, H.; O'Neil, C.; Nong, Z.; Watson, A.; Arpino, J. M.; Chu, M. W.; Holdsworth, D. W.; Gros, R.; Pickering, J. G. Collagenase-resistant collagen promotes mouse aging and vascular cell senescence. *Aging Cell* **2014**, *13*, 121-130.
- (5) Ashton, J. R.; Befera, N.; Clark, D.; Qi, Y.; Mao, L.; Rockman, H. A.; Johnson, G. A.; Badea, C. T. Anatomical and functional imaging of myocardial infarction in mice using micro-CT and eXIA 160 contrast agent. *Contrast Media Mol. Imaging* **2014**, *9*, 161-168.
- (6) Foster, W. K.; Ford, N. L. Investigating the effect of longitudinal micro-CT imaging on tumour growth in mice. *Phys. Med. Biol.* **2011**, *56*, 315-326.
- (7) Ghanavati, S.; Yu, L. X.; Lerch, J. P.; Sled, J. G. A perfusion procedure for imaging of the mouse cerebral vasculature by x-ray micro-CT. *J. Neurosci. Methods* **2014**, *221*, 70-77.
- (8) Schambach, S. J.; Bag, S.; Groden, C.; Schilling, L.; Brockmann, M. A. Vascular imaging in small rodents using micro-CT. *Methods* **2010**, *50*, 26-35.
- (9) Wong, M. D.; Dorr, A. E.; Walls, J. R.; Lerch, J. P.; Henkelman, R. M. A novel 3D mouse embryo atlas based on micro-CT. *Development* **2012**, *139*, 3248-3256.
- (10) Clark, D. P.; Ghaghada, K.; Moding, E. J.; Kirsch, D. G.; Badea, C. T. In vivo characterization of tumor vasculature using iodine and gold nanoparticles and dual energy micro-CT. *Phys Med Biol* **2013**, *58*, 1683-1704.
- (11) Granton, P. V.; Pollmann, S. I.; Ford, N. L.; Drangova, M.; Holdsworth, D. W. Implementation of dual- and triple-energy cone-beam micro-CT for postreconstruction material decomposition. *Med Phys* **2008**, *35*, 5030-5042.
- (12) Moding, E. J.; Clark, D. P.; Qi, Y.; Li, Y.; Ma, Y.; Ghaghada, K.; Johnson, G. A.; Kirsch, D. G.; Badea, C. T. Dual-energy micro-computed tomography imaging of

radiation-induced vascular changes in primary mouse sarcomas. *Int J Radiat Oncol Biol Phys* **2013**, *85*, 1353-1359.

(13) Tse, J. J.; Dunmore-Buyze, J.; Drangova, M.; Holdsworth, D. W. Dual-energy computed tomography using a gantry-based preclinical cone-beam microcomputed tomography scanner. *J Med Imaging (Bellingham)* **2018**, *5*, 033503.

(14) Johnson, T. R. Dual-energy CT: general principles. *AJR Am J Roentgenol* **2012**, *199*, S3-8.

(15) Badea, C. T.; Drangova, M.; Holdsworth, D. W.; Johnson, G. A. In vivo small-animal imaging using micro-CT and digital subtraction angiography. *Phys Med Biol* **2008**, *53*, R319-350.

(16) Shi, F.; Yang, Y.; Chen, J.; Sha, Y.; Shu, Y.; Wu, H. Dendrimer-Entrapped Gold Nanoparticles as Potential CT Contrast Agents for Localizing Sentinel Lymph Node via Indirect CT Lymphography on Rabbit Model. *Biomed Res Int* **2018**, *2018*, 1230151.

(17) Niranjana, K. M.; Badiger, N. M. K shell parameters of some lanthanide elements using bremsstrahlung. *Radiat. Phys. Chem.* **2015**, *107*, 59-64.

(18) Tse, J. J.; Dunmore-Buyze, P. J.; Drangova, M.; Holdsworth, D. W. Erbium-Based Perfusion Contrast Agent for Small-Animal Microvessel Imaging. *Contrast Media Mol Imaging* **2017**, *2017*, 7368384.

(19) Cruje, C.; Dunmore-Buyze, J.; MacDonald, J. P.; Holdsworth, D. W.; Drangova, M.; Gillies, E. R. Polymer Assembly Encapsulation of Lanthanide Nanoparticles as Contrast Agents for In Vivo Micro-CT. *Biomacromolecules* **2018**, *19*, 896-905.

(20) Punnoose, J.; Xu, J.; Sisniega, A.; Zbijewski, W.; Siewerdsen, J. H. Technical Note: spektr 3.0-A computational tool for x-ray spectrum modeling and analysis. *Med Phys* **2016**, *43*, 4711.

(21) Rit, S.; Oliva, M. V.; Brousmiche, S.; Labarbe, R.; Sarrut, D.; Sharp, G. In *The Reconstruction Toolkit (RTK), an open-source cone-beam CT reconstruction toolkit based on the Insight Toolkit (ITK)*, 2014; 2014.

(22) Ay, M. R.; Mehranian, A.; Maleki, A.; Ghadiri, H.; Ghafarian, P.; Zaidi, H. Experimental assessment of the influence of beam hardening filters on image quality and patient dose in volumetric 64-slice X-ray CT scanners. *Phys Med* **2013**, *29*, 249-260.

(23) Kawashima, H.; Ichikawa, K.; Nagasou, D.; Hattori, M. X-ray dose reduction using additional copper filtration for abdominal digital radiography: Evaluation using signal difference-to-noise ratio. *Phys Med* **2017**, *34*, 65-71.

(24) Primak, A. N.; Fletcher, J. G.; Vrtiska, T. J.; Dzyubak, O. P.; Lieske, J. C.; Jackson, M. E.; Williams, J. C., Jr.; McCollough, C. H. Noninvasive differentiation of uric acid

versus non-uric acid kidney stones using dual-energy CT. *Acad Radiol* **2007**, *14*, 1441-1447.

(25) Tran, D. N.; Straka, M.; Roos, J. E.; Napel, S.; Fleischmann, D. Dual-energy CT discrimination of iodine and calcium: experimental results and implications for lower extremity CT angiography. *Acad Radiol* **2009**, *16*, 160-171.

## Chapter 5

### 5 Conclusion and Future Directions

#### 5.1 Summary of Thesis Results

Dual energy (DE) computed tomography (CT) has the capability to impact medicine and preclinical research by providing quantitative information that can quantify vessel density, detect nascent lesions, and identify perfusion restoration or inhomogeneities within tissues. A library of instrumentation techniques and scan protocols have been developed for DE CT, with the goal of acquiring a pair of images that reports the attenuation of a given volume to two different x-ray distributions. While DE image acquisition has benefitted from technical advancements in CT, the contrast agents that are used are still predominantly composed of iodinated small molecules, which were first developed in the 1970s. Recent work has demonstrated that lanthanide-based contrast agents have optimized properties for DE decomposition,<sup>1</sup> specifically when using *in vivo* micro-CT scanners. By adopting nanoparticle design strategies that were developed for therapeutics and disease diagnosis, this thesis took advantage of technical advancements in nanotechnology and polymer science to develop a long-circulating contrast agent containing lanthanides that can be utilized for *in vivo* DE micro-CT of mouse vasculature.

In Chapter 2, erbium nanoparticles encapsulated within amphiphilic block copolymers – either synthesized in customized lengths or purchased – were fabricated. The amphiphilic block copolymers that were used contained poly(ethylene) glycol (PEG), which is a polymer that is widely used in *in vivo* applications, and is known to introduce temporary stealth properties to its cargo, enabling them to evade the immune system.<sup>2-4</sup> By measuring erbium concentrations by inductively-coupled plasma mass spectrometry and observing *in vitro* colloidal stability *via* dynamic light scattering measurements of the hydrodynamic diameters of the assemblies in water, saline and a mouse serum mimic, the most promising copolymer was selected for further characterization. PEG-poly(lactic acid) assemblies demonstrated *in vitro* colloidal stability for at least an hour and were able to concentrate a high loading of 100 mg/mL of erbium for intravenous injections of mice. The injected

subjects were imaged by micro-CT and CT contrast enhancements of over 250 HU were observed in the vasculature for at least an hour, which well exceeds *in vivo* micro-CT scan time requirements. Moreover, although the synthesis technique and *in vivo* scans were demonstrated using erbium as contrast material, it can easily be substituted by any other lanthanide given that the same number of moles is used in the synthesis as the different lanthanide have very similar chemistry.

While the agent that was synthesized in Chapter 2 provided high vascular contrast for periods that meet micro-CT scan time requirements, the scanned subjects frequently expired within two days of intravenous injections. Hence, an alternative nanoparticle design was explored in Chapter 3, where in lieu of using an amphiphilic polymer to encapsulate nanoparticles, PEG was grafted directly onto the lanthanide nanoparticle surface, which was NaGdF<sub>4</sub> in this study, resulting in particles with smaller overall diameters. The new formulation still suspends at least 100 mg/mL of lanthanides, and permitted survival for at least 5 days. Imaging and quantitative analysis of gadolinium in tissues showed the presence of contrast agent in clearance organs including the liver and spleen and very low amounts in other organs. *In vitro* cell culture experiments, subcutaneous injections, and analysis of mouse body weight suggested that the agents exhibited low toxicity. Histological analysis of tissues 5 days after injection of the contrast agent showed cytotoxicity in the spleen, but no abnormalities were observed in the liver, lungs, kidneys, and bladder. CT contrast enhancements of at least 245 HU were observed in the blood pool, which however, slowly started decreasing in as little as 10 minutes after injections. Hence, we observed a tradeoff between circulation time and animal viability for the formulations presented in this Chapter and in Chapter 2, where the longer the circulation time, the lower the chances of animal viability. Since the ultimate goal of this thesis was to demonstrate the feasibility of *in vivo* DE CT of the vasculature, the formulation from Chapter 2, which provided longer circulation times, was selected for further imaging studies, to maintain as much contrast as possible in the blood pool of the scanned subjects.

In Chapter 4, I demonstrated the feasibility of *in vivo* DE micro-CT using a gadolinium contrast agent that was synthesized as presented in Chapter 2. A tube potential of 90 kVp

was selected, and the spectral separation between the low-energy and high-energy spectra was optimized using SPEKTR 3.0 simulations. This protocol was implemented by the interleaved acquisition of DE CT images, through cylindrical shell filters composed of copper and a solution of gadolinium in water (obtaining high- and low-energy images, respectively), and an automated filter exchange mechanism. However, since the filters and mouse bed had to be set up outside the micro-CT gantry, the delay between injection time and scan time resulted in lower vascular contrast than anticipated. Sub-voxel displacements were also observed between mouse positions in the low-energy and high-energy images. Nonetheless, fiducial marker beads enabled the co-registration of DE images, for volume decomposition by the matrix factorization algorithm. The results show that the *in vivo* DE CT technique that can produce quantitative images of decomposed soft tissue, bone and gadolinium-enhanced vessels volumes that can identify major vessels from surrounding bone, which can be used with any pre-clinical, gantry-based micro-CT scanner. Vessels at least 0.25 mm in diameter can be distinguished from surrounding bone, which can be improved by reducing set up time, possibly increasing *in vivo* vascular contrast. While further studies are required to optimize subject setup and to investigate the ability of this technique to overcome partial volume effects, our results demonstrate the feasibility of *in vivo* DE CT of the vasculature.

## 5.2 Future Directions

This thesis presented methods to synthesize two versions of long-circulating lanthanide-based nanoparticle contrast agents that can be used for micro-CT imaging of the vasculature, characterized these agents *in vitro* and *in vivo*, and demonstrated the feasibility of DE micro-CT imaging of the mouse vasculature *in vivo*. The results that were obtained from the characterization of the agents in this thesis indicate opportunities that can further improve the viability of the injected animals, and prospective applications of the *in vivo* DE micro-CT technique that is presented.

### 5.2.1 Non-rigid Nanoparticles as Contrast Agents

In Chapter 3, one version of the synthesized contrast agents (PPEG<sub>2000</sub>-GdNP, which demonstrated transient hydrodynamic diameters as measured by dynamic light scattering

*in vitro*) was found to accumulate at a lower concentration in the liver and the spleen than the colloiddally stable version (PPEG<sub>5000</sub>-PPEG<sub>1000</sub>-GdNP). It is suspected that the size transience of PPEG<sub>2000</sub>-GdNP – demonstrated within minutes of incubation with saline and a mouse serum mimic – promoted mobility and reduced accumulation in RES organs. This was previously demonstrated by other researchers that studied nanogels of varying rigidity, reporting greater particle mobility and lower accumulation in clearance organs with less rigid nanogels than rigid nanogels.<sup>5, 6</sup> Hence, nanoparticles that are less rigid than PPEG<sub>2000</sub>-GdNP, but have the same physical properties (*i.e.* PEG-coated with a hydrodynamic diameter of close to 50 nm) can be studied.

Most biocompatible polymers exhibit gradual degradation *in vivo*, including PEG. However, polymers can be developed such that they degrade when exposed to specific stimuli, such as light, change in pH, or mechanical force. Such polymers are either degradable stimuli responsive polymers, which require multiple stimuli events to completely degrade,<sup>7</sup> or self-immolative polymers (SIPs), which can depolymerize from end-to-end after cleavage of a stimuli-responsive end cap. The main advantage of using SIPs are the tunability of their end-caps. Specifically, polyglyoxylates are a promising class of SIPs that have been synthesized in the form of poly(methyl glyoxylate) (PMeG)<sup>8</sup> and poly(ethyl glyoxylate) (PEtG),<sup>9</sup> which the Gillies group specializes in. PEtG can be coupled to PEG to create an amphiphilic diblock copolymer (PEG-PEtG) that can be used to encapsulate the lanthanide nanoparticles that were synthesized in this thesis within polymer assemblies. Lanthanide nanoparticle assemblies encapsulated within PEG-PEtG will likely demonstrate similar circulation times as the assemblies that were studied in Chapter 2, except that they have the potential to accumulate at lower concentrations in RES organs due to their more rapid degradation.

### 5.2.2 Imaging Abnormal Tissues *via* Vascular Permeability

Vascular permeability is a property that accompanies tissue abnormalities, such as tumors and soft tissue injury.<sup>10, 11</sup> Nanoparticles are known to accumulate in tumors, and have been used to opacify tumor tissues in micro-CT images,<sup>12</sup> as well as in DE micro-CT scans.<sup>13</sup> Similarly, some previous evidence to show that the damage induced by ischaemia-reperfusion injury alters vascular permeability in the heart,<sup>11</sup> where nanoparticle

accumulation has been demonstrated *in vivo*.<sup>14</sup> The contrast agents presented in Chapters 2 and 3 can be used to image tumors and ischaemic insult, both using single energy micro-CT and in DE micro-CT. Since extravascular micro-CT relies on contrast agent localization in the tissue of interest, lower administration volumes are required, with even lower concentration requirements when performing DE micro-CT scans as presented in Chapter 4. For instance, the imaging technique presented can be used to observe the response of tumors or ischaemic tissue in the heart to therapeutic drugs.

### 5.2.3 Evaluating *In Vivo* Vessel Density

One of the main advantages of DE CT is its ability to overcome the partial volume effect, which would be especially useful to quantify microvessel density. For instance, an optimized version of the DE CT technique that is presented in Chapter 4 can be used to obtain quantitative images of gadolinium-enhanced vessels, which would represent blood vessel density. With an optimized *in vivo* longitudinal DE CT technique, the response of injured muscles to vascular endothelial growth factors can be quantified.

## 5.3 Summary

In conclusion, this thesis has described the development of a lanthanide-based nanoparticle contrast agent that can be used for *in vivo* micro-CT imaging of the mouse vasculature. The contrast agents presented can concentrate a high loading of 100 mg/mL of gadolinium for intravenous injections of mice. They introduced CT contrast enhancements of at least 245 HU for at least 30 minutes, and for as long as one hour, which well exceeds *in vivo* micro-CT scan time requirements. Moreover, although the synthesis techniques and *in vivo* scans were demonstrated using gadolinium and erbium as contrast materials, they can easily be substituted by any other lanthanide. An *in vivo* DE CT technique which can be used with any pre-clinical, gantry-based micro-CT scanner was also presented. The *in vivo* technique produced quantitative images of decomposed soft tissue, bone and gadolinium-enhanced vessels volumes, which was capable of distinguishing major vessels from surrounding bone. The long-circulating lanthanide contrast agents that were developed in this thesis, when used in combination with the DE CT technique presented, have the potential to become a powerful tool for preclinical research of the microvasculature.

## 5.4 References

- (1) Tse, J. J.; Dunmore-Buyze, J.; Drangova, M.; Holdsworth, D. W. Dual-energy computed tomography using a gantry-based preclinical cone-beam microcomputed tomography scanner. *J Med Imaging (Bellingham)* **2018**, *5*, 033503.
- (2) Butcher, N. J.; Mortimer, G. M.; Minchin, R. F. Drug delivery: unravelling the stealth effect. *Nat. Nanotechnol.* **2016**, *11*, 310-311.
- (3) Yang, Q.; Jones, S. W.; Parker, C. L.; Zamboni, W. C.; Bear, J. E.; Lai, S. K. Evading immune cell uptake and clearance requires PEG grafting at densities substantially exceeding the minimum for brush conformation. *Mol. Pharmacol.* **2014**, *11*, 1250-1258.
- (4) Suk, J. S.; Xu, Q.; Kim, N.; Hanes, J.; Ensign, L. M. PEGylation as a strategy for improving nanoparticle-based drug and gene delivery. *Adv Drug Deliv Rev* **2016**, *99*, 28-51.
- (5) Merkel, T. J.; Chen, K.; Jones, S. W.; Pandya, A. A.; Tian, S.; Napier, M. E.; Zamboni, W. E.; DeSimone, J. M. The effect of particle size on the biodistribution of low-modulus hydrogel PRINT particles. *J Control Release* **2012**, *162*, 37-44.
- (6) Zhang, L.; Cao, Z.; Li, Y.; Ella-Menye, J. R.; Bai, T.; Jiang, S. Softer zwitterionic nanogels for longer circulation and lower splenic accumulation. *ACS Nano* **2012**, *6*, 6681-6686.
- (7) Fan, B.; Gillies, E. R., Self-immolative polymers. In *Encyclopedia of polymer science and technology*, Wiley-VCH Verlag: 2015; pp 1-35.
- (8) Brachais, C. H.; Huguet, J.; Bunel, C. Synthesis, characterization and stabilization of poly(methyl glyoxylate). *Polymer* **1997**, *38*, 4959-4964.
- (9) Burel, F.; Rossignol, L.; Pontvianne, P.; Hartman, J.; Couesnon, N.; Bunel, C. Synthesis and characterization of poly(ethyl glyoxylate) – a new potentially biodegradable polymer. *epoly* **2003**, *3*.
- (10) Maeda, H. Tumor-selective delivery of macromolecular drugs via the EPR effect: background and future prospects. *Bioconjug Chem* **2010**, *21*, 797-802.
- (11) Weis, S. M. Vascular permeability in cardiovascular disease and cancer. *Curr Opin Hematol* **2008**, *15*, 243-249.
- (12) Samei, E.; Saunders, R. S.; Badea, C. T.; Ghaghada, K. B.; Hedlund, L. W.; Qi, Y.; Yuan, H.; Bentley, R. C.; Mukundan, S., Jr. Micro-CT imaging of breast tumors in rodents using a liposomal, nanoparticle contrast agent. *Int J Nanomedicine* **2009**, *4*, 277-282.
- (13) Clark, D. P.; Ghaghada, K.; Moding, E. J.; Kirsch, D. G.; Badea, C. T. In vivo characterization of tumor vasculature using iodine and gold nanoparticles and dual energy micro-CT. *Phys Med Biol* **2013**, *58*, 1683-1704.

- (14) Lundy, D. J.; Chen, K. H.; Toh, E. K.; Hsieh, P. C. Distribution of Systemically Administered Nanoparticles Reveals a Size-Dependent Effect Immediately following Cardiac Ischaemia-Reperfusion Injury. *Sci Rep* **2016**, *6*, 25613.

## Appendix A: Supporting Information for Chapter 2

### General Materials

Erbium chloride, PEG monomethyl ether (mPEG,  $M_n = 2000, 5000$ ), PEG-poly(propylene glycol)-PEG (poloxamers) (PEG<sub>76</sub>-PPG<sub>22</sub>-PEG<sub>76</sub> for  $M_n = 8400$ , PEG<sub>137</sub>-PPG<sub>34</sub>-PEG<sub>137</sub> for  $M_n = 14600$ ),  $\epsilon$ -caprolactone ( $\epsilon$ -CL), methanesulfonic acid, 1,5,7-triazabicyclo[4.4.0]dec-5-ene (TBD), diisopropylethylamine (DIPEA), benzoic acid, 1-pyrenemethanol, and 450 nm cellulose acetate membrane syringe filters were purchased from Millipore Sigma (Oakville, ON). L-lactide, ammonium fluoride, oleic acid, and 1-octadecene were purchased from Alfa Aesar (Ward Hill, MA). Sodium hydroxide, calcium hydride, methanol, hexane, tetrahydrofuran (THF), hydrochloric acid, nitric acid, and SEC grade *N,N*-dimethylformamide (DMF) were purchased from Caledon Laboratories (Georgetown, ON). Ethanol was purchased from Commercial Alcohols (Tiverton, ON). Deuterated chloroform ( $CDCl_3$ ) was purchased from Cambridge Isotope Laboratories (Andover, MA). Dry toluene was obtained from a solvent purification system, and  $\epsilon$ -CL was distilled from calcium hydride, both stored over molecular sieves. PEG was dried by heating at 110 °C for 1 hour under high vacuum immediately before use. An erbium standard with a concentration of 10,000  $\mu\text{g/mL}$  was purchased from Delta Scientific Laboratory Products Ltd. (Mississauga, ON). Spectra/Por 6 dialysis tubing (50 kDa MWCO) was obtained from Spectrum Laboratories (Rancho Dominguez, CA). Normal saline (0.9 % NaCl) was purchased from Cardinal Health (Mississauga, ON). Mouse Primary Antibody Isotype Control, which is a mouse serum mimic, fetal bovine serum (FBS), Glutamax (100X) solution Penstrep (100X), and Dulbecco's modified Eagle's medium were obtained from Invitrogen Corporation (Camarillo, CA). C57BL/6 male mice (25–30 g) were purchased from Jackson Laboratories (Bar Harbor, ME), isoflurane from Baxter Corporation (Mississauga, ON) and diphenhydramine from Sandoz (Boucherville, QC).

### General methods

The nanoparticle hydrodynamic diameters were measured by dynamic light scattering (DLS) using a Zetasizer Nano ZS instrument (Malvern Instruments Ltd, Malvern UK) at

room temperature (25°C) in a quartz cuvette (1 mg/mL). Transmission electron microscopy (TEM) was performed using a Philips CM10 (Philips, Amsterdam) using an acceleration voltage of 80 kV. A drop from a suspension of the samples in water (1 mg/mL) was deposited onto a copper grid and air-dried overnight. Samples were centrifuged in 50 mL tubes using a VWR Clinical 200 centrifuge with a 28° fixed-angle rotor. <sup>1</sup>H (400 MHz) nuclear magnetic resonance (NMR) spectra were obtained using a Varian Inova 400 spectrometer (Mississauga, ON). Chemical shifts are reported in parts per million (ppm) and were calibrated against residual solvent signals of chloroform (CDCl<sub>3</sub>, δ 7.27). Size exclusion chromatography (SEC) data were obtained using a Waters 515 pump (Waters Limited, Mississauga, ON) equipped with an Optilab rEX detector (Wyatt Technologies, Santa Barbara, CA) and two PLgel 5 μm mixed-D (300 mm × 7.5 mm) columns connected in series (Varian, Canada). Samples (5 mg/mL) dissolved in the eluent, composed of 10 mM LiBr and 1% (v/v) NEt<sub>3</sub> in DMF at 85 °C were injected (100 μL) at a flow rate of 1 mL/min and calibrated against polystyrene standards. Molecular weights are reported in g/mol. The erbium content of samples that were digested and preserved with aqua regia (2%) were measured by inductively coupled plasma mass spectrometry (ICP-MS) using the Agilent 1260 Infinity HPLC connected directly to a new Agilent 7700 Series ICP-MS (Santa Clara, CA).

## Synthesis of NaErF<sub>4</sub> nanoparticles (ErNP)

ErNP were synthesized based on a previously reported method with modifications (Figure A.1) <sup>1,2</sup>. Erbium chloride (1660 mg, 6.0 mmol, 1.0 equiv), oleic acid (90 mL), and 1-octadecene (90 mL) were magnetically stirred and subjected to high vacuum. The resulting mixture was heated to 120 °C for 1 hour, then cooled to 50 °C under argon. Ammonium fluoride (900 mg, 24.5 mmol, 4.0 equiv) and sodium hydroxide (600 mg, 15 mmol, 2.5 equiv) were dissolved in 50 mL of methanol and added dropwise to the cooled mixture. The solution was kept under the same conditions for 30 minutes. It was then heated to 65 °C under vacuum for 30 minutes to evaporate methanol, and then to 100 °C for another 30 minutes to evaporate water. High vacuum was removed and the mixture was placed under an argon atmosphere. The mixture was heated to 300 °C for 2 hours and cooled to room temperature for purification.

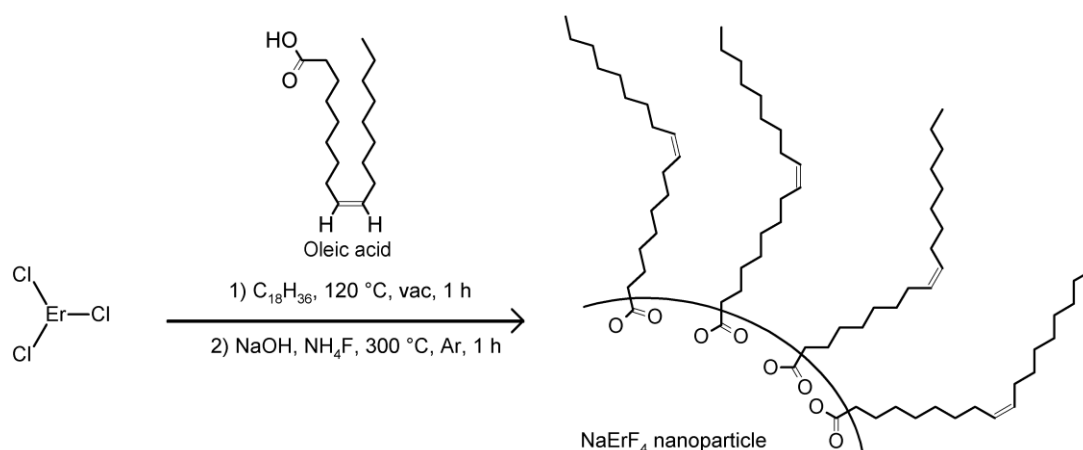


**Figure A.1** Synthesis of oleate-coated NaErF<sub>4</sub> nanoparticles.

To precipitate the nanoparticles, ethanol was added to the resulting solution at a 5:1 volume ratio and centrifuged at 6000 rpm for 30 minutes. The supernatant was decanted, the nanoparticles were redispersed in THF, and the solution was centrifuged again. Sedimented nanoparticles were dried under vacuum overnight and stored at room temperature. A 1 mg/mL sample of the nanoparticles was prepared in THF for characterization by DLS and TEM.

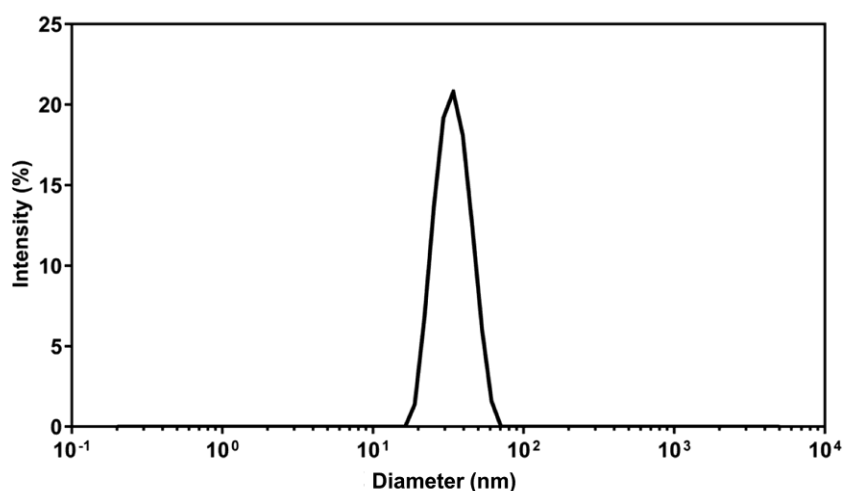


**Figure A.2** Intensity distributions of ErNP in THF measured by DLS.

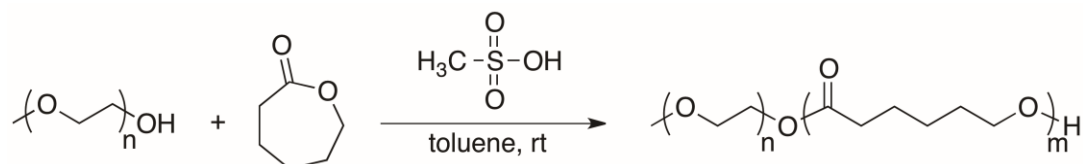
## Synthesis of PEG-PCL diblock copolymers

PEG-PCL diblock copolymers (of varying molecular weights) were synthesized via ring opening polymerization of  $\epsilon$ -CL using mPEG as an initiator (Table A.1) following a previously reported method with some modifications (Scheme A.1)<sup>3</sup>. mPEG (0.50 g) and toluene (5 mL) and were added to a flame-dried round bottom flask.  $\epsilon$ -CL and methanesulfonic acid were then added in varying ratios to obtain different polymer chain length targets. The solution was stirred for 5-6 hours at room temperature. DIPEA (32 mg, 0.25 mmol, 1.0 or 2.5 equiv) was added to quench the reaction. The solution was added to hexane (250 mL) to precipitate the resulting diblock copolymer. The supernatant was decanted and polymer precipitation was repeated twice. The polymer was dried under vacuum overnight and refrigerated. <sup>1</sup>H NMR spectroscopy and SEC were used to characterize the diblock copolymers.

**Table A.1.** Experimental details of PEG-PCL diblock copolymers synthesis.

Sample name	mPEG				$\epsilon$ -CL			methanesulfonic acid		
	M <sub>w</sub> (g/mol)	m (mg)	n (mmol)	equiv	V (mL)	n (mmol)	equiv	m (mg)	n (mmol)	equiv
PEG <sub>45</sub> -PCL <sub>20</sub>	2000	500	0.25	1.0	0.5	5.51	18.0	24	0.25	1.0
PEG <sub>45</sub> -PCL <sub>51</sub>	2000	500	0.25	1.0	1.0	9.02	36.1	13	0.25	1.0
PEG <sub>114</sub> -PCL <sub>51</sub>	5000	500	0.1	1.0	0.5	5.87	58.7	10	0.1	1.0
PEG <sub>114</sub> -PCL <sub>97</sub>	5000	500	0.1	1.0	1.0	7.22	72.2	5	0.1	1.0

**Scheme A.1.** Synthesis of PEG-PCL.



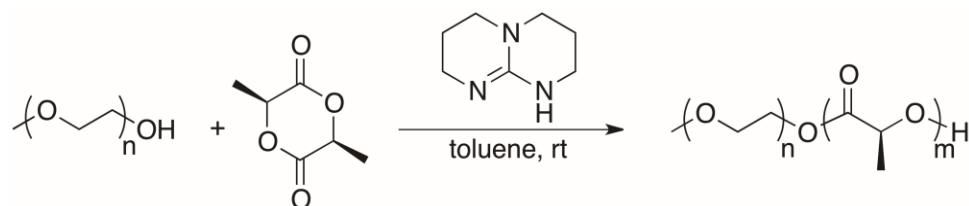
## Synthesis of PEG-PLA diblock copolymers

PEG-PLA diblock copolymers (of varying molecular weights) were synthesized via ring opening polymerization of L-lactide using mPEG as an initiator (Table A.2) following a previously reported method with some modifications (Scheme A.2) <sup>4</sup>. mPEG and toluene (5 mL) were added to a flame-dried round bottom flask. L-lactide and TBD were then added in varying ratios to obtain different polymer chain lengths. The solution was stirred for 5 minutes at room temperature. Benzoic acid (30 mg, 0.25 mmol, 1.0 or 2.5 equiv) was added to quench the reaction. After that, the solution was added to hexane (250 mL) to precipitate the resulting diblock copolymers. The supernatant was decanted and polymer precipitation was repeated twice. The polymer was dried under vacuum overnight and refrigerated. <sup>1</sup>H NMR spectroscopy and SEC were used to characterize the diblock copolymers.

**Table A.2.** Experimental details of PEG-PLA diblock copolymers synthesis.

Sample name	mPEG				L-lactide			methanesulfonic acid		
	M <sub>w</sub> (g/mol)	m (mg)	n (mmol)	equiv	m (g)	n (mmol)	equiv	m (mg)	n (mmol)	equiv
PEG <sub>45</sub> -PLA <sub>25</sub>	2000	500	0.25	1.0	0.50	4.51	18.0	24	0.25	1.0
PEG <sub>45</sub> -PLA <sub>52</sub>	2000	500	0.25	1.0	1.00	9.02	36.1	13	0.25	1.0
PEG <sub>114</sub> -PLA <sub>53</sub>	5000	500	0.1	1.0	0.65	5.87	58.7	10	0.1	1.0
PEG <sub>114</sub> -PLA <sub>122</sub>	5000	500	0.1	1.0	0.80	7.22	72.2	5	0.1	1.0

**Scheme A2.** Synthesis of PEG-PLA.



## Characterization of diblock copolymers

Data obtained from  $^1\text{H}$  NMR (Figures A.3-A.10) and SEC (Figures A.11-A.14) are summarized in Table 1. Typical signals of PEG, PCL and PLA components were utilized to calculate the molecular weights of diblock copolymers. The signal at 3.65 ppm ( $-\text{CH}_2\text{CH}_2-$ ) was assigned to the PEG block. Signals at 1.34-1.43, 1.58-1.67, 2.26-2.33 and 4.02-4.08 ppm were assigned to different methylene protons ( $-\text{CH}_2-$ ) of PCL blocks. The molar ratio of polymerized CL to PEG was determined by integrating peak intensities of methylene protons from the PEG block at 3.60-3.65 ppm and PCL block at 4.02-4.08 ppm. This was repeated for PLA where signals at 1.21-1.22, 1.56-1.61 and 5.14-5.19 ppm were assigned to the PLA block and peak integrations from the PLA block at 5.14-5.19 ppm were used to calculate the molar ratio of polymerized LA to PEG. The peaks around 2.36 and 7.15-7.30 corresponds to residual toluene (as do the peaks around the chloroform-d peak). The NMR and SEC results for all the synthesized polymers are as follows, where  $M_n^a$  is the number average molecular weight from NMR,  $M_n^b$  is the SEC-measured number average molecular weight and the dispersity from SEC is  $D$ .

PEG<sub>45</sub>-PCL<sub>20</sub>:  $^1\text{H}$  NMR ( $\text{CDCl}_3$ , 400 MHz):  $\delta$  4.06 (t,  $J = 7.0$  Hz, 40H), 3.65 (s, 182H), 2.31 (t,  $J = 7.7$  Hz, 41H), 1.64 (tt,  $J = 6.5, 13.0$  Hz, 80H), 1.34 – 1.41 (m, 41H).  $M_n^a = 4300$  g/mol. SEC:  $M_n^b = 5600$  g/mol,  $M_w = 6200$  g/mol,  $D = 1.1$ .

PEG<sub>45</sub>-PCL<sub>51</sub>:  $^1\text{H}$  NMR ( $\text{CDCl}_3$ , 400 MHz):  $\delta$  4.06 (t,  $J = 7.0$  Hz, 101H), 3.65 (s, 182H), 2.82 (s, 31H), 2.31 (t,  $J = 7.9$  Hz, 103H), 1.64 (tt,  $J = 6.5, 13.2$  Hz, 214H), 1.34 – 1.40 (m, 106H).  $M_n^a = 7800$  g/mol. SEC:  $M_n^b = 6300$  g/mol,  $M_w = 8800$  g/mol,  $D = 1.4$ .

PEG<sub>114</sub>-PCL<sub>51</sub>:  $^1\text{H}$  NMR ( $\text{CDCl}_3$ , 400 MHz):  $\delta$  4.06 (t,  $J = 6.9$  Hz, 101H), 3.65 (s, 455H), 2.40 (s, 32H), 2.31 (t,  $J = 7.9$  Hz, 128H), 1.64 (tt,  $J = 6.6, 14.5$  Hz, 258H), 1.35-1.40 (m, 133H).  $M_n^a = 10900$  g/mol. SEC:  $M_n^b = 9500$  g/mol,  $M_w = 10500$  g/mol,  $D = 1.1$ .

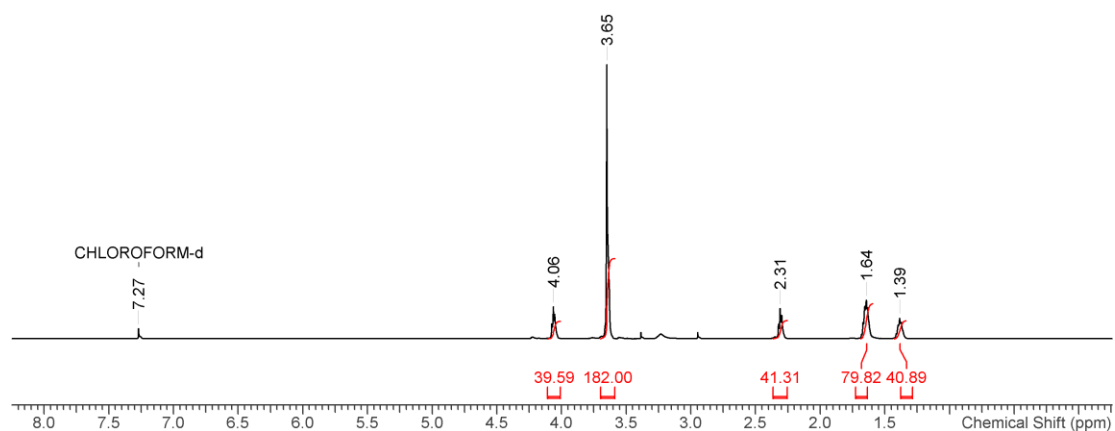
PEG<sub>114</sub>-PCL<sub>97</sub>:  $^1\text{H}$  NMR ( $\text{CDCl}_3$ , 400 MHz):  $\delta$  4.06 (t,  $J = 7.1$  Hz, 195H), 3.65 (s, 455H), 2.31 (t,  $J = 7.8$  Hz, 247H), 1.66 (tt,  $J = 6.7, 14.2$  Hz, 392H), 1.39 (tt,  $J = 7.5, 16.1$  Hz, 199H).  $M_n^a = 16100$  g/mol. SEC:  $M_n^b = 10300$  g/mol,  $M_w = 13400$  g/mol,  $D = 1.3$ .

PEG<sub>45</sub>-PLA<sub>25</sub>: <sup>1</sup>H NMR (CDCl<sub>3</sub>, 400 MHz): δ 5.17 (q, J = 8.1 Hz, 25H), 3.65 (s, 182H), 1.52 – 1.59 (m, 81H). M<sub>n</sub><sup>a</sup> = 4300 g/mol. SEC: M<sub>n</sub><sup>b</sup> = 5200 g/mol, M<sub>w</sub> = 6200 g/mol, Đ = 1.2.

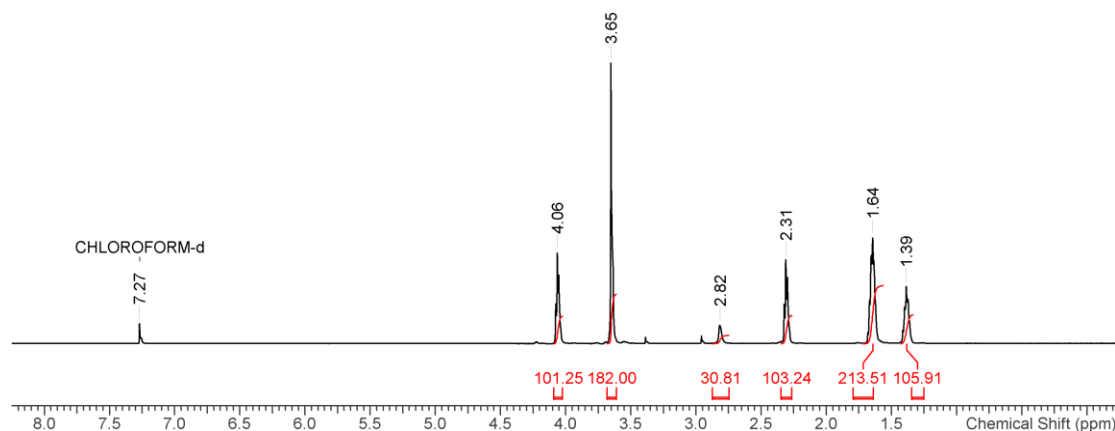
PEG<sub>45</sub>-PLA<sub>52</sub>: <sup>1</sup>H NMR (CDCl<sub>3</sub>, 400 MHz): δ 5.19 (q, J = 8.3 Hz, 52H), 3.68 (s, 182H), 1.57 – 1.63 (x, 167H). M<sub>n</sub><sup>a</sup> = 6700 g/mol. SEC: M<sub>n</sub><sup>b</sup> = 9600 g/mol, M<sub>w</sub> = 10600 g/mol, Đ = 1.1.

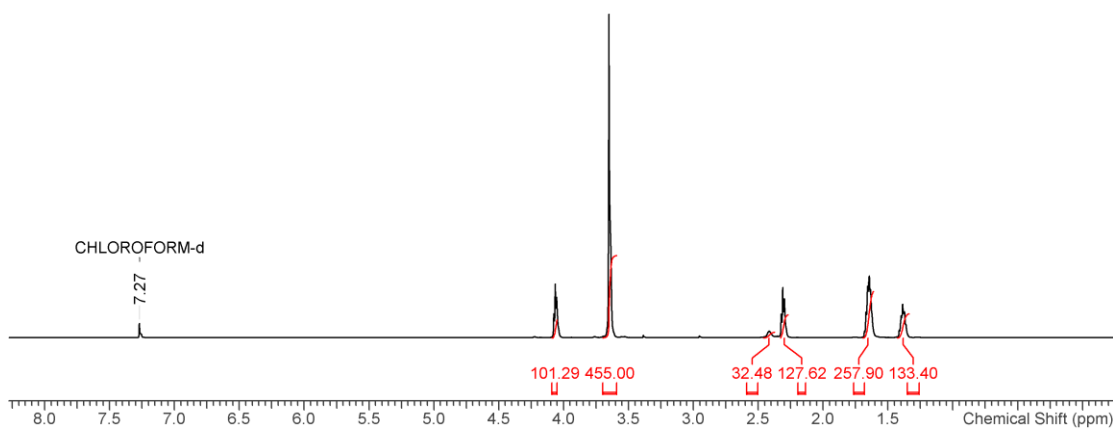
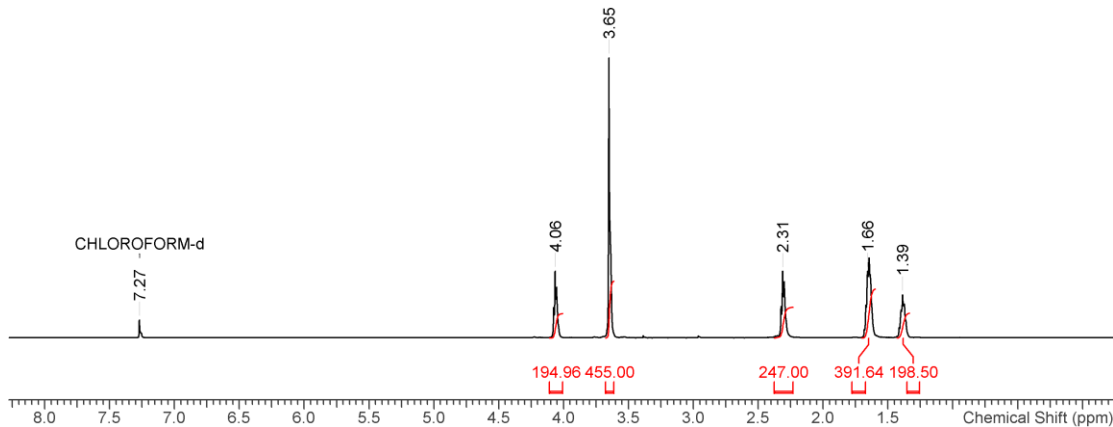
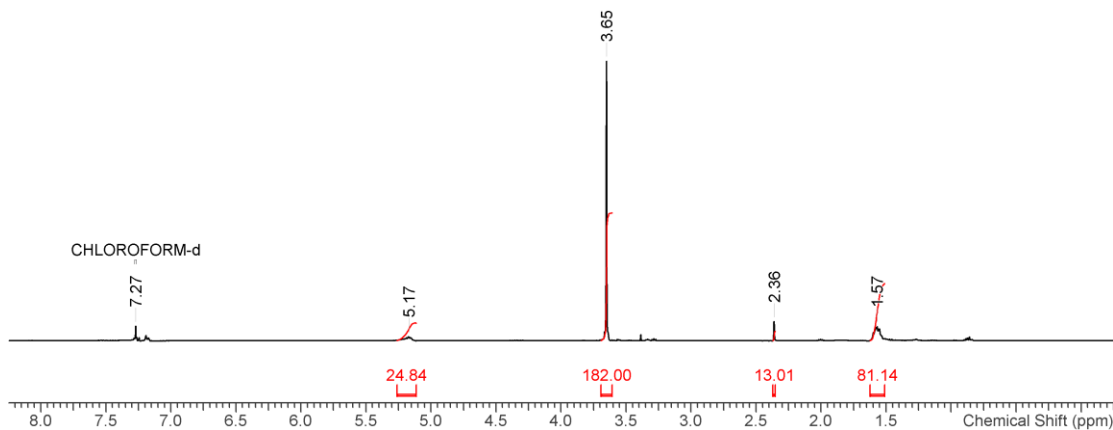
PEG<sub>114</sub>-PLA<sub>53</sub>: <sup>1</sup>H NMR (CDCl<sub>3</sub>, 400 MHz): δ 5.18 (q, J = 8.1 Hz, 53H), 3.65 (s, 455H), 1.53 – 1.60 (m, 188H). M<sub>n</sub><sup>a</sup> = 9800 g/mol. SEC: M<sub>n</sub><sup>b</sup> = 10500 g/mol, M<sub>w</sub> = 12700 g/mol, Đ = 1.3.

PEG<sub>114</sub>-PLA<sub>122</sub>: <sup>1</sup>H NMR (CDCl<sub>3</sub>, 400 MHz): δ 5.18 (q, J = 8.2 Hz, 122H), 3.65 (s, 455H), 1.53 – 1.60 (m, 417H). M<sub>n</sub><sup>a</sup> = 16000 g/mol. SEC: M<sub>n</sub><sup>b</sup> = 13500 g/mol, M<sub>w</sub> = 18900 g/mol, Đ = 1.4.



**Figure A3.** <sup>1</sup>H NMR spectrum of PEG<sub>45</sub>-PCL<sub>20</sub> (CDCl<sub>3</sub>, 400 MHz).



**Figure A4.**  $^1\text{H}$  NMR spectrum of PEG<sub>45</sub>-PCL<sub>51</sub> ( $\text{CDCl}_3$ , 400 MHz).**Figure A5.**  $^1\text{H}$  NMR spectrum of PEG<sub>114</sub>-PCL<sub>51</sub> ( $\text{CDCl}_3$ , 400 MHz).**Figure A6.**  $^1\text{H}$  NMR spectrum of PEG<sub>114</sub>-PCL<sub>97</sub> ( $\text{CDCl}_3$ , 400 MHz).

**Figure A7.**  $^1\text{H}$  NMR spectrum of PEG<sub>45</sub>-PLA<sub>25</sub> ( $\text{CDCl}_3$ , 400 MHz). Note that the polymer contains trace residual toluene.

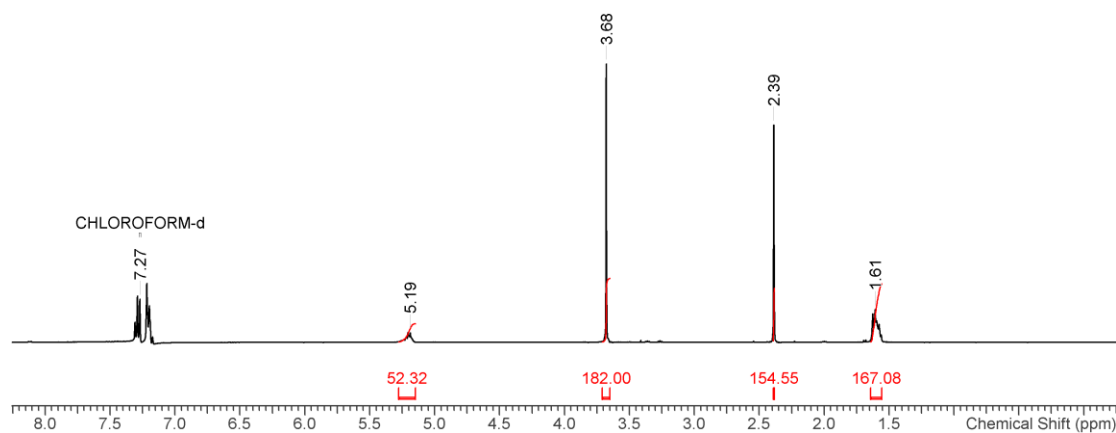


**Figure A8.**  $^1\text{H}$  NMR spectrum of PEG<sub>45</sub>-PLA<sub>52</sub> ( $\text{CDCl}_3$ , 400 MHz). Note that the polymer contains trace residual toluene.

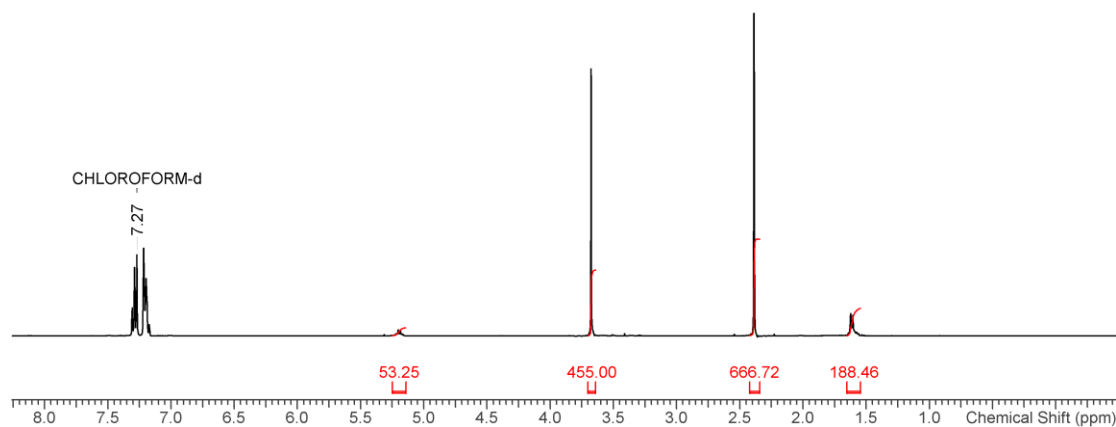


**Figure A9.**  $^1\text{H}$  NMR spectrum of PEG<sub>114</sub>-PLA<sub>53</sub> ( $\text{CDCl}_3$ , 400 MHz). Note that the polymer contains trace residual toluene.

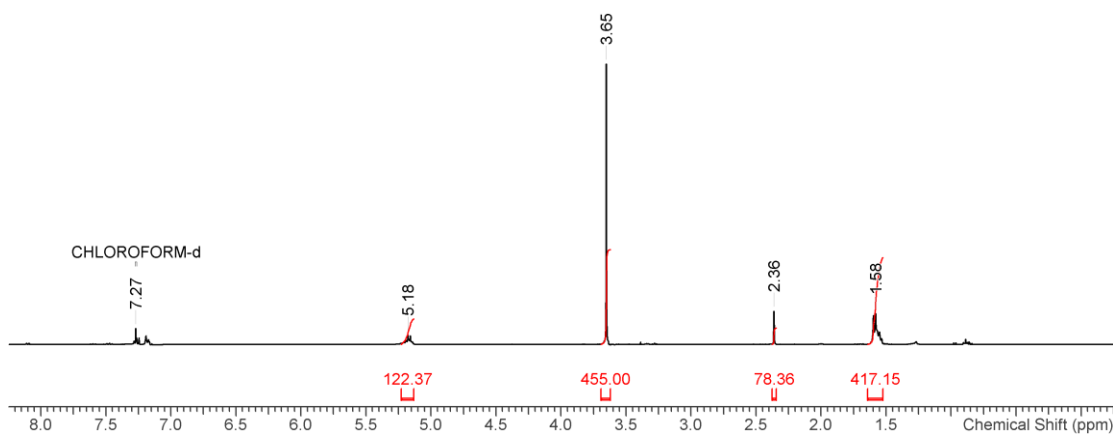


**Figure A.10.**  $^1\text{H}$  NMR spectrum of  $\text{PEG}_{114}\text{-PLA}_{122}$  ( $\text{CDCl}_3$ , 400 MHz). Note that the polymer contains trace residual toluene.

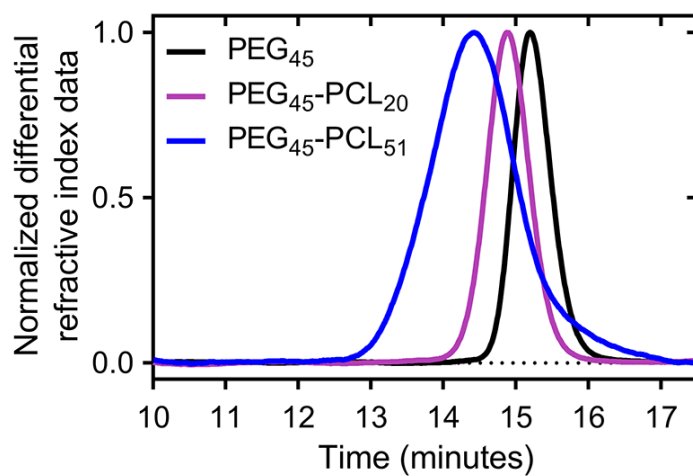


**Figure A.11.** SEC traces of the  $\text{mPEG}_{45}$  ( $M_n = 3900$  g/mol,  $D = 1.1$ ) initiator,  $\text{PEG}_{45}\text{-PCL}_{20}$  ( $M_n = 5600$  g/mol,  $D = 1.1$ ) and  $\text{PEG}_{45}\text{-PCL}_{51}$  ( $M_n = 6300$  g/mol,  $D = 1.4$ ).

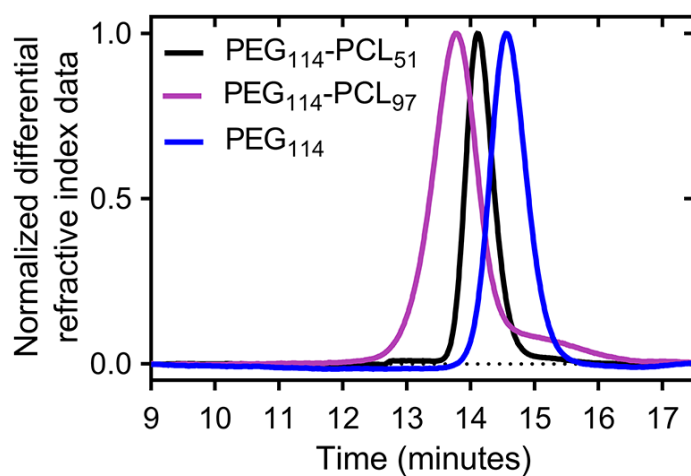


**Figure A.12.** SEC of the PEG<sub>114</sub> ( $M_n = 7100$  g/mol,  $D = 1.1$ ) initiator, PEG<sub>114</sub>-PCL<sub>51</sub> ( $M_n = 9500$  g/mol,  $D = 1.1$ ) and PEG<sub>114</sub>-PCL<sub>97</sub> ( $M_n = 10300$  g/mol,  $D = 1.3$ ).

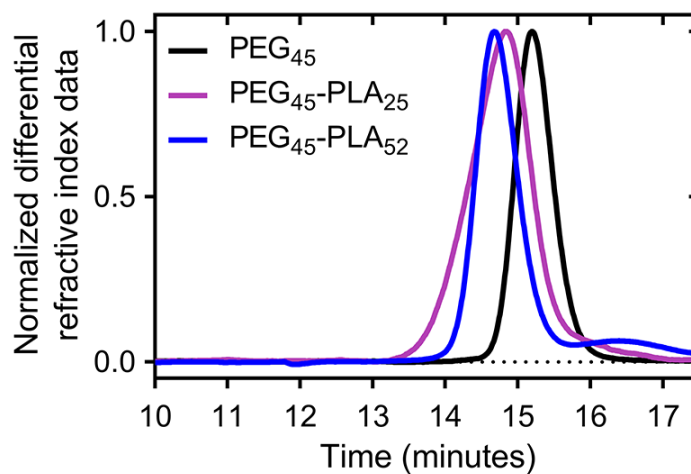


**Figure A.13.** SEC of the PEG<sub>45</sub> ( $M_n = 3900$  g/mol,  $D = 1.1$ ) initiator, PEG<sub>45</sub>-PLA<sub>25</sub> ( $M_n = 5200$  g/mol,  $D = 1.2$ ) and PEG<sub>45</sub>-PLA<sub>52</sub> ( $M_n = 9600$  g/mol,  $D = 1.1$ ).

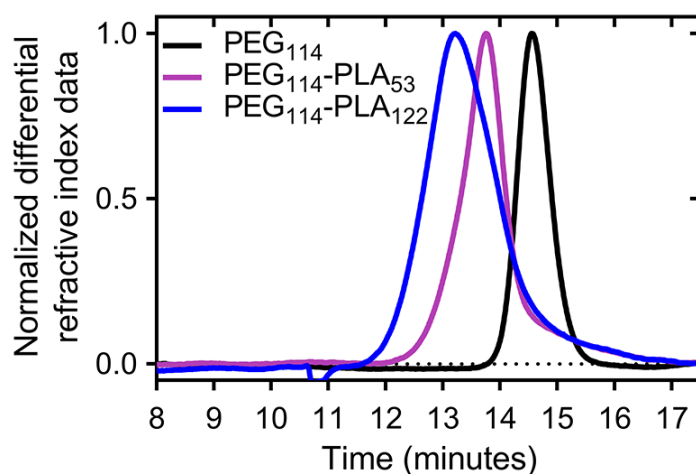


**Figure A.14.** SEC of the PEG<sub>114</sub> ( $M_n = 7100$  g/mol,  $D = 1.1$ ) initiator, PEG<sub>114</sub>-PLA<sub>53</sub> ( $M_n = 10500$  g/mol,  $D = 1.3$ ) and PEG<sub>114</sub>-PLA<sub>122</sub> ( $M_n = 13500$  g/mol,  $D = 1.4$ ).

### Self-assembly of polymeric nanoparticles (without ErNP) via nanoprecipitation

In 0.2 mL of THF, 8 mg of copolymer were dissolved. The solution was then added dropwise to 1.8 mL of deionized water under magnetic stirring. After 1 hour, stirring was stopped and the solution was left uncapped for 12 hours to allow for organic solvent evaporation. The solutions were dialyzed against 100 mL of deionized water for 2 days with 5 solvent changes. A 450 nm syringe filter was used to separate large aggregates and the samples were characterized by DLS (Figure A.15) and TEM (Figure A.16).

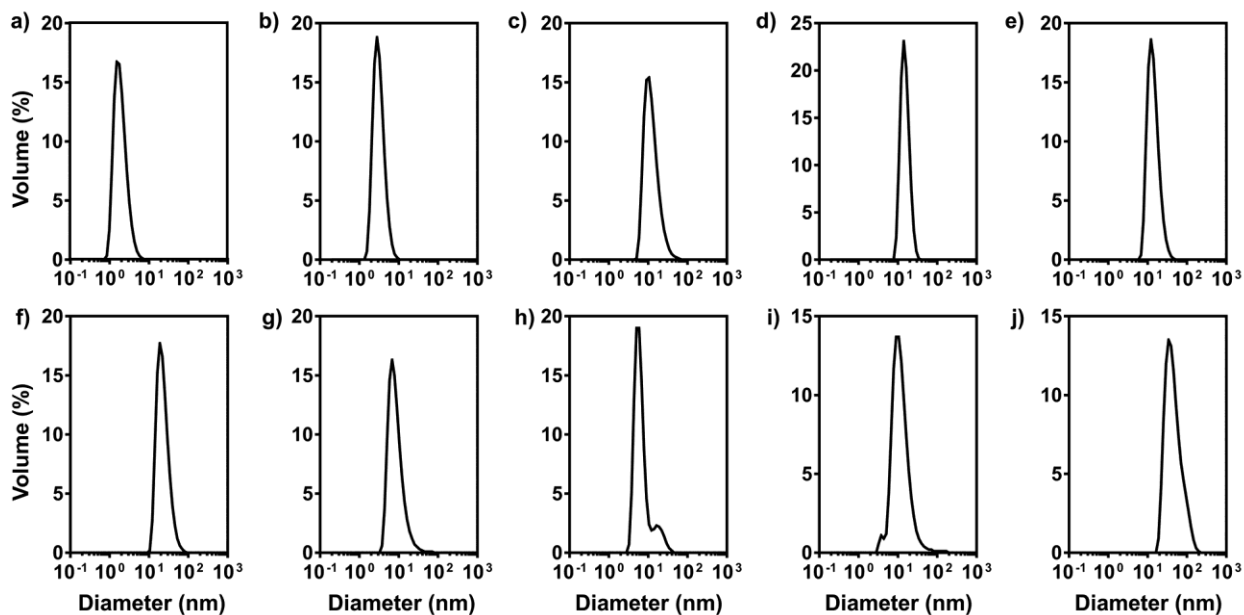


**Figure A.15.** Volume diameter distributions of polymeric nanoparticles prepared using a) PEG<sub>76</sub>-PPG<sub>22</sub>-PEG<sub>76</sub>, b) PEG<sub>137</sub>-PPG<sub>34</sub>-PEG<sub>137</sub>, c) PEG<sub>45</sub>-PCL<sub>20</sub>, d) PEG<sub>45</sub>-PCL<sub>51</sub>, e) PEG<sub>114</sub>-PCL<sub>51</sub>, f) PEG<sub>114</sub>-PCL<sub>97</sub>, g) PEG<sub>45</sub>-PLA<sub>25</sub>, h) PEG<sub>45</sub>-PLA<sub>52</sub>, i) PEG<sub>114</sub>-PLA<sub>53</sub>, and j) PEG<sub>114</sub>-PLA<sub>122</sub>, as measured by DLS.

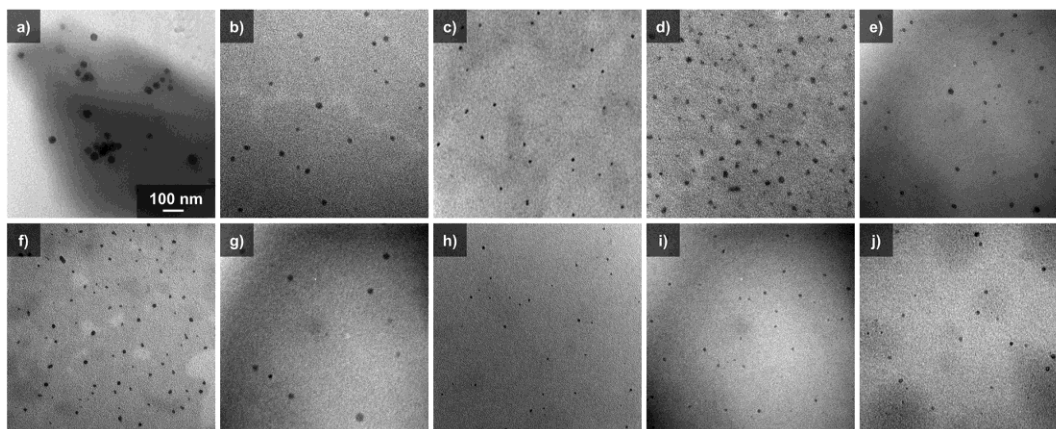


**Figure A.16.** TEM images of assemblies prepared from a) PEG<sub>76</sub>-PPG<sub>22</sub>-PEG<sub>76</sub>, b) PEG<sub>137</sub>-PPG<sub>34</sub>-PEG<sub>137</sub>, c) PEG<sub>45</sub>-PCL<sub>20</sub>, d) PEG<sub>45</sub>-PCL<sub>51</sub>, e) PEG<sub>114</sub>-PCL<sub>51</sub>, f) PEG<sub>114</sub>-PCL<sub>97</sub>, g) PEG<sub>45</sub>-PLA<sub>25</sub>, h) PEG<sub>45</sub>-PLA<sub>52</sub>, i) PEG<sub>114</sub>-PLA<sub>53</sub>, and j) PEG<sub>114</sub>-PLA<sub>122</sub>.

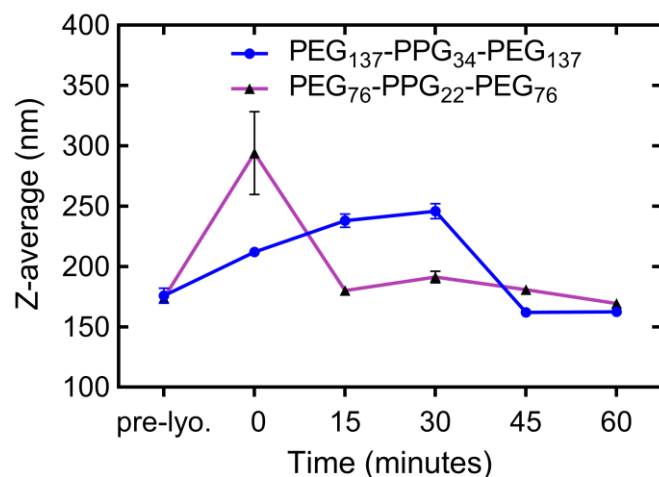


**Figure A.17.** The colloidal stability of the PEG-PPG-PEG-encapsulated ErNP. The PEG<sub>76</sub>-PPG<sub>22</sub>-PEG<sub>76</sub> assemblies, which had a Z-average hydrodynamic diameter of  $174 \pm 4$  nm redispersed in saline at a diameter of  $294 \pm 34$  nm, while the PEG<sub>137</sub>-PPG<sub>34</sub>-PEG<sub>137</sub> assemblies, which had an initial diameter of  $176 \pm 6$  nm in size redispersed at  $212 \pm 2$  nm. Although a larger increase in size was observed initially with the PEG<sub>76</sub>-PPG<sub>22</sub>-PEG<sub>76</sub> assemblies, the hydrodynamic diameter of both samples fluctuated around 200 nm for up to 60 minutes.

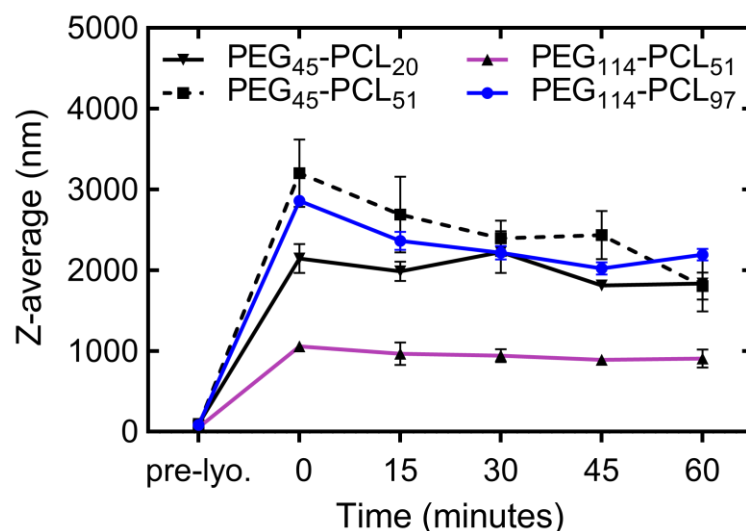


**Figure A.18.** The colloidal stability of the PEG-PCL-encapsulated ErNP. All assemblies redispersed in saline as micron-sized particles.

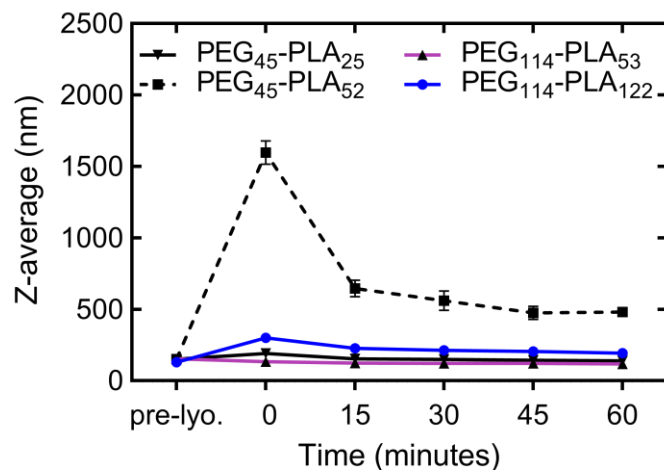


**Figure A.19.** The colloidal stability of the PEG-PLA-encapsulated ErNP. The PEG<sub>45</sub>-PLA<sub>52</sub> and PEG<sub>114</sub>-PCL<sub>122</sub> encapsulations redispersed saline at larger diameters. The PEG<sub>45</sub>-PLA<sub>25</sub> and PEG<sub>114</sub>-PCL<sub>53</sub> encapsulations maintained their hydrodynamic diameters after dispersion in saline and remained stable for 60 minutes.

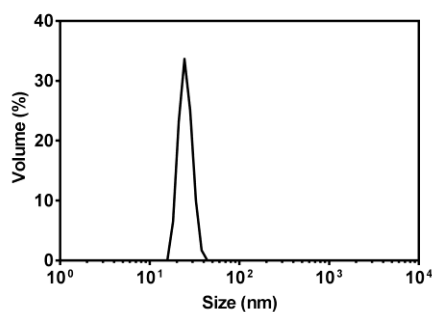


**Figure A20.** DLS volume distribution of diameters for the mouse serum mimic alone, without any assemblies. The instrument reported that the data quality was not good due to the count rate being too low. This suggested that the proteins in the serum mimic would have minimal interference in the analysis of the assemblies (Figure A21).

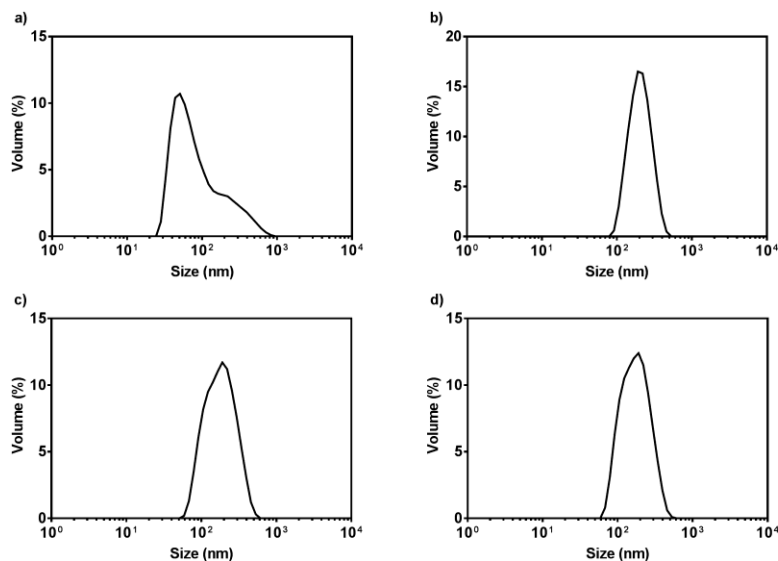


**Figure A21.** DLS volume distributions of diameters for the polymer-encapsulated ErNP in a mouse serum mimic. The PEG<sub>114</sub>-PLA<sub>53</sub>:ErNP ratios are a) 4:1, b) 2:1, c) 1:1 and d) 0.5:1.

## Critical aggregation concentration measurements

The critical aggregation concentrations (CAC) of the 1:1 and 0.5:1 PEG<sub>114</sub>-PLA<sub>53</sub>:ErNP assemblies were determined using pyrene as the fluorescent probe.<sup>5</sup> The assemblies were prepared as described in the manuscript with and without ErNP. Each suspension was lyophilized and redispersed in 0.1 M, pH 7.4 phosphate buffer at a polymer concentration of 1 mg/mL. The resulting solution was diluted to prepare concentrations from 0.001 - 1 mg/mL of polymer. Each of these solutions (1 mL) was added to a vial containing 0.025 mg of pyrene, and was incubated for 20 h at 37 °C. The fluorescence emission spectrum (350-700 nm) of each solution was obtained using an excitation wavelength of 334 nm. The emission intensities of the first vibronic band ( $I_1$ ) of pyrene at 371 nm and its third vibronic band ( $I_3$ ) at 382 nm were obtained and the  $I_1/I_3$  ratio was plotted against  $\log_{10}[\text{concentration (mg/L)}]$  to give a sigmoidal curve. The CAC was determined to be the point of intersection between the horizontal linear segment at low concentration and the linear region of negative slope.

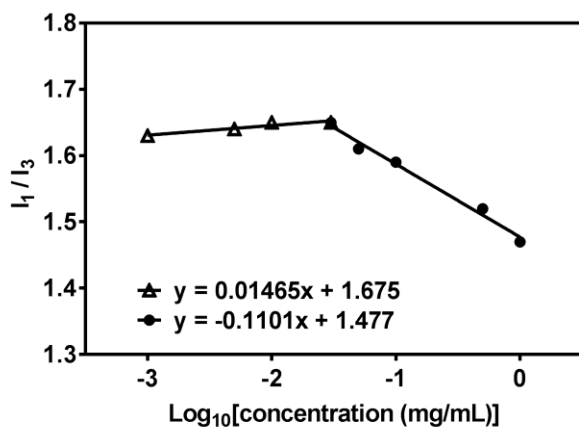


**Figure A22.** Ratio of the emission intensities ( $I_1/I_3$ ) versus  $\text{Log}_{10}$  of the polymer concentration in mg/mL for the PEG<sub>114</sub>-PLA<sub>53</sub> only assembly. The CAC was determined to be at 0.026 mg/mL.

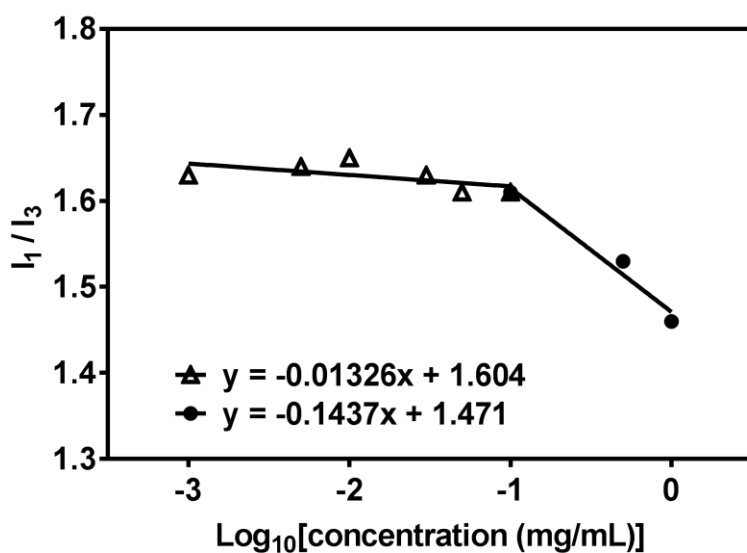


**Figure A23.** Ratio of the emission intensities ( $I_1/I_3$ ) versus  $\text{Log}_{10}$  of the polymer concentration in mg/mL for the 1:1 PEG<sub>114</sub>-PLA<sub>53</sub>:ErNP ratio. The CAC was determined to be at 0.096 mg/mL.

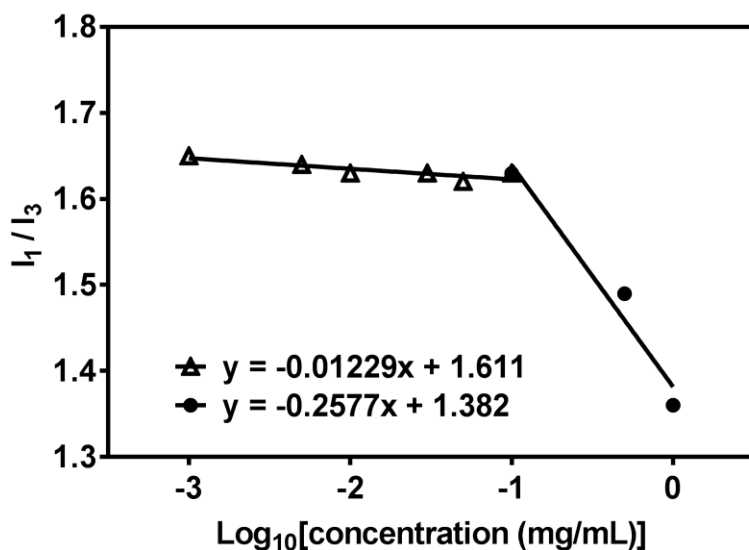


**Figure A24.** Ratio of the emission intensities ( $I_1/I_3$ ) versus  $\text{Log}_{10}$  of the polymer concentration in mg/mL for the 0.5:1 PEG<sub>114</sub>-PLA<sub>53</sub>:ErNP ratio. The CAC was determined to be at 0.117 mg/mL.

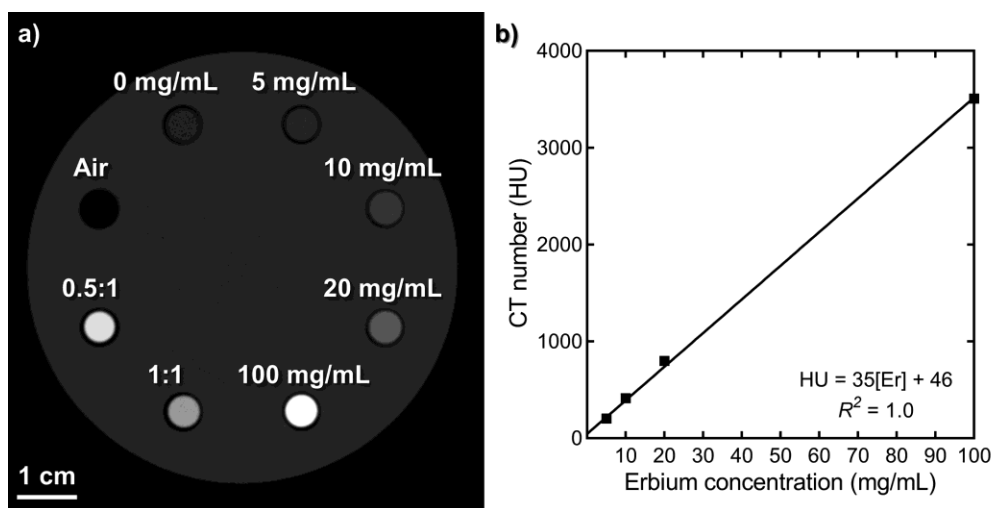


**Figure A25.** (a) Micro-CT image (at 80 kVp) of calibration standards containing known concentrations of erbium chloride, which were used to determine the erbium content of the 0.5:1 and 1:1 PEG<sub>114</sub>-PCL<sub>53</sub>:ErNP formulations. (b) Measured CT number vs. known erbium concentration.

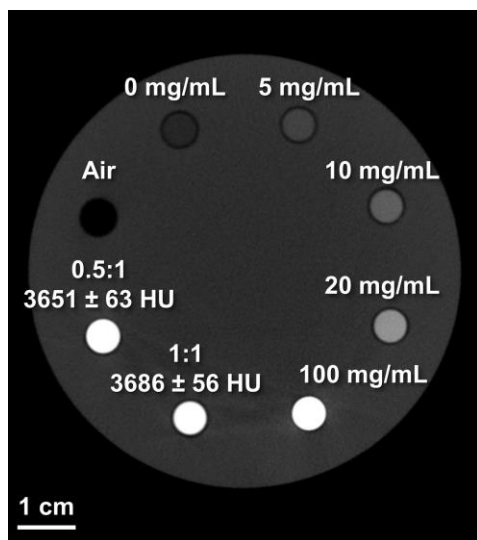


**Figure A26.** Micro-CT image (at 80 kVp) of the erbium calibration standards and the concentrated 0.5:1 and 1:1 PEG<sub>114</sub>-PCL<sub>53</sub>:ErNP formulations. The CT numbers of the concentrated solutions verified the suspension of over 100 mg/mL of erbium in each of the formulations.

## Cell viability assay

C2C12 mouse myoblast cells were seeded in a Nunclon 96-well U-bottom transparent polystyrol plate to obtain approximately 10,000 cells/well in 100  $\mu$ L of Dulbecco's modified Eagle's medium containing serum, glutamax, and antibiotics. The cells were allowed to adhere to the plate in a 5% CO<sub>2</sub> incubator at 37 °C for 24 h. The growth medium was then aspirated and replaced with either solutions of sodium dodecyl sulfate (SDS) in the cell culture medium at concentrations of 0.2, 0.15, 0.10, or 0.05 mg/mL, which were used as positive controls, serial dilutions of the contrast agent, or fresh medium. The cells were then incubated at 37°C (5% CO<sub>2</sub>) for 24 h. The medium was again aspirated and replaced with 110  $\mu$ L of fresh medium containing 0.5 mg/mL (3-(4,5-dimethylthiazol-2-yl)-2,5-diphenyltetrazolium bromide) (MTT). After 4 h of incubation (37°C, 5% CO<sub>2</sub>), the MTT solution was carefully aspirated and the purple crystals were dissolved by addition of 50  $\mu$ L of spectroscopic grade dimethyl sulfoxide (DMSO). After shaking (1 s, 2 mm amp, 654 rpm), the absorbance of the wells at 540 nm was read using an M1000-Pro plate reader (Tecan). The absorbance of wells prepared in the same way but without cells was subtracted as a background and the cell viability was calculated relative to wells containing

cells that were exposed only to the culture medium. Cell viability was detected for cells exposed to only to the lowest concentrations of SDS, confirming the sensitivity of the assay.

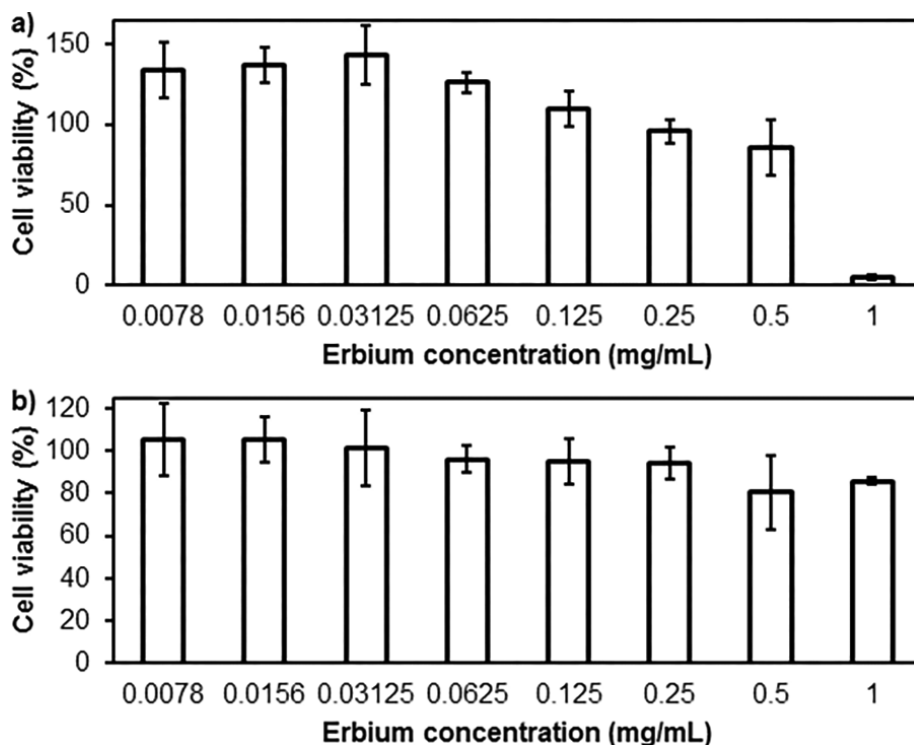


**Figure A27.** *In vitro* toxicity as determined by the MTT assay of the contrast agent formulated with a) 1:1 and b) 0.5:1 polymer to erbium mass ratios.

### *In Vivo* reaction test in subcutaneous tissue

C57BL/6 mice (25-30 g) were injected with 0.2 mL of the 1:1 (n = 2) and 0.5:1 (n = 2) mass ratio formulations of the contrast agent. These animals were scanned before contrast agent administration, and 2 minutes and two weeks post-injection. The animals were scanned using general micro-CT imaging and analysis methods as described in the manuscript. Representative images of a mouse from each group are shown in Figure A29. Both formulations of the contrast agent localized near the injection site for up to two weeks after injection. The animals were sacrificed at the two week timepoint for subcutaneous and dermal tissue gross examination (Figure A30). Both the dermal and subcutaneous tissue appeared normal.

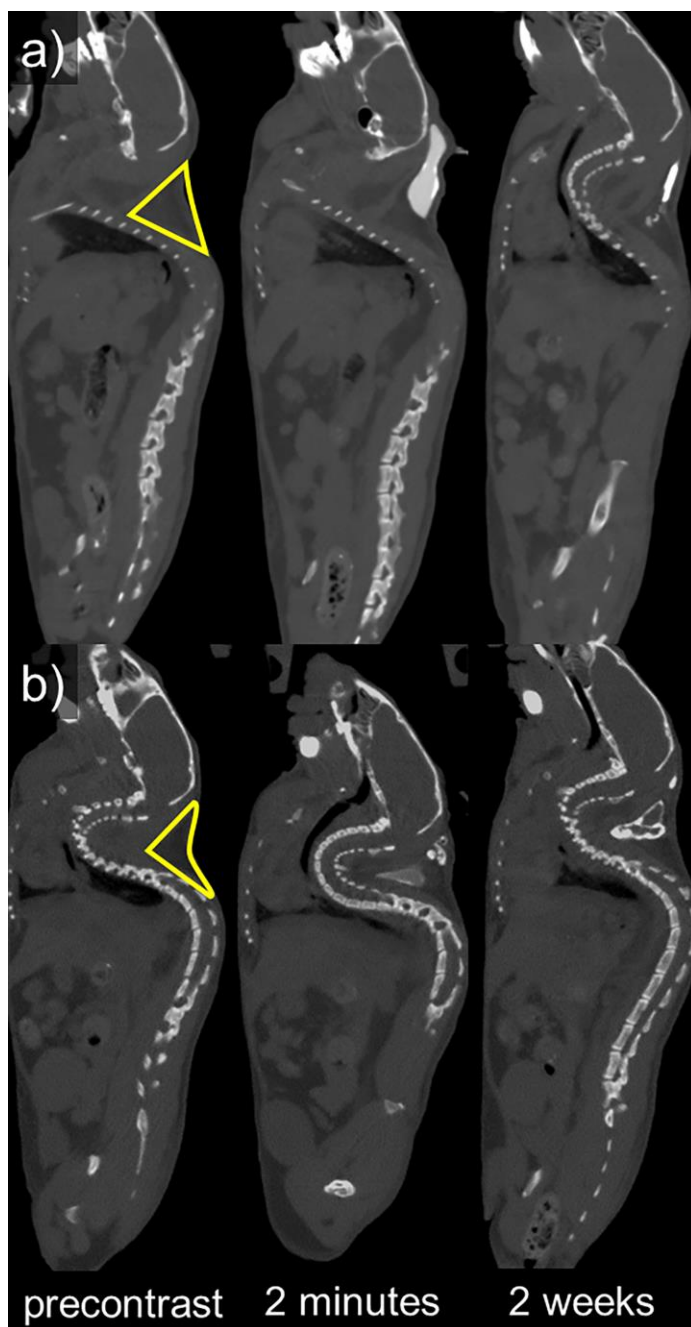


**Figure A28.** Representative sagittal micro-CT images showing mice that received contrast agent formulated at a) 1:1 and b) 0.5:1 PEG<sub>114</sub>-PLA<sub>53</sub>:ErNP mass ratios subcutaneously. The location of the injection site (subcutaneous tissue) is outlined in the precontrast image.

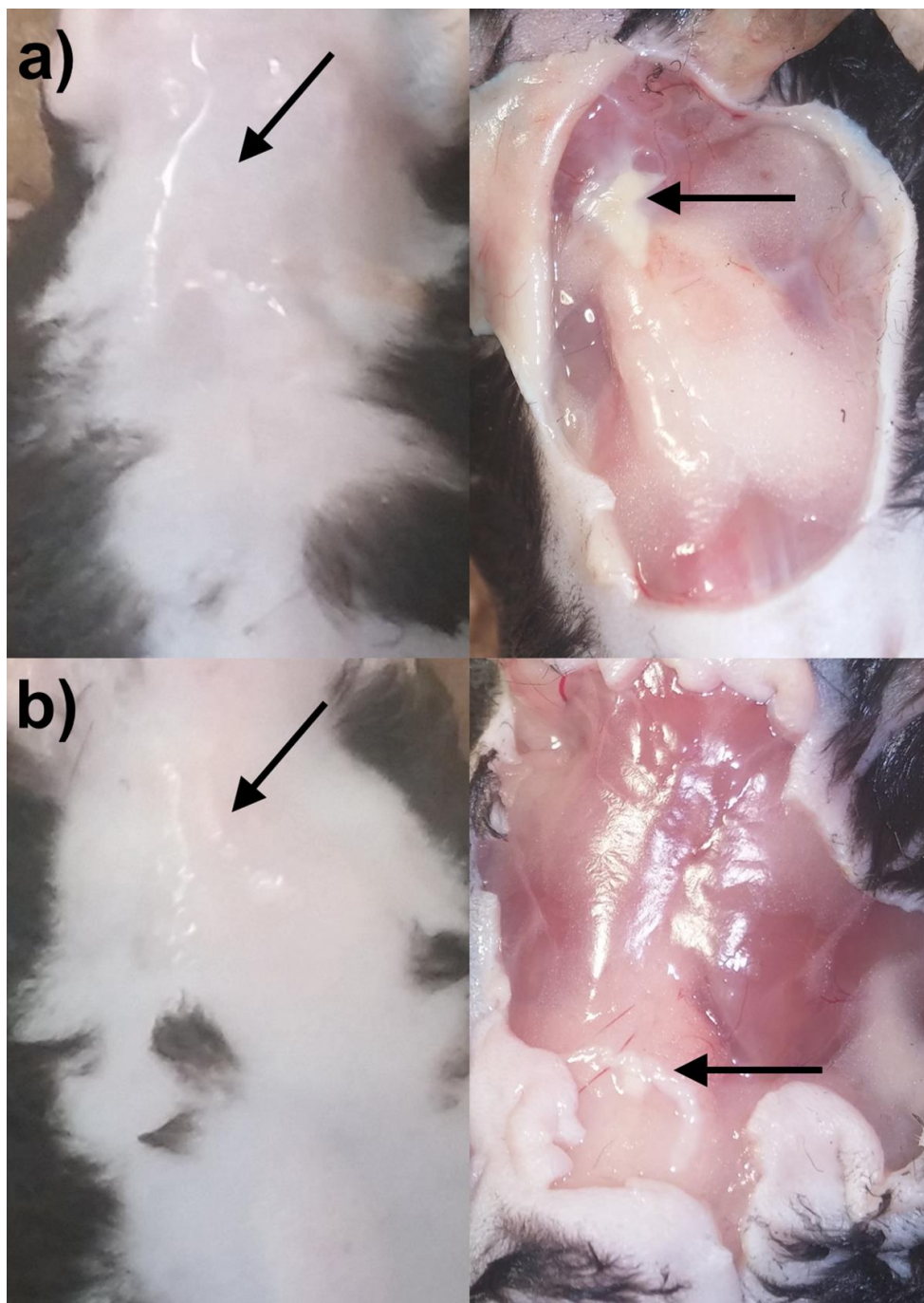


**Figure A29.** Dermal (left) and subcutaneous (right) tissue of mice that received contrast agent formulated at a) 1:1 and b) 0.5:1 PEG<sub>114</sub>-PLA<sub>53</sub>:ErNP mass ratios. The arrows indicate the injection site and contrast agent localization.

## References

- (1) Li, Z.; Zhang, Y. An efficient and user-friendly method for the synthesis of hexagonal-phase NaYF<sub>4</sub>:Yb, Er/Tm nanocrystals with controllable shape and upconversion fluorescence. *Nanotechnology* **2008**, *19*, 345606-345610.
- (2) Zhao, G.; Tong, L.; Cao, P.; Nitz, M.; Winnik, M. A. Functional PEG-PAMAM-tetraphosphonate capped NaLnF<sub>4</sub> nanoparticles and their colloidal stability in phosphate buffer. *Langmuir* **2014**, *30*, 6980-6989.
- (3) Couffin, A.; Delcroix, D.; Martín-Vaca, B.; Bourissou, D.; Navarro, C. Mild and efficient preparation of block and gradient copolymers by methanesulfonic acid catalyzed ring-opening polymerization of caprolactone and trimethylene carbonate. *Macromolecules* **2013**, *46*, 4354-4360.
- (4) Lohmeijer, B.; Pratt, R.; Leibfarth, F.; Logan, J.; Long, D.; Dove, A.; Nederberg, F.; Choi, J.; Wade, C.; Waymouth, R.; Hedrick, J. Guanidine and amidine organocatalysts for ring-opening polymerization of cyclic esters. *Macromolecules* **2006**, *39*, 8574-8583.
- (5) Basu Ray, G.; Chakraborty, I.; Moulik, S. P. Pyrene absorption can be a convenient method for probing critical micellar concentration (cmc) and indexing micellar polarity. *J. Colloid. Interface. Sci.* **2006**, *294*, 248-254.

## Appendix B: Supporting Information for Chapter 3

### General Materials

Gadolinium chloride hexahydrate, PEG monomethyl ether (mPEG,  $M_n = 1000, 2000, 5000$ ), and 450 nm cellulose acetate membrane syringe filters were purchased from Millipore Sigma (Oakville, ON). Sterile disposable filter units 450 nm pore size were purchased from ThermoFisher Scientific (Ottawa, ON). Ammonium fluoride, oleic acid, 1-octadecene, and phosphoryl trichloride were purchased from Alfa Aesar (Ward Hill, MA). Sodium hydroxide, hexane, tetrahydrofuran (THF), hydrochloric acid, and nitric acid were purchased from Caledon Laboratories (Georgetown, ON). Ethanol was purchased from Commercial Alcohols (Tiverton, ON). Dry toluene was obtained from a solvent purification system and was stored over molecular sieves. PEG was dried by heating at 110 °C for 1 hour under high vacuum immediately before use. A gadolinium standard with a concentration of 10,000 µg/mL was purchased from Delta Scientific Laboratory Products Ltd. (Mississauga, ON). Spectra/Por 6 dialysis tubing (50 kDa MWCO) was obtained from Spectrum Laboratories (Rancho Dominguez, CA). Normal saline (0.9 % NaCl) was purchased from Cardinal Health (Mississauga, ON). Mouse Primary Antibody Isotype Control, which is a mouse serum mimic, fetal bovine serum (FBS), Glutamax (100X) solution Penstrep (100X), and Dulbecco's modified Eagle's medium were obtained from Invitrogen Corporation (Camarillo, CA). C57BL/6 male mice (25–30 g) were purchased from Jackson Laboratories (Bar Harbor, ME), and isoflurane from Baxter Corporation (Mississauga, ON).

### General characterization methods

The nanoparticle hydrodynamic diameters were measured by dynamic light scattering (DLS) using a Zetasizer Nano ZS instrument (Malvern Instruments Ltd, Malvern UK) at room temperature (37°C) in a quartz cuvette (1 mg/mL). Transmission electron microscopy (TEM) was performed using a Philips CM10 (Philips, Amsterdam) using an acceleration voltage of 80 kV. A drop from a suspension of the samples in cyclohexane or water (1 mg/mL) was deposited onto a copper grid and air-dried overnight. Samples were

centrifuged in 50 mL tubes using a VWR Clinical 200 centrifuge with a 28° fixed-angle rotor. The gadolinium content of samples that were digested and preserved with aqua regia<sup>1</sup> (2%) were measured by inductively coupled plasma mass spectrometry (ICP-MS) using the Agilent 1260 Infinity HPLC connected directly to a new Agilent 7700 Series ICP-MS (Santa Clara, CA).

## Synthesis of gadolinium nanoparticles (GdNP)

Specifically, the GdNP in this study are NaGdF<sub>4</sub> nanocrystals and were synthesized based on a previously reported method with some modifications.<sup>2, 3</sup> Gadolinium chloride hexahydrate (2230 mg, 6.0 mmol, 1.0 equiv), oleic acid (90 mL), and 1-octadecene (90 mL) were magnetically stirred and subjected to high vacuum. The resulting mixture was heated to 120°C for 1 hour, then cooled to 50 °C under argon. Ammonium fluoride (900 mg, 24.5 mmol, 4.0 equiv) and sodium hydroxide (600 mg, 15 mmol, 2.5 equiv) were dissolved in 50 mL of methanol and added dropwise to the cooled mixture. The solution was kept under the same conditions for 30 minutes. It was then heated to 65 °C under vacuum for 30 minutes to evaporate methanol, and then to 100 °C for another 30 minutes to evaporate water. High vacuum was removed, and the mixture was placed under an argon atmosphere. The mixture was heated to 300 °C for 2 hours and cooled to room temperature for purification.

To precipitate the nanoparticles, ethanol was added to the resulting solution at a 5:1 volume ratio and centrifuged at 6000 rpm for 30 minutes. The supernatant was decanted, the nanoparticles were redispersed in THF, and the solution was centrifuged again. Sedimented nanoparticles were dried under vacuum overnight and stored at room temperature. A 1 mg/mL sample of the nanoparticles was prepared in cyclohexane for characterization by DLS and TEM.

## Purification of PEG-coated nanoparticles

The solution containing PEG-coated GdNP were dialyzed against 4 L of milliQ water over 24 hours, with 5 dialysate changes. The resulting solution was filtered *via* sterile vacuum filtration (450 nm pore size), and then lyophilized.

## Linear regression of CT contrast and gadolinium concentration

The relationship between CT contrast and gadolinium concentration was first confirmed by micro-CT. Gadolinium chloride was diluted in saline at gadolinium concentrations of 5, 10, 15 and 100 mg/mL, which acted as calibration standards. The dried contrast agent was dissolved in saline to contain 100 mg/mL of gadolinium; the mass of dried contrast agent required to obtain 100 mg/mL of gadolinium was determined from ICP-MS data. The linear regression between CT contrast (in HU) and gadolinium concentration was then used to calculate the gadolinium content of the contrast agent.

## Cell viability assay

C2C12 mouse myoblast cells were seeded in a Nunclon 96-well U-bottom transparent polystyrol plate to obtain approximately 10,000 cells/well in 100  $\mu$ L of Dulbecco's modified Eagle's medium containing serum, glutamax, and antibiotics. The cells were allowed to adhere to the plate in a 5% CO<sub>2</sub> incubator at 37 °C for 24 h. The growth medium was then aspirated and replaced with either solutions of sodium dodecyl sulfate (SDS) in the cell culture medium at concentrations of 0.2, 0.15, 0.10, or 0.05 mg/mL, which were used as positive controls, serial dilutions of the contrast agent, or fresh medium. The cells were then incubated at 37°C (5% CO<sub>2</sub>) for 24 h. The medium was again aspirated and replaced with 110  $\mu$ L of fresh medium containing 0.5 mg/mL (3-(4,5-dimethylthiazol-2-yl)-2,5-diphenyltetrazolium bromide) (MTT). After 4 h of incubation (37°C, 5% CO<sub>2</sub>), the MTT solution was carefully aspirated and the purple crystals were dissolved by addition of 50  $\mu$ L of spectroscopic grade dimethyl sulfoxide (DMSO). After shaking (1 s, 2 mm amp, 654 rpm), the absorbance of the wells at 540 nm was read using an M1000-Pro plate reader (Tecan). The absorbance of wells prepared in the same way but without cells was subtracted as a background and the cell viability was calculated relative to wells containing cells that were exposed only to the culture medium. Cell viability was detected for cells exposed to only to the lowest concentrations of SDS, confirming the sensitivity of the assay.

## *In vivo* reaction test in subcutaneous tissue

C57BL/6 mice (25-32 g) were injected with 0.2 mL of saline (n=2), PPEG<sub>2000</sub>-GdNP (n=2), or PPEG<sub>5000</sub>-PPEG<sub>1000</sub>-GdNP (n=2) subcutaneously, in the dorsal interscapular region. These animals were scanned immediately after injection, and two weeks after. The animals were scanned using general micro-CT imaging and analysis methods as described in the manuscript. Representative images of a mouse from each group are shown in Figure B.3. While both formulations of the contrast agent localized near the injection site for up to two weeks, lower contrast was visualized at the two-week timepoint, suggesting clearance of the contrast agent over time. after injection. The animals were sacrificed at the two-week timepoint for subcutaneous, dermal tissue and clearance organs gross examination. All tissues appeared normal.

## Supplementary Results

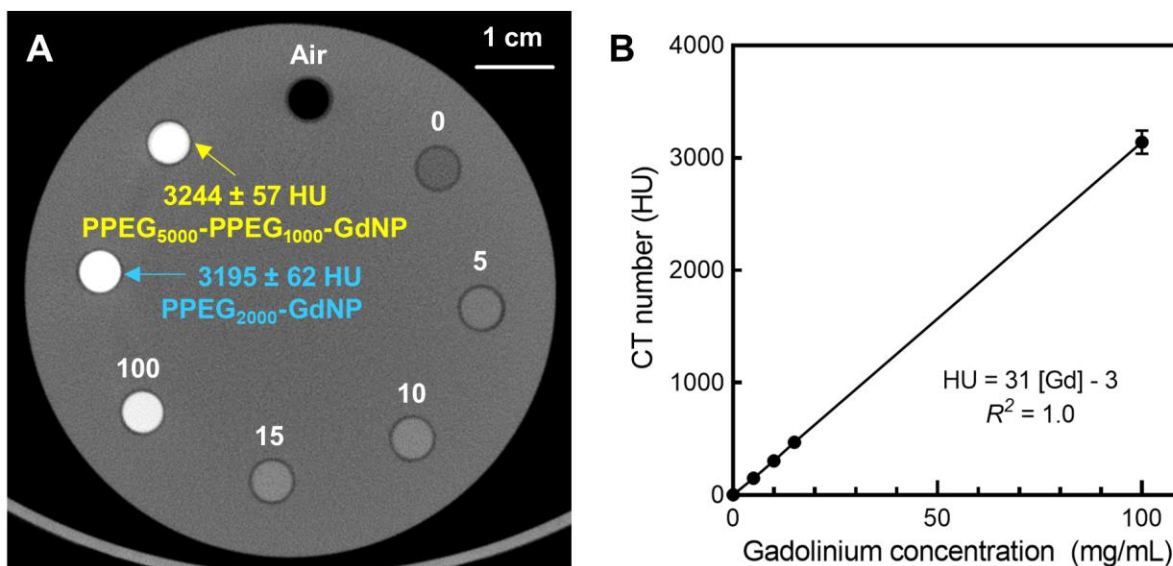


**Figure B.1.** A) Micro-CT image (at 80 kVp) of calibration standards containing known concentrations of gadolinium chloride, which were used to determine the gadolinium content of the PPEG<sub>2000</sub>-GdNP and PPEG<sub>5000</sub>-PPEG<sub>1000</sub>-GdNP. B) Measured CT number vs. known gadolinium concentration. The CT numbers of the concentrated solutions verified the suspension of 100 mg/mL of gadolinium in each of the formulations. C) *In vitro* cell viability as determined by MTT assay. No effect on viability was observed.

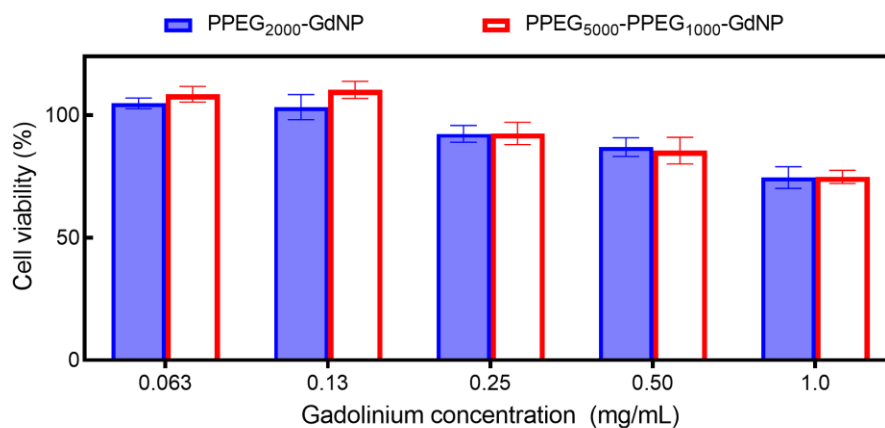


**Figure B.2.** *In vitro* toxicity as determined by the MTT assay of the contrast agent. PPEG<sub>2000</sub>-GdNP and PPEG<sub>5000</sub>-PPEG<sub>1000</sub>-GdNP did not cause toxicities to mouse myoblast cells *in vitro*.

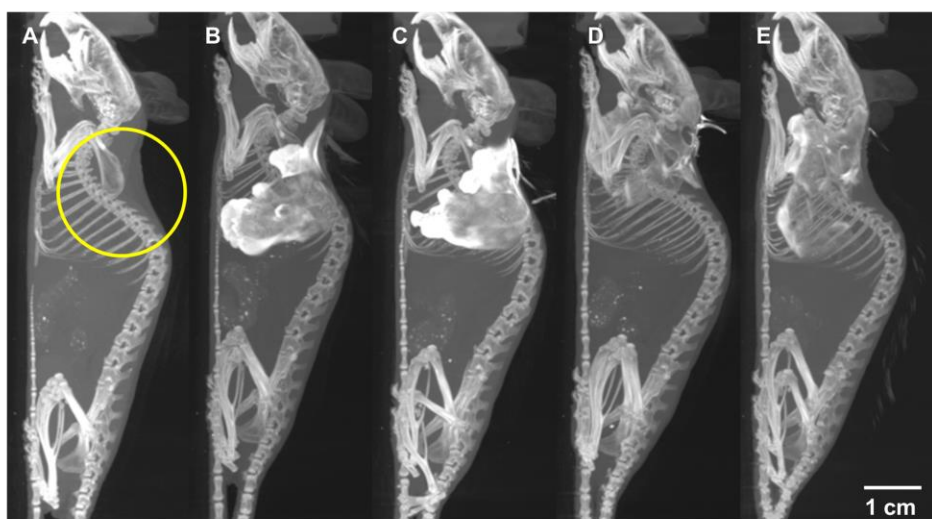


**Figure B.3.** Thick maximum intensity projections (5 cm) of mice injected subcutaneously. Representative subjects were imaged immediately after injection with A) saline, B) PPEG<sub>2000</sub>-GdNP, and C) PPEG<sub>5000</sub>-PPEG<sub>1000</sub>-GdNP. Images were also taken 2 weeks post-injections with D) PPEG<sub>2000</sub>-GdNP, and E) PPEG<sub>5000</sub>-PPEG<sub>1000</sub>-GdNP. The injection site (*i.e.* dorsal interscapular region) is identified by the circle in A.

## Histological analysis of excised tissues

Hematoxylin stains the nucleus purple, while eosin counterstains the cytosol and extracellular matrix pink.<sup>4</sup> The heart, kidney and bladder tissues of injected mice demonstrate no difference from control mouse tissues. Despite high gadolinium concentrations in the liver, no difference in histological images were observed. The trace amounts of gadolinium that were found in the lungs of PPEG<sub>5000</sub>-PPEG<sub>1000</sub>-GdNP-injected mice did not result in notable differences. Contrasting histological staining is demonstrated in the spleen, where control tissues have higher nuclear density than PPEG<sub>2000</sub>-GdNP- and PPEG<sub>5000</sub>-PPEG<sub>1000</sub>-GdNP-injected mice. The spleen sections from the control mouse demonstrates a deeper pink stain than the sections from injected mice, which appear purple. Although representative sections are displayed in Figure B.4, similar images were observed from different regions of the excised tissue.

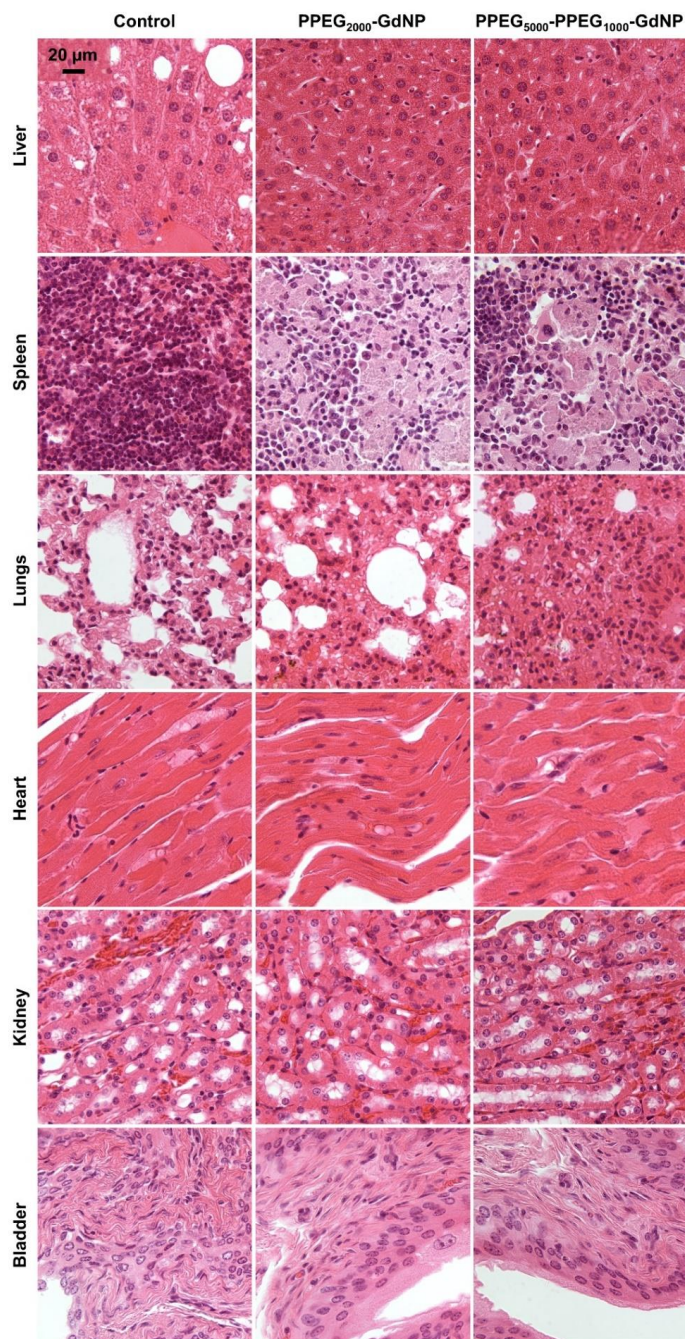


**Figure B.4.** Representative histology images for control and injected mice taken from tissues after 5 days of injection. The liver, lung, heart, kidney, and bladder tissues appear normal, while spleen tissue of the injected mice appear more purple than the staining observed in the control mouse, which appears pink.

## References

- (1) Dufort, S.; Le Duc, G.; Salome, M.; Bentivegna, V.; Sancey, L.; Brauer-Krisch, E.; Requardt, H.; Lux, F.; Coll, J. L.; Perriat, P.; Roux, S.; Tillement, O. The high radiosensitizing efficiency of a trace of gadolinium-based nanoparticles in tumors. *Sci. Rep.* **2016**, *6*, 29678.
- (2) Li, Z.; Zhang, Y. An efficient and user-friendly method for the synthesis of hexagonal-phase NaYF<sub>4</sub>:Yb, Er/Tm nanocrystals with controllable shape and upconversion fluorescence. *Nanotechnology* **2008**, *19*, 345606-345610.
- (3) Zhao, G.; Tong, L.; Cao, P.; Nitz, M.; Winnik, M. A. Functional PEG-PAMAM-tetraphosphonate capped NaLnF<sub>4</sub> nanoparticles and their colloidal stability in phosphate buffer. *Langmuir* **2014**, *30*, 6980-6989.
- (4) *Theory and practice of histological techniques / [edited by] John D. Bancroft, Marilyn Gamble.* 6th ed. ed.; Churchill Livingstone Elsevier: Edinburgh, 2008.

## Appendix C: Supporting Information for Chapter 4

### Matrix Factorization

The implementation of dual-energy computed tomography (DE CT) decompositions in Chapter 4 has been described in greater detail by Granton *et al.*<sup>1</sup> The decomposition algorithm relies on the solution of the following equations.

$$\mu_{soft\ tissue, HE} f_{soft\ tissue} + \mu_{bone, HE} f_{bone} + \mu_{gadolinium, HE} f_{gadolinium} = \mu_{HE} \quad (1)$$

$$\mu_{soft\ tissue, LE} f_{soft\ tissue} + \mu_{bone, LE} f_{bone} + \mu_{gadolinium, LE} f_{gadolinium} = \mu_{LE} \quad (2)$$

$$f_{soft\ tissue} + f_{bone} + f_{gadolinium} = 1 \quad (3)$$

In these equations, the known values are  $\mu_{soft\ tissue}$ ,  $\mu_{bone}$ , and  $\mu_{gadolinium}$ , which are linear attenuation coefficients measured in each volume element (voxel) of soft tissue, bone, and gadolinium, corresponding to the energy spectra indicated in the subscript (*i.e.* *HE* for high-energy and *LE* for low-energy), and  $\mu_{HE}$  and  $\mu_{LE}$ , which are linear attenuation coefficients in the high-energy and low-energy image, respectively. The algorithm solves for  $f_{soft\ tissue}$ ,  $f_{bone}$ , and  $f_{gadolinium}$ , which represent the volume fractions or the contribution of each material to the composition of a given voxel.

The linear attenuation coefficients are used interchangeably with the CT numbers that were measured from acquired CT images due to the linear relationship between the two. Hence,  $\mu_{soft\ tissue, HE}$ ,  $\mu_{bone, HE}$ , and  $\mu_{gadolinium, HE}$  were manually measured from calibrators, which were mouse-specific CT numbers from the bladder, femoral cortical bone, and abdominal aorta in the high-energy image, and likewise for low-energy CT numbers. The algorithm automatically extracts a three-dimensional  $\mu_{HE}$  and  $\mu_{LE}$  from the input low-energy and high-energy images. To calculate  $f_{soft\ tissue}$ ,  $f_{bone}$ , and  $f_{gadolinium}$ , the total for each voxel is restricted to 1 (*i.e.* 100% composition).

## CT Attenuations Used in the Decomposition Algorithm

**Table C.1.** Mouse-specific attenuation values that were used in the DE decomposition algorithm. CT attenuation was measured in  $(300 \mu\text{m})^3$  volumes, averaged from three ROIs within the same mouse tissue.

Mouse number	Attenuation in the low-energy image (HU)			Attenuation in the high-energy image (HU)		
	Bladder	Femoral Cortical Bone	Abdominal Aorta	Bladder	Femoral Cortical Bone	Abdominal Aorta
1	$57 \pm 33$	$1300 \pm 57$	$185 \pm 45$	$25 \pm 29$	$1203 \pm 43$	$160 \pm 22$
2	$26 \pm 22$	$1145 \pm 65$	$236 \pm 36$	$35 \pm 33$	$845 \pm 56$	$175 \pm 35$
3	$52 \pm 19$	$1250 \pm 35$	$225 \pm 37$	$-10 \pm 20$	$1050 \pm 55$	$170 \pm 29$
4	$-11 \pm 35$	$987 \pm 46$	$468 \pm 43$	$5 \pm 34$	$1039 \pm 39$	$466 \pm 53$
5	$19 \pm 25$	$1098 \pm 46$	$128 \pm 30$	$-42 \pm 25$	$827 \pm 38$	$104 \pm 39$
6	$80 \pm 19$	$1200 \pm 22$	$201 \pm 33$	$-20 \pm 24$	$909 \pm 46$	$111 \pm 34$
7	$52 \pm 22$	$1179 \pm 56$	$127 \pm 35$	$-30 \pm 43$	$954 \pm 39$	$101 \pm 30$
8	$3 \pm 37$	$1191 \pm 36$	$180 \pm 25$	$-54 \pm 42$	$974 \pm 55$	$131 \pm 29$

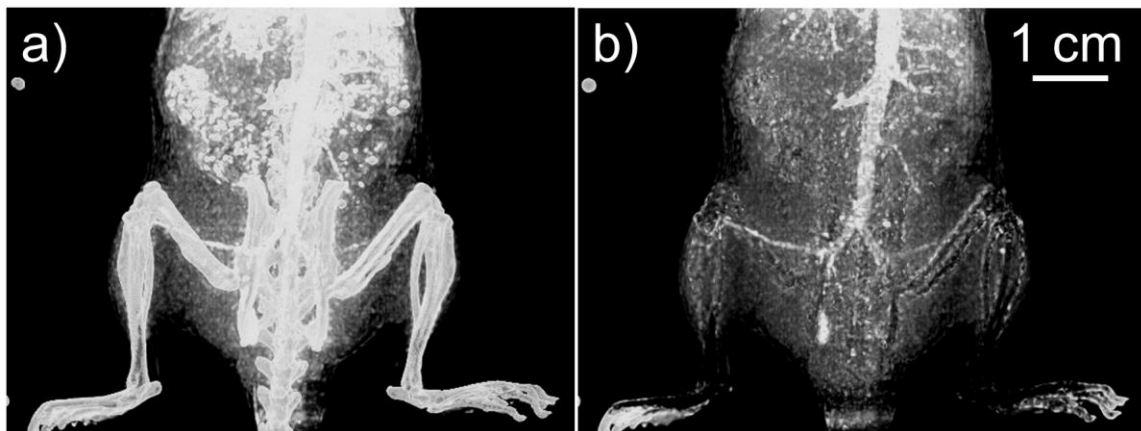


**Figure C.1.** Gadolinium-enhanced vessels image on a) non-registered and b) co-registered images. Substantial misclassification of bone and soft tissue in the gadolinium-enhanced vessels image occurs predominantly near tissue borders.

- (1) Granton, P. V.; Pollmann, S. I.; Ford, N. L.; Drangova, M.; Holdsworth, D. W. Implementation of dual- and triple-energy cone-beam micro-CT for postreconstruction material decomposition. *Med Phys* **2008**, *35*, 5030-5042.

## Appendix D: Copyright Permissions

RADIOLOGICAL SOCIETY OF NORTH AMERICA  
820 JORIE BLVD, OAK BROOK, IL 60523  
TEL 1-630-571-2670 FAX 1-630-571-7837  
RSNA.ORG



June 26, 2020

Charmainne Cruje

Canada

Dear Charmainne Cruje:

The Radiological Society of North America (RSNA®) is pleased to grant you permission to reproduce the following figures in print and electronic formats for use in your PhD thesis, provided you give full credit to the authors of the original publication.

Figures 10a, 10b, 10c, 10d  
Potter C A, Sodickson A D. Dual-energy CT in emergency neuroimaging: Added value and novel applications. *RadioGraphics* 2016;36:2186-2198.

This permission is a one-time, non-exclusive grant for English-language use and is exclusively limited to the usage stated and underlined above. The requestor guarantees to reproduce the material as originally published. Permission is granted under the condition that a full credit line is prominently placed (i.e. author name(s), journal name, copyright year, volume #, inclusive pages and copyright holder).

This permission becomes effective upon receipt of this signed contract. Please sign a copy of this agreement, return a signed copy to me and retain a copy for your files. Thank you for your interest in our publication.

[Print Name]: Charmainne Cruje

SIGNATURE: \_\_\_\_\_ Date: August 25, 2020

Sincerely,

Ashley E. Daly  
Senior Manager, Journal Rights & Communications  
Publications

Phone: 630-590-7771  
Fax: 630-590-7724  
E-mail: [permissions@rsna.org](mailto:permissions@rsna.org)

ELSEVIER LICENSE  
TERMS AND CONDITIONS

Aug 30, 2020

---

---

This Agreement between Charmainne Cruje ("You") and Elsevier ("Elsevier") consists of your license details and the terms and conditions provided by Elsevier and Copyright Clearance Center.

License Number	4855400319931
License date	Jun 24, 2020
Licensed Content Publisher	Elsevier
Licensed Content Publication	Mayo Clinic Proceedings
Licensed Content Title	Clinical Pharmacology, Uses, and Adverse Reactions of Iodinated Contrast Agents: A Primer for the Non-radiologist
Licensed Content Author	Jeffrey J. Pasternak, Eric E. Williamson
Licensed Content Date	Apr 1, 2012
Licensed Content Volume	87
Licensed Content Issue	4
Licensed Content Pages	13
Start Page	390
End Page	402

Type of Use	reuse in a thesis/dissertation
Portion	figures/tables/illustrations
Number of figures/tables/illustrations	1
Format	both print and electronic
Are you the author of this Elsevier article?	No
Will you be translating?	No
Title	Lanthanide nanoparticles as vascular contrast agents for in vivo dual energy micro-CT
Institution name	The University of Western Ontario
Expected presentation date	Sep 2020
Portions	2
	Charmaine Cruje
Requestor Location	Canada Attn: Charmaine Cruje
Publisher Tax ID	GB 494 6272 12
Total	0.00 CAD

SPRINGER NATURE LICENSE  
TERMS AND CONDITIONS

Aug 30, 2020

---

This Agreement between Charmaine Cruje ("You") and Springer Nature ("Springer Nature") consists of your license details and the terms and conditions provided by Springer Nature and Copyright Clearance Center.

License Number	4865440878712
License date	Jul 10, 2020
Licensed Content Publisher	Springer Nature
Licensed Content Publication	Nature Biotechnology
Licensed Content Title	Principles of nanoparticle design for overcoming biological barriers to drug delivery
Licensed Content Author	Elvin Blanco et al
Licensed Content Date	Sep 1, 2015
Type of Use	Thesis/Dissertation
Requestor type	academic/university or research institute
Format	print and electronic
Portion	figures/tables/illustrations
Number of figures/tables/illustrations	1

High-res required	no
Will you be translating?	no
Circulation/distribution	30 - 99
Author of this Springer Nature content	no
Title	Lanthanide nanoparticles as vascular contrast agents for in vivo dual energy micro-CT
Institution name	The University of Western Ontario
Expected presentation date	Sep 2020
Portions	Figure 5
	Charmainne Cruje
Requestor Location	Canada Attr: Charmainne Cruje
Total	0.00 CAD

**JOHN WILEY AND SONS LICENSE  
TERMS AND CONDITIONS**

Aug 30, 2020

---

---

This Agreement between Charmainne Cruje ("You") and John Wiley and Sons ("John Wiley and Sons") consists of your license details and the terms and conditions provided by John Wiley and Sons and Copyright Clearance Center.

License Number	4855400028749
License date	Jun 24, 2020
Licensed Content Publisher	John Wiley and Sons
Licensed Content Publication	NMR in Biomedicine
Licensed Content Title	Lipid-based nanoparticles for contrast-enhanced MRI and molecular imaging
Licensed Content Author	Klaas Nicolay, Arjan W. Griffioen, Geralda A. F. van Tilborg, et al
Licensed Content Date	Jan 31, 2006
Licensed Content Volume	19
Licensed Content Issue	1
Licensed Content Pages	23
Type of use	Dissertation/Thesis

Requestor type	University/Academic
Format	Print and electronic
Portion	Figure/table
Number of figures/tables	1
Will you be translating?	No
Title	Lanthanide nanoparticles as vascular contrast agents for in vivo dual energy micro-CT
Institution name	The University of Western Ontario
Expected presentation date	Sep 2020
Portions	Figure 1
	Charmainne Cruje
Requestor Location	Canada Attn: Charmainne Cruje
Publisher Tax ID	EU826007151
Total	0.00 CAD



Dear Ms. Cruje,

Thank you for seeking permission from SPIE to reprint material from our publications. The article you have requested to reprint from is published under Creative Commons (CC BY 4.0)—Gold Open Access. For articles published under CC BY 4.0, users are free to share (copy, distribute, and transmit), to remix (adapt), and to make commercial use of the Article under the following conditions:

**Attribution:** Users must attribute the contribution in the manner specified by the author or licensor (but not in any way that suggests that they or their use of the Article is endorsed by the Author or licensor). See citation formatting below.

**Notice:** For any reuse or distribution, users must make clear to others the license terms of this work, preferably using a link to the [Creative Commons webpage](#).

The full legal code of the CC BY 4.0 license can be found at <https://creativecommons.org/licenses/by/4.0/legalcode>.

**Citation format (Journals):**

Author(s), "Article Title," Journal Title and Volume Number (Issue), Article Number (Publication Date). [http://dx.doi.org/...](http://dx.doi.org/)

Please let me know if I may be of further assistance.

Sincerely,

SPIE is the international society for optics and photonics

<http://SPIE.org>

**SPIE.**

---

**From:** Charmainne Cruje  
**Sent:** Wednesday, July 15, 2020 9:52 AM  
**To:** reprint\_permission  
**Subject:** Reprint permission for thesis

Good afternoon,

I'd like to ask for permission to reprint the following:

**Title and author**

Dual-energy computed tomography using a gantry-based preclinical cone-beam microcomputed tomography scanner  
Justin J Tse, Joy Dunmore-Buyze, Maria Drangova, David W Holdsworth

**Volume, issue, and page numbers**

Volume 5, issue 3, 033503

**What you would like to reproduce**

Figure 4

**Where you will republish the requested material**

PhD Thesis

Thank you in advance for your consideration.

Sincerely,  
Charmainne

## Creative Commons Legal Code

---

### Attribution 4.0 International

Official translations of this license are available [in other languages](#).

Creative Commons Corporation ("Creative Commons") is not a law firm and does not provide legal services or legal advice. Distribution of Creative Commons public licenses does not create a lawyer-client or other relationship. Creative Commons makes its licenses and related information available on an "as-is" basis. Creative Commons gives no warranties regarding its licenses, any material licensed under their terms and conditions, or any related information. Creative Commons disclaims all liability for damages resulting from their use to the fullest extent possible.

#### **Using Creative Commons Public Licenses**

Creative Commons public licenses provide a standard set of terms and conditions that creators and other rights holders may use to share original works of authorship and other material subject to copyright and certain other rights specified in the public license below. The following considerations are for informational purposes only, are not exhaustive, and do not form part of our licenses.

**Considerations for licensors:** Our public licenses are intended for use by those authorized to give the public permission to use material in ways otherwise restricted by copyright and certain other rights. Our licenses are irrevocable. Licensors should read and understand the terms and conditions of the license they choose before applying it. Licensors should also secure all rights necessary before applying our licenses so that the public can reuse the material as expected. Licensors should clearly mark any material not subject to the license. This includes other CC-licensed material, or material used under an exception or limitation to copyright.

**Considerations for the public:** By using one of our public licenses, a licensor grants the public permission to use the licensed material under specified terms and conditions. If the licensor's permission is not necessary for any reason—for example, because of any applicable exception or limitation to copyright—then that use is not regulated by the license. Our licenses grant only permissions under copyright and certain other rights that a licensor has authority to grant. Use of the licensed material may still be restricted for other reasons, including because others have copyright or other rights in the material. A licensor may make special requests, such as asking that all changes be marked or described. Although not required by our licenses, you are encouraged to respect those requests where reasonable.

#### **Creative Commons Attribution 4.0 International Public License**

By exercising the Licensed Rights (defined below), You accept and agree to be bound by the terms and conditions of this Creative Commons Attribution 4.0 International Public License ("Public License"). To the extent this Public License may be interpreted as a contract, You are granted the Licensed Rights in consideration of Your acceptance of these terms and conditions, and the Licensor grants You such rights in consideration of benefits the Licensor receives from making the Licensed Material available under these terms and conditions.



Marketplace™

## Royal Society of Chemistry - License Terms and Conditions

This is a License Agreement between Charmaine Cruje ("You") and Royal Society of Chemistry ("Publisher") provided by Copyright Clearance Center ("CCC"). The license consists of your order details, the terms and conditions provided by Royal Society of Chemistry, and the CCC terms and conditions.

All payments must be made in full to CCC.

Order Date	29-Aug-2020	Type of Use	Republish in a thesis/dissertation
Order license ID	1059023-1	Publisher	RSC Pub
ISSN	2040-3372	Portion	Image/photo/illustration

### LICENSED CONTENT

Publication Title	Nanoscale	Publication Type	e-Journal
Article Title	Tantalum oxide nanoparticles as versatile contrast agents for X-ray computed tomography.	Start Page	7720
		End Page	7734
		Issue	14
Author/Editor	National Center for Nanoscience and Technology., Royal Society of Chemistry (Great Britain)	Volume	12
		URL	<a href="http://www.rsc.org/Publishing/journals/NR/index.asp">http://www.rsc.org/Publishing/journals/NR/index.asp</a>
Date	01/01/2009		
Language	English		
Country	United Kingdom of Great Britain and Northern Ireland		
Rightsholder	Royal Society of Chemistry		

### REQUEST DETAILS

Portion Type	Image/photo/illustration	Distribution	Worldwide
Number of images / photos / illustrations	1	Translation	Original language of publication
Format (select all that apply)	Electronic	Copies for the disabled?	No
Who will republish the content?	Academic institution	Minor editing privileges?	No
Duration of Use	Life of current edition	Incidental promotional use?	No
Lifetime Unit Quantity	Up to 499	Currency	CAD
Rights Requested	Main product		

### NEW WORK DETAILS

Title	Lanthanide nanoparticles as vascular contrast agent for micro-CT	Institution name	University of Western Ontario
-------	--	------------------	-------------------------------

Instructor name	Maria Drangova and Elizabeth R. Gillies	Expected presentation date	2020-09-01
-----------------	---	----------------------------	------------

#### ADDITIONAL DETAILS

---

Order reference number	N/A	The requesting person / organization to appear on the license	Charmaine Cruje
------------------------	-----	---	-----------------

#### REUSE CONTENT DETAILS

---

Title, description or numeric reference of the portion(s)	Tantalum oxide nanoparticles as versatile contrast agents for X-ray computed tomography	Title of the article/chapter the portion is from	Tantalum oxide nanoparticles as versatile contrast agents for X-ray computed tomography.
Editor of portion(s)	Shapiro, Erik M; Sempere, Lorenzo; Thomas, Jennifer; Kiupel, Matti; Blanco-Fernandez, Barbara; Shuboni, Dorela; Kenyon, Elizabeth; Volk, Maximilian C; Wieweora, Kaitlyn A.; Hix, Jeremy M. L.; Chakravarty, Shatadru	Author of portion(s)	Shapiro, Erik M; Sempere, Lorenzo; Thomas, Jennifer; Kiupel, Matti; Blanco-Fernandez, Barbara; Shuboni, Dorela; Kenyon, Elizabeth; Volk, Maximilian C; Wieweora, Kaitlyn A.; Hix, Jeremy M. L.; Chakravarty, Shatadru
Volume of serial or monograph	12	Issue, if republishing an article from a serial	14
Page or page range of portion	7720-7734	Publication date of portion	2020-01-01



## John Wiley & Sons - Books - License Terms and Conditions

This is a License Agreement between Charmainne Cruje ("You") and John Wiley & Sons - Books ("Publisher") provided by Copyright Clearance Center ("CCC"). The license consists of your order details, the terms and conditions provided by John Wiley & Sons - Books, and the CCC terms and conditions.

All payments must be made in full to CCC.

<b>Order Date</b>	31-Aug-2020	<b>Type of Use</b>	Republish in other published product
<b>Order license ID</b>	1059518-1	<b>Publisher</b>	WILEY-VCH PUB., INC. (GER); VCH VERLAGSGESELLSCHAFT MBH [ETC.]
<b>ISSN</b>	0570-0833	<b>Portion</b>	Image/photo/illustration

### LICENSED CONTENT

<b>Publication Title</b>	Angewandte Chemie. International edition in English	<b>Country</b>	Germany
<b>Author/Editor</b>	GESELLSCHAFT DEUTSCHER CHEMIKER.	<b>Rightsholder</b>	John Wiley & Sons - Books
<b>Date</b>	01/01/1962	<b>Publication Type</b>	Journal
<b>Language</b>	English		

### REQUEST DETAILS

<b>Portion Type</b>	Image/photo/illustration	<b>Distribution</b>	Worldwide
<b>Number of images / photos / illustrations</b>	1	<b>Translation</b>	Original language of publication
<b>Format (select all that apply)</b>	Electronic	<b>Copies for the disabled?</b>	No
<b>Who will republish the content?</b>	Academic institution	<b>Minor editing privileges?</b>	No
<b>Duration of Use</b>	Life of current edition	<b>Incidental promotional use?</b>	No
<b>Lifetime Unit Quantity</b>	Up to 499	<b>Currency</b>	CAD
<b>Rights Requested</b>	Main product		

### NEW WORK DETAILS

<b>Title</b>	Lanthanide nanoparticles as vascular contrast agents for in vivo dual energy micro-CT	<b>Produced by</b>	University of Western Ontario Thesis
<b>Author</b>	Charmainne Cruje	<b>Expected publication date</b>	2020-09-01

### ADDITIONAL DETAILS

---

Order reference number	N/A	The requesting person / organization to appear on the license	Charmaine Cruje
------------------------	-----	---	-----------------

### REUSE CONTENT DETAILS

---

Title, description or numeric reference of the portion(s)	Figure 1A	Title of the article/chapter the portion is from	A High-Performance Ytterbium-Based Nanoparticulate Contrast Agent for In Vivo X-Ray Computed Tomography Imaging
Editor of portion(s)	N/A	Author of portion(s)	GESELLSCHAFT DEUTSCHER CHEMIKER.
Volume of serial or monograph	51	Issue, if republishing an article from a serial	N/A
Page or page range of portion	1438	Publication date of portion	2011-12-30

## Curriculum Vitae

<b>Name:</b>	Charmainne Cruje
<b>Post-secondary Education and Degrees:</b>	Ph.D. Medical Biophysics The University of Western Ontario 2015-2020
	M.Sc. Biomedical Physics Ryerson University 2013-2015
	B.Sc. Physics Major, Minors in Mathematics and Biology The University of Toronto 2005-2010
<b>Honours and Awards:</b>	Nellie Farthing Fellowship in Medical Sciences 2018-2019
	Norman E. Nixon Marie Ramo Nixon Award 2018-2019
	Queen Elizabeth II Scholarship in Science and Technology 2017-2019
	Ontario Graduate Scholarship 2016-2017
	Western Graduate Research Scholarship 2015-2019
	Harold E. Johns Studentship Award 2008-2010
	Queen Elizabeth II Aiming for the Top Scholarship 2005-2006
<b>Related Work Experience</b>	Research Assistant The University of Western Ontario 2017-2019
	Teaching Assistant Ryerson University 2013-2015

## Publications

1. Cruje C, Dunmore-Buyze PJ, Nong Z, Lee JJ, Kiernan JA, Pickering JG, and Drangova M. 3D vessel-wall virtual histology of whole-body perfused mice using a novel heavy element stain. *Scientific Reports*. 2019;9(698):1-10.
2. Cruje C, Dunmore-Buyze PJ, MacDonald JP, Holdsworth DW, Drangova M, and Gillies ER. Polymer assembly encapsulation of lanthanide nanoparticles as contrast agents for in vivo micro-CT. *Biomacromolecules*. 2018;19(3):896-905.
3. Yohan D, Cruje C, Lu X, and Chithrani DB. Size-dependent gold nanoparticle interaction at nano–micro interface using both monolayer and multilayer (tissue-like) cell models. *Nano-Micro Lett*. 2016;8(1):44-53.
4. Cruje C, Yang C, Uertz J, van Prooijen M, and Chithrani DB. Optimization of PEG coated nanoscale gold particles for enhanced radiation therapy. *RSC Adv*. 2015;5(123):101525-32.
5. Carlone M, MacPherson M, Cruje C, Rangel A, McCabe R, and Nielsen M. Response to "Comment on 'ROC analysis in patient specific quality assurance' [Med. Phys. 40, 042103 (7pp.) (2013)]". *Med Phys*. 2015;42(7):4413.
6. Cruje C and Chithrani DB. Integration of peptides for enhanced uptake of PEGylated gold nanoparticles. *J Nanosci and Nanotech*. 2015;15(3):2125-31.
7. Yohan D, Cruje C, Lu X, and Chithrani DB. Elucidating the uptake and distribution of nanoparticles in solid tumors via a multilayered cell culture model. *Nano-Micro Lett*. 2015;7(2):127-137.
8. Cruje C and Chithrani DB. Polyethylene glycol density and length affects nanoparticle uptake by cancer cells. *J Nanomed Res*. 2014;1(1):00006.
9. Cruje C and Chithrani DB. Polyethylene glycol functionalized nanoparticles for improved cancer treatment. *Rev in Nanosci and Nanotech*. 2014;3(4):20-30.
10. Carlone M, Cruje C, Rangel A, McCabe R, Nielsen M, and MacPherson M. ROC analysis in patient specific quality assurance. *Med. Phys*. 2013;40(4):042103.

## Conference proceedings

1. Cruje C, Dunmore-Buyze PJ, Holdsworth DW, Gillies ER, and Drangova M. High-concentration gadolinium nanoparticles for pre-clinical vascular imaging. *Proc SPIE*. 2018;10573(105732N).
2. Cruje C, Tse J, Holdsworth DW, Gillies ER, and Drangova M. Blood-pool contrast agent for pre-clinical computed tomography. *Proc SPIE*. 2017;10132(101321M).

### Conference abstracts

1. Cruje C, Dunmore-Buyze PJ, Holdsworth DW, Gillies ER, and Drangova M (May 2019). Lanthanide nanoparticles as vascular contrast agents for microcomputed tomography. London Health Research Day, London, ON (Local, poster).
2. Cruje C, Grolman E, Dunmore-Buyze PJ, Holdsworth DW, Gillies ER, and Drangova M (March 2019). Lanthanide nanoparticles as vascular contrast agents for in vivo dual energy microcomputed tomography. ImNO Annual Meeting, London, ON (Regional, oral).
3. Dunmore-Buyze PJ, Cruje C, Nong Z, Lee JJ, Kiernan JA, Pickering JG, and Drangova M (March 2019). 3D micro-CT vessel-wall virtual histology: a novel tri-element stain and whole-body perfusion. ImNO Annual Meeting, London, ON (Regional, poster).
4. Tse J, Dunmore-Buyze PJ, Cruje C, Drangova M, and Holdsworth DW (March 2019). Soft tissue visualization of iodine-soaked samples via dual-energy computed tomography. ImNO Annual Meeting, London, ON (Regional, oral).
5. Grolman E, Cruje C, Drangova M, and Gillies ER (March 2019). Small gadolinium nanoparticles for pre-clinical computed tomography. ImNO Annual Meeting, London, ON (Regional, poster).
6. Cruje C, Dunmore-Buyze PJ, Holdsworth DW, Gillies ER, and Drangova M (May 2018). Lanthanide nanoparticles as vascular contrast agents for microcomputed tomography. Annual Canadian Biomaterials Meeting, Victoria, BC (International, oral).
7. Cruje C, Dunmore-Buyze PJ, Holdsworth DW, Gillies ER, and Drangova M (May 2018). Lanthanide nanoparticles as vascular contrast agents for microcomputed tomography. London Health Research Day, London, ON (Local, poster).
8. Cruje C, Dunmore-Buyze PJ, Holdsworth DW, Gillies ER, and Drangova M (March 2018). Lanthanide nanoparticles as vascular contrast agents for microcomputed tomography. ImNO Annual Meeting, Toronto, ON (Regional, oral).
9. Cruje C, Holdsworth DW, Gillies ER, and Drangova M (February 2018). High-concentration gadolinium nanoparticles for pre-clinical vascular imaging. SPIE Medical Imaging, Houston, TX (International, poster).
10. Cruje C, Holdsworth DW, Gillies ER, and Drangova M (July 2017). Gadolinium-based nanoparticles as contrast agents in CT. COMP Annual Scientific Meeting, Ottawa, ON (National, oral).

11. Cruje C, Holdsworth DW, Gillies ER, and Drangova M (May 2017). Gadolinium-based nanoparticles as vascular contrast agents for micro-computed tomography. Canadian Chemistry Conference and Exhibition, Toronto, ON (National, oral).
12. Cruje C, Holdsworth DW, Gillies ER, and Drangova M (March 2017). Gadolinium-based nanoparticles as vascular contrast agents in pre-clinical computed tomography. London Health Research Day, London, ON (Local, poster).
13. Cruje C, Holdsworth DW, Gillies ER, and Drangova M (March 2017). Gadolinium-based nanoparticles as vascular contrast agents in pre-clinical computed tomography. ImNO Annual Meeting, London, ON (Regional, oral).
14. Cruje C, Tse J, Holdsworth DW, Gillies ER, and Drangova M (February 2017). Blood-pool contrast agent for pre-clinical computed tomography. SPIE Medical Imaging, Orlando, FL (International, oral).
15. Cruje C, Nguon O, Gillies ER, and Drangova M (March 2016). Vascular contrast agent for pre-clinical dual energy computed tomography. ImNO Annual Meeting, Toronto, ON (Regional, oral).
16. Cruje C, Nguon O, Gillies ER, and Drangova M (March 2016). Vascular contrast agent for dual energy computed tomography. London Health Research Day, London, ON (Local, poster).
17. Cruje C and Chithrani DB (June 2015). Enhanced uptake of gold nanoparticles coated with polyethylene glycol. World Congress on Medical Physics and Biomedical Engineering, Toronto, ON (International, oral).
18. Cruje C and Chithrani DB (March 2015). Gold nanoparticles for chemotherapy. Current Research in Engineering, Science and Technology, Hamilton, ON (Local, oral).
19. Cruje C and Chithrani DB (March 2015). Gold nanoparticles for radiation therapy. RTi3 Radiation Therapy Conference, Toronto, ON (Regional, oral).
20. Cruje C and Chithrani DB (March 2015). Radiosensitization of cancer cells via cancer cell targeting gold nanoparticles. Molecular Med Tri-Con, San Francisco, CA (International, poster).
21. Cruje C and Chithrani DB (June 2014). Effect of pegylated gold nanoparticle core size on cancer cell uptake. CAP Congress, Sudbury, ON (National, oral).
22. Cruje C and Chithrani DB (June 2014). Polyethylene glycol coated gold nanoparticles. iBEST Symposium, Toronto, ON (Local, poster).
23. Sankrecha R, Cruje C, Crosier S, MacPherson M, Carlone M, and Wang Y (July 2011). Clinical implementation of electron monte carlo for breast boost radiation

therapy: a retrospective study to improve target volume dose coverage. Joint AAPM/COMP Meeting, Vancouver, BC (International, oral).

24. Nielsen M, Carlone M, Cruje C, MacPherson M. Validation of plan dose perturbation software for use in patient specific IMRT quality assurance (July 2011). Joint AAPM/COMP Meeting, Vancouver, BC (International, oral).